



# **DYNAMIC MODELLING OF INDUCTION MACHINES**

**Özdemir Göl**

**SUBMITTED FOR THE AWARD OF THE DEGREE OF  
DOCTOR OF PHILOSOPHY**

**in the  
Department of Electrical and Electronic Engineering  
at the  
University of Adelaide**

*Awarded 1993*

**March 1993**

## TABLE OF CONTENTS

Abstract	v
Statement	vii
Acknowledgement	viii
Nomenclature	ix
1 INDUCTION MACHINE MODELS	1
1.1 Prologue	1
1.2 This Thesis	4
1.3 Conventions and Notations	6
1.4 Maxwell's Field Equations	8
1.5 Possible Modelling Approaches	10
1.5.1 Field Approach	11
1.5.2 Circuit Approach	14
1.6 Solution Techniques	18
1.6.1 Analytical Methods	18
1.6.2 Numerical Methods	18
1.7 Scope of Application for Models	19
1.8 Object of Thesis Revisited	20

2.	HIGH FIDELITY HARMONIC CIRCUIT MODELS	22
2.1	Rationale for High Fidelity Circuit Modelling	22
2.2	Space Harmonics	23
2.2.1	Airgap m.m.f. of a Single Coil	23
2.2.2	Airgap m.m.f. of a Coil Group	29
2.2.3	Total Airgap m.m.f.	35
2.2.4	Airgap Flux	41
2.2.5	Induced e.m.f.s	42
2.2.6	Modelling Ramifications	45
2.2.7	Harmonic Truncation	46
2.3	Current Displacement	48
2.4	Core Losses	60
2.4.1	Hysteresis Losses	60
2.4.2	Eddy Current Losses	64
2.5	Saturation	76
2.6	The High Fidelity Harmonic Circuit Model	82
2.7	Time Harmonics	87
2.7.1	Supply Harmonics	88
2.7.2	Current Harmonics	91
2.8	Performance Prediction Using the Model	96
2.8.1	Sinusoidal Supply	99
2.8.2	Non-sinusoidal Conditions	102
3.	DYNAMIC MODELLING	108
3.1	Induction Machine Dynamics	108
3.2	Dynamic Modelling Approaches	112
3.3	Time Domain Formulation	115
3.4	State-Variable Formulation	119
3.5	Space Phasor Modelling	122

4.	A GENERAL MODEL	133
4.1	Preliminaries	133
4.1.1	Rationale for a General Model	133
4.1.2	The Discrete Circuit Model	135
4.1.3	Parameter Determination Aspects	139
4.2	Resistive Parameters	144
4.3	Inductive Parameters	146
4.3.1	Airgap Inductance of a Coil	148
4.3.2	Airgap Inductance of a Rotor Mesh	156
4.3.3	Slot Leakage Inductances	162
4.3.4	Coil-End Leakage Inductances	171
4.3.5	Mutual Inductances	174
4.4	Terminal Voltage Equations	233
4.5	Torque Equation	242
4.6	Model Utility	247
5.	MODEL VERIFICATION	248
5.1	Introduction	248
5.2	Test Results	249
5.2.1	Test Results - Machine I	249
5.2.2	Test Results - Machine II	257
5.3	High Fidelity Harmonic Circuit Model	267
5.3.1	Performance Prediction Using " 'Exact' Equivalent Circuit "	268
5.3.2	Performance Prediction with Enhanced Low-Order Models	274
5.3.3	Performance Prediction with High-Order High-Fidelity Model	290
5.4	Dynamic Modelling with Conventional	296

Models	
5.4.1 Dynamic Performance Prediction using Direct Phase Model	297
5.4.2 Dynamic Performance Prediction using d-q Model	303
5.4.3 Dynamic Performance Prediction using Space-Phasor Model	311
5.5 Dynamic Modelling with Discrete Circuit Model	317
5.5.1 Introduction	317
5.5.2 Model Formation	318
5.5.3 Simulation of Start-Up Transients (2-pole)	329
5.5.4 Effect of Parallel Connections on Start-Up Transients	352
5.5.5 Simulation of Rotor Discontinuities	360
5.5.6 Other Uses of Discrete Circuit Models	373
5.6 Observations	390
6. CONCLUSION	392
BIBLIOGRAPHY	395
APPENDICES	414
A.1 Calculation of Equivalent Coil Pitch	414
A.2 Machine I - Details	417
A.2.1 Name Plate Details	417
A.2.2 Core Details	417
A.2.3 Stator Winding Details	419

A.2.4 Model Parameters	420
A.3 Machine II - Details	423
A.3.1 Name Plate Details	423
A.3.2 Core Details	423
A.3.3 Stator Winding Details	425
A.3.4 Model Parameters	427
INDEX	428

## ABSTRACT

A great deal of attention has been paid to the modelling of induction machines under both steady state and dynamic operating conditions. Several different approaches adopted in formulating models include *field modelling*, based on the evaluation of the magnetic field within the machine space, and the *circuit modelling*, which uses lumped parameters. This thesis compares various different modelling approaches, and postulates that judiciously formed circuit models can be used in predicting, with acceptable accuracy, the performance of an induction machine under different operating conditions. Two approaches are developed in detail, both of which share a common starting point, namely the airgap magnetomotive force set up by a single energised coil. In the first approach, the magnetomotive force distribution is evaluated in terms of space harmonics, leading to the formation of high order harmonic circuit models. The inclusion in the models of such phenomena as saturation, current displacement and core losses dramatically improves the prediction accuracy, which justifies their being labelled as *high fidelity harmonic circuit models*. They are particularly suitable in evaluating any parasitic

behaviour under quasi dynamic operating conditions. The effects on the machine behaviour of a non-sinusoidal supply are accounted for by means of an aggregate time-harmonic supply model.

In contrast, the second approach is based on discrete circuit modelling, treating each coil within the machine as an individual circuit. The evaluation is carried out entirely in the time-domain, making the approach well suited to transient analysis. The generality of the model allows the global effects of local phenomena to be ascertained accurately. The validity of both modelling approaches is demonstrated by means of case studies.



## STATEMENT

This thesis contains no material which has been accepted for the award of any other degree or diploma in any University and that, to the best of my knowledge and belief, the thesis contains no material previously published or written by another person, except where due reference is made in the text of the thesis.

I consent to the thesis being made available for photocopying and loan.

Özdemir Göl

## ACKNOWLEDGEMENT

I gratefully acknowledge the support, encouragement and the able guidance I have received from Dr. A. M. Parker in the course of preparing this thesis.

## NOMENCLATURE

A	cross-sectional area, $\text{m}^2$
$\underline{A}$	vector magnetic potential, $\text{Wbm}^{-1}$
$\underline{a}$	unit vector in cartesian coordinates
$a$	number of parallel connections
$\underline{B}$	magnetic flux density, T
b	coil number within a group
C	number of coils in a group
$\tilde{c}$	wave number
D	damping coefficient, $\text{kg m}^2 \text{s}^{-1}$
$\underline{D}$	electric flux density, $\text{Cm}^{-2}$
$D^R$	rotor outer diameter, m
$D^S$	stator bore diameter, m
E	electromotive force, V
e	electromotive force (time variant), V
$\underline{E}$	electric field strength, $\text{Vm}^{-1}$
F	force, N
f	frequency, Hz

$F$	magnetomotive force, A
$f$	magnetomotive force (time variant), A
$G$	number of coil groups
$g$	the set of integers, i.e. $g = 0, \pm 1, \pm 2, \pm 3, \dots$
$H$	magnetic field strength, $\text{Am}^{-1}$
$h$	height, m
$I$	effective current, A
$i$	instantaneous current, A
$\Im$	imaginary part of a complex number
$J$	moment of inertia, $\text{kg m}^2$
$J$	current density, $\text{Am}^{-2}$
$j$	stator coil number
$k$	rotor mesh number
$\mathcal{K}$	skewing, m
$L$	inductance, H
$l$	length, m
$\mathcal{M}$	magnetisation, $\text{Am}^{-1}$
$m$	number of phases
$\underline{m}$	number of phase belts
$N$	number of turns per stator coil
$n$	rotational frequency, $\text{s}^{-1}$
$P$	active power, W
$p$	active power per unit volume, $\text{Wm}^{-3}$
$\mathcal{P}$	polarisation, $\text{Cm}^{-2}$
$p$	number of pole pairs
$P_e$	eddy current loss per unit volume, $\text{Wm}^{-3}$
$P_h$	hysteresis loss per unit volume, $\text{Wm}^{-3}$
$\mathbf{IP}$	Poynting vector, $\text{Wm}^{-2}$

$Q$	reactive power, VAR
$Q$	number of slots per pole
$q$	number of slots per pole per phase
$R$	resistance, $\Omega$
$\underline{r}$	unit vector
$\Re$	real part of a complex number
$\mathbb{R}$	reluctance, $H^{-1}$
$\mathcal{S}$	apparent power, VA
$S$	number of slots
$s$	slip
$T$	torque, Nm
$t$	time, s
$U$	potential difference, V
$u$	instantaneous voltage, V
$V$	scalar electric potential, V
$v$	velocity, $ms^{-1}$
$v$	volume, $m^3$
$W$	energy, W
$w$	energy density, $Wm^{-3}$
$w_b$	bar width, m
$w_c$	coil width, m
$w_o$	slot opening width, m
$w_s$	slot width, m
$X$	reactance, $\Omega$
$\chi$	distance, m
$Y$	admittance, S
$y$	number of slots per coil pitch
$y$	distance, m
$Z$	impedance, $\Omega$

$Z$	impedance, $\Omega$
$z$	distance, m
$\aleph$	slot angle, rad
$\alpha$	m.m.f. partitioning ratio over airgap circumference
$\underline{\alpha}$	angle (general), rad
$\underline{\beta}$	angle (general), rad
$\Gamma^R$	rotor circumference, m
$\Gamma^S$	stator bore circumference, m
$\gamma$	angular slot pitch, rad
$\Delta$	thickness of lamination, m
$\delta$	airgap distance, m
$\epsilon$	permittivity, $Fm^{-1}$
$\epsilon_0$	permittivity of vacuum, $8.854 \times 10^{-12} Fm^{-1}$
$\zeta$	m.m.f. partitioning ratio over a pole period
$\eta$	order of supply harmonic
$\Theta$	angular displacement between any two phase belts, rad
$\theta$	angular phase belt pitch, rad
$\vartheta$	rotor angular position, rad
$\vartheta_k$	angular position of $k^{\text{th}}$ rotor mesh, rad
$\iota$	linear phase belt pitch, m
$\kappa$	linear slot pitch, m
$\Lambda$	permeance, H
$\lambda$	permeance coefficient
$\mu$	order of current harmonic
$\mu$	permeability, $Hm^{-1}$
$\mu_0$	permeability of vacuum, $4\pi \times 10^{-7} Hm^{-1}$
$\mu_r$	relative permeability
$\nu$	order of space harmonic
$\Xi$	relative coil pitch

$\xi$	reluctivity, $\text{H}^{-1} \text{ m}$
$\rho$	volume charge density, $\text{Cm}^{-3}$
$\sigma$	conductivity, $\text{Sm}^{-1}$
$\zeta$	conductor density, $\text{m}^{-2}$
$\tau_c$	coil pitch, m
$\tau_p$	pole pitch, m
$\upsilon$	width of lamination region, m
$\Phi$	magnetic flux, Wb
$\phi$	phase displacement, rad
$\chi$	efficiency
$\Psi$	magnetic flux linkage, Wb
$\varphi$	phase delay, rad
$\omega$	angular frequency, $\text{rad s}^{-1}$



# 1

## INDUCTION MACHINE MODELS

### 1.1 Prologue

Induction machines belong to an elite amongst electromagnetic devices: over a century or so, they have reached maturity without losing the attraction they had at the beginning. This must be attributed to their simple and hence elegant structure, which teems with intellectually challenging problems, stemming from the presence of a spatially distributed magnetic field within the machine space traversing heterogeneous and partly anisotropic media with complex boundaries. While structural simplicity and innate robustness have assured the continuance of the universal popularity of induction machines, induction machine modelling has presented one of the most challenging tasks, which designers and users alike have pursued with fervent rigour from the outset.



Early induction machine models were ingeniously based on the concept of magnetically coupled circuits. These lumped parameter circuit models have proved their conceptual soundness in that they are still being used in one form or the other. Of these, the so-called "'exact' equivalent circuit" is the most well known.

The primordial models were characterised by extensive idealisations and simplifications. Some compensation for this simplification was provided by the introduction of "empirical constants", whilst realising that much more work needed to be done to increase the reliability of models, particularly to forecast any undesirable effects [1]. Such design choices as the ratio of stator slots to rotor slots, the winding configuration and the amount of skewing were all seen to have profound ramifications in terms of parasitic behaviour, manifested, among other things, by excessive noise, vibration or unsatisfactory run-up performance.

Parasitic behaviour had already been observed in the very early machines; for instance, already the second squirrel-cage induction machine exhibited by Dolivo Dobrovolski at an industrial fair in Hannover had suffered from the presence of cogging torques during start-up. The main preoccupation of induction machine designers thus became to be able to predict the quasi steady-state performance with reasonable accuracy [2]. However, users soon observed that evaluating the performance under transient conditions was equally important [3,4]. This observation appears to be at the root of a curious dichotomy which was to create major philosophical differences between the viewpoints of users and designers in terms of modelling. The former came to be solely interested in models capable of providing information on the external behaviour, without any regard to internal

phenomena. The latter had to, and did, maintain a keen interest in those internal aspects, of which users appeared to be oblivious, simply because it was the designers' responsibility to meet the operational requirements by means of a suitable arrangement of the internal aspects [2, 5, 6, 7, 8]. This dichotomy must be seen as the main cause of the chasm between the user and designer cultures. Unfortunately, most teachers of electrical machines have also embraced the user viewpoint, as evidenced from textbooks and classroom instruction, leading to an unbalanced view of induction machine modelling [9].

The philosophical differences have encouraged model development along various different paths. Designers have been anxious to improve model fidelity by paying closer attention to topology and materials whilst continuing to use circuit models [10,11]. Users, on the other hand, have become the major proponents of the so-called generalised electrical machine theory, based on terminal measurements and axis transformations [12,13]. In recent times, designers have had renewed interest in field modelling, since advances in digital computing have encouraged the application of numerical methods to solving field problems. Today, all approaches coexist, although circuit models are by and far the most preferred and relied upon type by both designers and users. This is probably best evidenced by the fact that, currently, field modelling techniques are mainly applied in order to obtain parameters of circuit models with greater accuracy, which are then used as the cardinal tools in evaluating the machine performance [14,15]. Reasons for this are pragmatic; ultimately the external performance, and not the internal phenomena, determine whether or not the machine is suitable for the task.

## 1.2 This Thesis

This thesis is based on the premise that there are occasions for which the conventional circuit models are unsuitable, either due to their coarseness or due to the extensive simplifying assumptions made in their formation. Such occasions may include, but are not limited to, the accurate prediction of performance characteristics for a balanced, symmetrical machine under normal operating conditions. However, conventional models are totally incapable of predicting the performance of a machine if, for instance, asymmetries are present, either arising from an unusual design or due to fault conditions. This is a serious handicap, especially if the *a priori* performance assessment of a machine affected by such features is an essential requirement. There is a shortfall of models capable of being used for predicting machine performance realistically when the machine deviates from the norm. This applies in particular to machine operation under dynamic conditions.

This thesis seeks to redress the shortfall. After an introductory review of the possible modelling approaches, the thesis proceeds by first developing steady state models which are capable of far greater prediction accuracy than is possible from the use of conventional low order models and then postulating generally applicable circuit models for realistic performance prediction under dynamic conditions. Initial emphasis on steady state models serves a dual purpose: it demonstrates the notional development of high-fidelity models suitable for the prediction of performance characteristics as required during routine machine design, and yields model parameters suitable for use in the subsequent development of dynamic models.

The models developed in this thesis are based on the notions that the -

- [a] modelling approach adopted must be appropriate to the task at hand,
- [b] resulting model must be reasonably simple to manipulate and
- [c] results predicted must be acceptably accurate.

The remainder of this chapter is devoted to an overview of main modelling techniques and the principles, on the basis of which they have been formed. The conventions and notations used throughout the thesis are explained in Section 1.3. Chapter 2 is based on my previous work and shows how harmonic modelling techniques can be employed to obtain high fidelity steady-state circuit models of induction machines. The resulting models are seen to be particularly suitable in predicting parasitic effects under quasi dynamic operating conditions. A great deal of care has been exercised in procuring the various model parameters, since the underlying considerations are equally relevant to the procurement of model parameters in the formulation of general models postulated later in the thesis. Chapter 3 introduces the notion of dynamic models for induction machines and gives examples of different approaches. Despite its brevity, Chapter 3 is pivotal in the further development of the thesis in that it lays the foundation for the dynamic modelling approach to be developed in the following chapter. Chapter 4 forms the bulk of the thesis, postulating a general circuit model capable of predicting machine

performance under both transient and steady state conditions. Chapter 5 shows the application of the modelling concepts developed in previous chapters, demonstrating the superiority of the resulting models when compared with conventional models. The main emphasis in this chapter is on discrete circuit models as a powerful tool in the *a priori* assessment of effects of asymmetries, attributable to either design peculiarities or faults, under dynamic operating conditions. Several cases are presented. Chapter 6 concludes the thesis with a brief review of the work presented.

### 1.3 Conventions and Notations

As far as practicable, the symbols and units used in this thesis are those recommended by ISO. Deviations should be clearly identifiable and are explained in both the text and the *nomenclature*. In addition, the following conventions are adopted throughout the thesis:







- Vector quantities are denoted by a tilde under a capital letter, viz.  $\underline{A}$ .
- A tilde above a symbol identifies a complex quantity, viz.  $\tilde{c}$ .
- Phasor quantities are differentiated from complex quantities in general by the use of a dot above a capital letter, viz.  $\dot{U}$ .
- Matrices are written in bold letters as square-bracketed quantities. For instance,  $[\mathbf{i}]$  represents a current matrix.

- In cases where matrices are concatenated to represent a system model, the resultant super matrix is shown using the egg-box notation, such as

$$\begin{bmatrix} [\mathbf{i}^S] \\ [\mathbf{i}^R] \end{bmatrix}$$

- Lower case letters are used for time-variant quantities, except where capital letters are used commonly to designate the same as in Maxwell's field equations.
- Capital letters are used to identify model parameters and generally time-invariant quantities.
- Superscripts are used to identify the region with which the specific quantity is associated.
- Capital S and R, when used as superscripts, designate stator and rotor affiliation respectively. For instance,  $L^R$  stands for a rotor inductance.
- In cases where rotor quantities are referred to the stator, these are primed, viz.  $'R^R$ .
- Subscripts are used for further identification. For example, the subscripts in  $L_{s,1}$  identify the slot leakage inductance for coil number 1.
- Both superscripts and subscripts are also used to imply mutuality. As an example,  $L_{1,2}^{S,R}$  designates the mutual inductance between stator coil 1 and rotor mesh 2.

- Lower case cursive  $p$  denotes the differential operator  $\frac{d}{dt}$ .
- In circuit models, the graphical symbols shown below have been used to differentiate between linear and non-linear model parameters.

	Linear	Non-linear
Resistance		
Reactance		
Impedance		

## 1.4 Maxwell's Field Equations

One needs to recognise that circuit models of induction machines, indeed those of all other electrical machines, are inextricably linked with spatially distributed electromagnetic fields [16]. This is why the abstract formulation of the magnetic field in terms of Maxwell's field equations assumes ultimate importance as the basis of any such model.

A spatially distributed magnetic field in any anisotropic medium can be completely described using the relativistic form of Maxwell's equations, given as below.

$$\nabla \times \underline{\underline{E}} = -\frac{\partial \underline{\underline{B}}}{\partial t} \quad (1)$$

$$\nabla \times \underline{\underline{H}} = \underline{\underline{J}} + \frac{\partial \underline{\underline{D}}}{\partial t} \quad (2)$$

$$\nabla \cdot \underline{\underline{D}} = \rho \quad (3)$$

$$\nabla \cdot \underline{\underline{B}} = 0 \quad (4)$$

and in conjunction with the following fundamental relationships.

$$\underline{\underline{D}} = \epsilon_0 \underline{\underline{E}} + \underline{\underline{P}} \quad (5)$$

$$\underline{\underline{B}} = \mu_0 (\underline{\underline{H}} + \underline{\underline{M}}) \quad (6)$$

$$d\underline{\underline{F}} = \rho d\upsilon (\underline{\underline{E}} + \underline{\underline{v}} \times \underline{\underline{B}}) \quad (7)$$

An alternative formulation of Equation (2) can be obtained by expressing  $\underline{\underline{H}}$  in terms of vector magnetic potential,  $\underline{\underline{A}}$ , defined as

$$\underline{\underline{B}} = \nabla \times \underline{\underline{A}} \quad (8)$$

The resulting form of the equation is commonly referred as the transient diffusion equation, which proves to be more suitable for use where iterative solution techniques are employed. However, it should be noted that the use of vector magnetic potential offers no advantage over and above applying Maxwell's equations directly, unless either the current density distribution is known or a reasonable approximation can be made in representing the current density distribution.



## 1.5 Possible Modelling Approaches

Various possible modelling approaches have become known over the years. These vary from low order circuit models obtained on the basis of terminal measurements on existing machines to three dimensional modelling techniques based on numerical methods. However, the following needs to be noted in adopting a suitable modelling approach.

- Modelling techniques which rely on terminal measurements for the determination of model parameters are only suitable for use as *a posteriori* models. Of necessity, such models are low order models, and although they can be extremely useful in evaluating the performance of an existing machine, they are of little, if any, value in terms of induction machine design [17,18].
- In the case of *a priori* models, as those used by designers, the model is formed on the basis of an intimate knowledge of the internal arrangements of the machine. Therefore, it is possible to obtain higher order, high fidelity models which are capable of greatly improved prediction accuracy. The modelling approaches to forming *a priori* models can be broadly categorised as the **field approach** and the **circuit approach**. The latter embraces both the electric circuit modelling approach [19,20] and magnetic circuit modelling approach [21,22,23]. It must be emphasised that the basis of all such models is the distribution of the electromagnetic field within the machine space, and the prediction accuracy depends, to a large degree, on the extent of approximations made in representing the field, regardless of which approach has been adopted.

**This thesis is primarily concerned with the formation of *a priori* models of induction machines, obtained using the circuit approach.**

### 1.5.1 Field approach

The knowledge of localised phenomena is of great importance to induction machine designers. The actual field distribution within the machine space ultimately determines the quality of performance; parasitic torques, noise, vibration and harmonic currents are all consequences of an unsuitable field distribution inside the machine. Therefore an exact representation of the field should enable the machine performance to be predicted accurately. Evidently, Maxwell's field equations would provide the foundation for such a complete model.

Unfortunately, techniques of analysis based on an analytical solution of Maxwell's equations are, due to the complexity of the boundaries, practically non-viable. The conditions are further exacerbated by the regional anisotropies and non-linearities. Even if solutions could be found, they would be of questionable value because of the difficulties in their interpretation. These difficulties have led to compromise techniques being proposed, which are formulated on the basis of field approximations within prominent regions [9,24,25].

Another modelling approach, based on Maxwell's equations, utilises the notion of "energy flux" as postulated by Poynting's theorem within various regions of the machine space [26]. If the energy flux, emanating from a given region is expressed as:

$$-\int_v \nabla \cdot \underline{\mathbf{P}} \, dv = \int_v \underline{\mathbf{J}} \times \underline{\mathbf{E}} \, dv + \frac{\partial}{\partial t} \int_v \left( \frac{1}{2} \epsilon E^2 + \frac{1}{2} \mu H^2 \right) \, dv \quad (9)$$

where  $\underline{\mathbf{P}}$  denotes the Poynting vector, defined by

$$\underline{\mathbf{P}} = \underline{\mathbf{E}} \times \underline{\mathbf{H}} \quad (10)$$

then for any given region within the machine, the first term on the right hand side of Equation (10) represents the power losses within the region, whereas the second term represents the rate of energy storage in the electric and magnetic fields respectively. For instance, applying Equation (10) to a rotor bar subregion within a slot region results in

$$-\int_v \nabla \cdot \underline{\mathbb{P}}_s^R d\upsilon = R_b^R i_b^{R^2} + L_b^R i_b^R \frac{di_b^R}{dt} \quad (11)$$

where  $R_b^R$  : rotor bar resistance,  $\Omega$

$L_b^R$  : rotor bar inductance, H.

The significance is that lumped parameters can be obtained, region by region, or subregion by subregion, directly from the evaluation of the Poynting vector. Thus the use of the Poynting vector can facilitate the formation of circuit models from field considerations. Model order can be controlled by the choice of the extent of the region or the subregion and, with reasonable assumptions, analytical solutions are relatively easy to obtain.

Numerical methods, on the other hand, are potentially capable of handling three-dimensional electromagnetic field problems without any restrictions [27]. However, they require the solution of a large number of linear equations. Evidently, only iterative methods are practical in obtaining convergent solutions and, as yet, computational effort required for complete solutions is almost unaffordable if three-dimensional, time-variant solutions are sought to be obtained accurately [15]. Even when it can be assumed that the field distribution is symmetrical, so that two-dimensional analysis yields a sufficiently accurate picture of the spatial

distribution of the field, the computational effort is enormous, except when steady state conditions are considered and grossly simplifying assumptions are made [28].

The most commonly used numerical method in induction machine analysis is the finite element analysis. Finite element methods of field solutions are particularly suitable in developing reasonable approximations in representing the current density distribution, since the method relies on successive iterations leading to convergent solutions. The use of vector magnetic potential offers computational advantages in facilitating this. The field is represented by the transient diffusion equation, which is obtained by substituting the vector magnetic potential of Equation (8) in Equation (2) and by rearranging as

$$\nabla \times (\xi \nabla \times \underline{A}) = -\sigma \left( \frac{\partial \underline{A}}{\partial t} + \nabla V \right) \quad (12)$$

where       $\xi$       : reluctance,  $H^{-1}m$   
               $\sigma$       : conductivity,  $Sm^{-1}$   
               $V$       : scalar electric potential, V.

Equation (12) can be used to obtain time-variant solutions on the basis of implicit time integration techniques, such as the Crank-Nicolson method, by evaluating the field sequentially in suitable time intervals [29, 30,31].

Although the field solutions on the basis of the foregoing are suitable in simulating the machine behaviour under quasi-dynamic operating conditions, the computational effort is extensive to analyse the transient

behaviour during even a very short period of time. This severely restricts the general application of finite element methods to the study of induction machine dynamics. Moreover, despite their intrinsic ability to deal with three dimensional field problems, most finite element solutions are based on the assumption of two dimensional symmetry for reasons stated previously . Furthermore, the practically important external aspects of behaviour still need to be determined by the use of circuit models, in that the information obtained from the finite element analysis is used in determining the model parameters of an associated lumped parameter circuit model [14,32,33]. This somewhat detracts from the promise that much more accurate performance predictions are possible if finite element models of induction machines are used in preference to lumped parameter circuit models [15]. Thus the main advantages of finite element techniques are seen to be their prowess in evaluating localised phenomena and in allowing parameters of circuit models to be ascertained with greater accuracy than is possible with conventional techniques [34,35]. For instance, saturation effects within their respective regions can be evaluated much more confidently with finite element analysis [15]. A further advantage of their use arises from being able to establish the initial conditions with greater accuracy for dynamic simulation when circuit models are used as the main tools in evaluating the transient behaviour of the machine.

### 1.5.2 Circuit approach

Since the inception of the induction machine around 1887 by Tesla, Ferraris and others, lumped parameter circuit models of induction machines have been in continuous use for the design and analysis of

induction machines. Hence, they have a long and well proven tradition for the prediction of overall machine characteristics.

At the outset, the emphasis was on the steady state operation and terminal behaviour. Several different modelling approaches have evolved over the years to cope with various problems presented by the specific tasks encountered by designers as well as users [36,37]. In the course of time, the emphasis has shifted from steady state analysis toward dynamic analysis [3]. Recently, this shift has accelerated, mainly due to the prevalence of variable speed operating schemes based on power electronics [38,39,40].

Initially, the circuit models proposed by early researchers were adapted to effect the transient analysis of induction machines [41]. These models are still used in one form or another. However, it is now widely recognised that such low-order models suffer from intrinsic weaknesses stemming from the assumptions made in their formation [17, 42, 43, 44]. Thus they are unlikely to be suitable in cases where the underlying simplifying assumptions are not justifiable.

Basically three approaches are possible when circuit modelling is adopted:

- 1 Phase models
- 2 Discrete circuit models
- 3 Combination of 1 and 2.

**Phase models** can vary from direct phase models to indirect models obtained on the basis of axis transformations. Direct phase models are also known as **a-b-c** models, whereas the derivative models based on phase

transformations are usually labelled as  $\alpha$ - $\beta$ -0 models, if referred to a stationary stator reference frame, and  $d$ - $q$ -0 models, if referred to a rotating reference frame attached to the rotor. The main advantage of a-b-c models is that the quantities predicted relate directly to physically measurable quantities [45,46]. Axis transformation techniques, on the other hand, offer computational advantages and generality, but suffer from being remote from physical quantities which can be measured directly.

Most phase models are formed on the basis of extensive assumptions [20]. The omission of phenomena responsible for certain effects from model formation is the main reason for poor correlation between the actual and predicted results in such models. This is simply because it is not possible to extract any information from a model relating to, for example, parasitic effects, unless the aspects which are responsible for their existence are incorporated in the model. For instance, all induction machines are subject to harmonic effects; these stem from non-sinusoidal time-variant quantities such as terminal voltages and currents, from the presence of slotted boundaries giving rise to permeance fluctuations as the rotor changes its position relative to the stator and the non-sinusoidal distribution of the airgap flux [47]. These effects are frequently represented in terms of time harmonics and space harmonics respectively [48, 49]. The absence of these harmonic effects from the model represents a serious shortcoming, if parasitic behaviour arising from harmonic interactions is significant.

The shortcomings can be overcome to a large extent by the use of the so-called *high fidelity* circuit models, which are based on the harmonic representation of non-sinusoidal quantities [50, 51]. In this approach the

harmonic effects are accounted for either by means of a single Fourier transform based on a discontinuous current sheet with sinusoidal currents or by means of multiple Fourier transforms, also accounting for the effects of permeance variations due to slotting as well as the non-sinusoidally varying currents [52, 53, 54]. This modelling approach is known to yield excellent correlation between actual and predicted results for balanced and symmetrical machines in steady state [20, 55]. The harmonic high-fidelity circuit models are particularly useful in the prediction of quasi-dynamic parasitic effects in most cases [56].

However, it has been observed that harmonic modelling is not always capable of accurately predicting parasitic behaviour, since the resulting model is basically still a global *per phase* model, which does not account for local aspects [57]. This concern is especially justifiable when asymmetries or discontinuities are present, whether they be intentional or unintentional [58, 59, 60, 61]. For instance, a high fidelity per phase model incorporating the higher order space and time harmonics is not capable of predicting parasitic behaviour which may be introduced by the presence of a fracture in the cage of a squirrel cage induction machine. In this case, **discrete circuit modelling** becomes attractive in the interest of accounting for the effect of localised phenomena. Discrete circuit models, which are derived by considering individual stator and rotor coils and the magnetic fields they link, constitute direct models. Hence, they are not restricted by the simplifying assumptions of transformation techniques. They are amenable to time-domain analysis, which makes them eminently suited to transient analysis. The price is the considerable increase in the number of simultaneous equations to be solved; the number of equations corresponds to the total number of stator and rotor coils. However, because the resulting equations are cyclic in form, the computational effort is not linearly proportional to the number of equations.



## 1.6 Solution Techniques

### 1.6.1 Analytical Methods

If, because of the simplifying assumptions adopted, the above modelling approaches lead to sets of linear differential equations, closed form solutions are relatively easy to obtain [62, 63, 64]. However, if the describing equations are non-linear with time-variant coefficients, analytical methods prove to be difficult, in which case iterative methods become indispensable.

### 1.6.2 Numerical Methods

In the case of circuit models, the mathematical description of the induction machine in the form of a set of simultaneous, non-linear differential equations with time variant coefficients can be solved using numerical methods [65]. Of these, one-step algorithms known as Runge-Kutta methods are widely used owing to their inherent stability and relatively modest memory requirements. Gauss-Seidel iterative methods may be employed to enhance the computational efficacy of Runge-Kutta methods.

The use of numerical techniques also facilitates the evaluation of field models [66]. Developments in computing capabilities have made it entirely feasible albeit limited to find solutions to Maxwell's equations by means of numerical methods [67]. In applying numerical methods to the analysis of time-variant magnetic fields, one approach has been to break down the field problem into two components: one describing its distribution in space, the other giving its time behaviour. The former is then treated using finite element methods, whereas the latter is evaluated

using a time-stepping procedure. Both implicit and explicit finite element techniques can be applied, although implicit techniques offer computational advantages owing to the larger time increments permissible and the inherent unconditional stability. But, considerably smaller time increments become essential as fast transients are investigated, thus diminishing the computational advantage of the implicit techniques [29, 31].

## 1.7 Scope of Application for Models

Induction machine models in their various guises, as postulated in the foregoing, are indispensable in evaluating the various different aspects of induction machine behaviour. For example, the simple lumped parameter phase models or their derivatives obtained on the basis of axis transformations are useful in the approximate assessment of the *steady state* behaviour of a symmetrical machine under *balanced* supply conditions, provided the simplifying assumptions made in their formation are justifiable [68]. The effect of external asymmetries, such as *unbalanced* supply conditions or unbalanced external impedances for the secondary circuits, can be accounted for by the use of modified versions of the reduced order models in conjunction with symmetrical components [59, 69]. The reduced order model representations are especially attractive in the development of control strategies for induction machine drives [70, 71, 72] and in investigating multi-machine system behaviour [73, 74]. However, if parasitic behaviour arising from such aspects as the finite distribution of windings, saturation of the magnetic core and the non-

uniform current distribution in conductors is to be projected accurately, the model fidelity must be enhanced. This can be done in a number of ways; high fidelity harmonic circuit models [19, 55], field models based on finite element analysis [27, 29, 75] and hybrid models obtained from a combination of field models and circuit models have all been successfully employed [14, 34, 76]. Direct or transformed phase models can also be used to evaluate the machine performance under *transient* conditions [77]. In so doing, one commonly assumes that the rotor speed remains constant during transient operation, which leads to a set of differential equations with linear coefficients. Other techniques for transient analysis include complex frequency domain formulations [57,78] and current vector approach [79, 80, 81, 82].

The consequences of localised phenomena are best evaluated using distributed parameter models. Finite element models [35, 83, 84] and discrete circuit models belong to this category [85, 86]. Both types are intrinsically suitable for the assessment of both the steady state and dynamic regimes, although in the case of finite element models the extent of computational effort may pose severe restrictions on usability when transient behaviour is to be evaluated.

## **1.8 Object of Thesis Revisited**

The object of this thesis is to show how effective circuit models can be formulated which are capable of predicting with acceptable accuracy the performance of an induction machine under either steady state or transient conditions or both. Two approaches will be presented:

1 harmonic modelling

2 discrete circuit modelling.

Both approaches emanate from the consideration of the airgap flux distribution due to a single coil. However, harmonic modelling is based on the Fourier transform at the single coil level, facilitating the transition from the time domain to the complex domain, whereas the discrete circuit modelling is effectuated entirely in the time domain. The high fidelity harmonic circuit models, formed using the harmonic modelling approach, are especially valuable in predicting accurately the machine performance under balanced quasi dynamic conditions. Still, they represent the aggregate effect of the energised coils on the performance of the machine without being able to account for local anomalies. This is where the discrete circuit modelling approach comes into its own: it intrinsically allows the localised features to be represented. Thus, this thesis will postulate discrete circuit models which can account for asymmetries, including discontinuities arising from faults, and which can be used in reliably predicting the induction machine performance under both transient and steady-state conditions.

# 2

## HIGH FIDELITY HARMONIC CIRCUIT MODELS

### 2.1 Rationale for High Fidelity Circuit Modelling

The commonly adopted assumptions in induction machine modelling lead to gross inaccuracies in performance prediction. There is substantiated and well documented justification for increasing model fidelity, if the ensuing models are to be reliable. It stands to reason that model fidelity can be enhanced by the inclusion in the model of parameters representative of phenomena which affect machine performance. Factors which behove consideration with the promise of improving the prediction accuracy are those rooted in the topology of the machine and the core materials.

It has been shown that the prediction accuracy of a per phase circuit model can be impressively improved if special attention is paid to the following aspects [20]:

- 1 space harmonics, which are attributable to the discrete distribution of the machine windings,
- 2 saturation effects due to the non-linearities in the permeability of the core materials,
- 3 non-uniform current density distribution in the conductors, especially in a cage rotor,
- 4 core losses due to eddy currents and hysteresis, and
- 5 time harmonics arising from the non-sinusoidal supply voltages and phase currents,

Circuit models which include the effects of harmonics constitute *harmonic circuit models*. Model fidelity of a harmonic circuit model can be improved greatly by incorporating in the model such other phenomena as those mentioned above; this leads to the formation of *high fidelity harmonic circuit models*. This chapter is devoted to the development of such, which are unquestionably of great value in the design of induction machines.

## 2.2 Space Harmonics

### 2.2.1 Airgap m.m.f. of a Single Coil

Harmonic circuit modelling of induction machines is based on the Fourier series representation of the magnetomotive force (m.m.f.) distribution due to the discrete placement of coils belonging to m-phases of a winding in individual slots. Considering a single short-pitched coil as in Figure 1, the corresponding harmonic m.m.f. expressions can be developed as shown below.

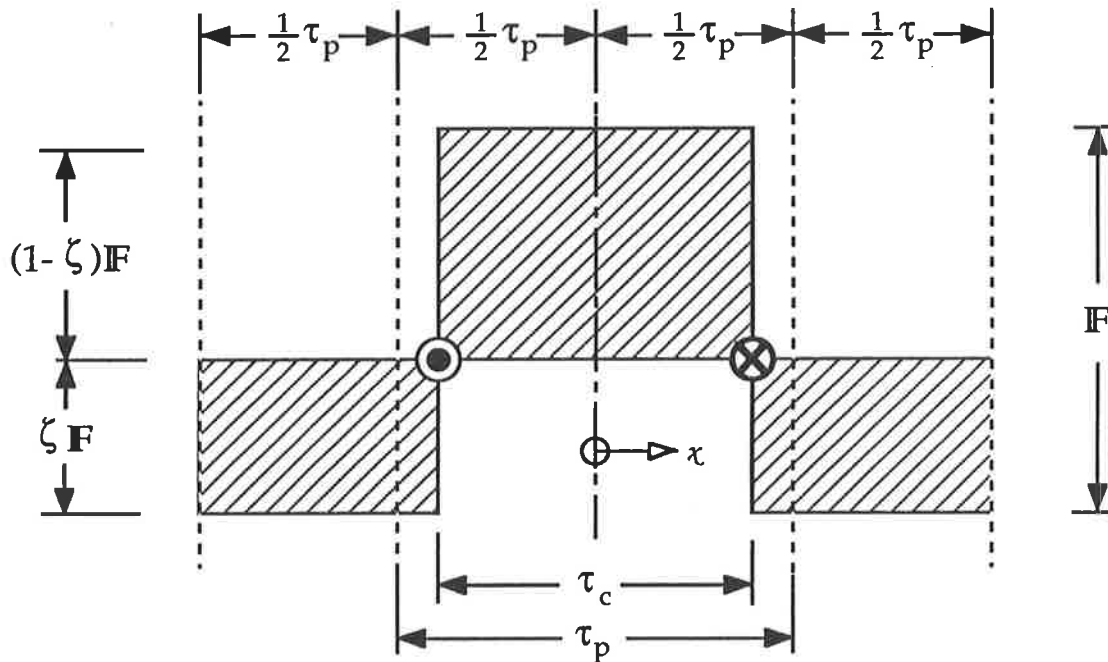


Figure 1

m.m.f. distribution of a single short-pitched coil over a pole pair

Figure 1 depicts the m.m.f. distribution of a short pitched coil over a pole period,  $2\tau_p$ , assuming the coil side to be concentrated at the slot centre and without accounting for the effect of slot openings. The abscissa is positioned in such a way that the principle of flux conservation is satisfied.  $\zeta$  denotes the m.m.f. partitioning ratio for this requirement, and can be obtained as

$$\zeta = \frac{\tau_c}{2\tau_p} \quad (13)$$

where  $\tau_c$  : coil pitch, m  
 $\tau_p$  : pole pitch, m.

Alternatively,  $\zeta$  can be given in terms of slot numbers corresponding to  $\tau_c$  and  $\tau_p$  as

$$\zeta = \frac{p(y-1)}{S^s} \quad (14)$$

where  $p$  : number of pole pairs  
 $y$  : number of slots per coil pitch  
 $S^s$  : number of stator slots.

If a current  $i(t)$  flows in a single, short-pitched coil with  $N$  turns, the resultant m.m.f. at a circumferential distance  $\chi$  for an instantaneous value of  $i(t)$  is given by

$$\mathbf{F}(\chi) = N i \quad (15)$$

Placing the origin arbitrarily at the centre of the coil as in Figure 1 and applying Fourier transform,  $\mathbf{F}(\chi)$  can be obtained, in terms of *space harmonics*, as

$$\mathbf{F}(\chi) = \sum_{v=1}^{\infty} \mathbf{F}_v \cos\left(v \frac{\chi}{\tau_p} \pi\right) \quad (16)$$

where

$$\mathbf{F}_v = \frac{1}{\tau_p} \int_0^{2\tau_p} \mathbf{F}(\chi) \cos\left(v \frac{\chi}{\tau_p} \pi\right) d\chi \quad (17)$$



Considering that  $\mathbf{F}(\chi)$  for various regions over a pole pair is

$$\mathbf{F}(\chi) = \begin{cases} (1-\zeta) \mathbf{F} & \text{if } 0 < \chi < \frac{1}{2} \tau_c \\ -\zeta \mathbf{F} & \text{if } \frac{1}{2} \tau_c < \chi < 2\tau_p - \frac{1}{2} \tau_c \\ (1-\zeta) \mathbf{F} & \text{if } 2\tau_p - \frac{1}{2} \tau_c < \chi < 2\tau_p \end{cases} \quad (18)$$

the value of  $\mathbf{F}_v$  can be calculated from

$$\mathbf{F}_v = \frac{1}{\tau_p} \left[ \int_0^{\frac{1}{2} \tau_c} (1-\zeta) \mathbf{F} \cos\left(v \frac{\chi}{\tau_p} \pi\right) d\chi - \int_{\frac{1}{2} \tau_c}^{2\tau_p - \frac{1}{2} \tau_c} \zeta \mathbf{F} \cos\left(v \frac{\chi}{\tau_p} \pi\right) d\chi + \int_{2\tau_p - \frac{1}{2} \tau_c}^{2\tau_p} (1-\zeta) \mathbf{F} \cos\left(v \frac{\chi}{\tau_p} \pi\right) d\chi \right] \quad (19)$$

as

$$\mathbf{F}_v = \mathbf{F} \frac{2}{v\pi} \sin\left(v \frac{\tau_c}{\tau_p} \frac{\pi}{2}\right) \quad (20)$$

The ratio of the coil pitch  $\tau_c$  to pole pitch  $\tau_p$  is the *relative coil pitch*  $\Xi$ , viz.

$$\Xi = \frac{\tau_c}{\tau_p} \quad (21)$$

Substituting  $\Xi$  in Equation (20) and with Equation (16), the m.m.f. expression for a single short-pitched coil is finally obtained as

$$\mathbf{F}(\chi) = \frac{2}{\pi} N i \sum_{v=1}^{\infty} \frac{1}{v} \sin\left(v \Xi \frac{\pi}{2}\right) \cos\left(v \frac{\chi}{\tau_p} \pi\right) \quad (22)$$

An alternative form of expression for the m.m.f. of Equation (22) can be given as

$$\mathbf{F}(\chi) = \frac{2}{\pi} N i \sum_{v=1}^{\infty} \frac{1}{v} k_{pv} \cos\left(v \frac{\chi}{\tau_p} \pi\right) \quad (23)$$

where

$$k_{pv} = \sin\left(v \Xi \frac{\pi}{2}\right) \quad (24)$$

The factor  $k_{pv}$  represents the effect of chording on each of the coil m.m.f. harmonics. Hence it is termed the *coil pitch factor* for the  $v^{\text{th}}$  space harmonic. Because of the asymmetrical distribution of the coil m.m.f. of a short pitched coil with reference to the circumferential abscissa, as depicted in Figure 1, both odd and even harmonics exist in Equations (22) and (23).

For a full-pitch coil,  $\Xi = 1$ . Thus, the m.m.f. expression is reduced to

$$\mathbf{F}(\chi) = \frac{2}{\pi} N i \sum_{v=1}^{\infty} \frac{1}{v} (-1)^g \cos\left(v \frac{\chi}{\tau_p} \pi\right) \quad (25)$$

where

$$g = v - 1 \quad (26)$$

$$v = 1, 3, 5, \dots \quad (27)$$

Since the m.m.f. of a full-pitch coil is distributed symmetrically with reference to the abscissa, only odd harmonics are present in Equation (25) as indicated by Equation (27). Evidently, the amplitude of each odd space harmonic for a full-pitch coil can be obtained as

$$\hat{\mathbf{F}}_v(\chi) \Big|_{\chi=0} = \frac{2}{\pi} N i \frac{1}{v} (-1)^g \quad (28)$$

### 2.2.2 Airgap m.m.f. of a Coil Group

The airgap m.m.f. for a group of coils comprising a pair of phase belts can be obtained by superposition on the basis of Equation (22). The resultant m.m.f. distribution for a coil group carrying the current  $i(t)$  is illustrated in Figure 2. It should be noted that the m.m.f. distribution depicted remains the same regardless whether the winding has identical coils or concentric coils, as long as phase belt positions are the same. Therefore any winding with identical coils can be replaced with one which has equivalent axisymmetric coils, as long as the number of slots per phase belt is an integer. This has obvious advantages in analytical terms since the axial symmetry is maintained. Provided that a corresponding equivalent axisymmetric coil pitch is defined for each coil within the group, the m.m.f. expression for the coil group can be obtained by superposition as

$$\mathbf{F}_c(\chi) = \sum_{b=1}^c \mathbf{F}_b(\chi) \quad (29)$$

where  $\mathbf{F}_c(\chi)$  : m.m.f. due to a group of  $c$  coils as a function of circumferential distance

$\mathbf{F}_b(\chi)$  : m.m.f. of  $b^{\text{th}}$  concentric and axisymmetric coil as a function of circumferential distance

The number of coils,  $C$ , within the coil group is given by

$$C = \frac{S}{2pm} = q \quad (30)$$

for a *single layer* winding and by

$$C = \frac{S}{pm} = 2q \quad (31)$$

in the case of a *double layer* winding, with

- S : number of slots
- p : number of pole pairs
- m : number of phases
- q : number of slots per pole per phase

The magnetomotive force for each of the individual coils within the coil group can be obtained as

$$\mathbf{F}_b(\chi) = \frac{2}{\pi} Ni \sum_{v=1}^{\infty} \frac{1}{v} \sin\left(v \Xi_b \frac{\pi}{2}\right) \cos\left(v \frac{\chi}{\tau_p} \pi\right) \quad (32)$$

where  $\Xi_b$  is the *relative coil pitch*, either for the axisymmetric coil  $b$  belonging to an axisymmetric winding or the equivalent axisymmetric coil  $b$  for a winding with identical coils. Obviously,  $\Xi_b$  is defined as

$$\Xi_b = \frac{\tau_{cb}}{\tau_p} = \frac{\tau_{cb}}{\tau_p} \quad (33)$$

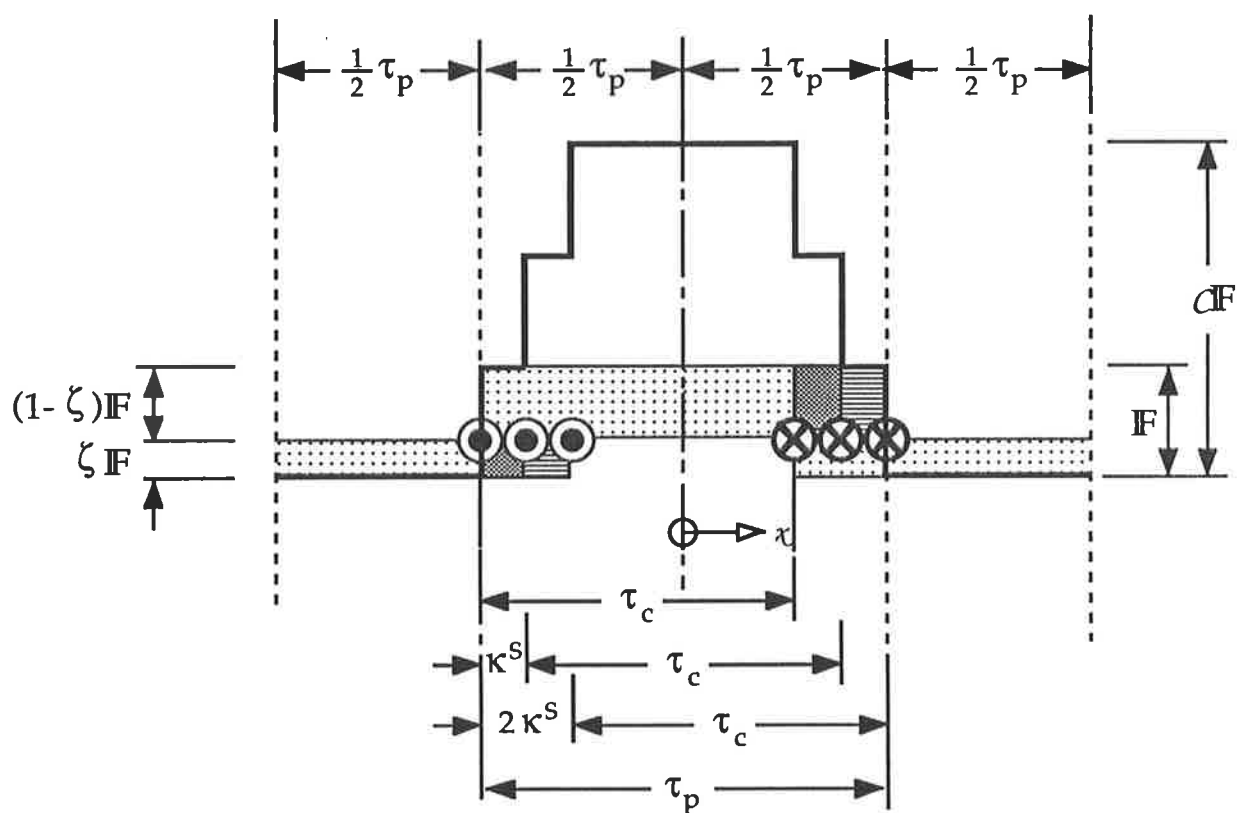


Figure 2

Magnetomotive force distribution over a pole pair due to a group of  $C$  coils

In the case of a winding with identical coils with a coil pitch  $\tau_c$ , the equivalent coil pitch  $\tau_{c_b}$  is obtained from

$$\tau_{c_b} = \tau_c - (q - a) \kappa^S \quad (34)$$

with

$$a = 2 \underline{b} - 1$$

$$\underline{b} = 1, 2, \dots, q \quad (35)$$

$\underline{b}$  denotes the number of the fictitious equivalent coil within the coil group (See Appendix 1 for further details). With these considerations, the airgap m.m.f. for a coil group can be expressed as

$$\mathbb{F}_C(\chi) = \frac{2}{\pi} Ni \sum_{\underline{b}=1}^c \sum_{v=1}^{\infty} \frac{1}{v} \sin\left(v \Xi_{\underline{b}} \frac{\pi}{2}\right) \cos\left(v \frac{\chi}{\tau_P} \pi\right) \quad (36)$$

On the other hand, in Equation (36) the summation term given by

$$\sum_{\underline{b}=1}^c \sin\left(v \Xi_{\underline{b}} \frac{\pi}{2}\right)$$

can be replaced by introducing the *coil group factor*, defined as

$$k_{cv} = \frac{1}{C} \sum_{b=1}^c \sin \left( v \Xi_b \frac{\pi}{2} \right) \quad (37)$$

This reduces Equation (36) to

$$F_C(\chi) = \frac{2}{\pi} C N i \sum_{v=1}^{\infty} \frac{1}{v} k_{cv} \cos \left( v \frac{\chi}{\tau_p} \pi \right) \quad (38)$$

It should be noted that the coil group factor,  $k_{cv}$ , can also be expressed in terms of a *coil pitch factor*,  $k_{pv}$ , and a *distribution factor*,  $k_{dv}$ , as

$$k_{cv} = k_{pv} k_{dv} \quad (39)$$

In Equation (39), the coil pitch factor is given by Equation (24), whereas the distribution factor is defined as

$$k_{dv} = \frac{\sin v C \frac{\aleph}{2}}{C \sin v \frac{\aleph}{2}} \quad (40)$$

where slot angle,  $\aleph$ , is

$$\aleph = \frac{2\pi p}{S} \quad (41)$$



Equations (36) and (38) represent the airgap m.m.f. of the datum coil group. Evidently, the airgap m.m.f. of the  $(\epsilon+1)^{\text{th}}$  coil group can be obtained from similar considerations by taking into account its angular position with reference to this datum coil. For a symmetrical  $m$ -phase winding, the circumferential bore distance between two contiguous coil groups is

$$\iota = \frac{2\tau_p}{\underline{m}} \quad (42)$$

which corresponds, in "electrical" degrees, to an angular displacement of

$$\theta = \frac{2\pi}{\underline{m}} \quad (43)$$

where  $\underline{m}$  is the number of phase belts per pole pair. In Equations (42) and (43),  $\iota$  and  $\theta$  denote the *linear phase belt pitch* and *angular phase belt pitch* respectively. It follows that the angular displacement between the axes of the  $(\epsilon+1)^{\text{th}}$  coil group and the datum coil group must be

$$\Theta_{\epsilon+1} = \epsilon \theta \quad (44)$$

Consequently, using Equation (36), the m.m.f. of the  $(\epsilon+1)^{\text{th}}$  coil group can be expressed in the form

$$\mathbb{F}_c(\chi) \Big|_{\epsilon+1} = \frac{2}{\pi} \text{Ni} \Big|_{\epsilon+1} \sum_{\mathfrak{b}=1}^c \sum_{\nu=1}^{\infty} \frac{1}{\nu} \sin\left(\nu \Xi_{\mathfrak{b}} \frac{\pi}{2}\right) \cos\left[\nu \left(\frac{\chi}{\tau_p} \pi - \Theta_{\epsilon+1}\right)\right] \quad (45)$$

or, in reduced form as

$$\mathbf{F}_c(\chi) \Big|_{\varepsilon+1} = \frac{2}{\pi} CN i \Big|_{\varepsilon+1} \sum_{v=1}^{\infty} \frac{1}{v} k_{cv} \cos \left[ v \left( \frac{\chi}{\tau_p} \pi - \Theta_{\varepsilon+1} \right) \right] \quad (46)$$

Equation (46) thus represents the m.m.f. at a circumferential distance  $\chi$  due to the  $(\varepsilon+1)^{\text{th}}$  coil group with an angular displacement of  $\Theta_{\varepsilon+1}$ .

### 2.2.3 Total Airgap m.m.f.

The total airgap m.m.f., when all coil groups belonging to  $m$  phases of a winding are energised simultaneously with phase different currents, can be obtained by the superposition of all magnetomotive forces due to the individual coil groups. Thus, using Equation (45), the total airgap m.m.f. can be generally expressed as

$$\mathbf{F}(\chi, t)_{\text{total}} = \sum_{\varepsilon=0}^{\frac{m}{2}-1} \sum_{b=1}^c \sum_{v=1}^{\infty} i \Big|_{\varepsilon+1} \frac{1}{v} \sin \left( v \Xi_b \frac{\pi}{2} \right) \cos \left\{ v \left( \frac{\chi}{\tau_p} \pi - \Theta_{\varepsilon+1} \right) \right\} \quad (47)$$

So far, the magnetomotive force has been obtained in terms of the instantaneous value of the current,  $i$ . A more general m.m.f. expression can be obtained by considering the time variation of the current,  $i(t)$ . If, for convenience, the  $m$  phase currents can be assumed to be sinusoidal and balanced, the phase shift between two sequential currents is

$$\phi = \frac{2\pi}{m} \quad (48)$$

Considering the relationship between the number of phases,  $m$ , and the number of phase belts,  $\underline{m}$ , which is

$$\underline{m} = 2mp \quad (49)$$

the phase shift can also be given as

$$\phi = \frac{4\pi}{\underline{m}} p \quad (50)$$

or, with Equation (43), as

$$\phi = 2p\theta \quad (51)$$

Thus, with reference to the current of the datum coil group, the current  $i(t)$  for the  $(\epsilon+1)^{\text{th}}$  coil group has a phase delay of

$$\phi_{\epsilon+1} = \epsilon 2p\theta \quad (52)$$

or considering Equation (44)

$$\phi_{\epsilon+1} = 2p \Theta_{\epsilon+1} \quad (53)$$

With this phase delay, the current of the  $(\epsilon+1)^{\text{th}}$  coil group can be expressed as

$$i(t) \Big|_{\epsilon+1} = \sqrt{2} I \sin(\omega t - \phi_{\epsilon+1}) \quad (54)$$

Substituting this current into Equation (47) and using trigonometric identities, total airgap m.m.f. when all  $m$  phases of the winding are connected to an  $m$ -phase supply can be obtained as a function of both circumferential distance and time as

$$\mathbf{F}(\chi, t)_{\text{total}} =$$

$$= \frac{\sqrt{2}}{\pi} NI \sum_{\epsilon=0}^{\frac{m}{2}-1} \sum_{b=1}^c \sum_{v=1}^{\infty} \sin\left(v \Xi_b \frac{\pi}{2}\right) \left[ \sin(\alpha - v\beta) + \sin(\alpha + v\beta) \right]$$

$$(55)$$

where  $\underline{\alpha}$  and  $\underline{\beta}$  refer to the position in time and space respectively of the  $v^{\text{th}}$  m.m.f. harmonic for the  $(\varepsilon+1)^{\text{th}}$  coil group.  $\underline{\alpha}$  and  $\underline{\beta}$  are given as

$$\underline{\alpha} = \omega t - \phi_{\varepsilon+1} \quad (56)$$

and

$$\underline{\beta} = \frac{\chi}{\tau_p} \pi - \Theta_{\varepsilon+1} \quad (57)$$

It can be shown that

$$\begin{aligned} \sum_{\varepsilon=0}^{\frac{m}{2}-1} \sin(\underline{\alpha} \pm v \underline{\beta}) &= \sum_{\varepsilon=0}^{\frac{m}{2}-1} \sin \left[ \omega t \pm v \frac{\chi}{\tau_p} \pi + \left( \frac{v \pm 1}{p \pm 1} \right) \frac{\varepsilon}{m} 2\pi \right] = \\ &= \frac{\sin \left[ \left( \frac{v \pm 1}{p \pm 1} \right) \pi \right]}{\sin \left( \frac{v \pm 1}{m} \pi \right)} \sin \left[ \omega t \pm v \frac{\chi}{\tau_p} \pi + \frac{v \pm 1}{m} (m-1) \pi \right] \quad (58) \end{aligned}$$

The use of this identity eliminates the need for summation. However, the fraction of the sinusoids on the right hand side of Equation (58) yields the indeterminate form  $0/0$ , if

$$\frac{v \pm 1}{p \pm 1} = \text{integer} \quad \text{and} \quad \frac{v \pm 1}{m} = \text{integer.}$$

Thus, Equation (58) is not useful for practical application unless modified. The modification can be effected by applying L'Hôpital's rule, viz.

$$\lim_{x \rightarrow x_0} \frac{f(x)}{g(x)} = \lim_{x \rightarrow x_0} \frac{f'(x)}{g'(x)} \quad (59)$$

as

$$\lim_{x \rightarrow \frac{v}{p} \pm 1} \frac{\sin \pi x}{\sin \pi \frac{x}{m}} = \begin{cases} m & \text{if } \varepsilon, \frac{\varepsilon}{m} = \text{integer} \\ -m & \text{otherwise} \end{cases} \quad (60)$$

Incorporating in Equation (55) the results obtained in Equation (60), the total airgap m.m.f. can finally be expressed as

$$\mathbb{F}(\chi t)_{\text{total}} =$$

$$= \frac{\sqrt{2}}{\pi} mNI \sum_{b=1}^c \sum_{v=1}^{\infty} \sin\left(v \Xi \frac{\pi}{b2}\right) \sin\left[\omega t \pm v \frac{\chi}{\tau_p} \pi \pm \frac{m-1}{m} \left(\frac{v}{p} \pm 1\right) \pi\right]$$

(61)

Utilising Equation (46), changing the summation range to  $-\infty < v < \infty$  and accounting also for parallel connections within coil groups, Equation (61)

can be rearranged, leading to a compressed expression for the total airgap m.m.f. as

$$\begin{aligned}
 \mathbf{F}(\chi t)_{\text{total}} &= \\
 &= \frac{\sqrt{2}}{\pi} m \frac{C}{a} NI \sum_{v=-\infty}^{\infty} \frac{1}{v} \frac{k_{cv}}{\sin\left(v \frac{\pi}{2}\right)} \sin \left[ \omega t - v \frac{\chi}{\tau_p} \pi + \frac{m-1}{m} \left( \frac{v}{p} - 1 \right) \pi \right]
 \end{aligned}
 \tag{62}$$

Because of the symmetry of the total airgap m.m.f. distribution, in Equations (61) and (62) only odd harmonics exist, the orders of which are given by

$$v = 2gm + 1 \tag{63}$$

where

$$g = \dots\dots-3, -2, -1, 0, 1, 2, 3, \dots\dots \tag{64}$$

The symbol  $\mathbf{F}(\chi t)$  will be used in the remainder of this thesis to replace the symbol  $\mathbf{F}(\chi t)_{\text{total}}$  for the total m.m.f. as obtained in Equations (61) and (62).

### 2.2.4 Airgap Flux

Once the total airgap m.m.f. is known, the airgap flux density can be obtained as

$$B(\chi, t) = \mu_0 \frac{\mathbf{F}(\chi, t)}{\delta'} \quad (65)$$

where  $\delta'$  is the airgap distance, modified by Carter's factor to take into consideration the effect of slotting (87, 88). The airgap flux per pole,  $\Phi(t)$ , can thus be found as

$$\Phi(t) = \frac{\mu_0 l_c}{\delta'} \int_0^{\tau_p} \mathbf{F}(\chi, t) d\chi \quad (66)$$

Substituting Equation (62) into Equation (66) gives

$\Phi(t) =$

$$\frac{\sqrt{2} \mu_0 l_c}{\pi \delta'} m \frac{C}{a} NI \int_0^{\tau_p} \left\{ \sum_{v=-\infty}^{\infty} \frac{1}{v} \frac{k_{cv}}{\sin\left(\frac{v\pi}{2}\right)} \sin\left[\omega t - v \frac{\chi}{\tau_p} \pi + \frac{m-1}{m} \left(\frac{v}{p} - 1\right) \pi\right] \right\} d\chi \quad (67)$$



Carrying out the integration and rearranging yields

$$\Phi(t) = \frac{2\sqrt{2}}{\pi^2} \frac{\mu_0 l_c \tau_p}{\delta'} m \frac{C}{a} NI \sum_{v=-\infty}^{\infty} \frac{1}{v^2} \frac{k_{cv}}{\sin\left(v \frac{\pi}{2}\right)} \cos\left[\omega t + \frac{m-1}{m} \left(\frac{v}{p} - 1\right) \pi\right] \quad (68)$$

Thus, the airgap flux is represented in terms of space harmonics. Although individual harmonic fields link with all machine windings, the penetration depth, hence the extent of linkage, varies depending on the corresponding perceived frequency due to the relative motion between the stator and rotor circuits.

### 2.2.5 Induced e.m.f.s

The airgap flux per pole, as quantified in Equation (68) is responsible for inducing e.m.f.s in the coils it traverses. The e.m.f. induced in each of the phases of a polyphase winding can be derived on the basis of the following considerations.

The e.m.f. induced in the first coil side of the  $b^{\text{th}}$  coil due to the airgap flux is found from

$$e_{bI}(t) = -N \frac{d\Phi(t)}{dt} \quad (69)$$

as

$$e_{bI}(t) =$$

$$\frac{2\sqrt{2}}{\pi^2} \frac{\mu_0 l_c \tau_p}{\delta'} m \frac{C}{a} N^2 \omega I \sum_{v=-\infty}^{\infty} \frac{1}{v^2} \frac{k_{cv}}{\sin\left(v \frac{\pi}{2}\right)} \sin\left[\omega t + \frac{m-1}{m} \left(\frac{v}{p} - 1\right) \pi\right] \quad (70)$$

The e.m.f. induced in the second coil side of the  $b^{\text{th}}$  coil will be obtained with a phase delay of

$$\varphi = (1 - \Xi_b) \pi \quad (71)$$

as

$$e_{bII}(t) =$$

$$\frac{2\sqrt{2}}{\pi^2} \frac{\mu_0 l_c \tau_p}{\delta'} m \frac{C}{a} N^2 \omega I \sum_{v=-\infty}^{\infty} \frac{1}{v^2} \frac{k_{cv}}{\sin\left(v \frac{\pi}{2}\right)} \sin\left\{\omega t + \left[\frac{m-1}{m} \left(\frac{v}{p} - 1\right) - \varphi\right] \pi\right\} \quad (72)$$

In Equation (71),  $\Xi_b$  is the relative coil pitch. The e.m.f. induced in the  $b^{\text{th}}$  coil is found by the difference of the e.m.f.s for each coil side as

$$e_b(t) = e_{bI}(t) - e_{bII}(t) \quad (73)$$

which gives

$$e_b(t) =$$

$$= \frac{4\sqrt{2}}{\pi^2} \frac{\mu_0 l_c \tau_p}{\delta'} m \frac{C}{a} N^2 \omega I \sum_{v=-\infty}^{\infty} \frac{1}{v^2} \frac{k_{cv}}{\sin\left(v \frac{\pi}{2}\right)} \sin\left[\omega t + \frac{m-1}{m} \left(\frac{v}{p} - 1\right) \pi\right] \sin\left(v \Xi_b \frac{\pi}{2}\right) \quad (74)$$

Similarly, the e.m.f. in a coil group of  $C$  coils is procured by taking the complex sum of the coil e.m.f.s within the group, which gives

$$e_c(t) = \frac{4\sqrt{2}}{\pi^2} \frac{\mu_0 l_c \tau_p}{\delta'} m \frac{C^2}{a} N^2 \omega I \sum_{v=-\infty}^{\infty} \frac{1}{v^2} \frac{k_{cv}^2}{\sin\left(v \frac{\pi}{2}\right)} \sin\left[\omega t + \frac{m-1}{m} \left(\frac{v}{p} - 1\right) \pi\right] \quad (75)$$

Correspondingly, the e.m.f. of the phase winding becomes

$$e(t) = \frac{4\sqrt{2}}{\pi^2} \frac{\mu_0 l_c \tau_p}{\delta'} m p \frac{C^2}{a} N^2 \omega I \sum_{v=-\infty}^{\infty} \frac{1}{v^2} \frac{k_{cv}^2}{\sin\left(v \frac{\pi}{2}\right)} \sin\left[\omega t + \frac{m-1}{m} \left(\frac{v}{p} - 1\right) \pi\right] \quad (76)$$

## 2.2.6 Modelling Ramifications

Equation (76) has important ramifications from a modelling viewpoint; the harmonic e.m.f.s contained therein can be associated with corresponding harmonic reactances which can be used in a harmonic circuit model to represent the flux linkage between the stator and rotor. The corollary is that the effects which originate from the non-sinusoidal space distribution of the airgap flux due to the placement of conductors in discrete slots can be represented with greater fidelity in such a model. Such *harmonic magnetising reactances* can be obtained on the basis of the following considerations.

Using complex notation, Equation (76) can also be written as

$$\dot{E} = j \frac{4}{\pi^2} \frac{\mu_0 l_c \tau_p}{\delta'} m p \frac{C^2}{a} N^2 \omega \dot{I} \sum_{v=-\infty}^{\infty} \frac{1}{v^2} \frac{k_{cv}^2}{\sin\left(v \frac{\pi}{2}\right)} \quad (77)$$

or as

$$\dot{E} = jX \dot{I} \quad (78)$$

In Equation (78),  $jX$  represents an aggregate magnetising reactance, which comprises harmonic magnetising reactances as

$$X = \sum_{v=-\infty}^{\infty} X_v \quad (79)$$

where

$$|X_v| = \frac{4}{\pi^2} \frac{\mu_0 l_c \tau_p}{\delta'} m p \frac{C^2}{a} N^2 \left( \frac{k_{cv}}{v} \right)^2 \omega \quad (80)$$

In circuit modelling terms, Equation (79) is identical to a series connected set of magnetising reactances. The corollary is that the airgap flux components linking the stator and the rotor can now be modelled by means of these harmonic reactances. With careful modelling of the corresponding rotor circuit parameters, this allows, among other things, to evaluate the effect of rotor currents on the airgap field, hence the order of magnitude of secondary armature reaction.

### 2.2.7 Harmonic Truncation

The foregoing deliberations in this chapter concerning the harmonic modelling concepts may give the impression that the ensuing models are, of necessity, complex and therefore unsuitable for practical implementation due to the large number of harmonic circuits to be included in the model. This need not be so, since the order of the model, hence model complexity can be controlled by truncation of the harmonics. In practical terms, this means that only harmonics which can have an appreciable effect on the overall machine performance need to be included in the formation of a harmonic circuit model. Space harmonics which affect overall machine performance are those which mutually link with stator and rotor circuits. However, the magnetic coupling efficacy of space harmonics is inversely proportional to their harmonic order, as explained elsewhere in this thesis.

The winding factor spectrum can be used as an effective *truncation criterion*, in that it gives a direct indication of the orders of magnitude of the space harmonics present in the airgap flux. Thus harmonic orders and their respective magnitudes can be used as the basis for a judicious selection of the magnetising reactances for inclusion in the high fidelity harmonic circuit model. Figure 3 shows a typical winding factor spectrum.

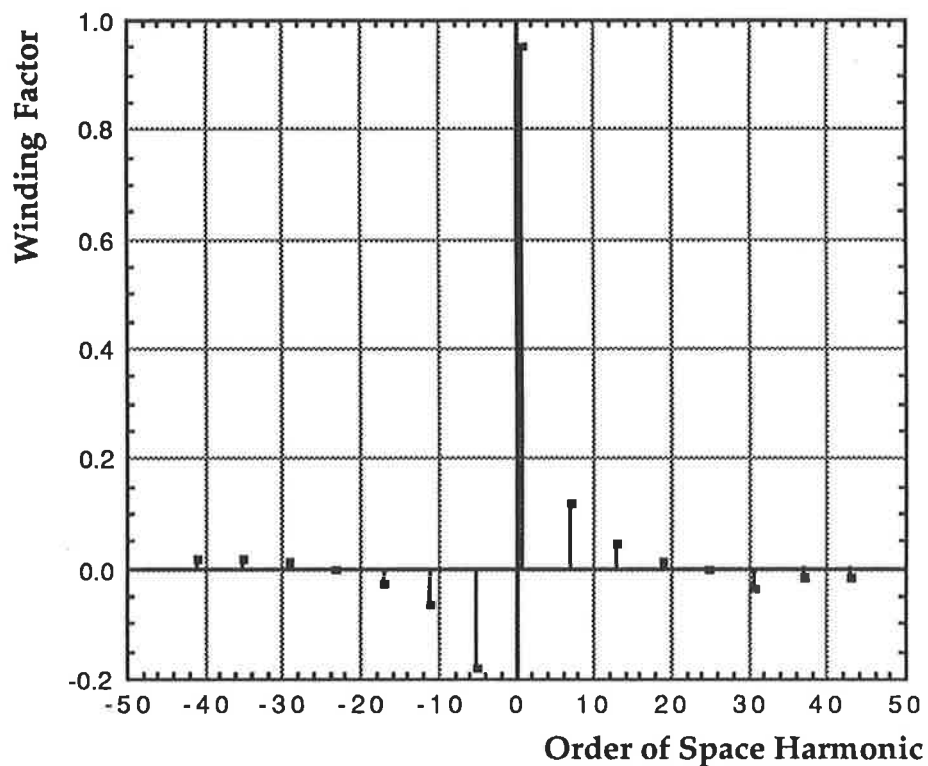


Figure 3

A typical winding factor spectrum

According to Figure 3, the 5<sup>th</sup> and 7<sup>th</sup> harmonics must be shown segregated in the model in addition to the fundamental, since they are the most significant; this would give a third order model. The inclusion of 11th and 13th harmonics would improve model fidelity since their contribution to the airgap field is considerable with 6.4% and 4.7% respectively. If the latter are included, this would result in a fifth order model, slightly increasing the computational effort. The remaining harmonics are to be collectively represented by means of a differential leakage reactance, since they virtually constitute leakage.

### 2.3 Current Displacement

When the conductors in the slots of an induction machine are traversed by time-variant magnetic fields, as is the case during operation, eddy currents result [89]. Although their sum within the conductor region is zero, their effect is paramount in that they modify both the distribution of conduction currents within the conductor and the distribution of the magnetic field, the time variation of which is responsible for their presence [90]. The resulting non-uniform current density distribution, generally known as *current displacement*, leads to an effective increase in the resistance of the conductor, with an associated increase in the ohmic losses [91,92]. In addition, the accompanying *magnetic field displacement* reduces the magnetic field leakage, which is reflected in a reduction of the corresponding leakage inductance values in circuit modelling terms [93].

Current displacement effects are put to good use in induction machine design in improving the starting performance of a motor, especially under direct-on-line starting conditions. This is done by the choice of conductor topology: in the rotor, the so-called deep-bar conductors are employed in slots where the slot height is much larger than the slot width. Such deep-bar configurations, as the one illustrated in Figure 4, favour the displacement of the rotor currents at high slip values, thus effectively increasing the rotor winding resistance when high torques are required. The effective resistance is progressively reduced as the motor runs up. At the operating speed the rotor resistance is at its lowest value, which is desirable from the viewpoint of rotor ohmic losses.

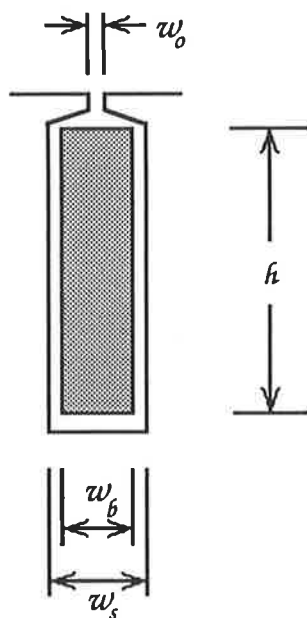


Figure 4

A typical rotor deep-bar configuration



Generally, eddy-current effects are not accounted for in induction machine circuit models on the premise that the winding resistances are insensitive to frequency. However, in cases where the phenomenon of current displacement is purposely utilised to improve the run-up performance of an induction motor, it becomes imperative that the eddy-current effects be modelled in the interest of improved prediction accuracy. Even in cases where eddy-currents are not consciously exploited to create the adaptive adjustment of the rotor impedance during the run-up, their inclusion in the model pays dividends in the form of a better correlation between the actual and predicted results, because current displacement effects discernibly affect performance, especially in squirrel-cage induction machines.

Current displacement in the conductors of an induction machine can be modelled by considering the Maxwell's equations in the form

$$\nabla \times \underline{\underline{H}} = \sigma \underline{\underline{E}} \quad (81)$$

$$\nabla \times \underline{\underline{E}} = -\mu \frac{d\underline{\underline{H}}}{dt} \quad (82)$$

Equations (81) and (82) can be combined to give the Laplacian of  $\underline{\underline{E}}$  as

$$\nabla^2 \underline{\underline{E}} = \sigma \mu \frac{d\underline{\underline{E}}}{dt} \quad (83)$$

In applying Equations (81) to (83) to the analysis of the current density distribution in a deep bar rotor, it is to be observed that the orientation of the magnetic field strength is almost perpendicular to the slot walls due to

the large disparity of the permeabilities between the slot space and the core. Relationships are illustrated in Figure 5 for a rectangular rotor conductor. Assuming that the rotor bars do not completely occupy the slot space as illustrated in Figure 4, the application of Equations (81) to (83) to the path enclosing the element ( $w_s, dy$ ) gives

$$w_s \frac{\partial \underline{\underline{H}}}{\partial y} = w_b \underline{\underline{J}} \quad (84)$$

$$\frac{\partial \underline{\underline{E}}}{\partial y} = -\mu_0 \frac{\partial \underline{\underline{H}}}{\partial t} \quad (85)$$

$$\frac{\partial^2 \underline{\underline{E}}}{\partial y^2} = \frac{w_b}{w_s} \sigma \mu_0 \frac{\partial \underline{\underline{E}}}{\partial t} \quad (86)$$

Evidently, in the case of a die-cast rotor cage, the bar width is the same as the slot width, in which case

$$\frac{w_b}{w_s} = 1 \quad (87)$$

Assuming the time variation of  $\underline{\underline{H}}$  and  $\underline{\underline{E}}$  to be sinusoidal, Equations (84) to (86) can be conveniently expressed in time-harmonic form as

$$\frac{d\tilde{\underline{\underline{H}}}}{dy} = \frac{w_b}{w_s} \tilde{\underline{\underline{J}}} \quad (88)$$

$$\frac{d\tilde{\underline{\underline{E}}}}{dy} = -j \omega \mu_0 \tilde{\underline{\underline{H}}} \quad (89)$$

$$\frac{d^2 \tilde{\underline{\underline{E}}}}{dy^2} = j \omega \frac{w_b}{w_s} \sigma \mu_0 \tilde{\underline{\underline{E}}} \quad (90)$$

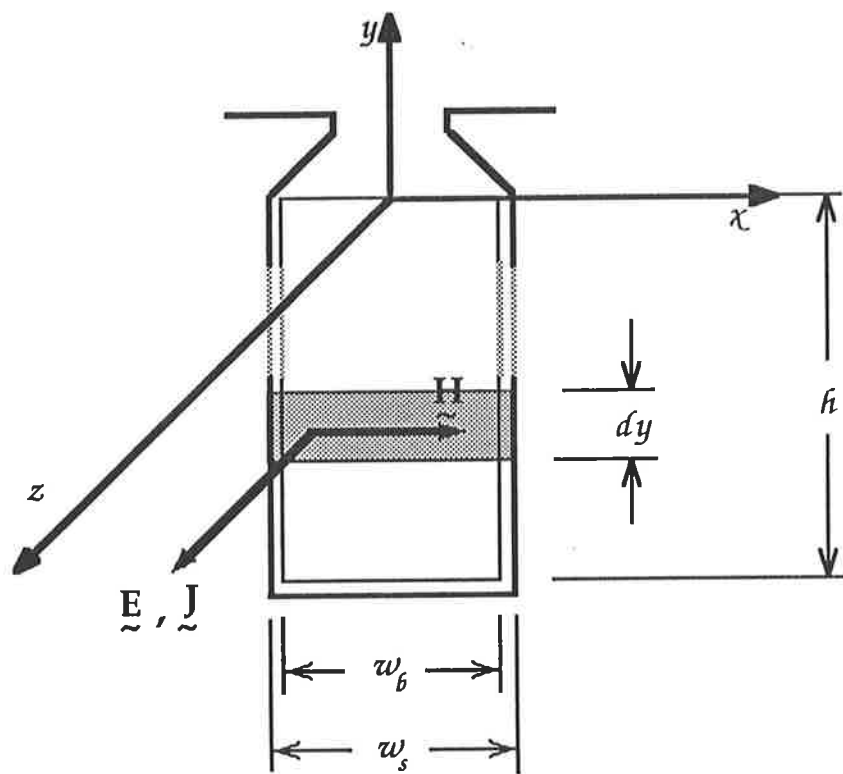


Figure 5

Electromagnetic relationships within a rotor slot  
with a deep-bar

Equation (90) is the Helmholtz equation in one dimension, the solution of which gives the electric field strength within the slot as a function of the radial distance  $y$  as

$$\tilde{E} = C_1 e^{\tilde{c} y} + C_2 e^{-\tilde{c} y} \quad (91)$$

where

$$\tilde{c} = (1 + j) \sqrt{\frac{1}{2} \frac{w_b}{w_s} \omega \sigma \mu_0} \quad (92)$$

The inverse of the radical term in Equation (92) represents the depth into the conductor at which the electric field strength  $\underline{E}$  has been attenuated to  $(e^{-1})^{\text{th}}$  of its surface value. Thus, it can be termed the *characteristic penetration depth*,  $\delta_p$ , defined as

$$\delta_p = \sqrt{\frac{w_s}{w_b} \frac{2}{\omega \sigma \mu_0}} \quad (93)$$

With this, Equation (92) can be rearranged to give

$$\tilde{c} = \frac{(1 + j)}{\delta_p} \quad (94)$$

$\tilde{c}$  is the so-called *wave number* of the conducting medium. At power frequencies, the actual penetration depth is in the order of four to eight times that given by Equation (93). Obviously, the higher the frequency, the less the penetration depth becomes. This is why high order harmonic airgap fields can be deemed not to link with the rotor conductors, justifying their being counted as leakage elsewhere in this thesis.

The magnetic field strength  $\tilde{H}$  within the slot can be obtained by substituting Equation (91) in Equation (89), which gives

$$\tilde{H} = \frac{\tilde{c}}{j \omega \mu_0} \left( C_1 e^{\tilde{c} y} - C_2 e^{-\tilde{c} y} \right) \quad (95)$$

The constants  $C_1$  and  $C_2$  are obtainable from the boundary conditions, constituted as

$$\tilde{H} \Big|_{y=0} = \frac{\tilde{I}}{w_s} = \frac{\tilde{c}}{j \omega \mu_0} (C_1 - C_2) \quad (96)$$

and

$$\tilde{H} \Big|_{y=-h} = 0 = \frac{\tilde{c}}{j \omega \mu_0} \left( C_1 e^{-\tilde{c} h} - C_2 e^{\tilde{c} h} \right) \quad (97)$$

which yield

$$C_1 = \frac{\tilde{I}}{w_s} \frac{j \omega \mu_0}{\tilde{c}} \frac{e^{\tilde{c} h}}{2 \sinh(\tilde{c} h)} \quad (98)$$

$$C_2 = \frac{\tilde{I}}{w_s} \frac{j \omega \mu_0}{\tilde{c}} \frac{e^{-\tilde{c} h}}{2 \sinh(\tilde{c} h)} \quad (99)$$

Substitution of these constants into Equation (95) gives the magnetic field strength as

$$\tilde{H} = \frac{\tilde{I}}{w_s} \frac{\sinh[\tilde{c}(h+y)]}{\sinh(\tilde{c}h)} \quad (100)$$

The current density within the conductor can now be found with the aid of Equation (84) as

$$\tilde{J} = \tilde{I} \frac{\tilde{c}}{w_b} \frac{\cosh[\tilde{c}(h+y)]}{\sinh(\tilde{c}h)} \quad (101)$$

Figure 6 illustrates the variation of current density distribution along the slot height for a typical deep-bar configuration.

The corresponding ohmic losses for the conductor region can be ascertained generally from the use of the *instantaneous Poynting vector* for the region defined as

$$\underline{\tilde{P}} = \sigma \underline{\tilde{J}} \times \underline{\tilde{H}} \quad (102)$$

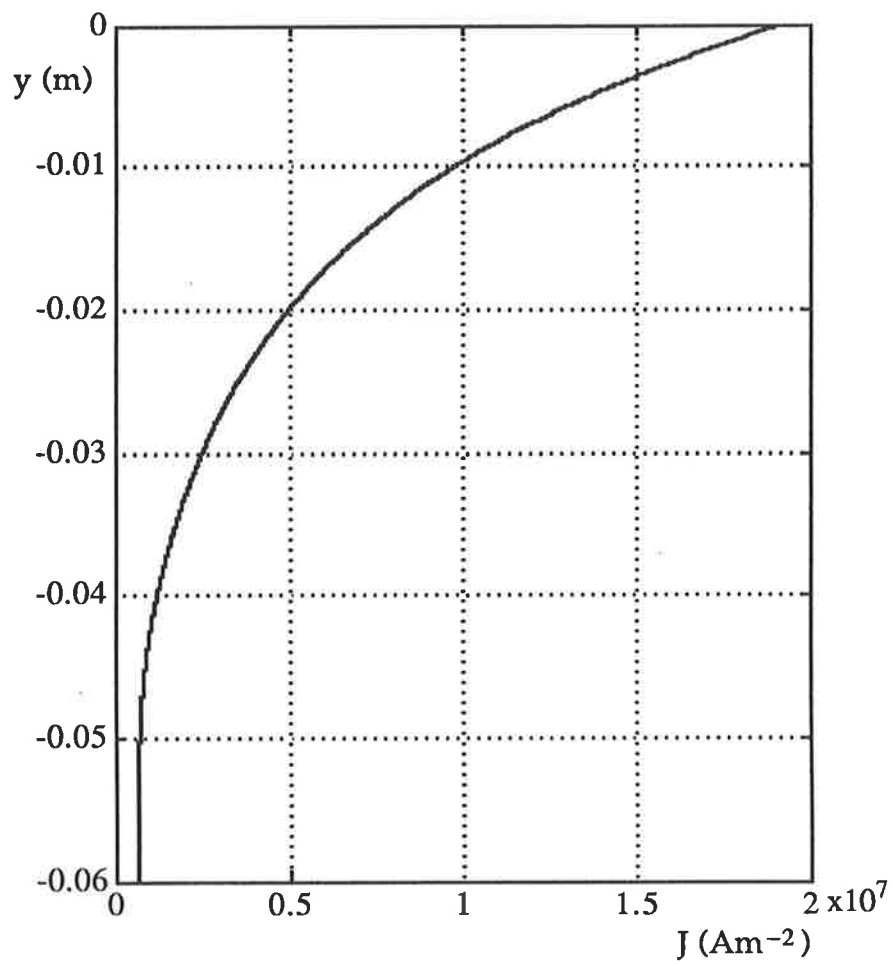


Figure 6

Current density variation in a deep-bar : an example

However, in line with the preceding deliberations, the losses will be obtained here by the use of a corresponding *complex Poynting vector*, which can be defined in time-harmonic form as

$$\tilde{\mathbf{P}} = \frac{1}{\sigma} \tilde{\mathbf{J}} \tilde{\mathbf{H}}^* \quad (103)$$

The real component of  $\tilde{\mathbf{P}}$  is the time average of the instantaneous Poynting vector. The active power loss and hence the ohmic losses within the conductor region can be determined by integrating the complex Poynting vector over the surface enclosing the conductor region in question as

$$\tilde{\mathbf{S}} = \int_s \tilde{\mathbf{P}} \, ds \quad (104)$$

In the case of a prismatic deep bar as in Figures 3 and 4, the region is defined by the surface area of the bar embedded in the core. It follows that the complex power for this region is

$$\tilde{\mathbf{S}} = \frac{l_c w_s}{\sigma} \left[ \tilde{\mathbf{J}} \Big|_{y=0} \tilde{\mathbf{H}}^* \Big|_{y=0} - \tilde{\mathbf{J}} \Big|_{y=h} \tilde{\mathbf{H}}^* \Big|_{y=h} \right] \quad (105)$$

Substituting Equations (100) and (101) and rearranging yields



$$\tilde{\mathcal{S}} = \frac{l_c}{\sigma w_b} \tilde{I} \tilde{I}^* \tilde{c} \coth(\tilde{c} h) \quad (106)$$

Equation (106) represents the complex power for the conductor region in question and, as such, can also be written in terms of active and reactive power components as

$$\tilde{\mathcal{S}} = P + jQ \quad (107)$$

Equation (107) enables effective values for the resistance and inductance of the portion of the conductor embedded in a slot to be obtained. This can be done by comparing the values of resistance and inductance, obtained under the assumption of uniform current density distribution, with their effective values derived from the real and imaginary components of the complex power given by Equation (107).

Considering that the bar resistance for uniform current density distribution is

$$R_{b0} = \frac{l_c}{\sigma w_b h} \quad (108)$$

Equation (106) can be formulated as

$$\tilde{\mathcal{S}} = R_{b0} \tilde{I} \tilde{I}^* \tilde{c} h \coth(\tilde{c} h) \quad (109)$$

which can be developed to give

$$\tilde{S} = R_{b_0} \tilde{I} \tilde{I}^* \left[ f_P \left( \frac{h}{\delta_p} \right) + j f_Q \left( \frac{h}{\delta_p} \right) \right] \quad (110)$$

where

$$f_P \left( \frac{h}{\delta_p} \right) = \frac{h}{\delta_p} \frac{\sinh \left( 2 \frac{h}{\delta_p} \right) + \sin \left( 2 \frac{h}{\delta_p} \right)}{\cosh \left( 2 \frac{h}{\delta_p} \right) - \cos \left( 2 \frac{h}{\delta_p} \right)} \quad (111)$$

and

$$f_Q \left( \frac{h}{\delta_p} \right) = \frac{3\delta_p}{2h} \frac{\sinh \left( 2 \frac{h}{\delta_p} \right) - \sin \left( 2 \frac{h}{\delta_p} \right)}{\cosh \left( 2 \frac{h}{\delta_p} \right) - \cos \left( 2 \frac{h}{\delta_p} \right)} \quad (112)$$

In modelling terms the above is tantamount to an increase in the bar resistance with an associated decrease in the bar inductance, leading, respectively, to new effective parameter values given by:

$$R_{b_{\text{eff}}} = R_{b_0} f_P \left( \frac{h}{\delta_p} \right) \quad (113)$$

$$L_{b_{\text{eff}}} = L_{b_0} f_Q \left( \frac{h}{\delta_p} \right) \quad (114)$$

## 2.4 Core Losses

The cyclic excitation of the laminated core of an induction machine results in heating of the core due to the losses arising from the process. These losses arise due to the combined effect of hysteresis and eddy currents. These phenomena affect the behaviour of the machine both electromagnetically and thermally. Therefore, it is important that core losses be modelled as accurately as practicable for the reliability of performance predictions.

### 2.4.1 Hysteresis Losses

Hysteresis losses are conceptually easy to quantify; every time the hysteresis loop is traversed, an amount of energy corresponding to the area bounded by the hysteresis loop is irreversibly lost in the core in the form of heat energy. The difficulty in modelling terms lies therein that the shape of the hysteresis characteristic is uniquely dependent on the core material, and, basically, the mathematical modelling of the curve has to be done on the basis of measured material properties using curve fitting techniques.

Assuming that such a mathematical description exists, hysteresis losses for cyclic excitation between two limits of magnetic flux density as shown in Figure 7 can be obtained on the basis of Equation (115) below. It should be noted that Figure 7 represents the *static* hysteresis loop, which in this case was obtained for an actual core using the so-called "six step" method.

$$Y = \int H^{\uparrow} dB - \int H^{\downarrow} dB \quad (115)$$

where  $H^{\uparrow}$  and  $H^{\downarrow}$  designate the values of the magnetic field strength  $H$  along the integration path for the ascending and descending branches respectively.  $\Upsilon$  is the hysteresis loss per unit volume of the core region, within which the depicted magnetisation conditions apply, every time the loop is traversed.

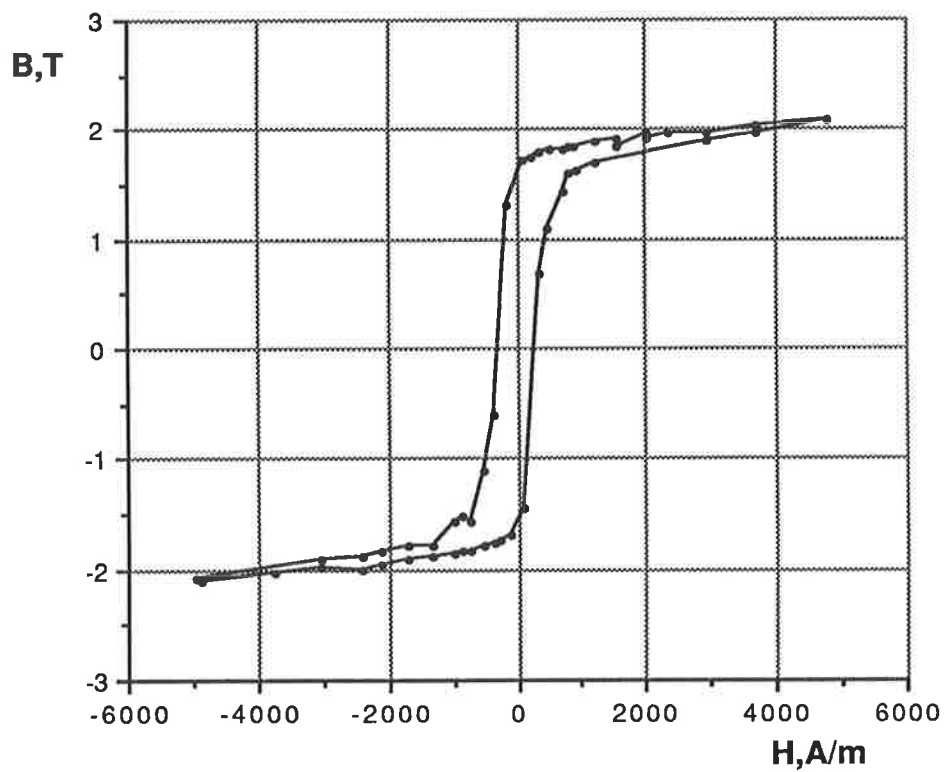


Figure 7

Typical hysteresis loop for ferromagnetic core material

The hysteresis loss per second per unit volume within the  $n^{\text{th}}$  core region can be obtained from

$$p_{h_n} = f_n \Upsilon \quad (116)$$

where  $f_n$  : frequency of cyclic magnetisation within the  $n^{\text{th}}$  region  
 $\Upsilon$ : hysteresis loss per loop traverse per unit volume

Hysteresis loss for the core region can then be found from

$$P_{h_n} = \int_v p_{h_n} \, dv \quad (117)$$

as

$$P_{h_n} = f_n \int_v \Upsilon \, dv \quad (118)$$

Evidently, the total hysteresis loss for the core is obtained as

$$P_h = \sum_n p_{h_n} \quad (119)$$

where  $n$  denotes the relevant region.

In circuit modelling terms, Equation (119) can also be expressed as

$$P_h = \sum_v P_{h_v} \quad (120)$$

$P_{h_v}$  is the hysteresis loss to be associated with the  $v^{\text{th}}$  space harmonic in the harmonic circuit model. Considering that hysteresis losses can be conceptually represented as ohmic losses, one can write

$$P_h = m \frac{E^2}{R_h} = m \sum_v \frac{E_v^2}{R_{h_v}} \quad (121)$$

where  $m$  is the number of phases and  $v$  is the relevant space harmonic order.  $E_v$  is the so-called airgap e.m.f. for the  $v^{\text{th}}$  harmonic as defined previously.  $R_{h_v}$  represents the resistive parameters to model the corresponding hysteresis losses and can be quantified as

$$R_{h_v} = R_{h_{y_v}} \frac{E_v}{E} \quad (122)$$

### 2.4.2 Eddy Current Losses

Core losses, which have their origin in the eddy currents, are referred to as *eddy current losses* or alternately as *Foucault losses*. Their modelling can be done on the basis of Maxwell's equations.

Figure 8 illustrates a partial lamination region within the core of an induction machine. Since the thickness of laminations is much smaller than their other dimensions, the end effects are to be deemed negligible. Placing the origin of coordinates at half way the thickness of lamination, the magnetic field strength anywhere along the thickness of lamination can be expressed, with the aid of Equation (95), as

$$\tilde{H} = \frac{\tilde{c}}{j\omega\mu} \left( C_1 e^{\tilde{c}z} - C_2 e^{-\tilde{c}z} \right) \quad (123)$$

The factors  $C_1$  and  $C_2$  can be obtained from the boundary conditions. Since the value of the magnetic field strength is the same for both surfaces of the region under consideration, the boundary conditions are given by

$$\tilde{H} \Big|_{z=\frac{\Delta}{2}} = H_{\Delta} = \frac{\tilde{c}}{j\omega\mu} \left( C_1 e^{-\tilde{c}\frac{\Delta}{2}} - C_2 e^{\tilde{c}\frac{\Delta}{2}} \right) \quad (124)$$

and

$$\tilde{H} \Big|_{z=-\frac{\Delta}{2}} = H_{\Delta} = \frac{\tilde{c}}{j\omega\mu} \left( C_1 e^{\tilde{c}\frac{\Delta}{2}} - C_2 e^{-\tilde{c}\frac{\Delta}{2}} \right) \quad (125)$$

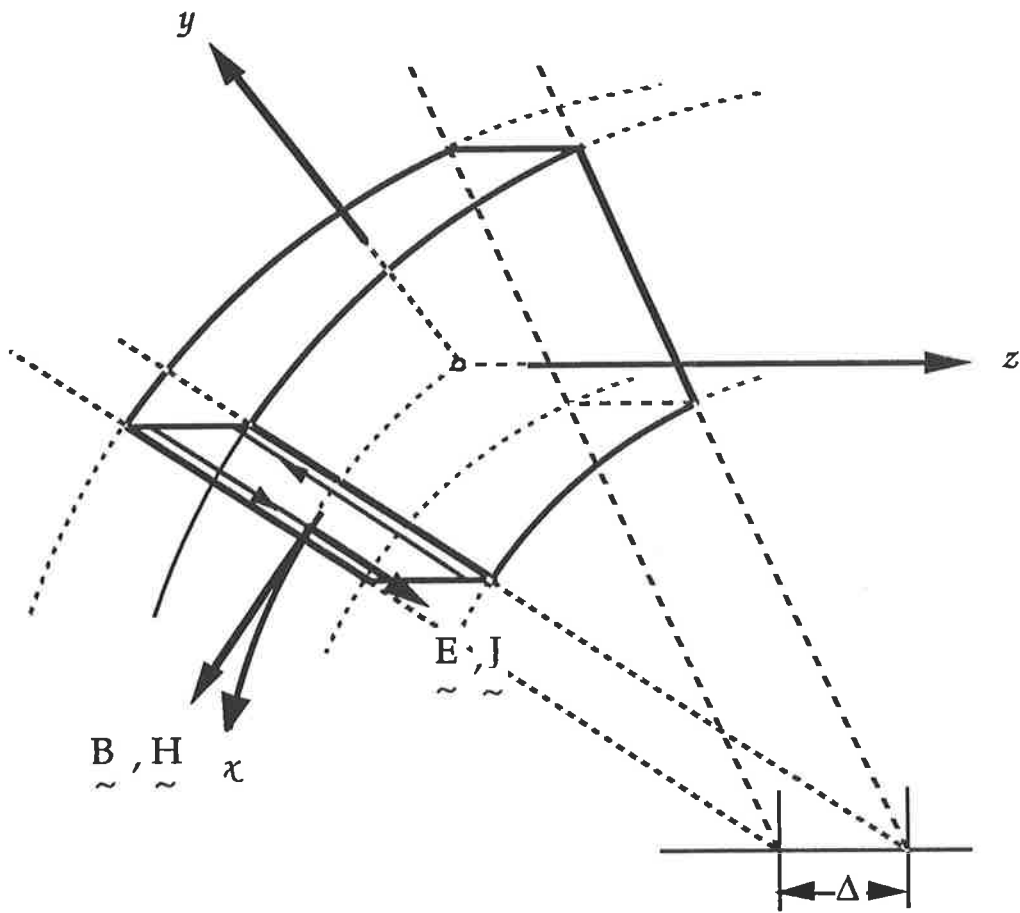


Figure 8

A partial core lamination region



which yield

$$C_1 = -C_2 = \frac{j\omega\mu H_\Delta}{2\tilde{c} \cosh\left(\tilde{c}\frac{\Delta}{2}\right)} \quad (126)$$

Substituting Equation (126) in Equation (123) gives the magnetic field strength as

$$\tilde{H} = H_\Delta \frac{\cosh(\tilde{c} z)}{\cosh\left(\tilde{c}\frac{\Delta}{2}\right)} \quad (127)$$

The magnetic flux density within the lamination can now be obtained, as a function of the axial distance  $z$ , as

$$\tilde{B} = \mu H_\Delta \frac{\cosh(\tilde{c} z)}{\cosh\left(\tilde{c}\frac{\Delta}{2}\right)} \quad (128)$$

Figure 9 exemplifies the magnetic flux density distribution across the thickness of lamination. As can be seen, the magnetic flux density distribution is no longer uniform, increasing toward the outer surfaces, thus constituting a *flux displacement*.

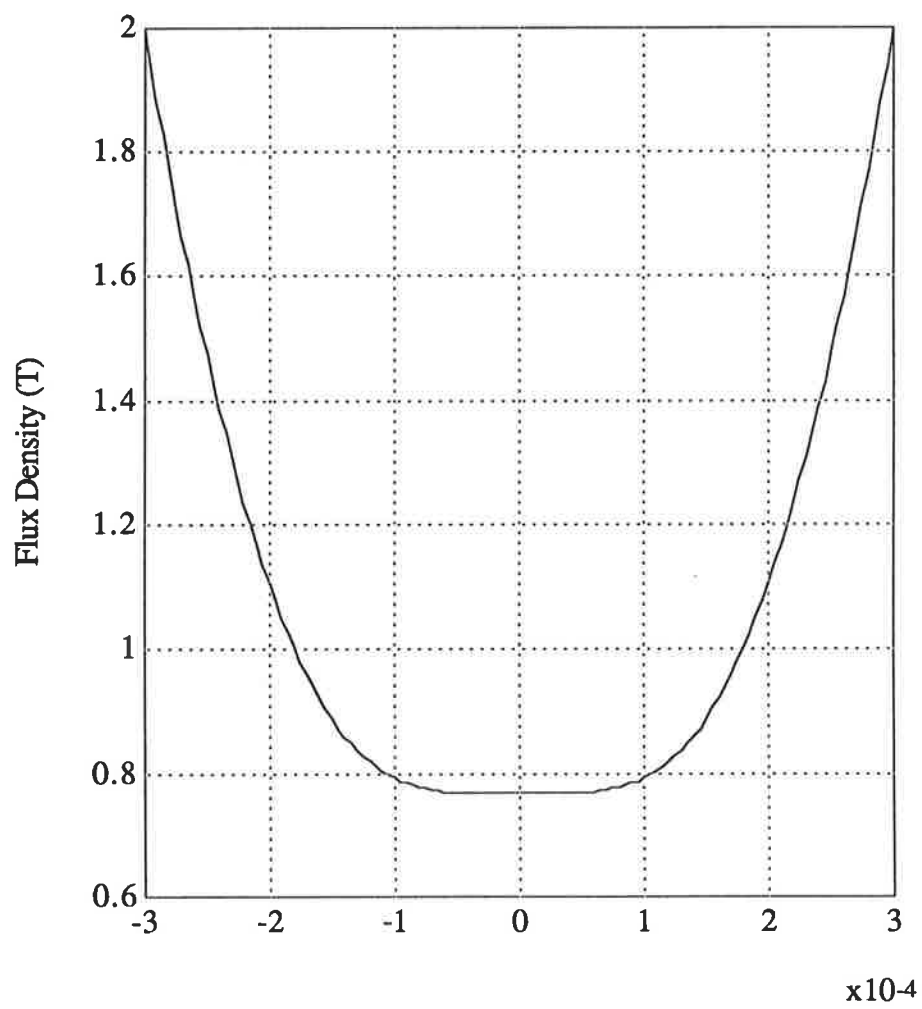


Figure 9

Flux displacement across a lamination

The current density within the lamination can be obtained with Equations (88) and (127) as

$$\tilde{J} = - \frac{\partial \tilde{H}}{\partial z} = - \tilde{c} H_{\Delta} \frac{\sinh(\tilde{c} z)}{\cosh\left(\tilde{c} \frac{\Delta}{2}\right)} \quad (129)$$

the absolute value of which is given, as a function of axial distance within the lamination boundaries, by

$$|\tilde{J}| = \sqrt{2} \frac{H_{\Delta}}{\delta_{p\Delta}} \sqrt{\frac{\cosh\left(\frac{2z}{\delta_{p\Delta}}\right) - \cos\left(\frac{2z}{\delta_{p\Delta}}\right)}{\cosh\left(\frac{\Delta}{\delta_{p\Delta}}\right) + \cos\left(\frac{\Delta}{\delta_{p\Delta}}\right)}} \quad (130)$$

where  $\delta_{p\Delta}$  is the characteristic penetration depth for the lamination region.

$\delta_{p\Delta}$  is obtained in a way similar to that of Equation (93) as

$$\delta_{p\Delta} = \sqrt{\frac{2}{\omega\sigma\mu}} \quad (131)$$

Figure 10 illustrates the distribution of the current density across the thickness of a lamination.

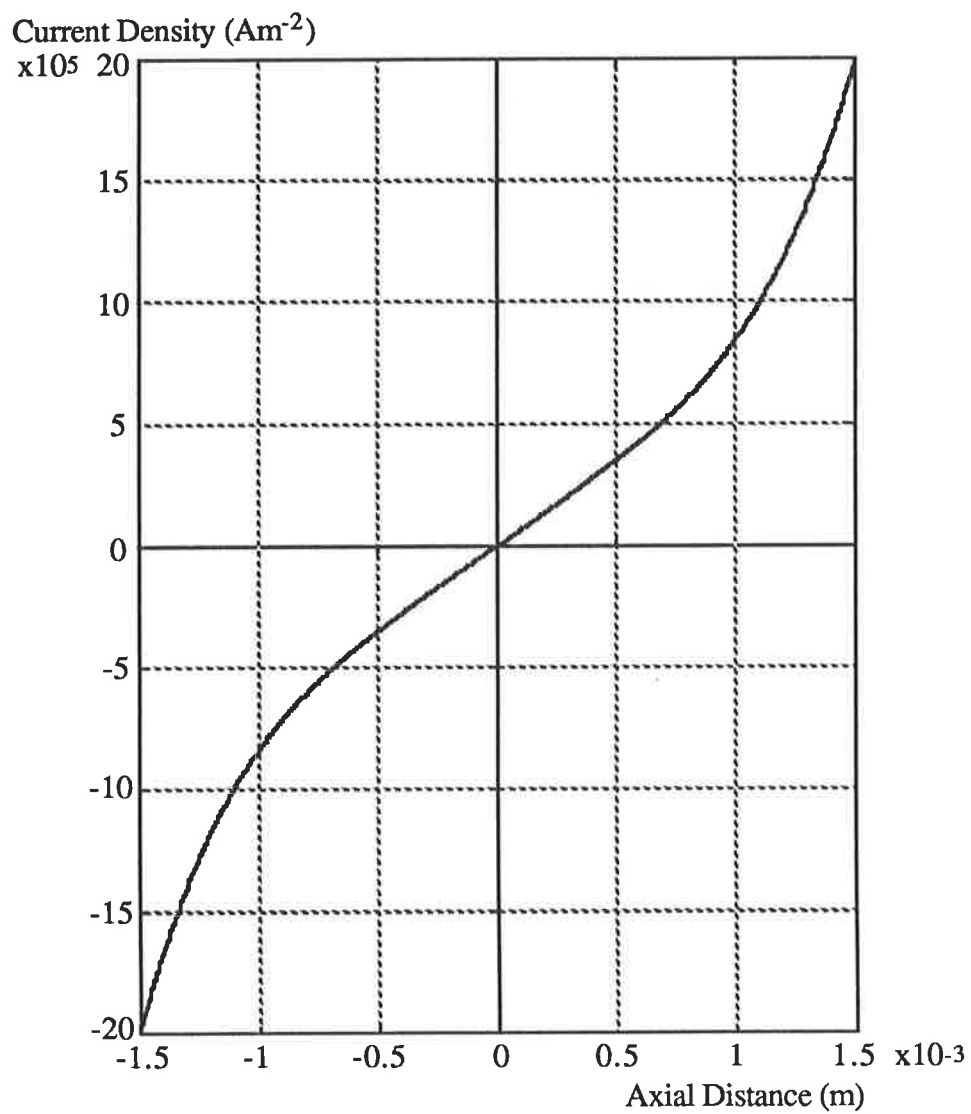


Figure 10

Current density distribution across a lamination

The total flux traversing the region of lamination can be obtained by integration as

$$\tilde{\Phi} = \int_{-\frac{1}{2}\Delta}^{\frac{1}{2}\Delta} \tilde{B} v dz = \frac{2\mu v H_{\Delta}}{\bar{c}} \operatorname{tanh}\left(\bar{c} \frac{\Delta}{2}\right) \quad (132)$$

the magnitude of which is

$$\hat{\Phi} = 2\mu v \delta_{p\Delta} H_{\Delta} \sqrt{\frac{\operatorname{cosh}\left(\frac{\Delta}{\delta_{p\Delta}}\right) - \cos\left(\frac{\Delta}{\delta_{p\Delta}}\right)}{\operatorname{cosh}\left(\frac{\Delta}{\delta_{p\Delta}}\right) + \cos\left(\frac{\Delta}{\delta_{p\Delta}}\right)}} \quad (133)$$

Hence, the mean magnetic flux density within the region can be found as

$$\bar{B} = 2\mu H_{\Delta} \frac{\delta_{p\Delta}}{\Delta} \sqrt{\frac{\operatorname{cosh}\left(\frac{\Delta}{\delta_{p\Delta}}\right) - \cos\left(\frac{\Delta}{\delta_{p\Delta}}\right)}{\operatorname{cosh}\left(\frac{\Delta}{\delta_{p\Delta}}\right) + \cos\left(\frac{\Delta}{\delta_{p\Delta}}\right)}} \quad (134)$$

The eddy current losses per unit volume within the region under consideration can be found from

$$p_e = \frac{1}{\sigma \Delta} \int_{-\frac{1}{2}\Delta}^{\frac{1}{2}\Delta} |\tilde{J}|^2 dz \quad (135)$$

which yields

$$p_e = \frac{1}{24} \sigma \omega^2 \Delta^2 \bar{B}^2 f\left(\frac{\Delta}{\delta_{p\Delta}}\right) \quad (136)$$

where

$$f\left(\frac{\Delta}{\delta_{p\Delta}}\right) = \frac{3}{\frac{\Delta}{\delta_{p\Delta}}} \frac{\sinh\left(\frac{\Delta}{\delta_{p\Delta}}\right) - \sin\left(\frac{\Delta}{\delta_{p\Delta}}\right)}{\cosh\left(\frac{\Delta}{\delta_{p\Delta}}\right) - \cos\left(\frac{\Delta}{\delta_{p\Delta}}\right)} \quad (137)$$

Figure 11 gauges the sensitivity to the change in frequency of the eddy current losses.

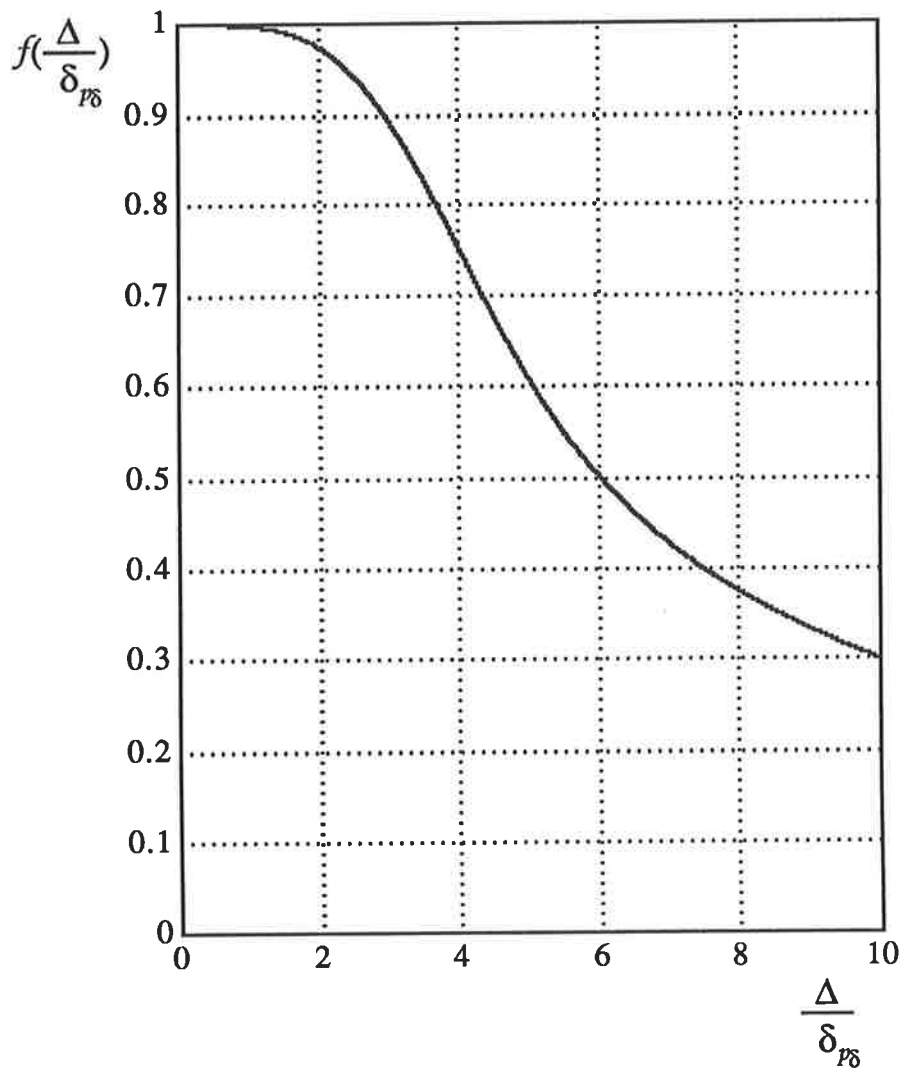


Figure 11

Frequency sensitivity of eddy current losses

As can be seen in Figure 11,  $f\left(\frac{\Delta}{\delta_{p\Delta}}\right) \approx 1$  at low frequencies, which allows Equation (136) to be simplified as

$$p_e = \frac{1}{24} \sigma \omega^2 \Delta^2 \bar{B}^2 \quad (138)$$

or as

$$p_e = k'_e f^2 \bar{B}^2 \quad (139)$$

Equation (139) is significant, because it shows that the determination of eddy-current losses can be considerably simplified in the case of slowly varying magnetic fields within the region.  $k'_e$  is the *eddy-current loss factor per unit volume* and is given by

$$k'_e = \frac{\sigma}{6} (\pi \Delta)^2 \quad (140)$$

A slightly modified version of Equation (139) is commonly used in routine design computations in calculating the eddy current losses in the ferromagnetic core of electromagnetic devices.



A similar simplification can be achieved in Equation (136) if the frequency is high. As seen in Figure 9, for  $\frac{\Delta}{\delta_{p\Delta}} > 4$ , Equation (137) can be approximated to a hyperbola, given as

$$f\left(\frac{\Delta}{\delta_{p\Delta}}\right) = \frac{3}{\frac{\Delta}{\delta_{p\Delta}}} \quad (141)$$

which allows Equation (136) to be simplified to

$$p_e = \frac{1}{8} \sigma \omega^2 \delta_{p\Delta} \Delta \bar{B}^2 \quad (142)$$

or

$$p_e = k_e'' f^2 \bar{B}^2 \quad (143)$$

where

$$k_e'' = \sqrt{\frac{\pi^3 \sigma}{4 \mu}} \Delta \quad (144)$$

$k_e''$  denotes the *eddy-current loss factor* per unit volume when the frequency is high.

The total eddy-current loss for the core can be ascertained from the regional eddy current losses obtained, using one of the Equations (136), (139) or (143), as

$$P_e = \sum_n \sum_{\mu} P_{e\mu_n} \quad (145)$$

where  $n$  denotes the number of the core regions. Equation (145) can be interpreted as

$$P_e = \sum_v P_{ev} = m \sum_v \frac{E_v^2}{R_{ev}} \quad (146)$$

$E_v$  is the airgap e.m.f. for the  $v^{\text{th}}$  harmonic as before.  $R_{ev}$  is the resistive harmonic circuit model parameter per phase to represent the eddy-current losses attributable to the  $\mu^{\text{th}}$  time harmonic associated with the  $v^{\text{th}}$  space harmonic. With

$$P_{ev} = \sum_n P_{e\mu_n} \Big|_v \quad (147)$$

representing the portion for the  $v^{\text{th}}$  harmonic of the total eddy current loss,  $R_{ev}$  can be determined as

$$\boxed{R_{ev} = m \frac{E_v^2}{P_{ev}}} \quad (148)$$

## 2.5 Saturation

The neglect of saturation has been a widespread practice in the formation of user-orientated induction machine models. However, both designers [6, 94, 95] and serious users [13, 96] have long been acutely aware of the importance of accounting for the finite and variable permeability of the core materials realistically, if performance predictions are to be accurate.

It is reasonable to expect that models derived on the basis of Maxwell's field equations would implicitly account for saturation effects. Principally, the inclusion in the Ampère's circuital law of a *bound current density*, defined as

$$\nabla \times \underline{\mathcal{M}} = \underline{J}_b \quad (149)$$

would model correctly the effect of the flux-variant permeability of the core. The problem is then reduced to the solution of Poisson's equation in relevant field regions. The source of difficulty is the multi-valued relationship between the magnetisation  $\underline{\mathcal{M}}$  and magnetic field strength  $\underline{H}$ , which is peculiarly characteristic of the core material used. The mathematical description of this magnetising relationship is, of necessity, linked to experimental techniques. The modelling complexities escalate if the anisotropic nature of most core materials is sought to be modelled rigorously, which necessitates the use of a tensor permeability.

Various approximation techniques have been developed in dealing with the problem of core non-linearity to avoid the virtually unaffordable complexities of such rigorous approaches. These include the use of:

- 1 numerical methods which seek to solve two-dimensional field equations by means of finite element analysis in which step-wise linearisation in an iterative mode is employed [84] or finite difference methods along with relaxation procedures [83],
- 2 analogue network analysers, in which saturation effects are simulated by means of carefully selected diodes [97], and
- 3 circuit models, in which *saturation factors*, obtained on the basis of the magnetisation characteristic for the core material, are introduced to modify saturation affected model parameters [20, 98].

Of these, the first two require extensive computational effort and hardware development respectively, whereas the third approach represents an attractively simple alternative. Provided that close attention is paid to the procurement of the relevant model parameters to reflect the nature of saturation effects within the various core regions, it promises sufficient accuracy in circuit modelling terms [99, 100].

It is known that saturation effects are most pronounced in the tooth-tip region at large slip values [98, 101, 102]. This region hosts both the fundamental of the airgap field and its higher harmonics; the latter penetrate barely beyond the tooth-tip region. As a result, this region is

usually the first to be driven into saturation as the magnetic field strength increases as a result of larger currents associated with increasing slip. Figure 12 illustrates a typical tooth-tip region for a stator with semi-closed slots.

Closer attention needs to be paid to the shaded region over a slot pitch, representative of the situation elsewhere around the airgap periphery. The saturation of this region manifests itself in the form of a flattening of the airgap flux distribution, which designers have traditionally accounted for by the use of saturation factors obtained from the comparison of unsaturated and saturated peripheral flux distributions [6].

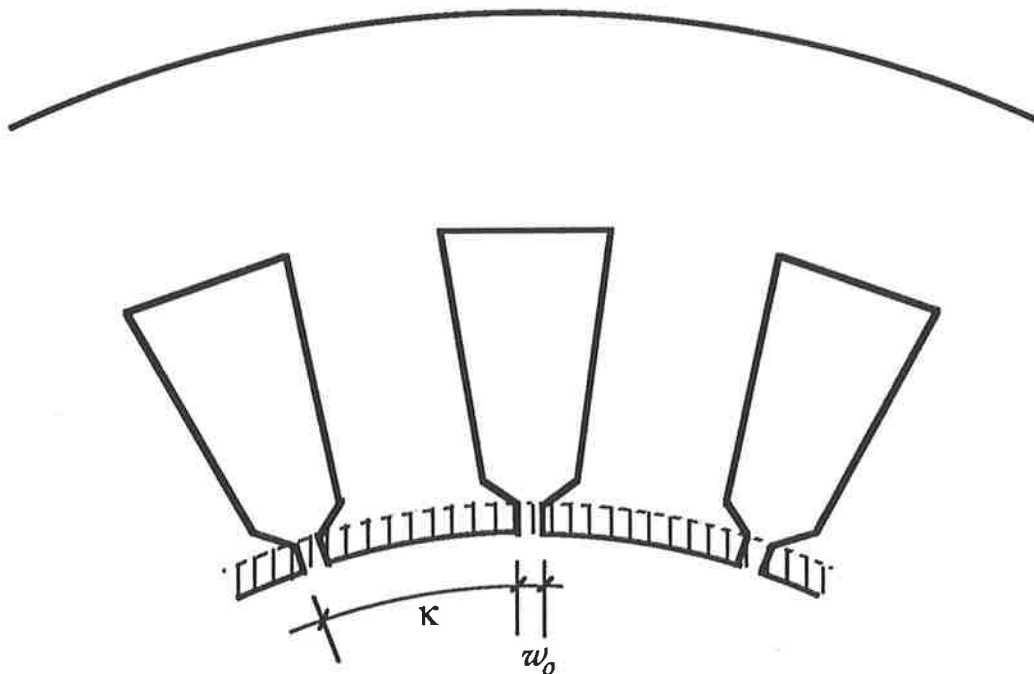


Figure 12

A typical tooth-tip region

It will be assumed that in this region the flux  $\Phi|_k$  traverses serially the tooth-tip and slot-opening subregions over the span of a slot pitch with the same uniform flux density. Thus, it is possible to obtain a single composite magnetisation characteristic to represent the magnetic behaviour of the entire tooth-tip region by the application of the *shearing method*, as illustrated in Figure 13.

The slope of the curve  $\square$  corresponds to the composite incremental permeance  $\Lambda|_{w_o}$  for the tooth-tip region comprising the tooth-tip and the slot opening subregions.  $\Lambda|_{w_o}$  can also be obtained from flux relationships within the tooth-tip region as outlined below. Obviously, these considerations apply to tooth-tip regions of both the stator and the rotor.

The m.m.f. for each of the slot-opening and tooth-tip subregions, respectively, is given by

$$\mathbf{F}|_{w_o} = \frac{\Phi|_{w_o}}{\Lambda|_{w_o}} \quad (150)$$

and

$$\mathbf{F}|_t = \frac{\Phi|_t}{\Lambda|_t} \quad (151)$$

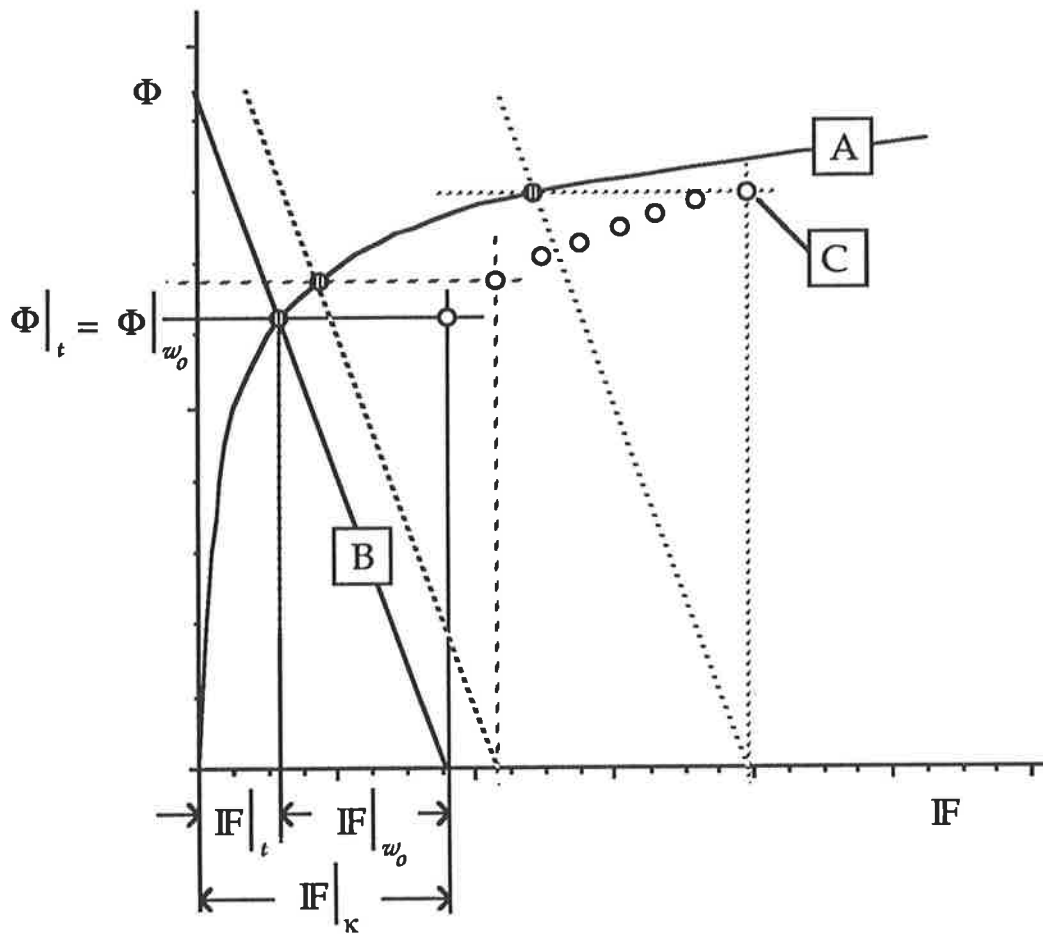


Figure 13

Application of shearing method to obtain a composite magnetisation characteristic for the tooth-tip region

- A  $\Phi=f(\mathbf{F})$  for teeth
- B  $\Phi=f(\mathbf{F})$  for slot opening
- C  $\Phi=f(\mathbf{F})$  for tooth-tip region (inverted)

where  $\Lambda|_w$  and  $\Lambda|_t$  denote the permeance for the slot opening subregion and tooth-tip subregion respectively and are given by

$$\Lambda|_{w_o} = \frac{\mu_0 A|_{w_o}}{w_o} \quad (152)$$

and

$$\Lambda|_t = \frac{\mu A|_t}{\kappa - w_o} \quad (153)$$

Total m.m.f. for the region spanning a slot pitch can thus be obtained as

$$\mathbf{F}|_{\kappa} = \mathbf{F}|_{w_o} + \mathbf{F}|_t = \frac{\Phi|_{\kappa}}{\Lambda|_{w_o'}} \quad (154)$$

where  $\Lambda|_{w_o'}$  is the composite permeance for the tooth-tip region. Substituting Equations (150) and (151) into Equation (152) and rearranging gives:

$$\Lambda|_{w_o'} = \frac{\mu_0 A|_{\kappa}}{w_o'} \quad (155)$$

which accounts for the flux-variant permeance for the tooth-tip region by means of the term  $w_o'$  given as

$$w_o' = w_o + \frac{\kappa - w_o}{\mu_r^{\kappa}} \quad (156)$$



Equation (156) can be interpreted as representing an apparent widening of the slot opening as the core is driven into saturation, if the equivalent composite tooth-tip region is represented in its entirety by means of a fictitious composite material occupying the space across the slot opening. The effect of permeability variation can thus be emulated by a flux-variant slot opening, by substituting the apparent slot opening  $w_o'$  for the actual slotting opening  $w_o$  in all instances where  $w_o$  is used in determining model parameters [20].

## 2.6 The High Fidelity Harmonic Circuit Model

The above considerations lead to the formation of a high fidelity harmonic circuit model as depicted in Figure 16. The model is based on the concept of harmonic magnetising reactances developed in Section 2.2.6. Each of these reactances represents a magnetic coupling with the rotor circuits at a unique harmonic frequency. In this context, it is noteworthy that to a stationary observer the time variation of the space harmonics occurs with the supply frequency, whereas a rotor-bound observer perceives their effect to be in the nature of time harmonics. The harmonic e.m.f.s which are induced in the rotor circuits in response to these harmonics give rise to harmonic currents and fluxes, the effects of which can be modelled uniquely by means of harmonic sub-circuits.

Since the penetration depth rapidly decreases with increasing frequency, not all of the airgap harmonics link effectively with the rotor circuits. Such harmonic components of the airgap field can be justifiably considered to constitute *leakage* and are modelled by means of a differential leakage reactance in the stator circuit, obtained by subtracting these from the total magnetising reactance. Similar considerations lead to the definition of a differential leakage reactance for the rotor.

The partial model of Figure 14 shows the details of the stator parameters, accounting for saturation. Figure 15 shows the various harmonic model parameters in close-up. Figure 16 represents a complete high fidelity harmonic circuit model, which assumes that all airgap space harmonics are gainfully linked with the rotor. As can be seen, the model accounts for saturation, stator and rotor core losses and current displacement in the rotor conductors in addition to the space harmonics. The effect of skewing, if applicable, is considered by the inclusion of skew leakage reactances. Coil-end leakage is also taken into account by means of coil-end leakage reactances [20]. Table 1 gives a summary of the various model parameters shown in Figures 14 and 15.

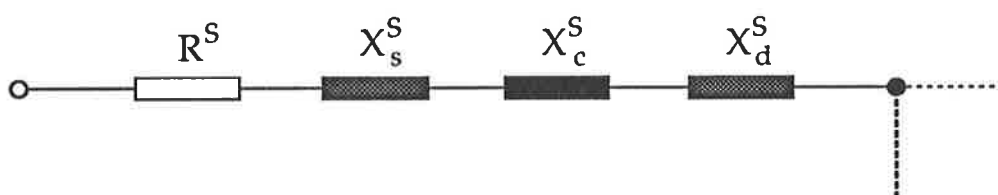


Figure 14

Details of the stator parameters

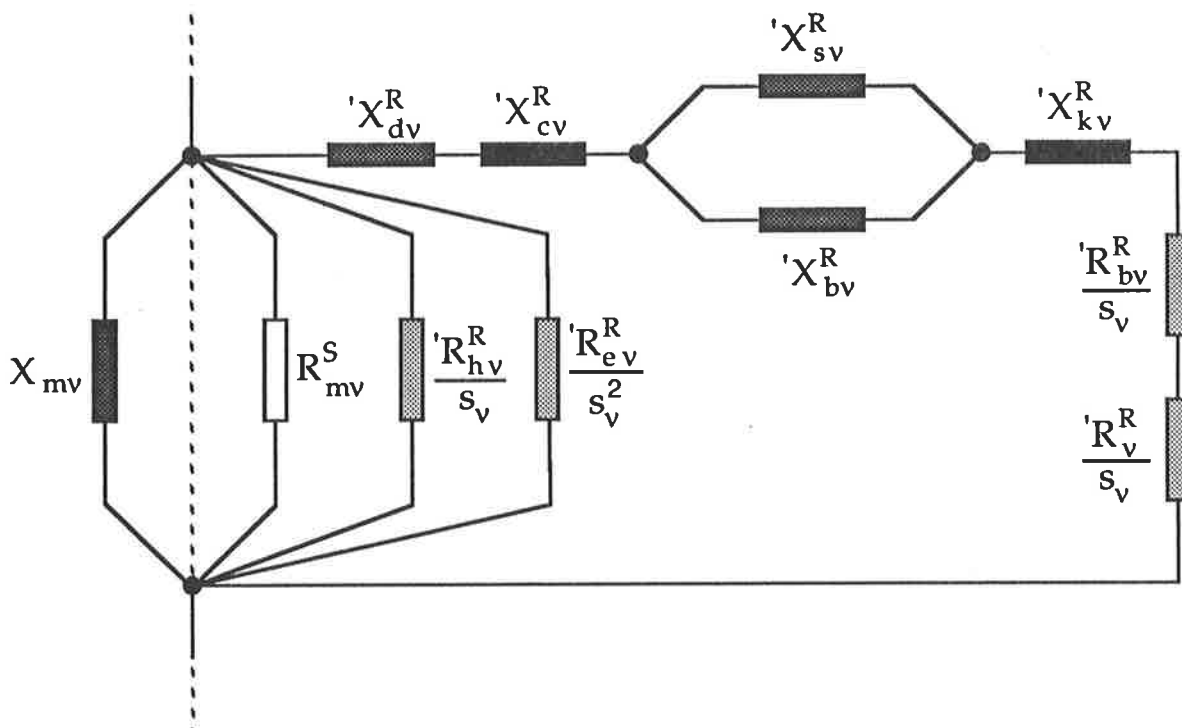


Figure 15

Partial high-fidelity harmonic circuit model in close-up

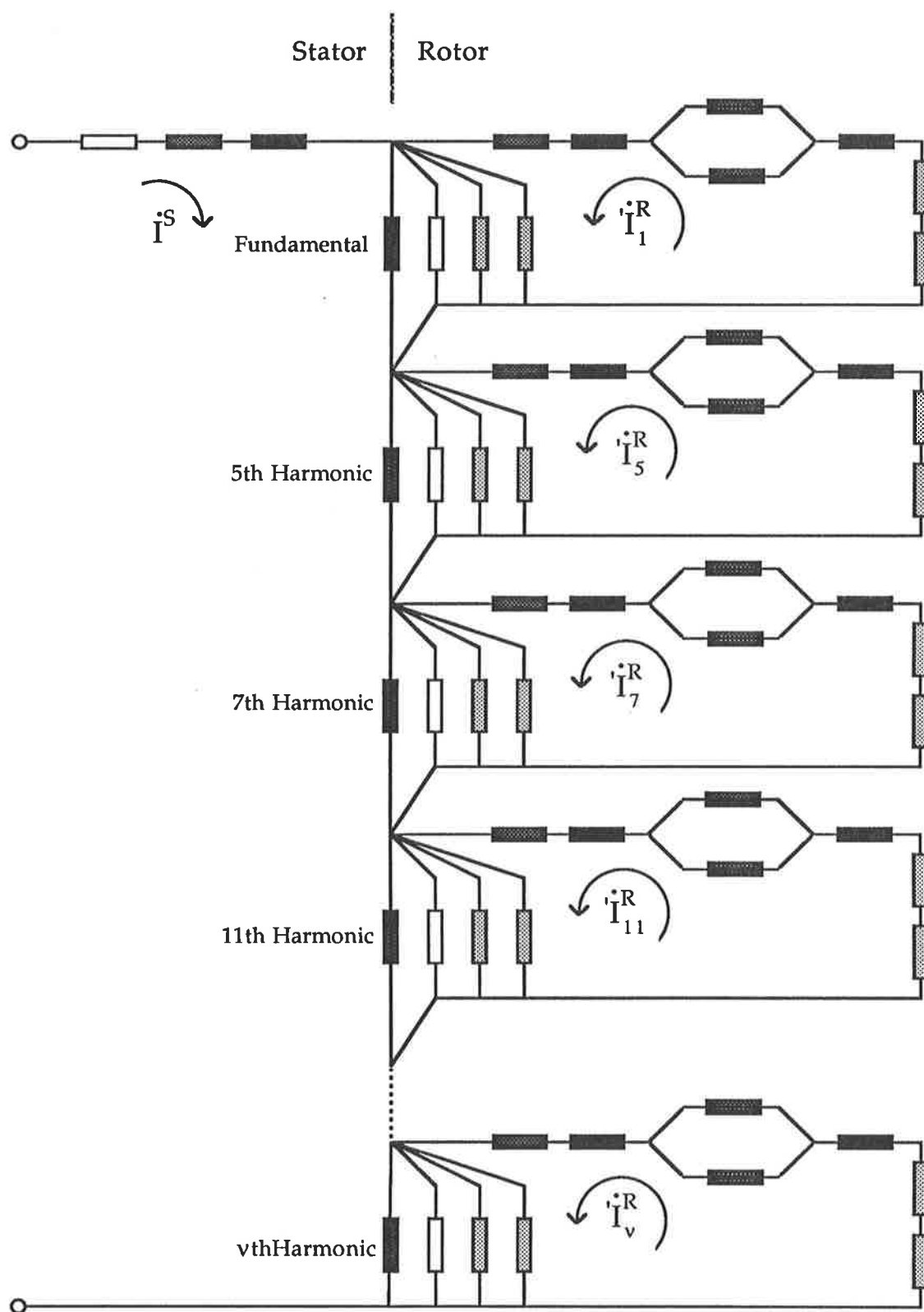


Figure 16

High fidelity harmonic circuit model of an induction machine

**Table 1**

Summary of model parameters for a high-fidelity harmonic circuit model

$R^S$	stator winding resistance
$X_s^S$	stator slot leakage reactance
$X_c^S$	stator coil-end leakage reactance
$X_{dv}^S$	differential leakage reactance, defined as the residue of airgap harmonic fields not linking effectively with the rotor circuits
$X_{mv}$	magnetising reactance, representing the relevant space harmonic, the linkage of which with the rotor circuits is significant
$R_{mv}$	stator core losses (considered to be invariant for a given supply voltage and frequency)
$R_{hv}^R$	hysteresis losses in the rotor core
$R_{ev}^R$	eddy current losses in the rotor core
$X_{dv}^R$	differential leakage reactance, defined as the residue of rotor harmonic fields not linking effectively with the stator circuits
$X_{cv}^R$	rotor coil-end leakage reactance
$X_{sv}^R$	rotor slot leakage reactance
$X_{bv}^R$	reactance to model the effect the decremental effect of current displacement on the rotor slot leakage reactance
$X_{kv}^R$	skew leakage reactance
$R_v^R$	rotor winding resistance
$R_{bv}^R$	incremental resistance to account for the effect of current displacement on the rotor winding resistance
$s_v$	slip for the $v^{\text{th}}$ space harmonic

## 2.7 Time Harmonics

In general, induction machine analysis is carried out with the assumption that the supply is a sinusoidal voltage source. However, this assumption is not realistic in drive applications when variable frequency solid state devices are deployed in operating an induction machine [103, 104]. Even when the supply voltage is sinusoidal, the assumption of a sinusoidal current may not hold because of non-linearities. In such cases, a more rigorous modelling approach becomes obligatory, if the prediction is to be acceptably accurate.

Basically two approaches are possible in modelling non-sinusoidal time variant quantities: one deals with the non-sinusoidal supply *per se* [43], the other proceeds from the known characteristics of the non-sinusoidal current [105]. Both approaches are based on the Fourier transform, representing the time variant quantities in terms of harmonics. The resulting harmonic terms are commonly referred to as *time harmonics*. In the following a distinction will be made between time harmonics depending whether they are deemed to arise solely from the supply conditions or from the waveshape of the phase current. The former will be termed *supply harmonics*, whereas the latter will be referred to as *current harmonics* and their harmonic orders will be shown with  $\eta$  and  $\mu$  respectively.

### 2.7.1 Supply Harmonics

In the case of a non-sinusoidal voltage source, the supply voltage can be represented by a Fourier series as

$$u(t) = \bar{U} + \sum_{\eta=1}^{\infty} U_{\eta \cos} \cos(\eta\omega t) + \sum_{\eta=1}^{\infty} U_{\eta \sin} \sin(\eta\omega t) \quad (157)$$

where  $\bar{U}$  represents the average value of the supply voltage if it has a d.c. component.  $\bar{U}$ ,  $U_{\eta \cos}$  and  $U_{\eta \sin}$  can be obtained from

$$\bar{U} = \frac{1}{T} \int_0^T u(t) dt \quad (158)$$

$$U_{\eta \cos} = \frac{2}{T} \int_0^T u(t) \cos(\eta\omega t) dt \quad (159)$$

$$U_{\eta \sin} = \frac{2}{T} \int_0^T u(t) \sin(\eta\omega t) dt \quad (160)$$

Alternatively, the use of the complex form of the Fourier transform may be attractive due to the compactness of the resulting expressions, in which case the voltage may be given as

$$u(t) = \sum_{-\infty}^{\infty} \dot{U}_{\eta} e^{-j\eta\omega t} \quad (161)$$

where  $\dot{U}_{\eta}$ , the  $\eta^{\text{th}}$  harmonic voltage in phasor form, can be found as the complex Fourier coefficient from

$$\dot{U}_{\eta} = \frac{1}{T} \int_0^T u(t) e^{-j\eta\omega t} dt \quad (162)$$

In terms of circuit modelling, Equations (157) and (161) can be interpreted as representing a set of sinusoidal supplies, connected in series, the frequencies of which cover the range from zero to infinity. This interpretation leads to the general model representation illustrated in Figure 17, in which each time harmonic translates into a harmonic voltage source with a harmonic related frequency and zero internal impedance.



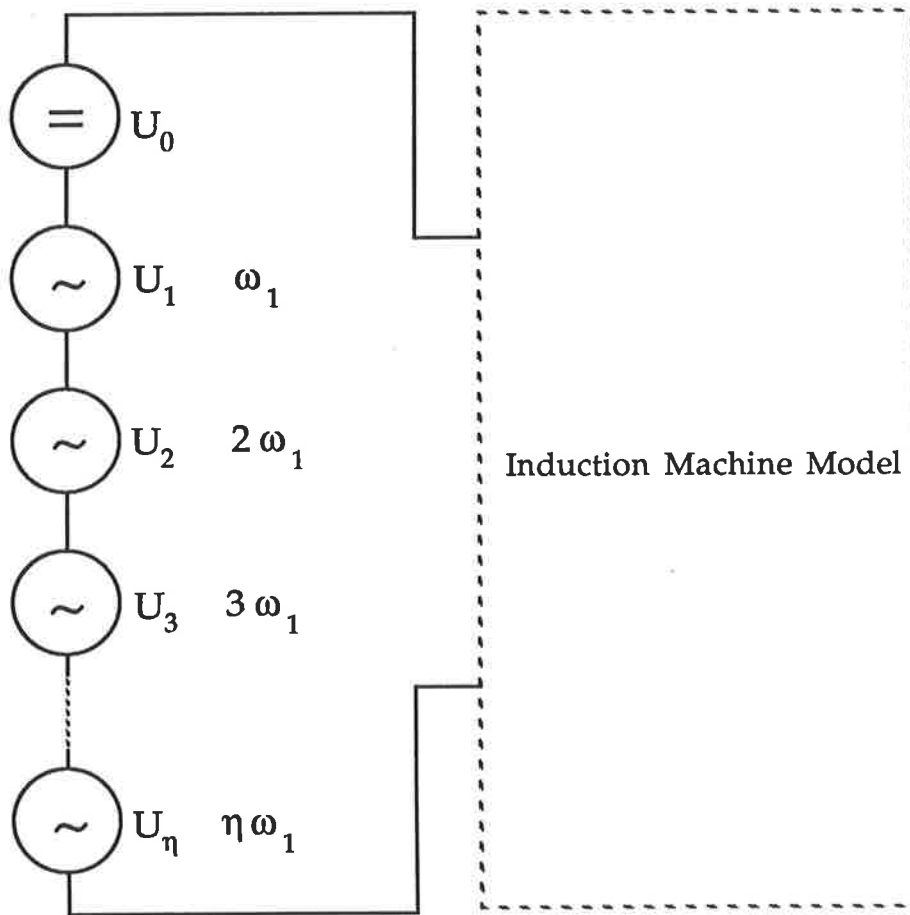


Figure 17

Harmonic supply model for a non-sinusoidal voltage source

Clearly, a harmonic circuit model as developed previously can be substituted in Figure 17 if the effects of both the time harmonics originating from a non-sinusoidal supply and the space harmonics originating in the discrete winding distribution are to be evaluated. It is obvious that, in view of applicability, similar truncation considerations apply as in the case of space harmonics. Thus, only those supply harmonics, the effects of which are likely to be significant will be included in the supply model; this can be assessed in advance by a spectral analysis. The approach is demonstrated in Figure 18, in which a third order supply model is used together with a third order high fidelity model to exemplify the method.

### 2.7.2 Current Harmonics

A somewhat limited alternative in modelling for time harmonics can be devised on the basis of a harmonic analysis of the non-sinusoidal phase current. Obviously, this presupposes that the current waveshape is known under all operating conditions. With this supposition the non-linear phase current can be expressed by means of a Fourier series. Assuming the current waveshape is periodic, but not symmetrical, this leads to a general expression as

$$i(t) = \bar{I} + \sum_{\mu=1}^{\infty} I_{\mu\cos} \cos(\mu \omega t) + \sum_{\mu=1}^{\infty} I_{\mu\sin} \sin(\mu \omega t) \quad (163)$$

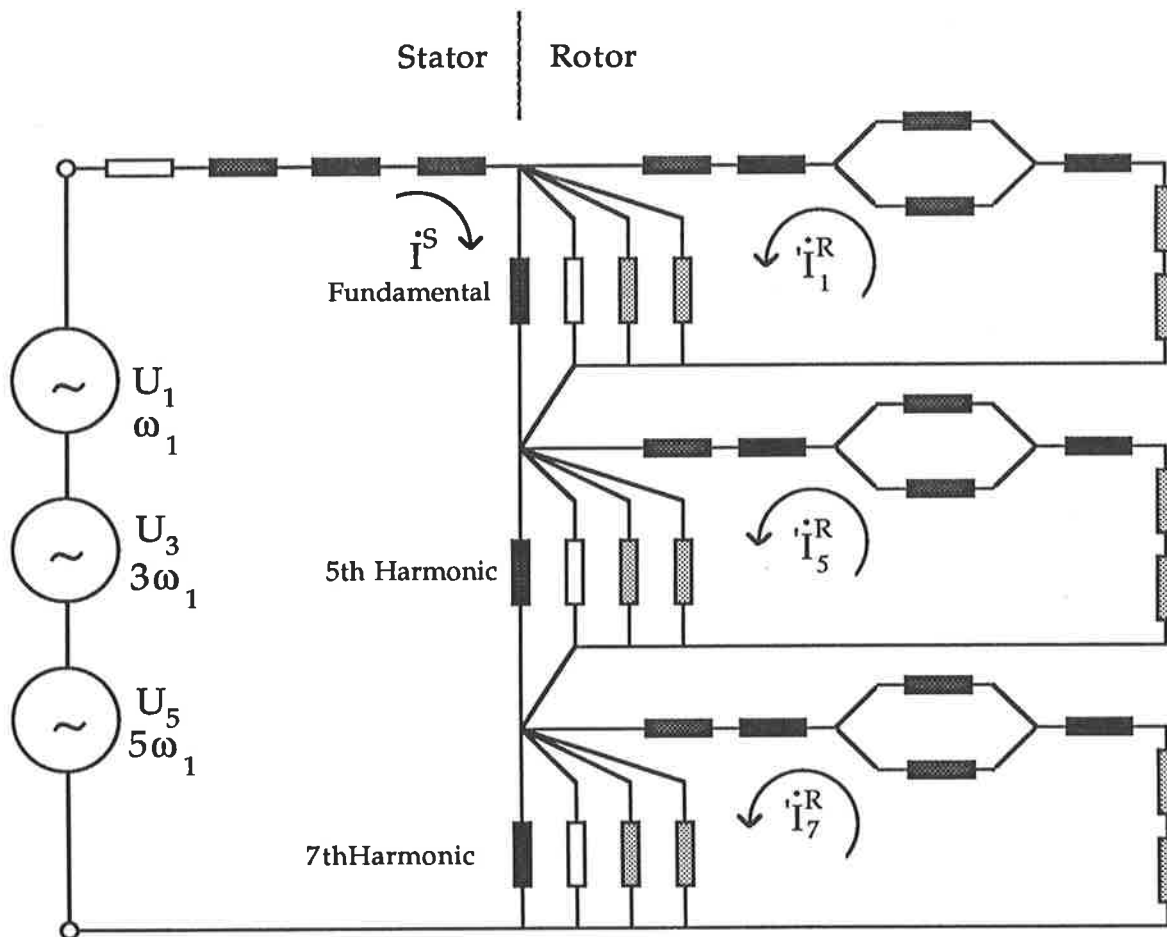


Figure 18

A composite supply-induction machine model

with  $\mu$  denoting the order of current harmonic.  $\bar{I}$ ,  $I_{\mu\cos}$  and  $I_{\mu\sin}$  can be obtained from

$$\bar{I} = \frac{1}{T} \int_0^T i(t) dt \quad (164)$$

$$I_{\mu\cos} = \frac{2}{T} \int_0^T i(t) \cos(\mu \omega t) dt \quad (165)$$

$$I_{\mu\sin} = \frac{2}{T} \int_0^T i(t) \sin(\mu \omega t) dt \quad (166)$$

The above equations can also be expressed using the complex form of the Fourier transform as

$$i(t) = \sum_{-\infty}^{\infty} \dot{I}_{\mu} e^{-j\mu\omega t} \quad (167)$$

where  $\dot{I}_{\mu}$  the  $\mu^{\text{th}}$  harmonic phasor current, is obtained as the complex Fourier coefficient from

$$\dot{I}_{\mu} = \frac{1}{T} \int_0^T i(t) e^{-j\mu\omega t} dt \quad (168)$$

the main advantage being the compactness of the resulting equations.

Evidently, Equation (163), representing the most general form of a non-sinusoidal current, can be substituted in Equation (47) to reflect the effect on the airgap m.m.f. of non-sinusoidal currents. This forms the basis of a modified harmonic circuit model, in which the effects of time harmonics, originating in the non-sinusoidal currents, are included in addition to space harmonics.

The approach is to be illustrated below for a symmetrical non-sinusoidal current waveshape, for which Equation (163) reduces to

$$i(t) = \sum_{\mu=1}^{\infty} I_{\mu \sin} \sin(\mu \omega t) \quad (169)$$

or, in complex notation, to

$$\dot{I} = \sum_{\mu=1}^{\infty} \dot{I}_{\mu \sin} \quad (170)$$

The corresponding e.m.f. for the non-sinusoidally distributed airgap field is

$$\dot{E} = j \sum_{\mu=1}^{\infty} \sum_{\nu=-\infty}^{\infty} X_{\nu \mu} \dot{I}_{\mu \sin} \quad (171)$$

where  $X_{\nu \mu}$  represents the reactance for the  $\nu^{\text{th}}$  space harmonic at the frequency of the  $\mu^{\text{th}}$  time harmonic.

Equation (171) suggests that an aggregate harmonic model can be devised, in which the current harmonics form a parallel-connected set of harmonic current sources, supplying a string of space harmonic reactances. Figure 19 illustrates the generalisation of the concept: a harmonic current source model is interconnected to an induction machine model to account for non-linearity of the current. It is to be noted that no flux-variant parameters need be included in the harmonic circuit model of Figure 19, since it is reasonable to suggest that these effects are implicit in the harmonic current source postulated.

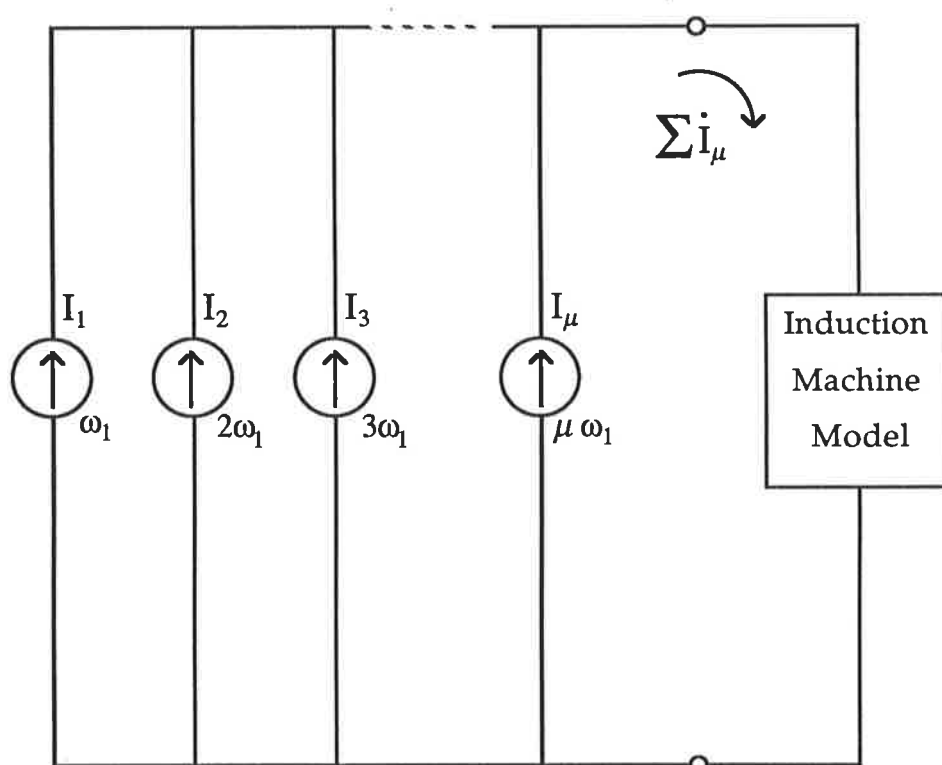


Figure 19

A composite harmonic current source - induction machine model

## 2.8 Performance Prediction Using the Model

The use of high fidelity harmonic circuit models enables far more accurate performance predictions to be made for an induction machine under *quasi-dynamic* operating conditions than is possible when conventional low-order circuit models are employed. A *reduced parameter* high fidelity harmonic circuit model will be used below to illustrate the method of obtaining performance characteristics from the model by a slip-stepping procedure.

Figure 20 shows the complete modified model with reduced parameters, which is identical to the high-fidelity harmonic circuit model of Figure 16 in terms of terminal behaviour. Evidently, the stator impedance is

$$\dot{Z}^s = R^s + j (X_s^s + X_c^s + X_d^s) \quad (172)$$

as before, where  $X_d^s$  denotes the differential leakage reactance as postulated in Section 2.2.7. Parameter reduction is effected as illustrated in Figure 21; the partial high fidelity model of Figure 15 is reduced to an equivalent harmonic circuit model with the same harmonic mesh current as before.

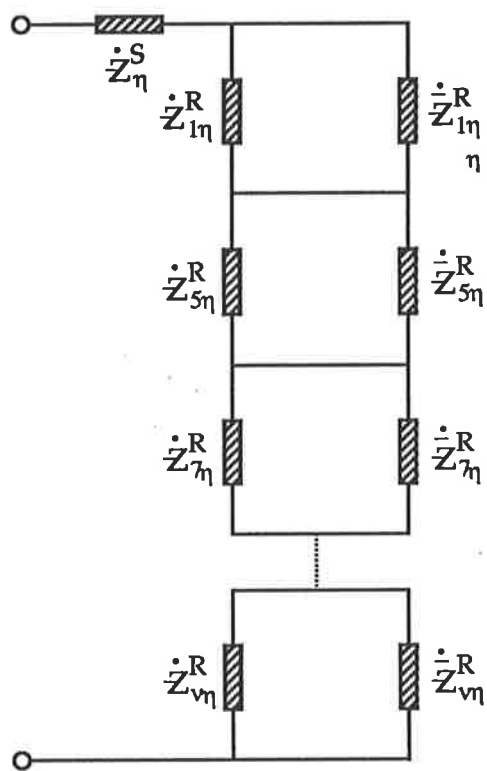


Figure 20

Reduced parameter high-fidelity harmonic circuit model



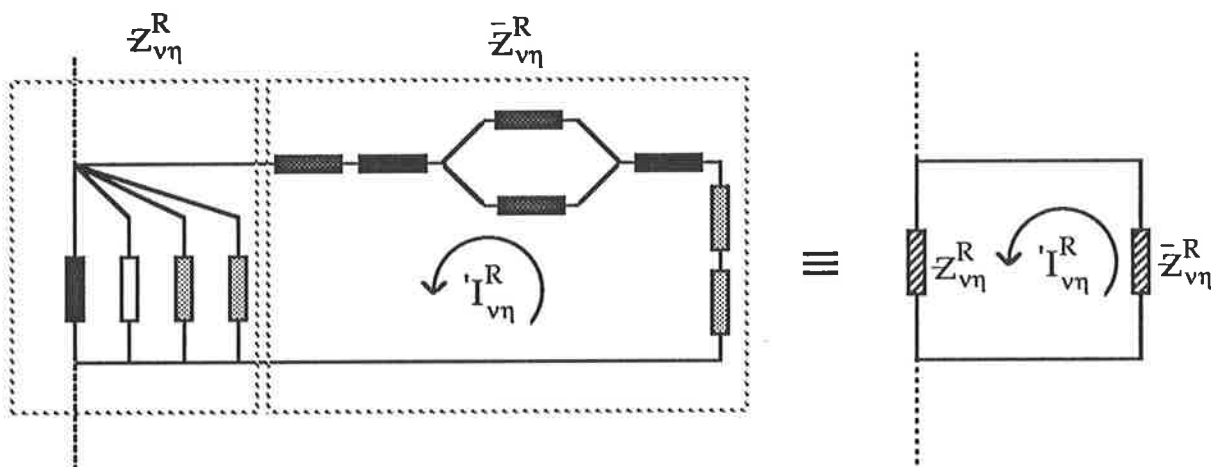


Figure 21

Model reduction

### 2.8.1 Sinusoidal Supply

In the case of a sinusoidal supply, space harmonic currents can be obtained from

$$\begin{array}{c} \dot{U}^S \\ \vdots \\ 0 \end{array} = \begin{array}{cccccccc} \dot{Z}^{SR} & \dot{Z}_1^R & \dot{Z}_5^R & \dot{Z}_7^R & \dot{Z}_{11}^R & \dots & & \dot{Z}_v^R \\ & \dot{Z}_1^R & & & & & 0 & \\ & \dot{Z}_5^R & & & & & & \\ & \dot{Z}_7^R & & & & & & \\ & \dot{Z}_{11}^R & & & & & & \\ & \dots & & & & & & \\ & \dot{Z}_v^R & & & & & & \end{array} \begin{array}{c} \dot{I}^S \\ \dot{I}_1^R \\ \dot{I}_5^R \\ \dot{I}_7^R \\ \dot{I}_{11}^R \\ \dots \\ \dot{I}_v^R \end{array} \quad (173)$$

where

$$\dot{Z}^{SR} = \dot{Z}^S + \sum_v \dot{Z}_v^R \quad (174)$$

and

$$\dot{Z}_v = \dot{Z}_v^R + \dot{Z}_v^R \quad (175)$$

with the impedances on the right-hand-side of Equations (173) to (175) as depicted in Figure 21. In short-hand notation, Equation (173) can also be written as

$$\begin{bmatrix} \dot{U} \end{bmatrix} = \begin{bmatrix} \dot{Z}_v \end{bmatrix} \begin{bmatrix} \dot{I}_v \end{bmatrix} \quad (176)$$

with

$$\left[ \dot{\mathbf{z}}_v \right] = \left[ \dot{\mathbf{z}}_{gh} \right] \quad (177)$$

The elements of the impedance matrix can be generalised as

$$\dot{\mathbf{z}}_{gh} = \begin{cases} \dot{\mathbf{z}}^S + \sum_v \dot{\mathbf{z}}_v^R & ; g, h=1 \\ \dot{\mathbf{z}}_v^R + \dot{\mathbf{z}}_v^R & ; g=h \quad g, h=2,3,\dots, v \\ \dot{\mathbf{z}}_v^R & ; g \neq h \text{ and } g=1 \quad h=2,3,\dots, v \\ & \text{or } g=2,3,\dots, v \quad h=1 \\ 0 & ; \text{ otherwise } g \neq h \end{cases} \quad (178)$$

Correspondingly, currents can be obtained from

$$\left[ \dot{\mathbf{i}}_v \right] = \left[ \dot{\mathbf{Y}}_v \right] \left[ \dot{\mathbf{U}} \right] \quad (179)$$

which yields, for each slip-step, currents in phasor form as

$$\dot{\mathbf{i}}^s \Big|_{s=s+\Delta s} = \left| \dot{\mathbf{i}}^s \right| e^{-j\phi^s} \Big|_{s=s+\Delta s} \quad (180)$$

and

$$\dot{I}_v^R \Big|_{s=s+\Delta s} = \left| \dot{I}_v^R \right| e^{-j\phi_v^R} \Big|_{s=s+\Delta s} \quad (181)$$

for stator and rotor respectively.

The knowledge of currents facilitates the prediction of performance characteristics, including the all-important torque-slip characteristic. The latter can be obtained by interpreting the harmonic rotor circuits as a series connected set of rotors on the same shaft sharing the same stator. With this interpretation, the torque produced by each harmonic rotor for each slip-step can be found as

$$T_v \Big|_{s=s+\Delta s} = m \frac{\left| \dot{I}_v^R \right|^2 R_v^R}{s_v} \Big|_{s=s+\Delta s} \quad (182)$$

giving the total torque as

$$T \Big|_{s=s+\Delta s} = \sum_v T_v \Big|_{s=s+\Delta s} \quad (183)$$

Evidently, the phase lag between the stator current and the terminal voltage is

$$\phi^s = \tan^{-1} \left( \frac{\Re[\dot{I}^s]}{\Im[\dot{I}^s]} \right) \quad (184)$$

from which the power factor versus slip behaviour for the machine can be determined. On the other hand, input power at any slip-step is found from

$$P|_{s=s+\Delta s} = m \Re \left( \dot{U}^s \dot{i}^{s*} \Big|_{s=s+\Delta s} \right) \quad (185)$$

allowing the efficiency to be calculated as

$$\chi = \frac{\omega T}{P} \Big|_{s=s+\Delta s} \quad (186)$$

## 2.8.2 Non-Sinusoidal Conditions

The performance of an induction machine under non-sinusoidal conditions may be carried out on the basis of the deliberations in Sections 2.7.1 or 2.7.2 for a non-sinusoidal supply or a non-sinusoidal current respectively. In the case of the former, this can be done by the conglomeration of a harmonic voltage source model with a *reduced parameter* high fidelity harmonic circuit model, as illustrated in Figure 22.

Evidently, for each supply harmonic the relationships are the same as in Section 2.8.1. Thus, a set of terminal voltage equations will be obtained for each harmonic frequency. This can be expressed in matrix notation as

$$\begin{bmatrix} \dot{V}_\eta \end{bmatrix} = \begin{bmatrix} \dot{Z}_{v\eta} \end{bmatrix} \begin{bmatrix} \dot{i}_{v\eta} \end{bmatrix} \quad (187)$$

The first term on the right hand side of Equation (187) represents a unique impedance matrix for each harmonic frequency. The corresponding currents are given by

$$\begin{bmatrix} \dot{\mathbf{I}}_{v\eta} \end{bmatrix} = \begin{bmatrix} \dot{\mathbf{Y}}_{v\eta} \end{bmatrix} \begin{bmatrix} \dot{\mathbf{V}}_{\eta} \end{bmatrix} \quad (188)$$

The resultant current for the operation of the induction machine from a non-sinusoidal supply can thus be obtained by the superposition of the time harmonic currents found in Equation (188) as

$$\sum_{\eta=-\infty}^{\infty} \sum_{v=-\infty}^{\infty} \begin{bmatrix} \dot{\mathbf{I}}_{v\eta} \end{bmatrix} = \sum_{\eta=-\infty}^{\infty} \prod_{v=-\infty}^{\infty} \begin{bmatrix} \dot{\mathbf{Y}}_{v\eta} \end{bmatrix} \begin{bmatrix} \dot{\mathbf{V}}_{\eta} \end{bmatrix} \quad (189)$$

The left hand side of Equation (189) designates the spectra of supply-harmonic currents for each space harmonic, yielding both amplitude and phase information in each case.

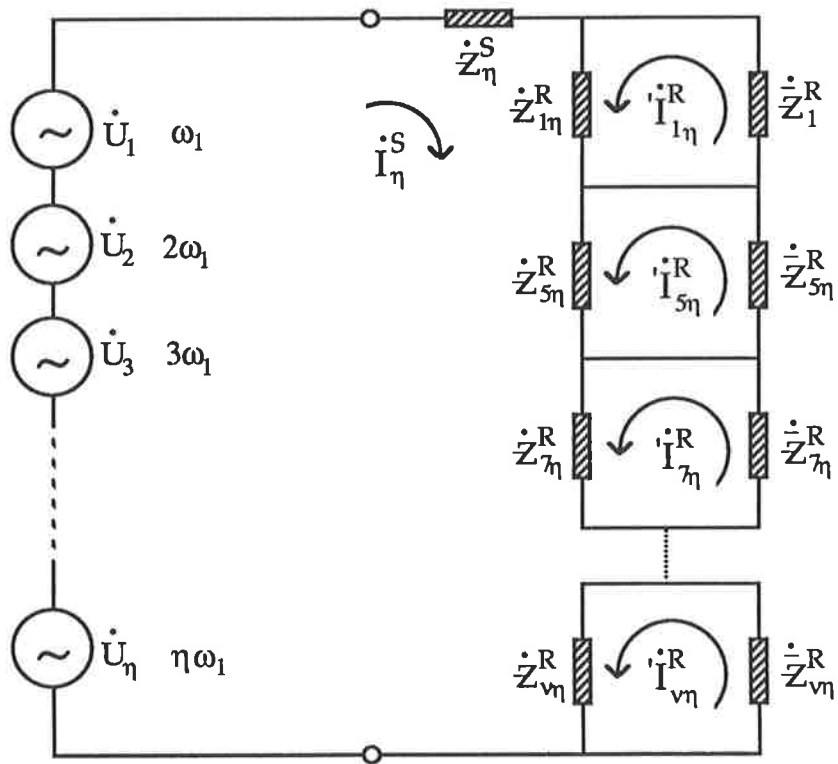


Figure 22

A conglomerate supply/induction-machine model

Performance characteristics can be obtained as before once the currents are known. For instance, the electromagnetically produced torque can be found by slip-stepping through the operating range as

$$T|_{s=s+\Delta s} = \sum_{\eta} \sum_{\nu} T_{\nu\eta}|_{s=s+\Delta s} \quad (190)$$

Analogously, the effect on the machine performance of non-sinusoidal currents can be analysed by means of a conglomerate model comprising a harmonic current source model and a *linear parameter* harmonic circuit model. This is illustrated in Figure 23.

Again, individual branch currents need to be obtained for each current harmonic before embarking on an analysis of the machine performance. In matrix notation the currents are

$$\begin{bmatrix} \dot{\mathbf{I}} \end{bmatrix} = \begin{bmatrix} \dot{\mathbf{I}}_{11}^R & \dot{\mathbf{I}}_{51}^R & \dot{\mathbf{I}}_{71}^R & \dots & \dots & \dot{\mathbf{I}}_{\nu 1}^R \\ \dot{\mathbf{I}}_{12}^R & \dot{\mathbf{I}}_{52}^R & \dot{\mathbf{I}}_{72}^R & \dots & \dots & \dot{\mathbf{I}}_{\nu 2}^R \\ \dot{\mathbf{I}}_{13}^R & \dot{\mathbf{I}}_{53}^R & \dot{\mathbf{I}}_{73}^R & \dots & \dots & \dot{\mathbf{I}}_{\nu 3}^R \\ \dots & \dots & \dots & \dots & \dots & \dots \\ \dot{\mathbf{I}}_{1\mu}^R & \dot{\mathbf{I}}_{5\mu}^R & \dot{\mathbf{I}}_{7\mu}^R & \dots & \dots & \dot{\mathbf{I}}_{\nu\mu}^R \end{bmatrix} \quad (191)$$

where the elements of the current matrix are obtained from

$$\dot{\mathbf{I}}_{\nu\mu}^R = \dot{\mathbf{I}}_{\nu\mu} \frac{\dot{\mathbf{Z}}_{\nu\mu}^R}{\dot{\mathbf{Z}}_{\nu\mu}^R + \dot{\mathbf{Z}}_{\nu\mu}^R} \quad (192)$$



The resultant torque can be determined on the basis of similar considerations as before. In this instance, it is more appropriate to represent the harmonic torque components in matrix form as

$$[\mathbf{T}] = \begin{bmatrix} T_{11} & T_{51} & T_{71} & \dots & \dots & T_{v1} \\ T_{12} & T_{52} & T_{72} & \dots & \dots & T_{v2} \\ T_{13} & T_{53} & T_{73} & \dots & \dots & T_{v3} \\ \dots & \dots & \dots & \dots & \dots & \dots \\ T_{1\mu} & T_{5\mu} & T_{7\mu} & \dots & \dots & T_{v\mu} \end{bmatrix} \quad (193)$$

where the subscripts  $v$  and  $\mu$  serve to identify the order of space harmonic and current harmonic respectively. The total torque for any slip can now be obtained, by superposition, from Equation (193) as

$$T|_{s=s+\Delta s} = \sum_{\mu} \sum_v [T_{v\mu}]|_{s=s+\Delta s} \quad (194)$$

where  $[T_{v\mu}]$  denotes the elements of the torque matrix of Equation (193) and can be found for any slip as

$$[T_{v\mu}]|_{s=s+\Delta s} = m \frac{|\dot{i}_{v\mu}^R|^2 R_v^R}{s_{v\mu}} \Big|_{s=s+\Delta s} \quad (195)$$

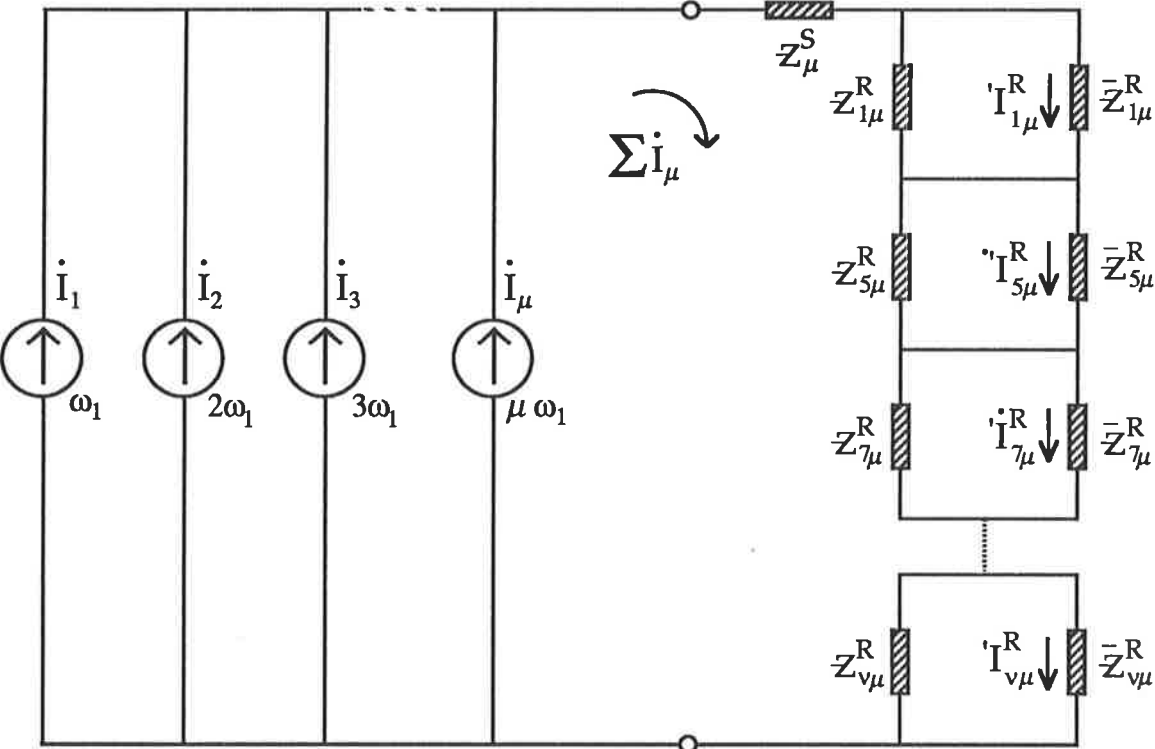


Figure 23

A conglomerate induction-machine/drive model comprising harmonic current sources and a linear-parameter harmonic circuit model

# 3

## DYNAMIC MODELS

### 3.1 The Object

The object of this chapter is to identify the physical bases for the dynamic modelling of induction machines and to provide a brief overview of the various approaches suitable for analysis. The overview is provided for two reasons:

- 1 to elucidate the possible options
- 2 to lay the foundation for the methods of analysis used in dealing with the general models to be developed in Chapter 4.

It is not the purpose of this chapter to elaborate on the relative merits or shortcomings of one method in comparison with another. The emphasis is on possible approaches to model formation and on methods of solution.

### 3.2 Induction Machine Dynamics

Every induction machine is subject to dynamic operating conditions of different and varying proportions. The dynamic regime for a mains driven induction motor, started direct-on-line, may differ in scope from that of step changes in the load of a machine fed from a solid-state variable speed drive [106, 107]. However, transient phenomena are present in both cases. On the other hand, it is not possible to draw conclusions as to how an induction machine will behave under transient conditions from the study of steady state or quasi-dynamic performance of the machine. Because even if the steady-state performance of an induction machine may be entirely satisfactory, its transient behaviour during a dynamic regime may not be. Thus, it is of utmost importance, both from an operational viewpoint and in terms of machine design, to devise models capable of dealing with induction machine dynamics.

Far too long it has been taken for granted that neglecting the effects of non-sinusoidal supply conditions and non-sinusoidal airgap m.m.f. distribution along with the assumption of a linear core and uniform current distribution can lead to performance predictions which can be taken seriously [42, 109]. However, it is now becoming well recognised that the validity of transients predicted depend on the validity of the mathematical models used [17, 110, 111]. This recognition is reflected in the wide range of dynamic models being developed, all of which strive to improve prediction accuracy [47, 112, 113]. Such developments are accompanied by efforts to keep the ensuing models simple [114, 115].

Since dynamic regime implies time variation of the quantities of concern, this invariably involves the solution of differential equations in one form

or the other. Evidently, the knowledge of initial conditions is critical to the reliable evaluation of such equations.

Energy storage parameters play a dominant role in shaping the transient behaviour of an induction machine during such a dynamic regime. Thus the resulting variations in magnetic fields and speed of rotation will have ramifications in terms of the total energy balance for the induction machine, which will tend toward a new equilibrium state.

Evidently, the transient processes taking place during the dynamic regime can be described in general by the use *Lagrange's equation of motion* for rotating bodies which can be given as

$$[\mathcal{T}] = \frac{d}{dt} \left[ \frac{\partial \mathcal{L}}{\partial \dot{\chi}} \right] - \left[ \frac{\partial \mathcal{L}}{\partial \chi} \right] + \left[ \frac{\partial \mathcal{R}}{\partial \dot{\chi}} \right] \quad (196)$$

Equation (196) represents the general dynamic equation for a rotating electromagnetic system with  $n$  degrees of freedom in an holonomic reference frame, and includes both the terminal voltage equations and the torque equation. It states that  $\mathcal{T}$ , the *Lagrangian moment*, for a given rotating system can be obtained from its instantaneous energy balance conditions. Herein,  $\chi$  denotes collectively all system coordinates in an  $n$ -dimensional coordinate system whereas  $\dot{\chi}$  gives the time variation with reference to the system coordinates.  $\mathcal{L}$ , the *Lagrangian*, is defined as

$$[\mathcal{L}] = [\mathcal{K}] - [\mathcal{P}] \quad (197)$$

where  $\mathcal{K}$  is the generalised dynamic energy term, comprising both kinetic energy and magnetic energy components.  $\mathcal{P}$  represents the generalised

potential energy term. These two energy terms can be defined in their most general form as

$$[\mathcal{K}] = \frac{1}{2} [\mathbf{J} \dot{\chi}^2] \quad (198)$$

and

$$[\mathcal{P}] = \frac{1}{2} [\mathbf{K} \chi^2] \quad (199)$$

$\mathcal{R}$  in the third term on the right hand side of Equation (196) is the so-called *Raleigh dissipation function*, representing the total system losses. Its generalised form is

$$[\mathcal{R}] = [\mathbf{R} \dot{\chi}^2] \quad (200)$$

As is the case with the other terms in Equation (196),  $\mathcal{R}$  represents both the mechanical and electromagnetic loss components.

Lagrange's equation of motion is fundamental to the study of induction machine dynamics; in its different guises it forms the basis of the many and varied forms of dynamic models for induction machines. It offers a versatile general tool in analysing transient behaviour by the application of a variety of modelling approaches and solution methods.

### 3.3 Dynamic Modelling Approaches

Dynamic models for induction machines are formed on the basis of the principles embedded in the Lagrangian equation of motion. The differences amongst various models arise mainly from the

- 1 adoption of a particular modelling approach
- 2 choice of a method of solution and
- 3 selection of the reference frame within which models are formulated.

As pointed out previously, modelling approaches range from those based on field modelling to those utilising lumped parameter circuit models. The most common implementation of the former is by the use of finite element analysis [35]. The latter approach includes Park's notion of "two-reaction theory" on the one end of the spectrum [41] and the use of instantaneous complex quantities represented in terms of "space phasors" on the other end of the spectrum [79].

In the case of *finite element modelling*, Maxwell's equations are solved iteratively for a given region of the machine after having generated a finite element mesh of suitable resolution. The region is usually selected to cover an axial plane of the entire machine. Flux distribution within the region is then determined by evaluating the vector magnetic potential at every node. Phase currents are deduced by further post-processing [114]. Transient solutions to flux distribution and current are sought by the implementation of time-stepping procedures [29, 31]. Although it is principally feasible to determine the transient performance characteristics

for a given machine accurately, the computational effort is prohibitive for even very short durations of transients. Additional computational difficulties exist in dealing with relative motion between the rotor and the stator, making it difficult to obtain, for example, the torque-speed characteristic by direct computation. Thus, the application of finite element techniques is, as yet, practically viable mainly for the investigation of transients in a stationary induction machine, such as direct-on-line starting before the rotor starts to rotate [35, 117].

On the other hand, lumped parameter circuit models have been employed, since early on in analysing induction machine behaviour under dynamic conditions [3, 4, 78]. Most of the early work was performed using orthogonal models obtained by axis transformations [118, 119, 120], although direct models were occasionally employed. It was observed, however, that most circuit models used for transient analysis suffered, to a greater or lesser degree, from the assumptions made in their formation and that the prediction accuracy depended on the validity of the model used. Attempts were made to improve model fidelity [121, 122]. The difficulties in finding analytical solutions to the resulting non-linear simultaneous differential equations were overcome by the use of differential analysers and analog computers [109, 123, 124].

The popularity of the orthogonal models obtained by means of axes transformations appears to continue unabated. Nevertheless, it is now known that the usefulness of transformation techniques is restricted to somewhat idealised cases; although axis transformations allow solutions to the equations of motion to be obtained, their application for dynamic analysis is limited to cases where the idealisations in their formation can be justified [125]. Furthermore, the results found by the use of models



obtained by transformation techniques need to be transformed back if the findings are to be meaningful from a practical viewpoint. Direct phase models overcome this last objection, provided measures are taken to improve their fidelity [45, 58].

If idealisations are not justifiable, then model formation has to account for physical phenomena of import; such phenomena may include core nonlinearities [43, 96, 126] and the actual positioning of the windings [19]. This would enhance model fidelity. In this context, it should be noted that the high fidelity harmonic circuit models developed in Chapter 2 of this thesis conceivably offer scope in also enabling the transient behaviour to be predicted accurately, although their forte is the prediction of parasitic effects under quasi dynamic conditions. Discrete circuit models, on the other hand, allow flux linkages between the rotor and the stator and their time variation to be modelled much more realistically than is possible with low order lumped parameter circuit models. Their ability to assess the impact on the machine behaviour of localised effects at individual circuit level is an added bonus.

All above models can be formulated either in the *time domain* or as *state models* [125, 127]. If done in conjunction with direct simulation models, this yields directly useable results eliminating the necessity of domain transformations [128]. Closed form analytical solutions are virtually impossible when the system equations are non-linear, but results can be obtained by the use of numerical integration techniques [129].

An alternative modelling approach can be devised based on the notion of *space phasor*. The ensuing models can be effectively utilised for transient analysis [79, 81].

### 3.4 Time Domain Formulation

Assuming a general case with  $m$  stator phases and  $n$  rotor phases, the basic system equations can be constituted in the time domain in terms of circuit model parameters and system mechanics as:

$$[\mathbf{u}^S] = [\mathbf{R}^S] [\mathbf{i}^S] + [\mathbf{L}^{SS}] p[\mathbf{i}^S] + p[\mathbf{L}^{SR}] [\mathbf{i}^R] \quad (201)$$

$$[\mathbf{u}^R] = p[\mathbf{L}^{SR}]^T [\mathbf{i}^S] + [\mathbf{R}^R] [\mathbf{i}^R] + [\mathbf{L}^{RR}] p[\mathbf{i}^R] \quad (202)$$

$$T_e = T_L + J p\omega + D\omega \quad (203)$$

$$T_e = [\mathbf{i}^S]^T \frac{\partial}{\partial \theta^R} [\mathbf{L}^{SR}] [\mathbf{i}^R] \quad (204)$$

Equations (201) to (204) assume a uniform airgap, identical stator windings and identical rotor windings. The windings are assumed to be symmetrically distributed. Mechanical losses are represented by the damping coefficient  $D$  in Equation (203). Equations (201), (202) and (203) constitute a general dynamic model for an induction machine, corresponding to Equation (196). Terminal voltages and phase currents are to be expressed as

$$[\mathbf{u}^S] = [u_1^S \quad u_2^S \quad u_3^S \quad \dots \quad u_m^S]^T \quad (205)$$

$$[\mathbf{u}^R] = [0 \quad 0 \quad 0 \quad \dots \quad 0]^T \quad (206)$$

$$[\mathbf{i}^S] = [i_1^S \quad i_2^S \quad i_3^S \quad \dots \quad i_m^S]^T \quad (207)$$

$$[\mathbf{i}^R] = [i_1^R \quad i_2^R \quad i_3^R \quad \dots \quad i_n^R]^T \quad (208)$$

Stator and rotor resistances can be represented by an  $m$ -rowed and an  $n$ -rowed diagonal matrix respectively as

$$[\mathbf{R}^S] = \begin{vmatrix} R_1^S & 0 & 0 & & 0 \\ 0 & R_2^S & & \dots & \\ 0 & 0 & R_3^S & \dots & \\ & & \dots & \dots & \\ 0 & 0 & 0 & \dots & R_m^S \end{vmatrix} \quad (209)$$

and

$$[\mathbf{R}^R] = \begin{vmatrix} R_1^R & 0 & 0 & \dots & 0 \\ 0 & R_2^R & & \dots & 0 \\ 0 & 0 & R_3^R & \dots & 0 \\ \dots & \dots & \dots & & \dots \\ \dots & \dots & \dots & & \dots \\ 0 & 0 & 0 & \dots & R_n^R \end{vmatrix} \quad (210)$$

Stator and rotor inductances can be modelled by an  $m \times m$  and an  $n \times n$  square matrix respectively as

$$[\mathbf{L}^{SS}] = \begin{vmatrix} L_{1,1}^S & L_{1,2}^S & L_{1,3}^S & \dots & L_{1,m}^S \\ L_{2,1}^S & L_{2,2}^S & L_{2,3}^S & \dots & L_{2,m}^S \\ L_{3,1}^S & L_{3,2}^S & L_{3,3}^S & \dots & L_{3,m}^S \\ \dots & \dots & \dots & & \dots \\ L_{m,1}^S & L_{m,2}^S & L_{m,3}^S & & L_{m,m}^S \end{vmatrix} \quad (211)$$

and

$$[\mathbf{L}^{RR}] = \begin{pmatrix} L_{1,1}^R & L_{1,2}^R & L_{1,3}^R & \dots & L_{1,n}^R \\ L_{2,1}^R & L_{2,2}^R & L_{2,3}^R & \dots & L_{2,n}^R \\ L_{3,1}^R & L_{3,2}^R & L_{3,3}^R & \dots & L_{3,n}^R \\ \dots & \dots & \dots & \dots & \dots \\ \dots & \dots & \dots & \dots & \dots \\ L_{n,1}^R & L_{n,2}^R & L_{n,3}^R & \dots & L_{n,n}^R \end{pmatrix} \quad (212)$$

The matrices of Equations (211) and (212) are cyclic and symmetrical. The principal diagonal contains the self inductances. All other matrix elements correspond to the mutual inductances between the phases and can be generally expressed, for the stator and the rotor respectively, as

$$L_{g,h}^S = L_{h,g}^S = L_g^S \cos\left(|g-h| \frac{2\pi}{m}\right) \quad (213)$$

$$L_{i,j}^R = L_{j,i}^R = L_i^R \cos\left(|i-j| \frac{2\pi}{n}\right) \quad (214)$$

Mutual inductances between the stator and the rotor can be represented by an  $m \times n$  matrix

$$[\mathbf{L}^{SR}] = \begin{pmatrix} L_{1,1}^{S,R} & L_{1,2}^{S,R} & L_{1,3}^{S,R} & \dots & L_{1,m}^{S,R} \\ L_{2,1}^{S,R} & L_{2,2}^{S,R} & L_{2,3}^{S,R} & \dots & L_{2,m}^{S,R} \\ L_{3,1}^{S,R} & L_{3,2}^{S,R} & L_{3,3}^{S,R} & \dots & L_{3,m}^{S,R} \\ \dots & \dots & \dots & \dots & \dots \\ \dots & \dots & \dots & \dots & \dots \\ L_{n,1}^{S,R} & L_{n,2}^{S,R} & L_{n,3}^{S,R} & \dots & L_{n,m}^{S,R} \end{pmatrix} \quad (215)$$

where individual matrix elements can be found from

$$L_{g,i}^{S,R} = L_{g,i}^{S,R} \Big|_{\vartheta^R=0} \cos \left\{ \vartheta^R - (g-1) \frac{2\pi}{m} + (i-1) \frac{2\pi}{n} \right\} \quad (216)$$

With the model parameters thus defined, the system behaviour under dynamic conditions can be simulated digitally using numerical integration techniques.

### 3.5 State-Variable Formulation

In the general case of an induction machine with  $m$  stator phases and  $n$  rotor phases, leading to non-linear differential system equations with a large number of variables, state-variable formulation of system equations may prove to be more advantageous. Firstly, state-variable equations are inherently suitable for the implementation of computer methods in their solution. Secondly, non-linearities can be readily accommodated in a state-variable model which is valid for any input function and any set of initial conditions. These features render state-space models especially pertinent to the dynamic modelling of induction machines.

Principally, the state-variable formulation of system equations is based on

$$[\dot{\mathbf{x}}] = f\{[\mathbf{x}], [\mathbf{v}], t\} \quad (217)$$

where  $[\mathbf{x}]$  denotes the *state vector* and  $[\mathbf{v}]$  the *input vector*. System response is given by

$$[\mathbf{y}] = g\{[\mathbf{x}], [\mathbf{v}], t\} \quad (218)$$

where  $[\mathbf{y}]$  is the *output vector*. Clearly, the initial state  $[\mathbf{x}(0)]$  has a profound impact on the system's behaviour and must be duly accounted for.

For a rotational electromagnetic system, it is more illustrative to express Equation (217) as

$$[\dot{\mathbf{x}}] = [\mathbf{A}][\mathbf{x}] + [\mathbf{B}][\mathbf{v}] \quad (219)$$

where  $[A]$  : Bashkow A matrix

$[B]$  : constant matrix.

In the case of an induction machine with  $m$  stator phases and  $n$  rotor phases as stipulated previously, the state vector can be defined as

$$[x] = \begin{bmatrix} [i] \\ \omega \\ \theta \end{bmatrix} \quad (220)$$

with  $[i]$ ,  $\omega$  and  $\theta$  constituting the state-variables. Similarly, the input vector can be given as

$$[u] = \begin{bmatrix} [u] \\ T_L \\ 0 \end{bmatrix} \quad (221)$$

where  $[u]$  represents stator and rotor terminal voltages collectively.  $T_L$  is the load torque.

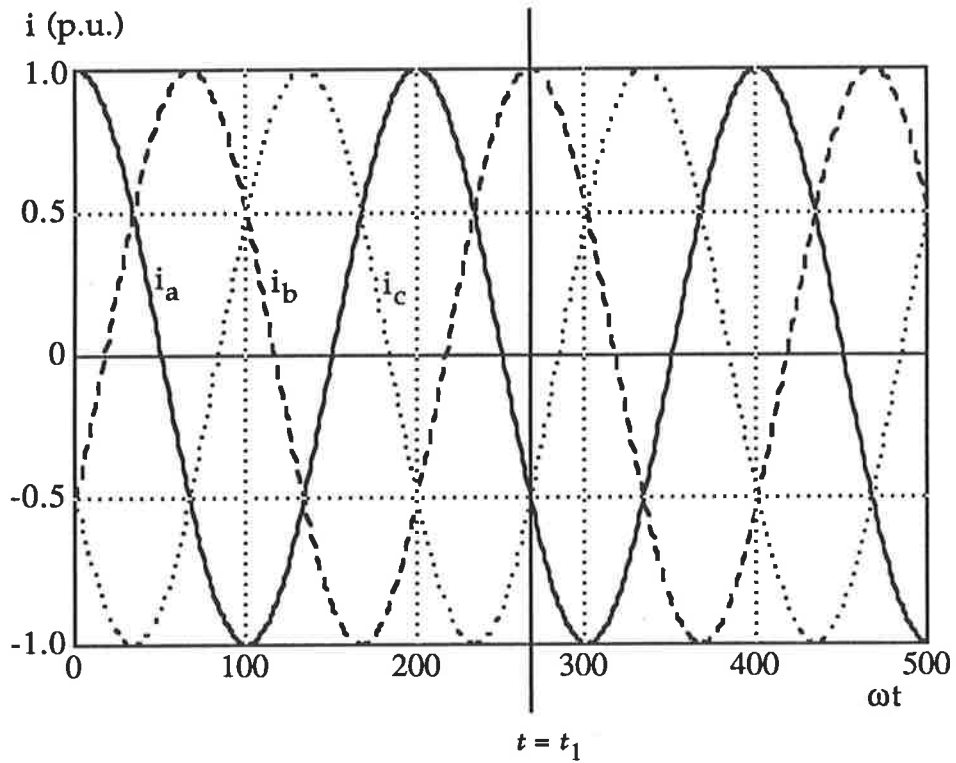


Figure 24

Phase currents for a three-phase stator winding

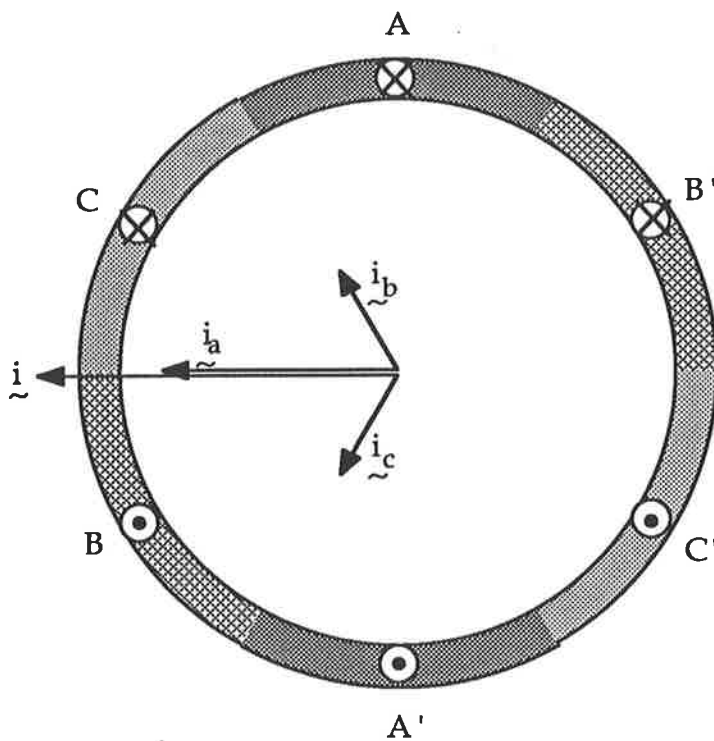


Figure 25

Space phasor relationships at time  $t = t_1$



For a three-phase winding, the current space phasor for each phase can be expressed in complex notation in terms of the instantaneous value of the current and angular position of the phase axis as

$$\underline{i}_a = i_a \underline{r}_a \quad (229)$$

$$\underline{i}_b = i_b \underline{r}_b \quad (230)$$

$$\underline{i}_c = i_c \underline{r}_c \quad (231)$$

where  $\underline{r}_a$ ,  $\underline{r}_b$  and  $\underline{r}_c$  denote unit vectors associated with phases a, b and c respectively. Generally, a unit vector as postulated can be defined for a phase n, in operational form, as

$$\underline{r}_n = e^{j\theta_n} \quad (232)$$

where  $\theta_n$  is the angular displacement of the  $n^{\text{th}}$  phase axis with reference to a datum. Thus, taking the magnetic axis of phase a as datum, the unit vectors for a symmetrical three-phase winding become

$$\underline{r}_a = e^{j0} \quad (233)$$

$$\underline{r}_b = e^{j120^\circ} \quad (234)$$

$$\underline{r}_c = e^{j240^\circ} \quad (235)$$

The unit vector associated with the  $n^{\text{th}}$  phase of an  $m$ -phase winding can be expressed as

$$\tilde{\mathbf{r}}_n = e^{j\frac{2\pi}{m}(n-1)} \quad (236)$$

Consequently, the resultant space phasor for an  $m$ -phase winding can be obtained as

$$\tilde{\mathbf{i}} = \sum_{n=1}^m \mathbf{i}_n e^{j\frac{2\pi}{m}(n-1)} \quad (237)$$

Equation (237) is representative of the total airgap m.m.f., a point mentioned previously. It is often convenient to express this as a *per phase* quantity. This can be done by considering that the total m.m.f. for an  $m$ -phase winding can be shown to be

$$\mathbf{F}(\chi t) = \frac{m}{2} \hat{\mathbf{F}} \cos(\theta - \omega t) \quad (238)$$

from which the current space phasor as a *per phase* quantity can be deduced as

$$\tilde{\mathbf{i}}^s = \frac{2}{m} \tilde{\mathbf{i}} \quad (239)$$

It stands to reason that the above arguments can be extended to other electromagnetic quantities. Thus, voltages and flux linkages, respectively, can be expressed in space phasor terms as

$$\underline{u}^s = \frac{2}{m} \underline{u} \quad (240)$$

and

$$\underline{\Psi}^s = \frac{2}{m} \underline{\Psi} \quad (241)$$

In Equations (240) and (241), the voltage and flux linkage terms are given by

$$\underline{u} = \sum_{n=1}^m \underline{u}_n \quad (242)$$

and

$$\underline{\Psi} = \sum_{n=1}^m \underline{\Psi}_n \quad (243)$$

whereas the individual phase quantities are defined with the aid of the unit vectors as in Equations (229) to (231). With these considerations, the stator terminal voltage equation in a stator bound reference frame can be written as

$$\underline{u}^s = \underline{R}^s \underline{i}^s + \frac{d\underline{\Psi}^s}{dt} \quad (244)$$



The current space phasors  $\underline{\tilde{i}}^S$  and  $\underline{\tilde{i}}^R$  are given in their respective coordinate systems as

$$\underline{\tilde{i}}^S = \left| \underline{\tilde{i}}^S \right| e^{j\theta^S} \quad (246)$$

and

$$\underline{\tilde{i}}^R = \left| \underline{\tilde{i}}^R \right| e^{j\theta^R} \quad (247)$$

where  $\theta^S$  and  $\theta^R$  represent the instantaneous angular position of the current space phasor in that reference frame. It is to be noted that the stator bound reference frame is stationary, whereas the rotor bound reference frame rotates at an angular velocity of  $\omega^R$ . The same current space phasors can be referred to an arbitrarily chosen orthogonal reference frame rotating at an angular velocity of  $\omega^\perp$  as

$$\perp \underline{\tilde{i}}^S = \left| \underline{\tilde{i}}^S \right| e^{j(\theta^S - \varphi^S)} \quad (248)$$

and

$$\perp \underline{\tilde{i}}^R = \left| \underline{\tilde{i}}^R \right| e^{j(\theta^R - \varphi^R)} \quad (249)$$

Equations (248) and (249) can be arranged as

$$\perp \underline{\tilde{i}}^S = \underline{\tilde{i}}^S e^{-j\varphi^S} \quad (250)$$

and

$$\perp \underline{\tilde{i}}^R = \underline{\tilde{i}}^R e^{-j\varphi^R} \quad (251)$$

The corollary is that any electromagnetic quantity in the stationary stator reference frame or in the rotating reference frame attached to the rotor can be expressed in any other orthogonal reference frame rotating at any speed by taking into account its angular displacement with this new coordinate system. Thus, the voltage space phasor of Equation (240) and the flux space phasor of Equation (241) can also be expressed in this third reference frame as

$$\underline{\underline{\perp}}\underline{\underline{u}}^s = \underline{\underline{u}}^s e^{-j\phi^s} \quad (252)$$

and

$$\underline{\underline{\perp}}\underline{\underline{\Psi}}^s = \underline{\underline{\Psi}}^s e^{-j\phi^s} \quad (253)$$

Considering that

$$\underline{\underline{i}}^s = \underline{\underline{\perp}}\underline{\underline{i}}^s e^{j\phi^s} \quad (254)$$

$$\underline{\underline{u}}^s = \underline{\underline{\perp}}\underline{\underline{u}}^s e^{j\phi^s} \quad (255)$$

$$\underline{\underline{\Psi}}^s = \underline{\underline{\perp}}\underline{\underline{\Psi}}^s e^{j\phi^s} \quad (256)$$

and

$$\underline{\underline{i}}^R = \underline{\underline{\perp}}\underline{\underline{i}}^R e^{j\phi^R} \quad (257)$$

$$\underline{\underline{u}}^R = \underline{\underline{\perp}}\underline{\underline{u}}^R e^{j\phi^R} \quad (258)$$

$$\underline{\underline{\Psi}}^R = \underline{\underline{\perp}}\underline{\underline{\Psi}}^R e^{j\phi^R} \quad (259)$$

the terminal voltage equations for the stator and the rotor can be re-written in the new reference frame as

$$\underline{u}^S = \underline{R}^S \underline{i}^S + \frac{d\underline{\Psi}^S}{dt} + j\omega^\perp \underline{\Psi}^S \quad (260)$$

$$\underline{u}^R = \underline{R}^R \underline{i}^R + \frac{d\underline{\Psi}^R}{dt} + j(\omega^\perp - \omega^R) \underline{\Psi}^R \quad (261)$$

The above manipulations constitute a *coordinate transformation*. Performance analysis can now be effected using the transformed coordinates. For instance, the substitution of the representative inductive parameters to describe the flux linkages and the description of the space phasor quantities by means of their real and imaginary components in the new coordinate system culminates in d-q-0 models, which can be beneficially employed in evaluating the machine performance under both the transient and the steady state conditions.

The instantaneous torque developed by the machine can be obtained from energy balance considerations, viz.

$$dE_{elec} = dE_{magn} + dE_{mech} + dE_{loss} \quad (262)$$

In Equation (262),  $dE_{elec}$  represents the differential electric energy exchange with the supply, whereas  $dE_{magn}$  corresponds to the differential magnetic energy storage.  $dE_{mech}$  is the differential mechanical energy component and  $dE_{loss}$  gives the differential system losses. The electric energy term on the left hand side of Equation (262) can be expressed as

$$dE_{elec} = P dt \quad (263)$$

with

$$P = \frac{3}{2} \Re \left[ \underline{u}^s \underline{i}^{s*} \right] \quad (264)$$

representing the power exchanged with the supply.

The magnetic energy term on the right hand side of Equation (262) can be conveniently obtained from the rest conditions as

$$dE_{magn} = \frac{3}{2} \Re \left[ \frac{d\underline{\Psi}^s}{dt} \underline{i}^{s*} + \frac{d\underline{\Psi}^R}{dt} \underline{i}^{R*} \right] \quad (265)$$

The differential mechanical energy term is given by

$$dE_{mech} = T d\varphi^\perp \quad (266)$$

where

$$d\varphi^\perp = \omega^\perp dt \quad (267)$$

with  $\omega^\perp$  representing the angular velocity at which the new reference frame moves relative to the stationary reference frame attached to the stator.

Substituting Equations (265) to (267) into Equation (262) and rearranging finally gives the instantaneous torque as

$$T = \frac{3}{2} \Im \left[ \underline{\Psi}^s \underline{i}^{s*} \right] \quad (268)$$

It should be noted that the above equations relating to energy and torque are reference-frame-invariant.



Bashkow A matrix is obtained as

$$[A]=\begin{array}{|c|c|c|} \hline -[L]^{-1}\{[R]+\omega\frac{\partial}{\partial\theta}[L]\} & 0 & 0 \\ \hline * & -\frac{D}{J} & 0 \\ \hline 0 & 1 & 0 \\ \hline \end{array}$$

(222)

and the *constant matrix* translates into

$$[B]=\begin{array}{|c|c|c|} \hline [L]^{-1} & 0 & 0 \\ \hline 0 & -\frac{1}{J} & 0 \\ \hline 0 & 0 & 0 \\ \hline \end{array}$$

(223)

The system response, including the torque-speed behaviour, can be obtained by substituting Equations (220) to (223) into Equation (219). It should be noted that the matrix element denoted "\*" in Equation (222) is a dependent variable and is thus to be obtained in the course of iterative computations.

### 3.6 Space Phasor Modelling

The space phasor modelling approach is based on the notion that the electromagnetic fields within the machine space can be represented by means of the currents causing them [79,80,108].

The m.m.f. of a single coil of  $N$  turns with an instantaneous current of  $i$  is

$$\mathbf{F} = N i \quad (224)$$

which gives rise to a flux

$$\Phi = \mathbf{F} \Lambda \quad (225)$$

where  $\Lambda$  is the corresponding permeance for the flux path. Since the flux is a vector quantity, Equation (225) can be written as

$$\underline{\Phi} = \underline{\mathbf{F}} \Lambda \quad (226)$$

thus assigning vector attributes to the m.m.f. This last equation states that the alignments of the vectors  $\underline{\Phi}$  and  $\underline{\mathbf{F}}$  coincide. Since the m.m.f. is set up by the instantaneous current  $i$ , Equation (226) can be rewritten as

$$\underline{\Phi} = \underline{i} N \Lambda \quad (227)$$

implying that the current is also a vector, the alignment of which coincides with that of the flux. With this interpretation, it becomes possible to use current as a *scaled vector* to model flux.

The above considerations can be extended to spatially distributed polyphase windings. For instance, if the instantaneous phase currents in a three-phase stator winding are  $i_a$ ,  $i_b$  and  $i_c$ , the resultant airgap flux can be represented by the sum of the corresponding *current vectors* as

$$\underline{i} = \underline{i}_a + \underline{i}_b + \underline{i}_c \quad (228)$$

In this interpretation, the "current vector" of each phase is radially directed along the magnetic axis of the phase winding. Since the vector attributes are *conferred* on the currents, the term *current space phasor*, rather than "current vector", would appear to more accurately describe the transformations based on the foregoing considerations.

It should be noted that assumptions of phase symmetry and sinusoidal flux density distribution are implicit in the above deliberations. It is also assumed that the end effects are negligible so that the modelling of the airgap field by means of space phasors can be effected in any plane perpendicular to the shaft axis along the length of the machine. However, the considerations apply regardless of the waveshape of the current. Therefore, non-sinusoidal supply conditions, supply unbalance and saturation effects can be modelled with relative ease.

The instantaneous relationships are illustrated in Figure 25 to correspond to the currents at time  $t_1$  as depicted in Figure 24.

# 4

## A GENERAL MODEL

### 4.1 Preliminaries

#### 4.1.1 Rationale for a General Model

The various different *aggregate circuit models* discussed so far in this thesis are entirely adequate in analysing the performance of balanced polyphase induction machines, as long as a cumulative representation of the electromagnetic effects by means of lumped phase parameters is justifiable; if the model fidelity is high, the prediction accuracy can be expected to be excellent. However, by their very nature, aggregate circuit models are insensitive to the effect on machine performance of important design details, such as skewing and winding connection. This applies regardless whether aggregate circuit models be direct phase models or their derivatives obtained by axis transformations. Furthermore, aggregate circuit models are totally unsuitable for analysing the performance of

machines with unusual design features or with faults; such may be present either as a consequence of topology or operating conditions. Clearly, this constitutes a serious shortcoming.

The foregoing observations apply equally to *harmonic models* which enable the effects on the machine performance of the discrete peripheral distribution to be assessed with greater accuracy; harmonic models are aggregate circuit models, and hence are unable to reflect the effect of such features as the presence of parallel paths in the winding, skewed slots and discontinuities in conductors, to name a few. Yet, these features are arguably of great significance to the performance of an induction machine.

These observations more than justify the interest in modelling discrete effects with greater rigour. *Discrete circuit models* are capable of accounting for the distributed nature of the machine windings, allowing the effects of features such as skewing and asymmetries to be assessed with far greater credibility than is possible with the use of cumulative circuit models. Since discrete circuit models constitute *direct models*, they are not bound by the constraints imposed on some aggregate models by domain transformations; performance analysis can be carried out in the time-domain which renders discrete circuit models admirably suitable for dynamic analysis. Furthermore, aggregate circuit models are implicit in discrete circuit models, as they can be derived from discrete circuit models with relative ease. An additional benefit is that the discrete circuit models enable parasitic behaviour in conventional balanced polyphase machines to be evaluated far more realistically than is possible with clustered phase models. All these features justify the designation of a discrete circuit model as *a general model*.

The underlying notion in the formation of a discrete circuit model is to account for the distributed nature of machine windings on a conductor-by-conductor basis. Evidently, a conductor bundle in a slot, forming a coil side, may be treated as a composite conductor, unless such phenomena as turn-to-turn short circuits are also to be modelled.

Discrete circuit modelling allows time domain analysis without having to resort to transformation techniques. This is an extremely useful feature in the dynamic modelling of induction machines. Yet, transition to the more conventional lumped parameter circuit models is relatively easy, since discrete coil considerations form the basis of such aggregate models as has been demonstrated earlier in this thesis. Too, there is no impediment to the conducting of any type of harmonic analysis with the use of discrete circuit models, should harmonic aspects be of interest.

The main difference between the harmonic circuit models developed in Chapter 2 and the discrete circuit models to be developed in this chapter is one of *aspect*; the former are founded on harmonic analysis whereas the latter have the intrinsic ability to allow the use of harmonic analysis if and when it is needed.

#### 4.1.2 The Discrete Circuit Model

A *discrete circuit model* of an induction machine constitutes a distributed circuit model, taking the notion of a general  $m,n$  phase model further to the individual circuit level. Figure 27 illustrates the concept for a cage induction machine where currents for all stator coil sides and rotor bars are accounted for separately. Figures 28 and 29 further illustrate the

concept, identifying the principal circuit parameters, further details of which are presented in the following sections. Provided that model parameters for each discrete circuit are determined with adequate accuracy, this model provides an effective means of induction machine analysis in a general sense.

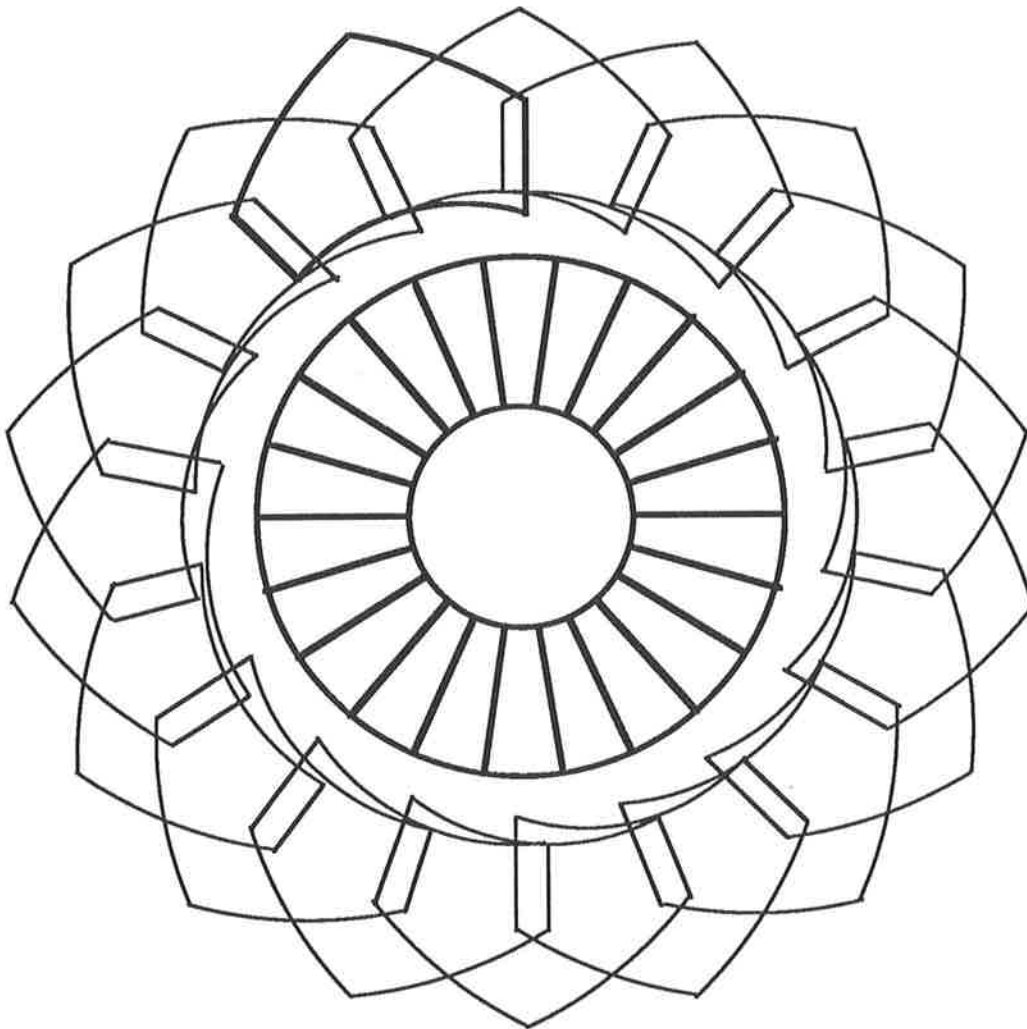


Figure 27

Conceptual graph of a discrete circuit model for a cage induction machine

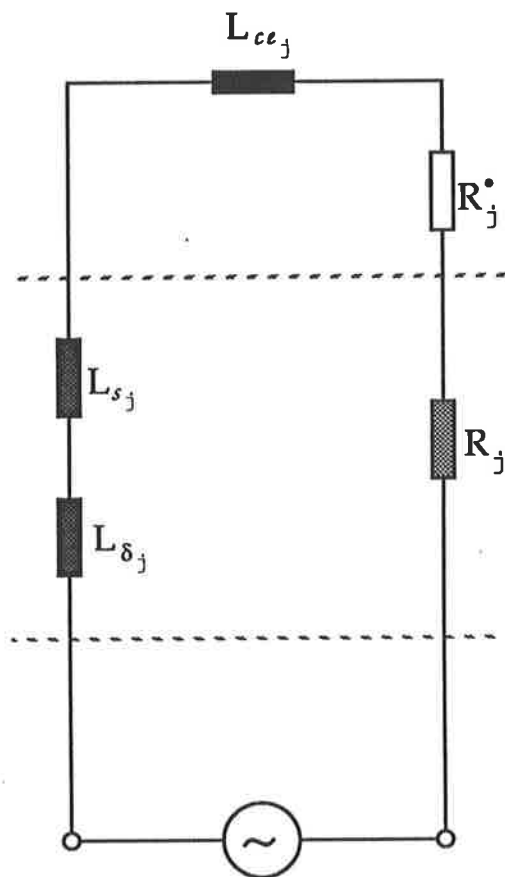


Figure 28

Principal discrete circuit model for a stator coil



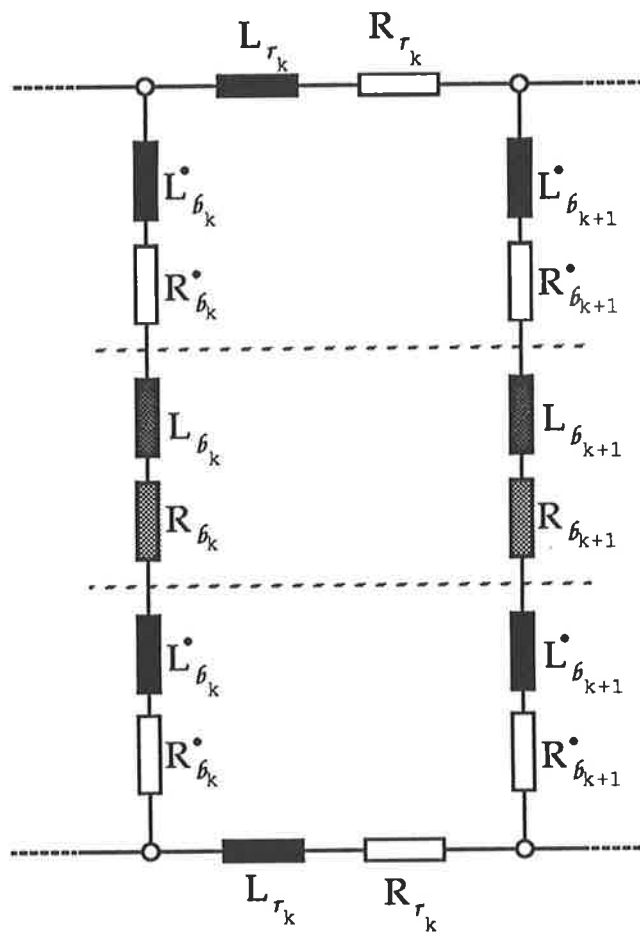


Figure 29

Principal discrete circuit model for a rotor mesh

The use of this model will lead to a set of terminal equations for the machine in the form

$$[ \mathbf{u}(t) ] = [ \mathbf{z}(\chi, t) ] [ \mathbf{i}(t) ] \quad (269)$$

yielding time-variant solutions for the currents, thus facilitating the determination of the other characteristics of significance.  $[ \mathbf{z}(\chi, t) ]$  denotes the complex machine impedance, which is both position-dependent and time-dependent due to relative motion between the stator and the rotor. It is to be emphasised that Equation (269) represents the most general form of terminal equations for the machine without any constraints on the voltage and current waveshapes and without the assumption of linearity.

Conceivably, the general model conceptualised in Figures 27 to 29 can be reduced to a-b-c models and, with the aid of phase transformations, to corresponding orthogonal models. However this would eliminate the major advantage of such a general discrete circuit model, namely the ability to assess, in time-domain, the impact on the global machine performance of effects in local circuits.

#### 4.1.3 Parameter Determination Aspects

It is consequential that the model parameters of a discrete circuit model for an induction machine be obtained with as great an accuracy as practicable, if the ensuing model has to be reliable in the prediction of performance under general operating conditions. Although this applies to both the

resistive and inductive model parameters, accurate determination of leakage inductances assumes particular importance since any inaccuracy in their estimation leads to largely inaccurate prediction of parasitic behaviour.

**In the following development of discrete circuit models it will be initially assumed that both stator and rotor slots are unskewed.**

In the case of resistances, the parameter determination is reasonably straightforward, especially if the effects of temperature variation can be deemed negligible and the current density distribution in the conductors is reasonably uniform. In most cases, heating effects can be safely assumed to be constant, allowing single valued resistive parameters to be used in the model. However, in the case of rapid transients, such as the run-up from stand-still of a large induction motor, this may lead to grossly erroneous performance predictions, when it becomes important to pay closer attention to modelling the temperature-dependency of conductor resistances. If current displacement in conductors is significant, then the incremental effect on the resistance of this must also be taken into account in the interest of increased accuracy.

Inductances too are affected by current displacement, if significant, and must be obtained on the basis of the non-uniform current density distribution within the conductor. Interestingly, the extent of current displacement may be variable along a given discrete circuit depending on the magnetic medium enclosing the various regions of the circuit. For instance, sections of rotor bars embedded in the core may be subject to severe distortion of the current density distribution whereas current displacement effect elsewhere in a cage winding may be negligible. This underscores the relevance of regionalising the circuit in obtaining its

overall inductance. In general, these regional inductances can be calculated using various approaches based on the

[1] flux linkage,

[2] magnetic energy, or

[3] permeance

of the region under consideration. In the case of [1] and [2], the use of Maxwell's equations allows the inductances to be obtained most generally.

[3] reduces the task to one of geometry.

Using flux linkage as the basis, inductance is obtained from the definition

$$L \equiv \frac{\Psi}{i} \quad (270)$$

where  $\Psi$  is the flux linkage, obtained as either

$$\Psi = \int_S \nabla \times \underline{A} \cdot d\underline{s} \quad (271)$$

or

$$\Psi = \oint_C \underline{A} \cdot d\underline{c} \quad (272)$$

Equations (270) to (272) are generally applicable and can be used in determining both the self inductance and the mutual inductance of the conductor region under consideration.

Alternatively, inductances can be obtained on the basis of **magnetic energy** considerations. Starting with the energy density for a given region, obtained from

$$w = \int_0^B \vec{H}(\vec{B}) \cdot d\vec{B} \quad (273)$$

the magnetic energy of the region can be expressed as

$$W = \int_v w \, dv \quad (274)$$

On the other hand, with the aid of Equations (2), (4) and (8), Equation (273) can also be expressed in terms of current density and vector magnetic potential as

$$W = \int_v \vec{J} \cdot \vec{A} \, dv \quad (275)$$

The integration over the conductor region concerned shows that the energy term is obtained as being proportional to the square of the total current passing through the conductor, allowing the self inductance of the conductor to be defined as

$$L \equiv \frac{2W}{i^2} \quad (276)$$

With Equation (276), the self inductance can thus be determined as

$$L = \frac{2}{i^2} \int_0^B \int_v \tilde{H}(\tilde{B}) \cdot \tilde{B} \, d\tilde{B} \, d\tilde{v} \quad (277)$$

The mutual inductance between any two conductors can be obtained from similar considerations.

Using the notion of **permeance**, various inductances can also be obtained from

$$L \equiv N^2 \Lambda \quad (278)$$

In *magnetic circuit* terms, permeance is defined by

$$\Lambda \equiv \frac{\Phi}{\mathbf{F}} \quad (279)$$

where  $\Phi$  : magnetic flux

$\mathbf{F}$  : magnetomotive force

All the above approaches can be employed in determining the inductive model parameters of a discrete circuit model for an induction machine, as will be demonstrated in this chapter. Since all methods lead virtually to the same results under similar conditions, the choice is influenced by the relative convenience one method offers over the others.

## 4.2 Resistive Parameters

Assuming that the temperature remains constant during operation, and further assuming that the current density distribution is uniform throughout the cross-section, the resistance can be obtained from

$$R = \frac{l}{\sigma A} \quad (280)$$

where  $l$  and  $A$  are the length and the cross-sectional area of the regional conductor respectively. In the case of a coil, either in the stator or the rotor,  $l$  corresponds to the total conductor length of all series connected *turns* which form a coil. Using the *mean turn length*,  $\bar{l}$ , the total conductor length for the coil,  $l$ , is found as

$$l = N \bar{l} \quad (281)$$

The mean turn length can be related to the machine topology by expressing it as

$$\bar{l} = 2 \left( l_c + \bar{l}_{ce} \right) \quad (282)$$

where  $l_c$  : core length  
 $\bar{l}_{ce}$  : mean coil-end length

With these considerations, the resistance of the  $j^{\text{th}}$  stator coil is given as

$$R_j^s = \frac{2 N^s}{\sigma A_s} \left( l_c + \bar{l}_{ce}^s \right) \quad (283)$$

and the resistance of the  $k^{\text{th}}$  rotor coil of a wound rotor as

$$R_k^R = \frac{2 N^R}{\sigma A_S} \left( l_c + \bar{l}_{ce}^R \right) \quad (284)$$

It is difficult to obtain the mean coil-end length deterministically from the machine topology, since it is subject to widely varying manufacturing practices. It is much more realistic to obtain  $\bar{l}_{ce}$  stochastically on the basis of data obtained from manufactured machines. Figure 30 illustrates how  $\bar{l}_{ce}$  can be obtained from such data, giving values for both the stator windings and the rotor windings if the rotor is "wound"<sup>1</sup>.

In the case of a **cage winding**, a distinction needs to be made between the bar and end-ring segments in determining the resistances for the corresponding rotor circuits. For convenience, it will be assumed here that the current density distribution is uniform. With this assumption, the resistances for the bar and the end-ring segments can be expressed, respectively, as

$$R_b = \frac{l_b}{\sigma A_b} \quad (285)$$

and

$$R_r = \frac{\pi \bar{D}_r}{\sigma A_r S^R} \quad (286)$$

---

<sup>1</sup> Data in Figure 30 stem from the author's own work in industry and are based on actually manufactured machines.



where	$l_b$	:	bar length, m
	$A_b$	:	cross-sectional area of the bar, m <sup>2</sup>
	$\bar{D}_r$	:	mean end-ring diameter, m
	$A_r$	:	cross-sectional area of the end-ring, m <sup>2</sup>
	$S^R$	:	number of rotor slots

Consequently, the resistance of the  $k^{\text{th}}$  rotor mesh becomes

$$R_k^R = 2 (R_b + R_r) \quad (287)$$

If current density distribution can not be assumed to be uniform, the effective resistance values will have to be obtained on the basis of a more rigorous analysis based on field considerations as has been demonstrated previously in Section 2.3. If so, a further distinction will have to be made between rotor bar regions embedded in the core and those outside the core as alluded to in Figure 29.

### 4.3 Inductive Model Parameters

The inductive model parameters represent the effects of regional magnetic fields on the discrete circuits with which they are coupled. For modelling purposes they can be categorised as

- 1] *self inductances*, representing the effect on a discrete circuit of the magnetic fields arising from its own current, and
- 2] *mutual inductances*, representing the effect on a discrete circuit of the magnetic fields set up by currents in any other discrete circuit.

Relative Mean Coil End Length

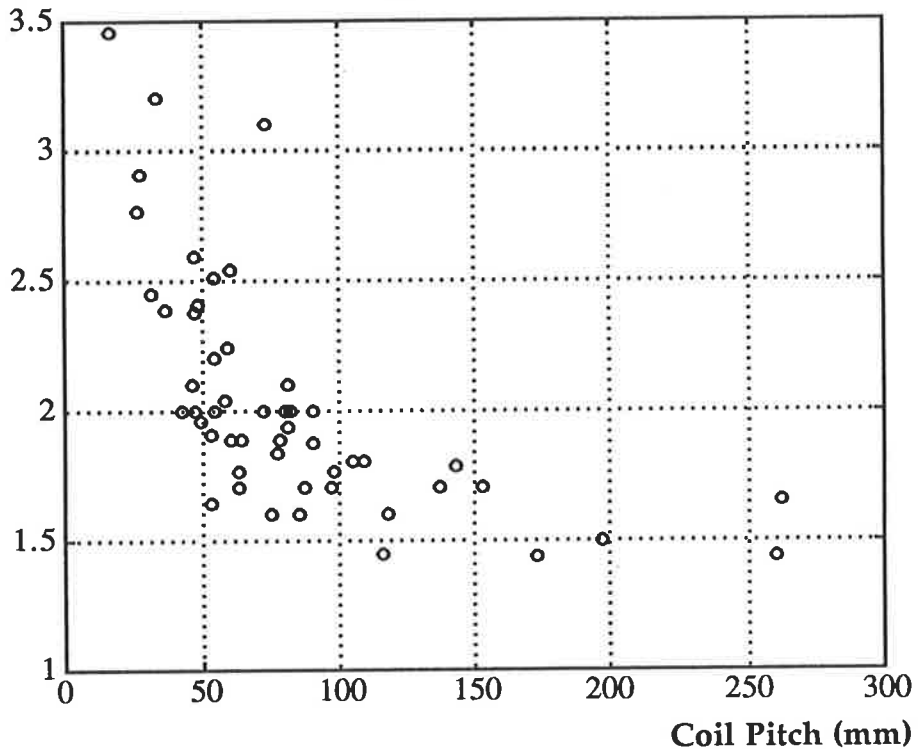


Figure 30

Relative mean coil-end length<sup>2</sup> for stator coils<sup>3</sup> as a function of coil pitch

<sup>2</sup> ratio of mean coil-end length to coil pitch

<sup>3</sup> also valid for rotor coils if values reduced to 65%

For the  $j^{\text{th}}$  stator coil, the self inductance will be defined, as

$$L_{j,j}^S = L_{\delta,j,j}^S + L_{s,j,j}^S + L_{ce,j,j}^S \quad (288)$$

where  $L_{\delta,j,j}^S$  : air gap inductance for the  $j^{\text{th}}$  stator coil  
 $L_{s,j,j}^S$  : slot leakage inductance for the  $j^{\text{th}}$  stator coil  
 $L_{ce,j,j}^S$  : coil end leakage inductance for the  $j^{\text{th}}$  stator coil

Similarly the self inductance of the  $k^{\text{th}}$  rotor circuit can be given by

$$L_{k,k}^R = L_{\delta,k,k}^R + L_{s,k,k}^R + L_{ce,k,k}^R \quad (289)$$

where  $L_{\delta,k,k}^R$  : air gap inductance for the  $k^{\text{th}}$  rotor circuit  
 $L_{s,k,k}^R$  : slot leakage inductance for the  $k^{\text{th}}$  rotor circuit  
 $L_{ce,k,k}^R$  : coil end leakage inductance for the  $k^{\text{th}}$  rotor circuit

Equation (289) applies regardless whether a discrete coil of a wound rotor or a rotor mesh of a cage rotor constitutes a rotor circuit.

#### 4.3.1 Airgap Inductance of a Coil

The airgap inductance of a single coil can be obtained conveniently from permeance considerations. The circumferential distribution of the airgap magnetomotive force due to the instantaneous value of a current flowing in a single short-pitched coil is illustrated in Figure 31.

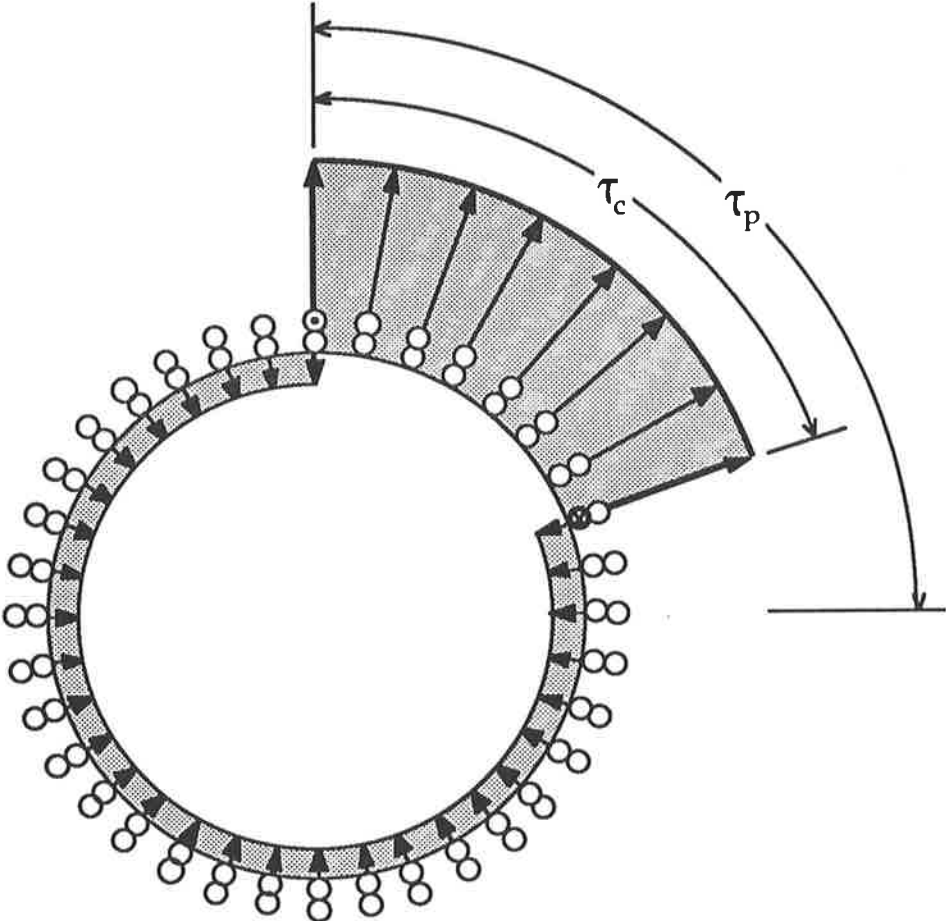


Figure 31

Circumferential distribution of magnetomotive force of a single short-pitched stator coil

$\tau_p$  : pole pitch

$\tau_c$  : coil pitch

For convenience, the m.m.f. distribution shown assumes negligible slot openings and concentrated windings at slot centres. Although the representation of Figure 31 has a stator bias, the considerations apply equally to the discrete coils of a wound rotor.

Figure 32 shows the circumferential airgap m.m.f. distribution due a single short-pitched coil in *developed* format. The circumferential axis is positioned to reflect the conservation of flux set up by the coil. Evidently, the total airgap m.m.f. due to the coil is

$$\mathbf{F} = NI \quad (290)$$

where  $N$  : number of turns of coil  
 $I$  : instantaneous value of coil current

Figure 33 illustrates the corresponding electromagnetic relationships with the aid of a magnetic circuit model. As can be seen, the model assumes infinite core permeability. The resultant flux, which traverses the two airgap segments serially, can now be expressed as

$$\Phi = \mathbf{F} \Lambda = \mathbf{F}_1 \Lambda_1 = \mathbf{F}_2 \Lambda_2 \quad (291)$$

The indices 1 and 2 refer to the airgap segments under the coil and the remainder respectively. Thus,  $\mathbf{F}_1$  is the portion of the total coil m.m.f. responsible for setting up the airgap flux  $\Phi$  under the coil, whereas  $\mathbf{F}_2$  is the portion of the total coil m.m.f. to set up the same airgap flux in the remainder of the airgap.  $\Lambda_1$  and  $\Lambda_2$  represent the corresponding airgap permeances.

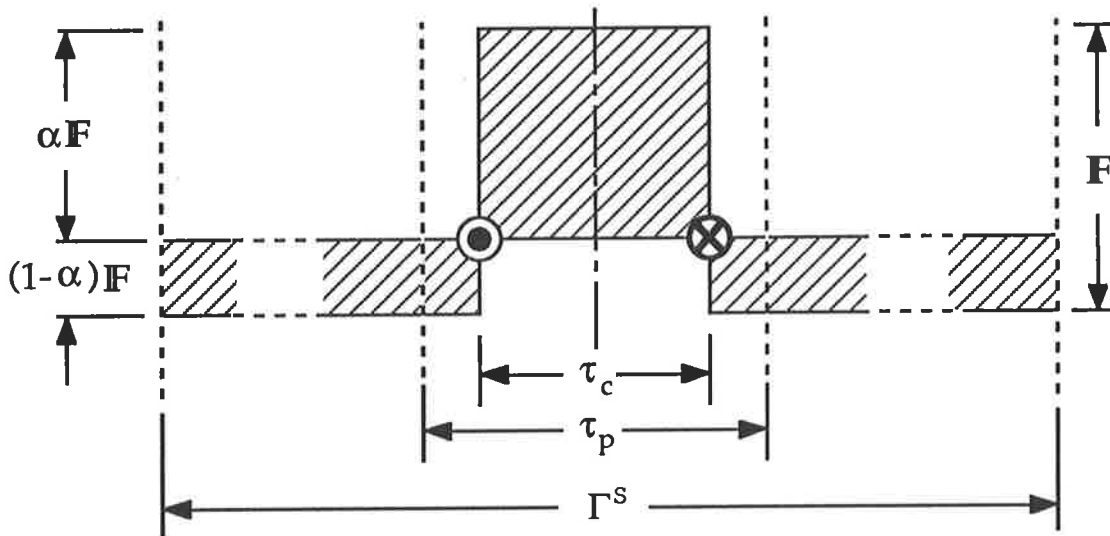


Figure 32

Developed representation of airgap m.m.f. distribution due to a single short pitched coil

- $\tau_c$  : coil pitch
- $\tau_p$  : pole pitch
- $\Gamma^S$  : stator bore circumference
- $\alpha$  : m.m.f. partitioning ratio

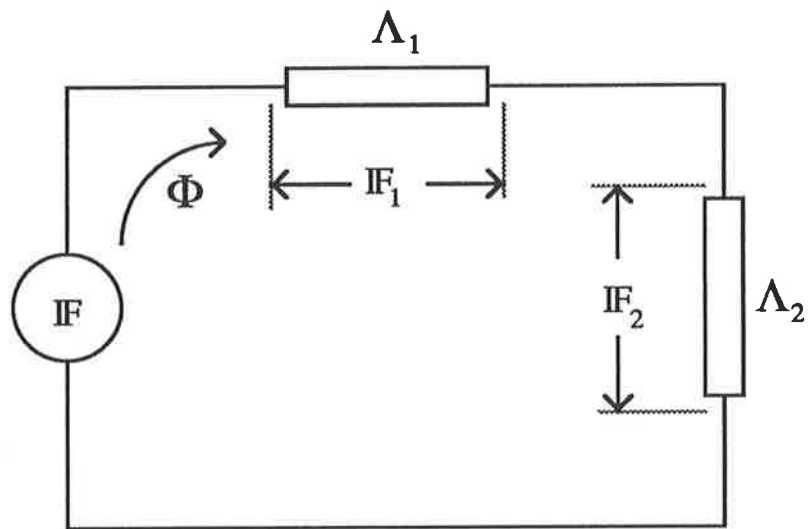


Figure 33

Magnetic circuit model with airgap permeances

With the m.m.f. partitioning ratio  $\alpha$ , defined as

$$\alpha = \frac{\mathbf{F}_1}{\mathbf{F}} \quad (292)$$

the magnetomotive force expression for the two airgap segments can be expressed as

$$\mathbf{F}_1 = \alpha \mathbf{F} \quad (293)$$

and

$$\mathbf{F}_2 = (1-\alpha) \mathbf{F} \quad (294)$$

In obtaining the permeances  $\Lambda_1$  and  $\Lambda_2$  for the airgap segments 1 and 2, the effect of doubly slotted boundaries need to be taken into account, if permeance variations are to be modelled correctly. This can be achieved in a variety of ways [130, 131, 132]. However, if the effect is moderate, accounting for the effect of slotting by the use of the modified airgap distance as in Carter's analysis yields an acceptable degree of accuracy in most cases. On this premise, the permeances  $\Lambda_1$  and  $\Lambda_2$  can be quantified as

$$\Lambda_1 = \frac{\mu_0 A_1}{\delta'} \quad (295)$$

and

$$\Lambda_2 = \frac{\mu_0 A_2}{\delta'} \quad (296)$$



$A_1$  and  $A_2$  are the cross-sectional areas for the airgap flux for the two segments under consideration and are given by

$$A_1 = l_c \tau_c \quad (297)$$

and

$$A_2 = l_c (\Gamma^s - \tau_c) \quad (298)$$

where  $l_c$  : core length  
 $\tau_c$  : coil pitch  
 $\Gamma^s$  : stator bore circumference

Substituting Equations (293), (294), (297) and (298) in Equation (291) and rearranging yields the m.m.f. partitioning ratio  $\alpha$  with

$$\alpha = 1 - \frac{\tau_c}{\Gamma^s} \quad (299)$$

This last expression can also be given in terms of a slot ratio as

$$\alpha = 1 - \frac{y^s - 1}{S^s} \quad (300)$$

by considering that

$$\tau_c = (y^s - 1) \kappa^s \quad (301)$$

and

$$\Gamma^s = S^s \kappa^s \quad (302)$$

where  $\kappa^s$  : linear stator slot pitch  
 $y^s$  : number of slots per stator coil pitch  
 $S^s$  : number of stator slots

Consequently the airgap flux can be obtained with Equation (291) as

$$\Phi = N \alpha \frac{\mu_0 \ell_c \tau_c}{\delta'} I \quad (303)$$

The flux linkage with the coil is

$$\Psi_{\delta,j}^s = N \Phi \quad (304)$$

which can also be expressed in terms of machine topology as

$$\Psi_{\delta,j,j}^s = N^2 \alpha \frac{\mu_0 \ell_c \tau_c}{\delta'} I \quad (305)$$

or in terms of an airgap permeance for the coil,  $\Lambda_{\delta,j,j}^s$ , as

$$\Psi_{\delta,j,j}^s = N^2 \Lambda_{\delta,j,j}^s I \quad (306)$$

where

$$\Lambda_{\delta,j,j}^s = \alpha \frac{\mu_0 \ell_c \tau_c}{\delta'} \quad (307)$$

With these considerations, the airgap inductance for the  $j^{\text{th}}$  stator coil is obtained as

$$L_{\delta, j, j}^s = N^2 \Lambda_{\delta, j, j}^s \quad (308)$$

The airgap inductance for the  $k^{\text{th}}$  rotor coil of a wound rotor can be found similarly as

$$L_{\delta, k, k}^R = N^2 \Lambda_{\delta, k, k}^R \quad (309)$$

Evidently,  $\Lambda_{\delta, k, k}^R$  is to be obtained with Equation (307) using the corresponding rotor parameters.

#### 4.3.2 Airgap Inductance of a Rotor Mesh

In the case of squirrel cage rotor, each rotor mesh, comprising a pair of contiguous rotor bars connected by means of end-ring segments can be viewed to constitute a discrete coil of a single turn. This is illustrated in Figure 34 for a rotor with  $n$  meshes; the current in the  $k^{\text{th}}$  mesh is  $i_k^R$ , with  $k = 1, \dots, n$ . The airgap inductance of the mesh can be obtained on the basis of similar considerations as for a discrete stator coil.

Figure 35 illustrates the circumferential distribution of the magnetomotive force in the airgap due to the presence of current in a single rotor mesh. Figure 36 shows the same m.m.f. distribution in developed form.

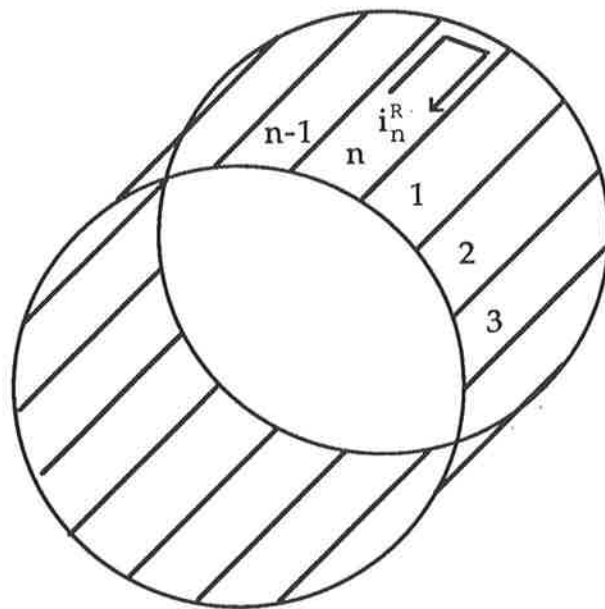


Figure 34

Rotor cage with mesh currents

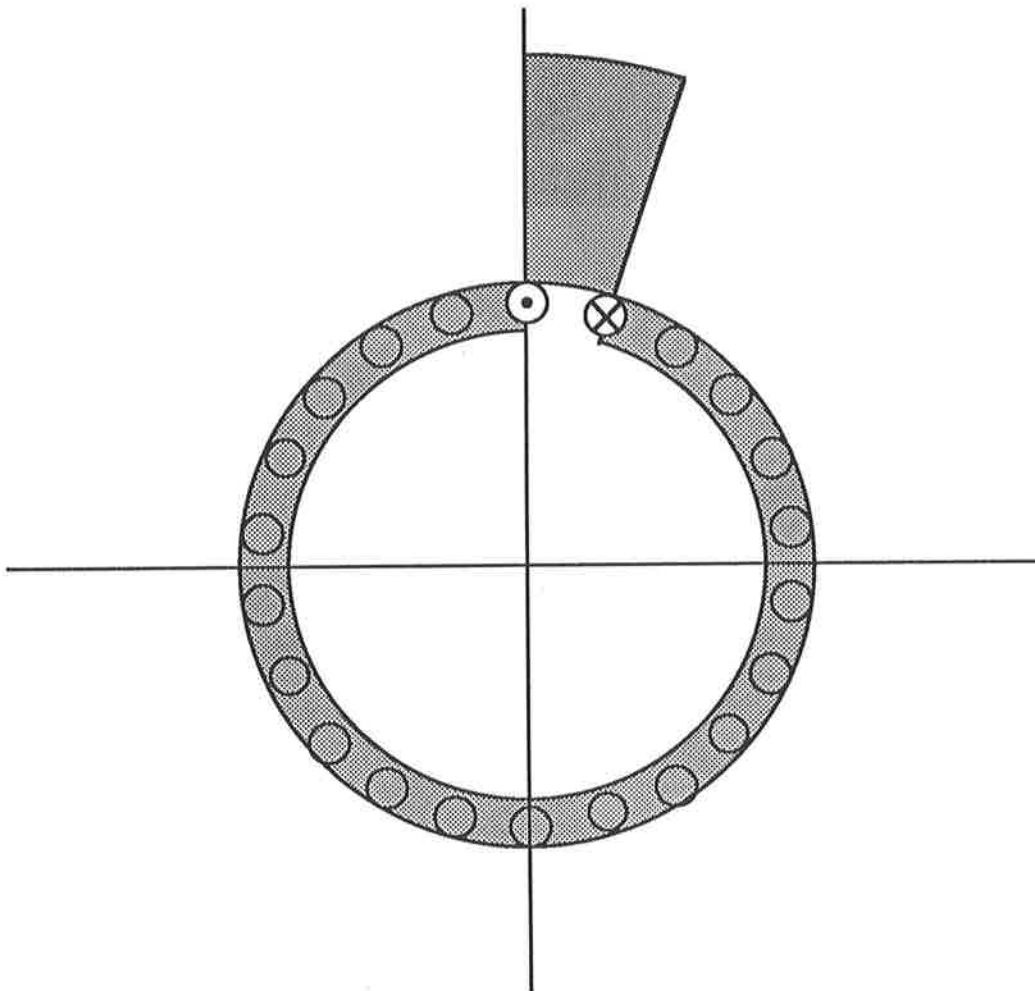


Figure 35

Circumferential m.m.f. distribution in airgap due to a rotor mesh current

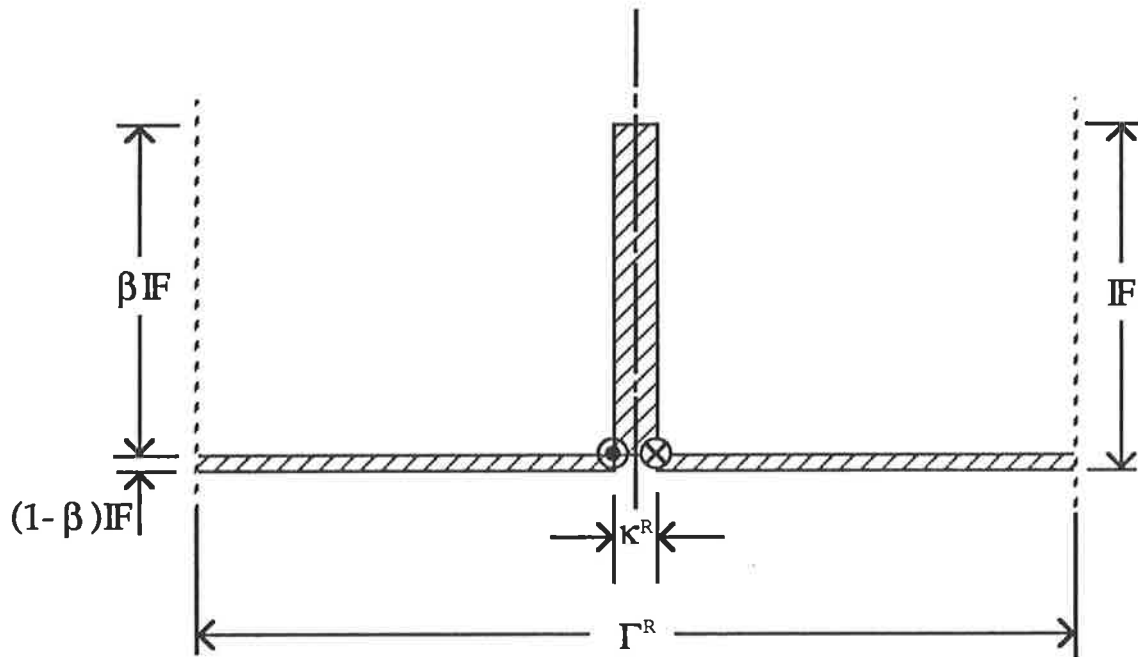


Figure 36

Developed representation of airgap m.m.f. distribution due to a single rotor mesh

$\kappa^R$  : rotor slot pitch

$\Gamma^R$  : rotor circumference

$\beta$  : m.m.f. partitioning ratio for rotor

With reference to Figures 34 to 36, the magnetomotive force of the  $k^{\text{th}}$  rotor mesh due to an instantaneous mesh current  $I_k^R$  is

$$\mathbf{F}_k^R = I_k^R \quad (310)$$

$\mathbf{F}_k^R$  is responsible for setting up an airgap flux of  $\Phi_\delta^R$ , which can be expressed as

$$\Phi_\delta^R = I_{k1}^R \Lambda = \beta I_{k1}^R \Lambda_{k1}^R = (1 - \beta) I_{k2}^R \Lambda_{k2}^R \quad (311)$$

where  $\Lambda_{k1}^R$  and  $\Lambda_{k2}^R$  represent the permeances of the airgap segments under the  $k^{\text{th}}$  rotor mesh and the remainder respectively.  $\beta$  is the m.m.f. partitioning ratio and can be obtained from the conservation of flux requirement.  $\Lambda_{k1}^R$  and  $\Lambda_{k2}^R$  are given by

$$\Lambda_{k1}^R = \frac{\mu_0 A_{k1}^R}{\delta'} \quad (312)$$

and

$$\Lambda_{k2}^R = \frac{\mu_0 A_{k2}^R}{\delta'} \quad (313)$$

where  $A_{k1}^R$  and  $A_{k2}^R$  are the cross-sectional areas for the airgap flux of the airgap segments in question. Evidently

$$A_{k1}^R = l_c \kappa^R \quad (314)$$

and

$$A_{k2}^R = l_c (\Gamma^R - \kappa^R) \quad (315)$$

where  $l_c$  : core length  
 $\kappa^R$  : linear rotor slot pitch  
 $\Gamma^R$  : rotor circumference

With Equations (311) to (315), the m.m.f. partitioning ratio for the rotor is obtained as

$$\beta = 1 - \frac{\kappa^R}{\Gamma^R} \quad (316)$$

In terms of slots numbers,  $\beta$  can also be expressed as

$$\beta = 1 - \frac{1}{S^R} \quad (317)$$

The linear rotor slot pitch  $\kappa^R$  is obtained from

$$\kappa^R = \frac{\pi D^R}{S^R}$$

where  $D^R$  : rotor outer diameter, m  
 $S^R$  : number of rotor slots

With the foregoing considerations, the airgap flux due to a rotor mesh current can be given by

$$\Phi_{\delta}^R = \frac{\mu_0 l_c \kappa^R}{\delta'} \beta I_k \quad (318)$$



The flux linkage with the mesh is

$$\Psi_{\delta}^R = 1 \times \Phi_{\delta}^R = 1^2 \times \Lambda_{\delta, k, k}^R \times I_k^R \quad (319)$$

which allows the airgap inductance of the  $k^{\text{th}}$  rotor mesh to be defined as

$$L_{\delta, k, k}^R = \Lambda_{\delta, k, k}^R \quad (320)$$

where

$$\Lambda_{\delta, k, k}^R = \frac{\mu_0 \ell_c K^R}{\delta'} \beta \quad (321)$$

### 4.3.3 Slot Leakage Inductances

The slot leakage inductance of a discrete circuit, whether it be in the stator or in the rotor, can be determined from the analysis of the magnetic field set up by the conductors in the slot. This can be done either by means of Maxwell's equations or using magnetic energy considerations. If Maxwell's equations are used, the task can be reduced to determining the flux linkages on the basis of Poisson's equation for the slot space occupied by the conductors and Laplace's equation elsewhere within the slot.

A substantial simplification can be achieved in the determination of the slot leakage inductance if the magnetic field alignment can be assumed to be perpendicular to the slot walls. The assumption is justifiable in most instances, except when the distance between the conductors and the slot walls is considerable, which may be the case in some high voltage windings due to the more stringent insulation requirements.

Assuming a sufficiently well behaved slot field distribution and considering a coil side occupying the whole or a part of the slot space, the slot leakage inductance can be obtained from magnetic energy considerations. The method will be illustrated for a typical stator slot as shown in Figure 37.

Placing in Figure 37 the coordinate origin at the bottom of the slot, the magnetic energy density at a height  $y'$ ,  $w(y')$  can be found as

$$w(y') = \frac{1}{2} B(y') H(y') \quad (322)$$

where  $B(y')$  and  $H(y')$  are the magnetic flux density and the magnetic field strength at  $y'$  respectively. Thus the energy stored within an infinitesimal layer of the slot volume at  $y'$  is given by

$$w(y') dv = \frac{1}{2} B(y') H(y') l_c w_s(y') dy' \quad (323)$$

In Equation (323),  $l_c$  is the core length. Integration over the slot volume gives the magnetic energy for the whole slot space as

$$W = \frac{1}{2} l_c \int B(y') H(y') w_s(y') dy' \quad (324)$$

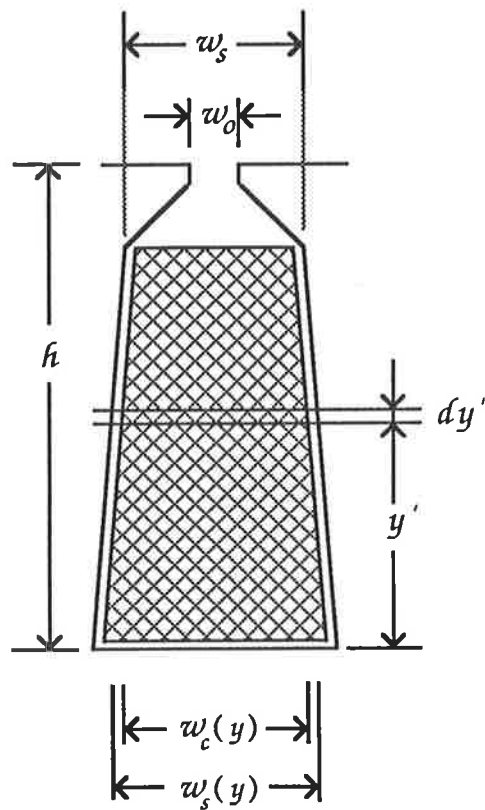


Figure 37

A typical stator slot

$w_s(y')$  : slot width at  $y'$ .

$w_c(y')$  : coil width at  $y'$ .

On the other hand, the magnetic field strength at  $y'$  can be found from

$$H(y') = \frac{\mathbf{F}(y')}{w_s(y')} \quad (325)$$

where  $\mathbf{F}(y')$  is the magnetomotive force at the slot height  $y'$  due to the current flowing in the conductors between the boundaries  $y = 0$  and  $y = y'$ .

Generally

$$\mathbf{F}(y') = \int_0^{y'} i(y') \zeta(y') w_c(y') dy' \quad (326)$$

where

- $i(y')$  : coil current at  $y'$
- $\zeta(y')$  : conductor density at  $y'$
- $w_c(y')$  : coil width at  $y'$

Conductor density alludes to the number of conductors per unit area of the slot cross-sectional area for a coil side. It is reasonable to assume the current to be the same in all conductors belonging to the coil in the slot and that the conductor density remains the same throughout the coil cross-sectional area. Then, Equation (326) reduces to

$$\mathbf{F}(y') = i \zeta \int_0^{y'} w_c(y') dy' \quad (327)$$

Substituting Equation (327) into Equation(325), the magnetic field strength becomes

$$H(y') = \frac{i \zeta \int_0^{y'} w_c(y') dy'}{w_s(y')} \quad (328)$$

Correspondingly, the magnetic flux density at  $y'$  can now be obtained from

$$B(y') = \mu_0 H(y') \quad (329)$$

as

$$B(y') = \mu_0 i \zeta \frac{\int_0^{y'} w_c(y') dy'}{w_s(y')} \quad (330)$$

Substituting Equations (325) and (330) into Equation (324) and rearranging yields

$$W = \frac{1}{2} \mu_0 i^2 \zeta^2 l_c \int_0^h \frac{1}{w_s(y)} \left[ \int_0^{y'} w_c(y') dy' \right]^2 dy \quad (331)$$

from which the slot leakage inductance for the first coil side of the coil under consideration can be obtained with the aid of Equation (331) as

$$L_{s,j,j,I}^s = \mu_0 \zeta^2 l_c \int_0^h \frac{1}{w_s(y)} \left[ \int_0^{y'} w_c(y') dy' \right]^2 dy \quad (332)$$

The slot leakage inductance of the second coil side,  $L_{s,j,j,II}^s$  is found from similar considerations. The coil leakage inductance for the  $j^{\text{th}}$  stator coil is then given by

$$L_{s,j,j}^s = L_{s,j,j,I}^s + L_{s,j,j,II}^s \quad (333)$$

Equation (333) allows the total slot leakage inductance for the coil to be determined when the slot leakage inductance varies from coil side to coil side, as is the case for a double layer winding. Evidently, for a single layer winding, with coil sides occupying identical slots

$$L_{s,j,j,I}^s \equiv L_{s,j,j,II}^s \quad (334)$$

In induction machine design, it has been customary to express permeances in terms of a *permeance coefficient* as

$$\Lambda = \mu l \lambda \quad (335)$$

which allows the effect of a particular topology to be assessed more readily by means of a dimensionless quantity. In the case of a stator slot of

arbitrary topology, the *slot leakage permeance coefficient* for the  $j^{\text{th}}$  stator coil can be given by the general expression

$$\lambda_{s,j,j}^s = \frac{\int_0^h \frac{1}{w_s(y)} \left[ \int_0^y w_c(y') dy' \right]^2 dy}{\left[ \int_0^h (w_c(y') dy') \right]^2} \quad (336)$$

with which the slot leakage inductance for a stator coil can be expressed in an alternative form as

$$L_{s,j,j}^s = N_s^{s2} \mu_0 \ell_c \left( \lambda_{s,j,j,I}^s + \lambda_{s,j,j,II}^s \right) \quad (337)$$

The slot leakage inductance for a rotor coil of a wound rotor is obtainable from similar considerations as

$$L_{s,k,k}^R = N_s^{R2} \mu_0 \ell_c \left( \lambda_{s,k,k,I}^R + \lambda_{s,k,k,II}^R \right) \quad (338)$$

In Equations (337) and (338),  $N_s^R$  and  $N_s^S$  denote the number of conductors per slot for stator and rotor respectively. Applying the above, the slot leakage permeance coefficient of a coil side, for the slot configuration shown in Figure 38, can be obtained as

$$\lambda_s = \frac{h_c}{3w_s} + \frac{2h_w}{w_s + w_o} + \frac{h_o}{w_o} \quad (339)$$

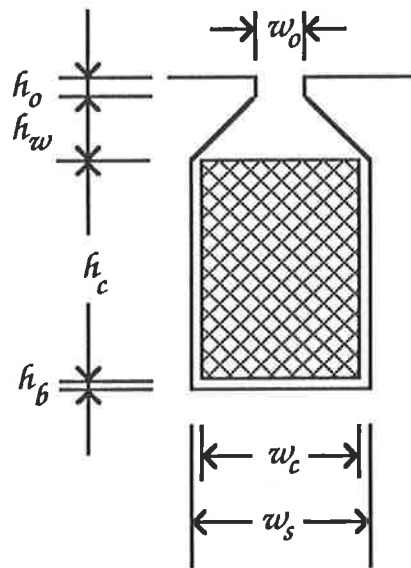


Figure 38

A slot example



For a squirrel cage induction machine with a single cage, the slot leakage inductance of a rotor mesh, consisting of two contiguous rotor bars and the corresponding end-ring segments, can be given by

$$L_{s,k,k}^R = 1^2 \times \Lambda_{s,k,k}^R \quad (340)$$

where

$$\Lambda_{s,k,k}^R = 2 \mu_0 l_c \lambda_{s,k,k}^R \quad (341)$$

In the case of a double cage rotor, a rotor mesh can be defined as consisting of an upper bar and a lower bar lying in two contiguous rotor slots and the corresponding end-ring segments. Then, the slot leakage permeance can be obtained as

$$\Lambda_{s,k,k}^R = \mu_0 l_c \left( \lambda_{s,k,k,u}^R + \lambda_{s,k,k,l}^R \right) \quad (342)$$

where  $\lambda_{s,k,k,u}^R$  and  $\lambda_{s,k,k,l}^R$  denote the permeance coefficient for the upper bar and the lower bar respectively.

#### 4.3.4 Coil-End Leakage Inductances

It is possible to accurately calculate the value of the coil-end leakage inductance from field considerations as

$$L_{cc, j, j}^s = \frac{1}{I_j^2} \int_v [\underline{B}_{cc, j}^s \cdot \underline{H}_{cc, j}^s] d\upsilon \quad (343)$$

where  $\underline{B}_{cc, j, j}^s$  and  $\underline{H}_{cc, j, j}^s$  denote the density and the field strength respectively of the magnetic flux linking with the coil-end of the  $j^{\text{th}}$  stator coil. Using the vector magnetic potential within the coil end region, Equation (343) can also be given as

$$L_{cc, j, j}^s = \frac{1}{I_j^2} \int_v [\underline{A}_{cc, j}^s \cdot \underline{J}_{cc, j}^s] d\upsilon \quad (344)$$

In contemplating the use of the above equations to calculate the inductive parameters describing the end-effects, it needs to be appreciated that the task is a complex one. Firstly, a three dimensional field is involved and secondly, the coil-end topology is subject to widely varying manufacturing practices, making a deterministic calculation of the associated inductances virtually impossible. Evidently, two-dimensional approximation techniques may be employed, assuming that the two-dimensional analysis neglecting the azimuthal field component in selected planes will yield useable results. However, the results are not commensurate with the computational effort.

The above should amply explain why induction machine designers have commonly used methods of calculation for coil-end leakage inductances

which are based on data gained from physical model investigations as well as from measurements on actually manufactured machines [5, 6, 20]. Such stochastic methods represent a realistic and viable alternative to field computations and have been proven to provide acceptably accurate results.

The coil-end leakage inductance of the  $j^{\text{th}}$  stator coil can be expressed in the form:

$$L_{ce, j, j}^s = N_s^{s2} \Lambda_{ce, j, j}^s \quad (345)$$

where  $\Lambda_{ce, j, j}^s$  represents the total coil-end leakage for the  $j^{\text{th}}$  stator coil. In terms of a permeance coefficient the coil-end leakage permeance can also be expressed as

$$\Lambda_{ce, j, j}^s = 2 \mu_0 \bar{l}_{ce}^s \lambda_{ce, j, j}^s \quad (346)$$

Analogously, the coil-end leakage inductance for a rotor coil of a wound rotor is given by

$$L_{ce, k, k}^R = N_s^{R2} \Lambda_{ce, k, k}^R \quad (347)$$

with

$$\Lambda_{ce, k, k}^R = 2 \mu_0 \bar{l}_{ce}^R \lambda_{ce, k, k}^R \quad (348)$$

In Equations (346) and (348),  $\bar{l}_{ce}$  is the mean coil-end length for the coil, as explained in Section 4.2. Its value can be ascertained from Figure 30.

If the rotor has a cage winding, the *end-rings* constitute the coil-ends. Therefore, an equivalent coil-end length, obtained as in Section 4.2, has to be substituted in the governing equations. With this consideration, the end-ring leakage inductance of a rotor mesh comprising two contiguous bars and the corresponding end-ring segments can be quantified as

$$L_{ce, k, k}^R = 1^2 \times \Lambda_{ce, k, k}^R \quad (349)$$

where

$$\Lambda_{ce, k, k}^R = 2 \mu_0 \bar{l}_{er}^R \lambda_{ce, k, k}^R \quad (350)$$

with

$$\bar{l}_{er}^R = \frac{\pi \bar{D}_r}{S^R} \quad (351)$$

Table 2 gives values of  $\lambda_{ce}$  which have been used with good results in calculating coil-end leakage inductances for induction machines [6, 10].

It needs to be emphasised that the values of permeance coefficient given in Table 2 take into account the mutual coupling of other conductors with the coil or the mesh under consideration. The ramification is that mutual inductances in the coil-end regions need not be modelled separately.

**Table 2**

Coil-end leakage permeance coefficients

		<b>S t a t o r</b>	
		Single Layer Winding	Double Layer Winding
<b>R o t o r</b>	Cage	0.35	0.20
	Single Layer Winding	0.50	0.35
	Double Layer Winding	0.40	0.30

#### 4.3.5 Mutual Inductances

Mutual inductances between the coils of a winding, with fixed relative spatial orientation with reference to one another, can be conveniently obtained from permeance considerations. The method is to be illustrated below for two identical stator coils occupying contiguous slots.

The circumferential airgap m.m.f. distribution due to the instantaneous current  $I^s$  existing in the  $j^{\text{th}}$  stator coil, depicted in Figure 32, is represented in magnified form in Figure 39 to emphasise that the resultant flux links with all other stator coils along the periphery.

Evidently, the related mutual inductances can be determined, coil by coil, from the knowledge of the flux linking both coils. Thus, for two arbitrary coils, a and b, this implies that the mutual inductances can be found from

$$L_{\delta, a, b} = L_{\delta, b, a} = \frac{\Psi_{a, b}}{I_a} \quad (352)$$

The index  $\delta$  in Equation (352) signifies that the flux linkages occur via the airgap.

Figure 40 illustrates the m.m.f. linkage between two coils in contiguous stator slots. The m.m.f. due to the current in the  $j^{\text{th}}$  coil, designated A-A', links with the  $(j+1)^{\text{th}}$  coil, designated B-B'. Coil B-B' experiences the mutual m.m.f. as comprising a positive component and a negative component, spanning over the peripheral regions B→A' and A'→B' respectively. These m.m.f. components are

$$\mathbf{F}_{j+}^s = \alpha \mathbf{F} \quad (353)$$

and

$$\mathbf{F}_{j-}^s = -(1 - \alpha) \mathbf{F} \quad (354)$$

In Equations (353) and (354),  $\mathbf{F}$  is the total m.m.f. of the  $j^{\text{th}}$  stator coil, given as

$$\mathbf{F} = N_j^s I_j^s \quad (355)$$

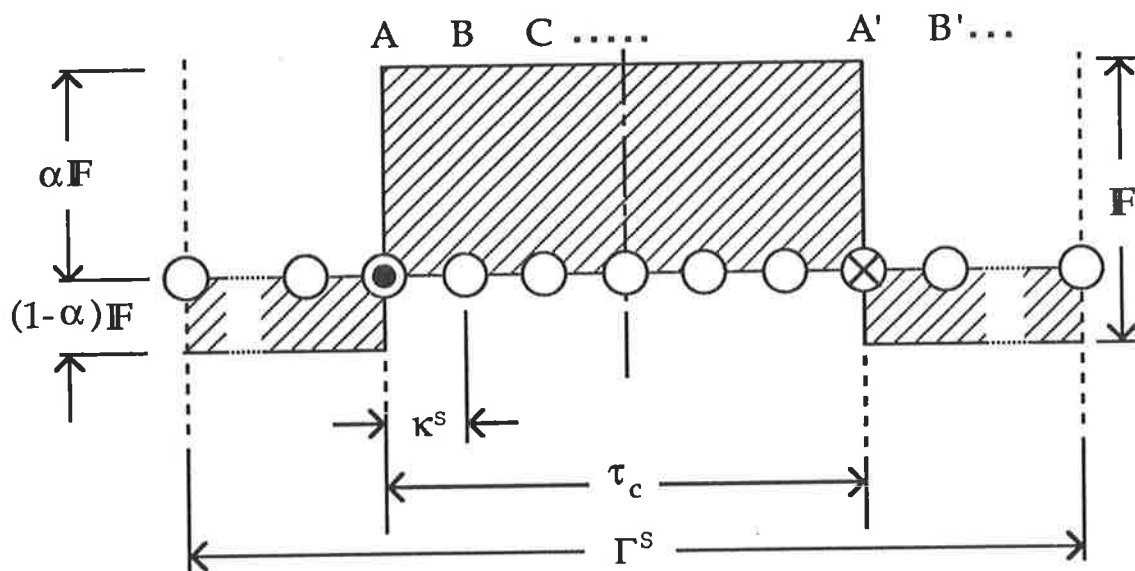


Figure 39

Circumferential distribution of airgap m.m.f. due to a stator coil  
in relation to other stator coils

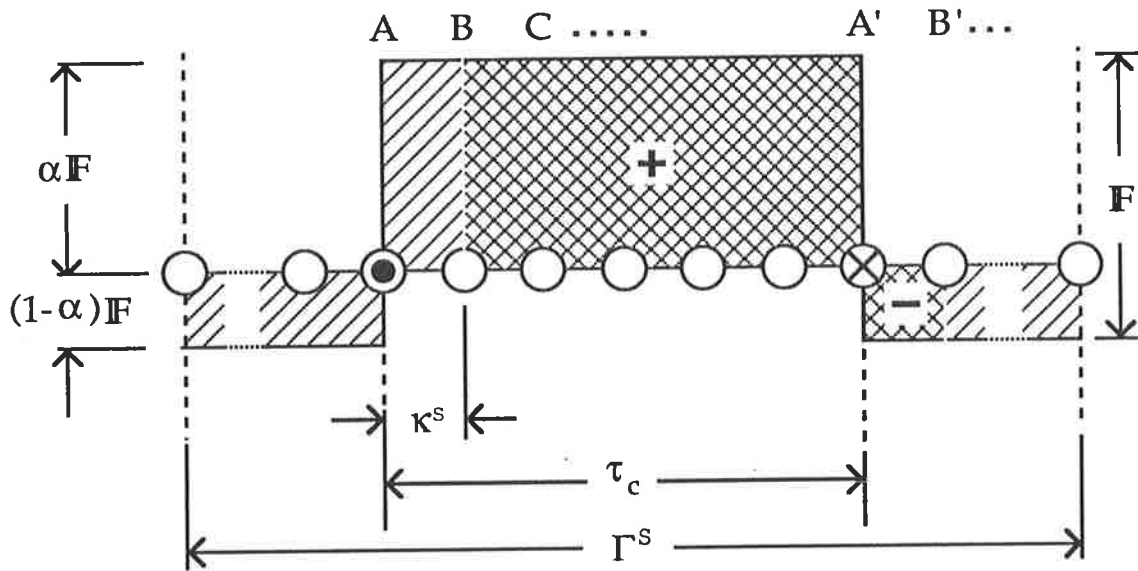


Figure 40

m.m.f. linkages between two coils in contiguous stator slots



On the other hand, the permeances of the peripheral regions  $B \rightarrow A'$  and  $A' \rightarrow B'$  can be expressed as

$$\Lambda_{\delta, j, j+1}^s \Big|_{B \rightarrow A'} = \frac{\mu_0 \ell_c (\tau_c - \kappa^s)}{\delta'} \quad (356)$$

and

$$\Lambda_{\delta, j, j+1}^s \Big|_{A' \rightarrow B'} = \frac{\mu_0 \ell_c \kappa^s}{\delta'} \quad (357)$$

The flux linking with the  $(j+1)^{\text{th}}$  coil can be obtained from

$$\Psi_{j+1}^s = \Psi_{j+1+}^s + \Psi_{j+1-}^s \quad (358)$$

$\Psi_{j+1+}^s$  and  $\Psi_{j+1-}^s$  denote the part linkages for regions  $B \rightarrow A'$  and  $A' \rightarrow B'$

respectively and are given by

$$\Psi_{j+1+}^s = N_{j+1}^s \mathbf{F}_{j+}^s \Lambda_{\delta, j, j+1}^s \Big|_{B \rightarrow A'} \quad (359)$$

and

$$\Psi_{j+1-}^s = N_{j+1}^s \mathbf{F}_{j-}^s \Lambda_{\delta, j, j+1}^s \Big|_{A' \rightarrow B'} \quad (360)$$

With Equations (352) to (355), (359) and (360), Equation (359) yields

$$\Psi_{j+1}^s = N_j^s N_{j+1}^s I_j^s \left[ \alpha \Lambda_{\delta, j, j+1}^s \Big|_{B \rightarrow A'} - (1-\alpha) \Lambda_{\delta, j, j+1}^s \Big|_{A' \rightarrow B'} \right] \quad (361)$$

Equation (361) has the general form

$$\Psi = L i \quad (362)$$

and hence can be rewritten as

$$\Psi_{j+1}^s = L_{\delta, j, j+1}^s I_j^s \quad (363)$$

Thus, the mutual inductance between the  $j^{\text{th}}$  stator coil and the  $(j+1)^{\text{th}}$  stator coil is obtained as

$$L_{\delta, j, j+1}^s = N_j^s N_{j+1}^s \Lambda_{\delta, j, j+1}^s \quad (364)$$

For identical stator coils, as is commonly the case

$$N_j^s = N_{j+1}^s = N^s \quad (365)$$

with which Equation (364) becomes

$$L_{\delta, j, j+1}^s = N^{s^2} \Lambda_{\delta, j, j+1}^s \quad (366)$$

Equation (366) can also be expressed in terms of a *mutual permeance coefficient* ,  $\lambda_{\delta, j, j+1}^s$  , as

$$L_{\delta, j, j+1}^s = N^{s2} \mu_0 \ell_c \lambda_{\delta, j, j+1}^s \quad (367)$$

where  $\lambda_{\delta, j, j+1}^s$  is obtainable, after substituting Equations (357) and (358) into Equation (362) and rearranging, as

$$\lambda_{\delta, j, j+1}^s = \frac{1}{\delta^s} [\alpha \tau_c - \kappa^s] \quad (368)$$

Similar considerations allow the mutual inductance between two **rotor coils** of a wound rotor, occupying contiguous rotor slots, to be expressed as

$$L_{\delta, k, k+1}^R = N_k^R N_{k+1}^R \Lambda_{\delta, k, k+1}^R \quad (369)$$

if the number of turns differs from coil to coil. For identical coils, the expression becomes

$$L_{\delta, k, k+1}^R = N^{R2} \Lambda_{\delta, k, k+1}^R \quad (370)$$

Alternatively, Equation (370) can be given by means of a permeance coefficient as

$$L_{\delta, k, k+1}^R = N^{R2} \mu_0 \ell_c \lambda_{\delta, k, k+1}^R \quad (371)$$

The above considerations are valid for pairs of contiguous coils. Mutual inductances between coils, which are further apart, can be determined using the same method by taking the separation between the coil sides into account. Thus, the mutual inductance between two identical coils which lie two slots apart can be determined from

$$L_{\delta, j, j+2}^s = N^{s^2} \Lambda_{\delta, j, j+2}^s \quad (372)$$

where mutual permeance is defined as

$$\Lambda_{\delta, j, j+2}^s = \mu_0 l_c \lambda_{\delta, j, j+2}^s \quad (373)$$

with

$$\lambda_{\delta, j, j+2}^s = \frac{1}{\delta'} [\alpha \tau_c - 2 \kappa^s] \quad (374)$$

The generalisation of the above considerations leads to the definition of the mutual permeance coefficient  $\lambda_{\delta, j, j+m}^s$  between any two stator coils lying  $m$  slots apart in the form

$$\lambda_{\delta, j, j+m}^s = \begin{cases} \frac{1}{\delta'} (\alpha \tau_c - m \kappa^s) & \text{if } 0 < m \leq y^s - 2 \\ * & \text{if } m = y^s \text{ and } m = S^s - y^s + 2 \\ -\frac{1}{\delta'} (1 - \alpha) \tau_c & \text{if } y^s < m \leq S^s - y^s + 1 \\ \frac{1}{\delta'} \{ \alpha \tau_c - [S^s - (m-1)] \kappa^s \} & \text{if } S^s - y^s + 2 < m \leq S^s \end{cases} \quad (375)$$

where  $y^s$  denotes the number of stator coils per coil pitch. The corresponding mutual inductances are to be obtained by

$$L_{\delta, j, j+m}^s = N^{s^2} \mu_0 l_c \lambda_{\delta, j, j+m}^s \quad (376)$$

\* alludes to the special case of two coil sides, belonging to separate coils, sharing a common slot, as is the case in double layer windings. This special case will be discussed next.

Figures 41 and 42 illustrate a **double layer winding**, Figure 41 shows a typical arrangement of coil sides in slots whereas the evolvent schematic of Figure 42 represents the relationships between stator coils. Each coil side shares the slot space with a coil side belonging to coils which lie one coil pitch apart on either side, as alluded to by  $m$  in Equation (375) in conjunction with \*. Thus the mutual inductance between the  $j^{\text{th}}$  coil and the  $(j+m)^{\text{th}}$  coil, assuming that the number of turns is different for the coils, can be generally obtained from

$$L_{s, j, j+m}^s = -N_j^s N_{j+m}^s \Lambda_{s, j, j+m}^s \quad (377)$$

For identical coils, the expression becomes

$$L_{s, j, j+m}^s = -N_j^{s^2} \Lambda_{s, j, j+m}^s \quad (378)$$

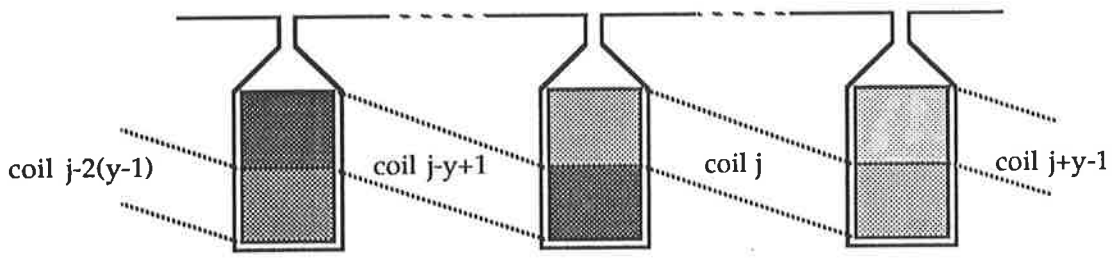


Figure 41  
Double-layer configuration

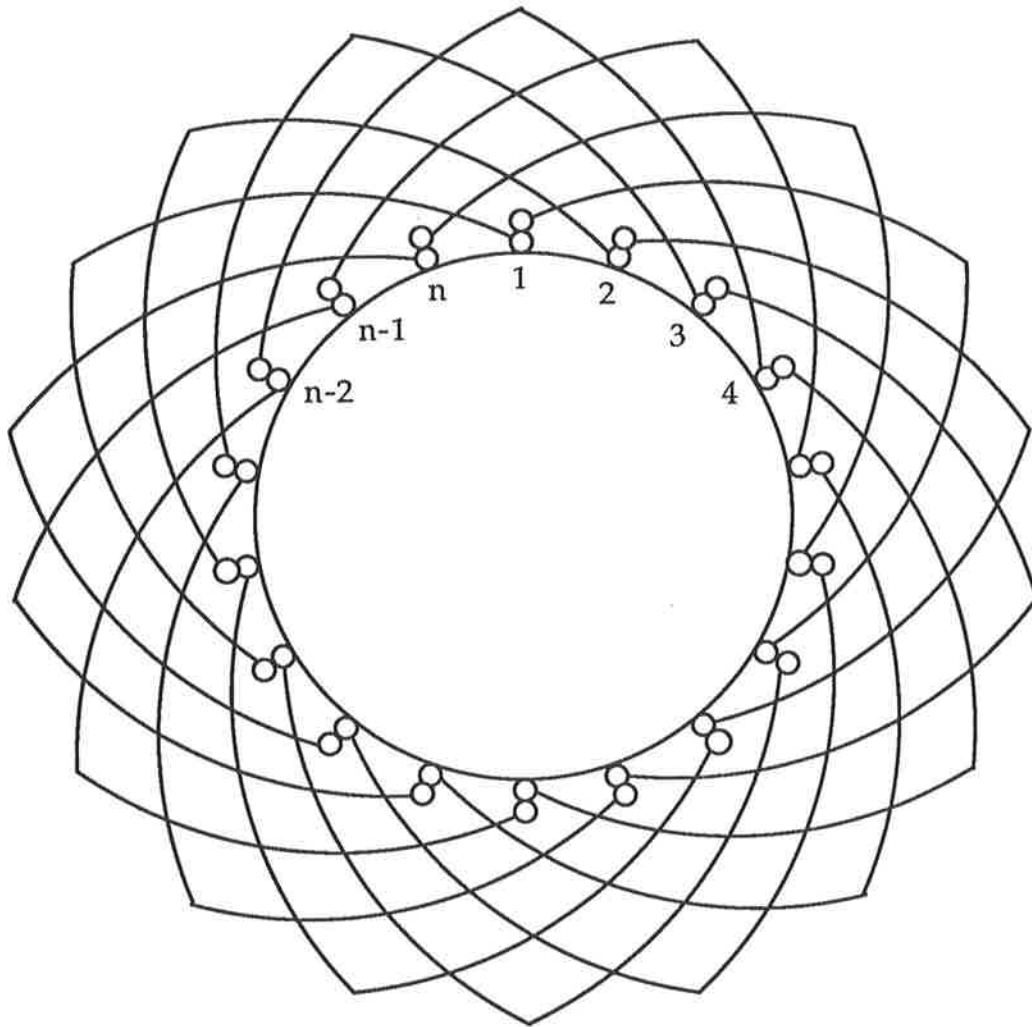


Figure 42

Evolute schematic for a double-layer winding

The negative sign in Equations (377) and (378) arises from the observation that the flow of current in the coil sides of a double-layer winding within the slot is in opposite directions. The index  $s$  signifies that the mutual coupling occurs within the slot. In terms of a mutual permeance coefficient, Equation (378) becomes

$$L_{s, j, j+m}^s = -N_j^{s^2} \mu_0 l_c \lambda_{s, j, j+m}^s \quad (379)$$

For  $m = y^s - 1$

$$\lambda_{\delta, j, j+m}^s = \frac{1}{\delta'} (\alpha \tau_c - m \kappa^s) + \lambda_{s, j, j+m}^s \quad (380)$$

and for  $m = S^s - y^s + 1$

$$\lambda_{\delta, j, j+m}^s = \frac{1}{\delta'} \left\{ \alpha \tau_c - (S^s - m) \kappa^s \right\} + \lambda_{s, j, j+m}^s \quad (381)$$

The mutual permeance coefficient  $\lambda_{s, j, j+m}^s$  of Equations (380) and (381) can be conveniently ascertained from magnetic energy considerations as before.



For a symmetrical polyphase winding with identical coils in identical stator slots, the mutual inductance between the upper coil side and the lower coil side is the same for all coils. Thus

$$\lambda_{s, j, j+m}^s = \lambda_{s, u, l}^s \quad (382)$$

indices  $u$  and  $l$  alluding to the upper coil side and the lower coil side respectively. With these stipulations, the mutual permeance coefficient for stator coils, placed as shown in Figure 43, can be obtained as

$$\lambda_{s, u, l} = \frac{h_c}{2w_s} + \frac{h_i}{w_s} + \frac{2h_w}{w_s + w_o} + \frac{h_o}{w_o} \quad (383)$$

The mutual permeance coefficients according to Equation (375) can be used for the systematic determination of the parametric inductances of the stator winding which can be represented in matrix form as

$$[\mathbf{L}^s] = [\mathbf{L}_{g, h}^s] \quad (384)$$

with  $g$  and  $h$  designating the column and the row of the matrix element. The inductance matrix thus obtained is both cyclic and symmetric. Evidently, self inductances of the stator coils occupy the diagonal of the matrix. All other matrix elements denote the mutual inductances between the coils and are to be obtained using Equations (375) to (381). The conceptual inductance matrix of Figure 44 illustrates the inductive relationships between the coils of a stator winding with eighteen coils. Table 3 explains the significance of the notations used in Figure 44 to designate the various inductances.

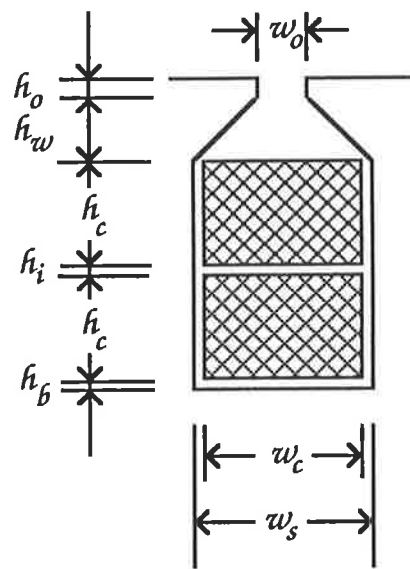


Figure 43

Coil sides of a double layer winding sharing a common slot

	1	2	3	4	5	6	7	8	9	10	11	12	13	14	15	16	17	18
1	◆	▲	×	★	*	*	⊕	⊕	⊕	⊕	⊕	⊕	⊕	*	*	★	×	▲
2	▲	◆	▲	×	★	*	*	⊕	⊕	⊕	⊕	⊕	⊕	⊕	*	*	★	×
3	×	▲	◆	▲	×	★	*	*	⊕	⊕	⊕	⊕	⊕	⊕	⊕	*	*	★
4	★	×	▲	◆	▲	×	★	*	*	⊕	⊕	⊕	⊕	⊕	⊕	⊕	*	*
5	*	★	×	▲	◆	▲	×	★	*	*	⊕	⊕	⊕	⊕	⊕	⊕	⊕	*
6	*	*	★	×	▲	◆	▲	×	★	*	*	⊕	⊕	⊕	⊕	⊕	⊕	⊕
7	⊕	*	*	★	×	▲	◆	▲	×	★	*	*	⊕	⊕	⊕	⊕	⊕	⊕
8	⊕	⊕	*	*	★	×	▲	◆	▲	×	★	*	*	⊕	⊕	⊕	⊕	⊕
9	⊕	⊕	⊕	*	*	★	×	▲	◆	▲	×	★	*	*	⊕	⊕	⊕	⊕
10	⊕	⊕	⊕	⊕	*	*	★	×	▲	◆	▲	×	★	*	*	⊕	⊕	⊕
11	⊕	⊕	⊕	⊕	⊕	*	*	★	×	▲	◆	▲	×	★	*	*	⊕	⊕
12	⊕	⊕	⊕	⊕	⊕	⊕	*	*	★	×	▲	◆	▲	×	★	*	*	⊕
13	⊕	⊕	⊕	⊕	⊕	⊕	⊕	*	*	★	×	▲	◆	▲	×	★	*	*
14	*	⊕	⊕	⊕	⊕	⊕	⊕	⊕	*	*	★	×	▲	◆	▲	×	★	*
15	*	*	⊕	⊕	⊕	⊕	⊕	⊕	⊕	*	*	★	×	▲	◆	▲	×	★
16	★	*	*	⊕	⊕	⊕	⊕	⊕	⊕	⊕	*	*	★	×	▲	◆	▲	×
17	×	★	*	*	⊕	⊕	⊕	⊕	⊕	⊕	⊕	*	*	★	×	▲	◆	▲
18	▲	×	★	*	*	⊕	⊕	⊕	⊕	⊕	⊕	⊕	*	*	★	×	▲	◆

Figure 44

Conceptual inductance matrix for a stator winding with 18 coils

**Table 3**  
Legend for inductance matrix of Figure 44

	Designation	Symbol
◆	Self inductance of jth coil	$L_{\delta,j,j}^s$
▲	Mutual inductance between jth & (j+1) <sup>th</sup> coil and jth & (j-1) <sup>th</sup> coil	$L_{\delta,j,j+1}^s, L_{\delta,j,j-1}^s$
✖	Mutual inductance between jth & (j+2) <sup>th</sup> coil and jth & (j-2) <sup>th</sup> coil	$L_{\delta,j,j+2}^s, L_{\delta,j,j-2}^s$
★	Mutual inductance between jth & (j+3) <sup>th</sup> coil and jth & (j-3) <sup>th</sup> coil	$L_{\delta,j,j+3}^s, L_{\delta,j,j-3}^s$
*	Mutual inductance between jth & (j+4) <sup>th</sup> coil and jth & (j-4) <sup>th</sup> coil	$L_{\delta,j,j+4}^s, L_{\delta,j,j-4}^s$
*	Mutual inductance between jth & (j+5) <sup>th</sup> coil and jth & (j-5) <sup>th</sup> coil	$L_{\delta,j,j+5}^s, L_{\delta,j,j-5}^s$
⊕	Mutual inductance between jth & (j-6) <sup>th</sup> coil occupying common slot	$L_{\delta,j,j-6}^s$
+	Mutual inductance between jth coil and all other coils	$L_{\delta,j,j+6}^s, L_{\delta,j,j\pm 7}^s$ to $L_{\delta,j,j\pm 12}^s$

A similar inductance matrix can be devised for the coils of a wound rotor as

$$[\mathbf{L}^R] = [L_{\delta, k, k+n}^R] \quad (385)$$

Obviously, rotor inductances will have to be found using the rotor related parameters as

$$\lambda_{\delta, k, k+n}^R = \begin{cases} \frac{1}{\delta'} (\alpha^R \tau_c^R - n \kappa^R) & \text{if } 0 < n < y^R - 2 \\ * & \text{if } n = y^R - 1 \\ -\frac{1}{\delta'} (1 - \alpha^R) \tau_c^R & \text{if } y^R < n < S^R - y^R + 1 \\ \frac{1}{\delta'} \{ \alpha^R \tau_c^R - [S^R - (j+n-1)] \kappa^R \} & \text{if } S^R - y^R + 2 < n < S^R \end{cases} \quad (386)$$

where  $y^R$  represents the number of rotor slots per coil pitch. Again, \* refers to the mutual linkage between the coil sides of a double layer winding occupying the same rotor slot, which can be determined as explained for the stator windings.

In the case of a **cage winding**, the mutual inductances between individual rotor meshes can be quantified simply from the consideration of the airgap m.m.f. distribution due to a given mesh current, which is illustrated in Figure 45.

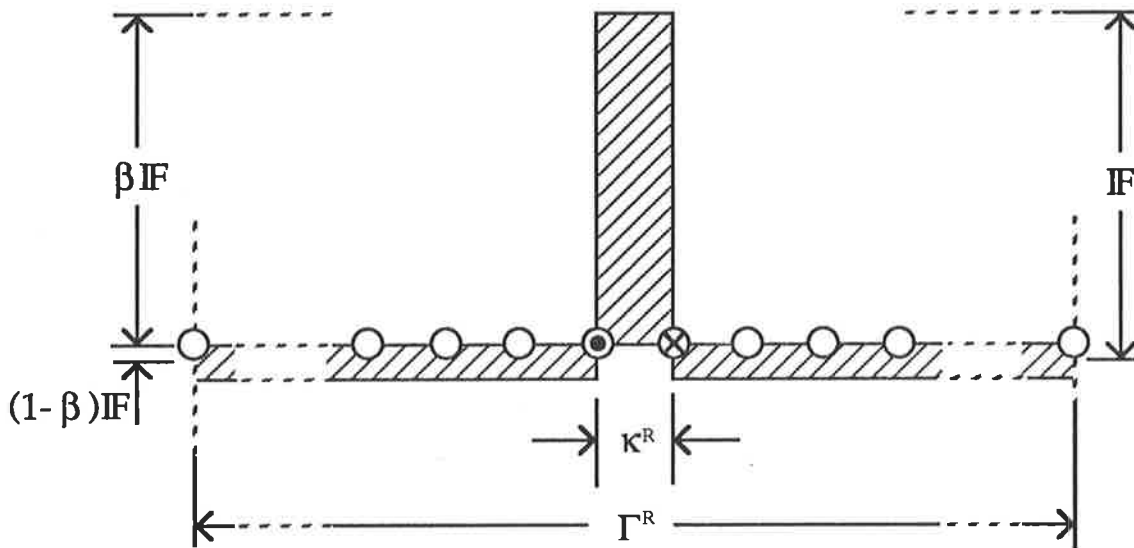


Figure 45

Circumferential distribution of airgap m.m.f. due to a rotor mesh

The instantaneous current  $I_k^R$  in the  $k^{\text{th}}$  rotor mesh is responsible for the magnetomotive force distribution illustrated in Figure 45. The mutual inductance between the  $k^{\text{th}}$  mesh and the  $(k+1)^{\text{th}}$  mesh can thus be determined from

$$L_{\delta, k, k+1} = L_{\delta, k+1, k} = \frac{\Psi_{k, k+1}}{I_k^R} \quad (387)$$

On the other hand, the flux linkage  $\Psi_{k, k+1}$  can be found as

$$\Psi_{k+1}^R = \mathbf{F}_{k+1}^R \Lambda_{\delta, k, k+1}^S \quad (388)$$

where

$$\mathbf{F}_{k+1}^R = -(1 - \beta) I_k^R \quad (389)$$

and

$$\Lambda_{\delta, k, k+1}^R = \mu_0 \ell_c \lambda_{\delta, k, k+1}^R \quad (390)$$

The permeance coefficient in Equation (390) is obtained as

$$\lambda_{\delta, k, k+1}^R = \frac{\kappa^R{}^2}{\delta' \Gamma^R} \quad (391)$$

which facilitates the mutual inductance between the  $k^{\text{th}}$  rotor mesh and the  $(k+1)^{\text{th}}$  rotor mesh to be obtained as

$$L_{\delta, k, k+1}^R = -\mu_0 \ell_c \frac{\kappa^R{}^2}{\delta' \Gamma^R} \quad (392)$$

Since the flux linkage between the  $k^{\text{th}}$  rotor mesh and all the other rotor meshes is identical, as is evident from Figure 45, the corresponding mutual inductances are all the same. Thus

$$L_{\delta, k, k+1}^R = L_{\delta, k, k+2}^R = L_{\delta, k, k+3}^R = \dots = L_{\delta, k, k+n}^R \quad (393)$$

where

$$n = 1, 2, 3, \dots, k-1$$

With these considerations, rotor inductances can be represented by the symmetric matrix

$$[\mathbf{L}^R] = [\mathbf{L}_{g, h}^R] \quad (394)$$

where  $L_{g, h}^R$  designates the elements of the inductance matrix. Matrix elements depicted by  $g = h$  represent the self inductances of the corresponding rotor meshes. All other matrix elements represent the mutual inductances between rotor meshes, which are identical. A conceptual rotor inductance matrix is illustrated in Figure 46 for a 22-slot rotor with a single cage.



	1	2	3	4	5	6	7	8	9	10	11	12	13	14	15	16	17	18	19	20	21	22	
1	●	*	*	*	*	*	*	*	*	*	*	*	*	*	*	*	*	*	*	*	*	*	*
2	*	●	*	*	*	*	*	*	*	*	*	*	*	*	*	*	*	*	*	*	*	*	*
3	*	*	●	*	*	*	*	*	*	*	*	*	*	*	*	*	*	*	*	*	*	*	*
4	*	*	*	●	*	*	*	*	*	*	*	*	*	*	*	*	*	*	*	*	*	*	*
5	*	*	*	*	●	*	*	*	*	*	*	*	*	*	*	*	*	*	*	*	*	*	*
6	*	*	*	*	*	●	*	*	*	*	*	*	*	*	*	*	*	*	*	*	*	*	*
7	*	*	*	*	*	*	●	*	*	*	*	*	*	*	*	*	*	*	*	*	*	*	*
8	*	*	*	*	*	*	*	●	*	*	*	*	*	*	*	*	*	*	*	*	*	*	*
9	*	*	*	*	*	*	*	*	●	*	*	*	*	*	*	*	*	*	*	*	*	*	*
10	*	*	*	*	*	*	*	*	*	●	*	*	*	*	*	*	*	*	*	*	*	*	*
11	*	*	*	*	*	*	*	*	*	*	●	*	*	*	*	*	*	*	*	*	*	*	*
12	*	*	*	*	*	*	*	*	*	*	*	●	*	*	*	*	*	*	*	*	*	*	*
13	*	*	*	*	*	*	*	*	*	*	*	*	●	*	*	*	*	*	*	*	*	*	*
14	*	*	*	*	*	*	*	*	*	*	*	*	*	●	*	*	*	*	*	*	*	*	*
15	*	*	*	*	*	*	*	*	*	*	*	*	*	*	●	*	*	*	*	*	*	*	*
16	*	*	*	*	*	*	*	*	*	*	*	*	*	*	*	●	*	*	*	*	*	*	*
17	*	*	*	*	*	*	*	*	*	*	*	*	*	*	*	*	●	*	*	*	*	*	*
18	*	*	*	*	*	*	*	*	*	*	*	*	*	*	*	*	*	●	*	*	*	*	*
19	*	*	*	*	*	*	*	*	*	*	*	*	*	*	*	*	*	*	●	*	*	*	*
20	*	*	*	*	*	*	*	*	*	*	*	*	*	*	*	*	*	*	*	*	●	*	*
21	*	*	*	*	*	*	*	*	*	*	*	*	*	*	*	*	*	*	*	*	*	●	*
22	*	*	*	*	*	*	*	*	*	*	*	*	*	*	*	*	*	*	*	*	*	*	●

Figure 46

Conceptual inductance matrix for a cage rotor with 22 bars

In the case of a **double cage rotor**, the mutual coupling between the lower bar and the upper bar also needs to be accounted for. The mutual inductance between the upper bar of the  $k^{\text{th}}$  mesh and the lower bar of the  $(k-1)^{\text{th}}$  mesh can be found as

$$L_{s,k,k-1}^R = -1^2 \times \Lambda_{s,k,k-1}^S \quad (395)$$

or, using a mutual permeance coefficient, as

$$L_{s,k,k-1}^R = -1^2 \times \mu_0 l_c \lambda_{s,k,k-1}^S \quad (396)$$

Of course, the mutual permeance coefficient representing the magnetic coupling between the upper rotor bar and the lower rotor bar is identical for all slots of a symmetrical cage winding housed in identical double slots.

Then, the mutual permeance coefficient can be given as

$$\lambda_{s,k,k-1}^R = \lambda_{s,u,l}^R \quad (397)$$

The mutual permeance coefficient  $\lambda_{s,u,l}^R$  can be found, with sufficient accuracy, from the difference of the slot leakage permeance coefficient of the upper bar and that of the lower bar. For a slot configuration as shown in Figure 47, this yields

$$\lambda_{s,u,l}^R = \left| \lambda_{s_u}^R - \lambda_{s_l}^R \right| \quad (398)$$

with

$$\lambda_{s_u} = \frac{\pi^2}{16} + \frac{h_o}{w_o} \quad (399)$$

and

$$\lambda_{s_f} = \frac{h_f}{3w_1} + \frac{h_b}{w_b} + \frac{\pi^2}{16} + \frac{h_o}{w_o} \quad (400)$$

Next, the mutual inductances between stator and rotor circuits need to be determined. Unlike all other mutual inductances considered so far, these are dependent on the peripheral position of the rotor relative to the stator and fluctuate between two limits as a result of the variation of the mutual flux coupling. The subsequent variation of the mutual inductance between stator and rotor circuits can be conveniently described on the basis of permeance considerations. The method is to be illustrated below, beginning with a **wound rotor** induction machine.

The developed schematic diagram of Figure 48 delineates the relationship across the airgap between a stator coil and a rotor coil. The datum for angular positions is set to coincide with the left hand coil side of the *stator coil 1*. In the case of the rotor, this means that the peripheral position of a rotor coil is to be measured in terms of the distance of its left hand coil side with reference to this datum.

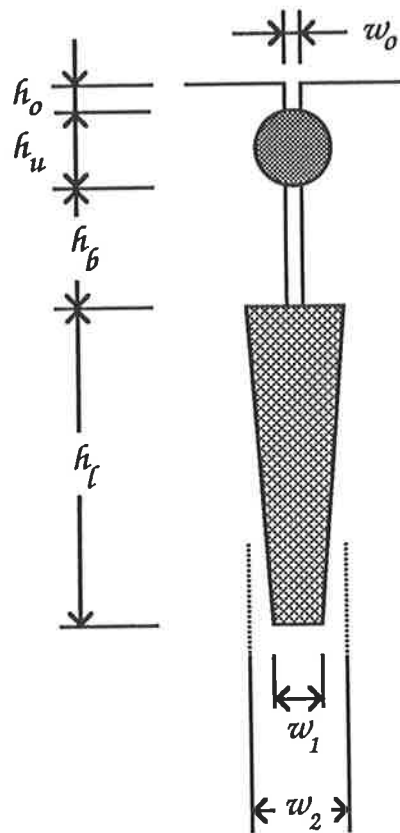


Figure 47

A typical double cage slot configuration

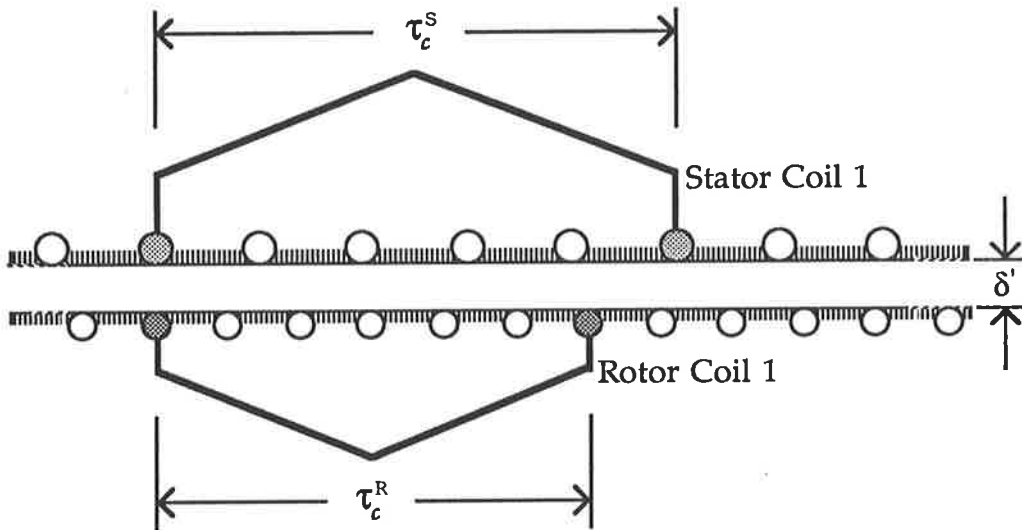


Figure 48

Developed schematic diagram showing relationship between a stator coil and a rotor coil

$\tau_c^S$  : stator coil pitch

$\tau_c^R$  : rotor coil pitch

Obviously, the total airgap m.m.f. of *stator coil 1* is

$$\mathbf{F}_1^s = N_1^s I_1^s \quad (401)$$

Initially it will be assumed that *rotor coil 1* is positioned as shown in Figure 49. In this position, a current existing in *stator coil 1* will set up a magnetomotive force which will link with the *rotor coil 1*. In the position shown, the mutual inductance between the two coils is maximum since all of the flux due the stator coil is linked with the rotor coil shown.

It is evident that the maximum flux linkage is maintained constant between this position and the next, when the right hand coil sides of the same two coils are aligned. The positive maximum flux linkage attained between these two positions is given by

$$\Psi_{1,1}^{s,R}(\lambda)_{\max^+} = N_1^R \alpha \mathbf{F}_1^s \mu_0 \ell_c \frac{1}{\delta'} \tau_c^R \quad (402)$$

When the left hand coil side of *rotor coil 1* coincides with the right hand coil side of *stator coil 1*, the flux linkage reaches its negative maximum value. This value is maintained until the right hand coil side of *rotor coil 1* is aligned with the left hand coil side of *stator coil 1*. The ensuing negative maximum flux linkage is obtained as

$$\Psi_{1,1}^{s,R}(\lambda)_{\max^-} = -N_1^R (1-\alpha) \mathbf{F}_1^s \mu_0 \ell_c \frac{1}{\delta'} \tau_c^R \quad (403)$$

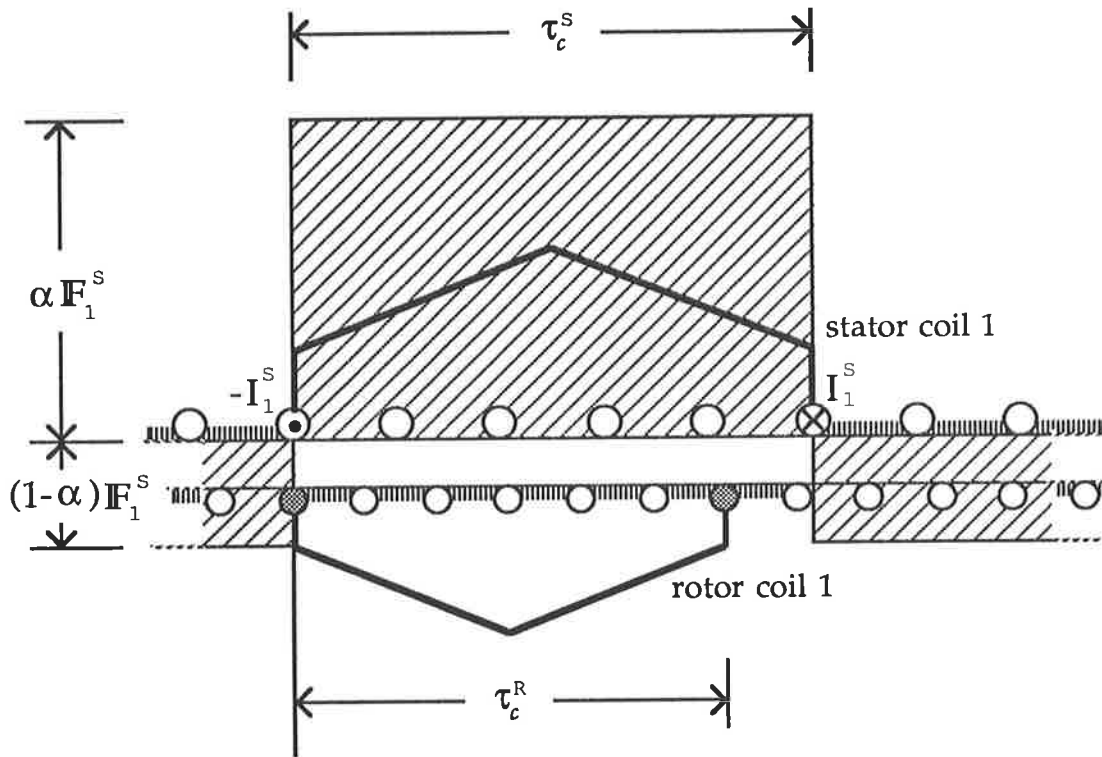


Figure 49

m.m.f. of a single stator coil and its relation to a rotor coil

Between these two regimes, the flux linkage undergoes a transitional variation. The situation is pictured in Figure 50, where *rotor coil 1* is shown as having travelled a circumferential distance  $\chi'$  along  $\chi$ -axis from the datum. *Rotor coil 1* is shaded for identification. The flux linkage at  $\chi'$  between *stator coil 1* and the *rotor coil 1* can be found from

$$\Psi_{1,1}^{S,R}(\chi) = \Psi_{1,1}^{S,R}(\chi) \Big|_{\chi' \rightarrow \tau_c^S} + \Psi_{1,1}^{S,R}(\chi) \Big|_{\tau_c^S \rightarrow \chi' + \tau_c^R} \quad (404)$$

The terms on the right hand side of Equation (404) represent the partial flux linkages which correspond to the partial m.m.f. linkages shown by  $\boxed{+}$  and  $\boxed{-}$  in Figure 50 and are to be obtained using

$$\Psi = N F \Lambda$$

as

$$\Psi_{1,1}^{S,R}(\chi) \Big|_{\chi' \rightarrow \tau_c^S} = N_1^R \alpha F_1^S \mu_0 \ell_c \frac{1}{\delta'} (\tau_c^S - \chi) \quad (405)$$

and

$$\Psi_{1,1}^{S,R}(\chi) \Big|_{\tau_c^S \rightarrow \chi' + \tau_c^R} = -N_1^R (1-\alpha) F_1^S \mu_0 \ell_c \frac{1}{\delta'} (\tau_c^R - \tau_c^S + \chi) \quad (406)$$

Alternatively, the mutual flux linkage between the two coils can be expressed in terms of a constant permeance and a variable m.m.f. linkage in the form

$$\Psi_{1,1}^{S,R}(\chi) = N_1^R \mathbf{F}_{\delta,1,1}^{S,R}(\chi) \Lambda_{\delta,1,1}^{S,R} \quad (407)$$



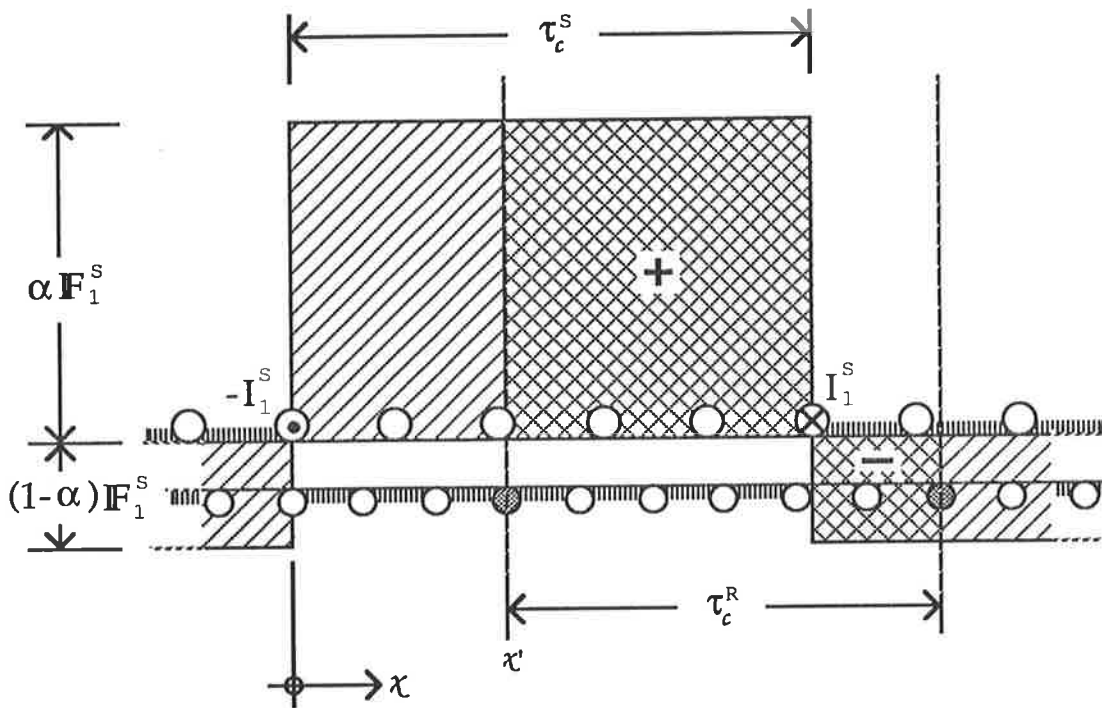


Figure 50

m.m.f. linkage between a stator coil and a rotor coil

The variation of m.m.f. linkage for a complete revolution of the rotor for various regions of overlap between the two coils is illustrated in Figure 51.

In the case of the m.m.f. being set up by a stator coil linking with a rotor coil, as discussed here, the mutual permeance can be given with reference to the rotor coil as

$$\Lambda_{\delta,1,1}^{S,R} = \mu_0 l_c \frac{\tau_c^R}{\delta} \quad (408)$$

By definition, the corresponding values of mutual inductance between *stator coil 1* and *rotor coil 1* are then obtainable from

$$L_{\delta,1,1}^{S,R}(\chi) = N_1^R \frac{F_{1,1}^{S,R}(\chi) \Lambda_{\delta,1,1}^{S,R}}{I_1^S} \quad (409)$$

The variation of the m.m.f. linkage between *stator coil 1* and *rotor coil 1* according to the above deliberations is depicted in Figure 52.

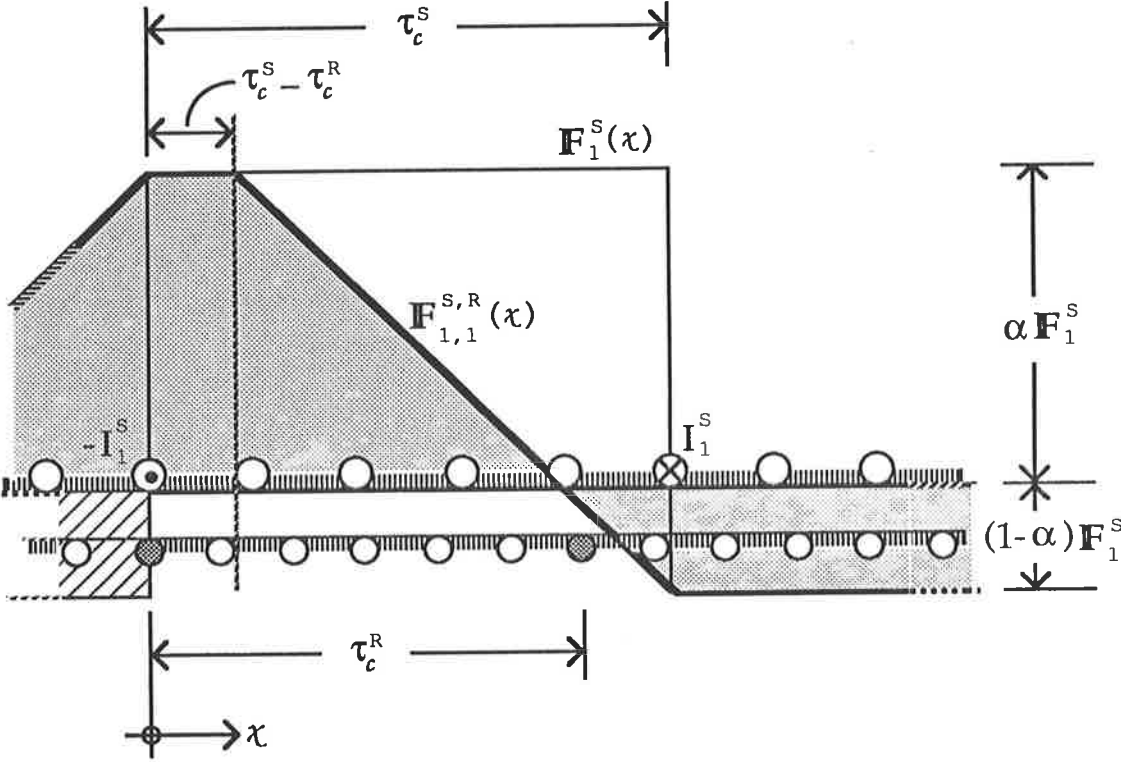


Figure 51  
Variation of m.m.f. linkage between *stator coil 1* and *rotor coil 1*  
as a function of rotor position

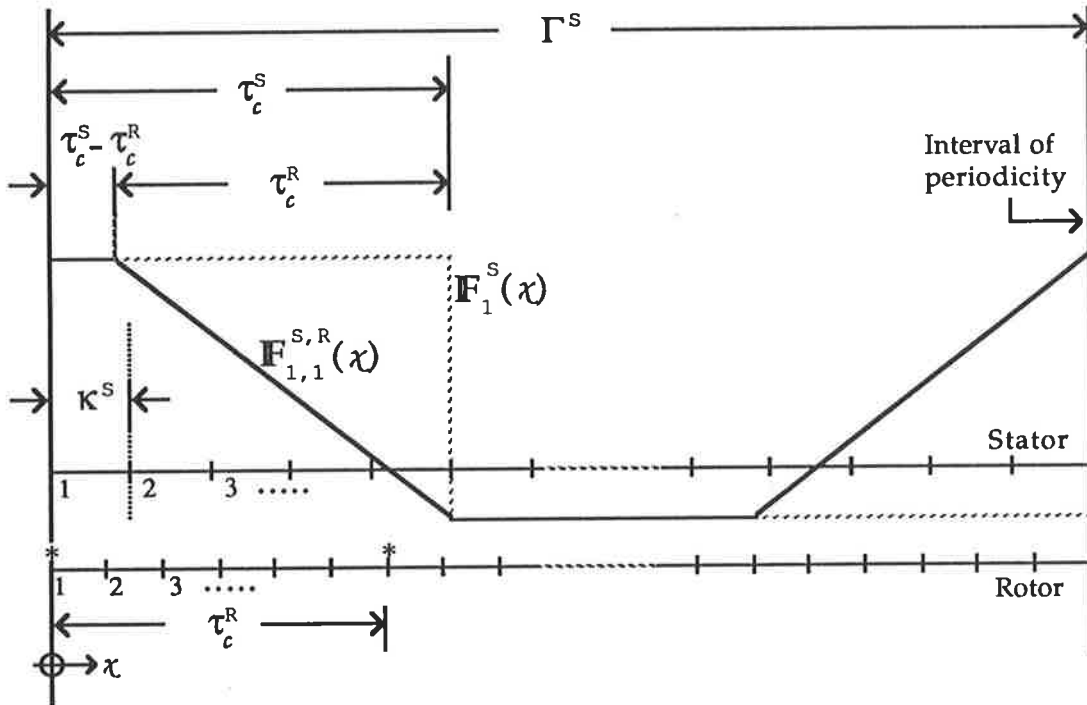


Figure 52

Variation of m.m.f. linkage between *stator coil 1* and *rotor coil 1*

Analytically, the variation of the m.m.f. linkage between *stator coil 1* and *rotor coil 1* for various peripheral regions alluded to in Figure 51 can be given as follows.

### Region 1

$$\mathbf{F}_{1,1}^{S,R}(\chi) \Big|_{0 \rightarrow (\tau_c^S - \tau_c^R)} = \alpha \mathbf{F}_1^S \quad (410)$$

### Region 2

$$\mathbf{F}_{1,1}^{S,R}(\chi) \Big|_{\tau_c^S - \tau_c^R \rightarrow \tau_c^S} = \frac{\mathbf{F}_1^S}{\tau_c^R} [\tau_c^S - (1-\alpha)\tau_c^R - \chi] \quad (411)$$

### Region 3

$$\mathbf{F}_{1,1}^{S,R}(\chi) \Big|_{\tau_c^S \rightarrow \Gamma^S - \tau_c^R} = -(1-\alpha)\mathbf{F}_1^S \quad (412)$$

### Region 4

$$\mathbf{F}_{1,1}^{S,R}(\chi) \Big|_{\Gamma^S - \tau_c^R \rightarrow \Gamma^S} = \frac{\mathbf{F}_1^S}{\tau_c^R} [\alpha\tau_c^R - \Gamma^S + \chi] \quad (413)$$

The mutual inductance between *stator coil 1* and *rotor coil 1* for each region can now be obtained by substituting the relevant m.m.f. equation from above into Equation (409). Adopting the form of expression in terms

of a permeance coefficient and considering the total m.m.f. of *stator coil 1* as given in Equation (401), this yields

$$L_{\delta,1,1}^{S,R}(\chi) = N_1^S N_1^R \mu_0 l_c \lambda_{\delta,1,1}^{S,R}(\chi) \quad (414)$$

Table 4 lists the values of mutual permeance coefficient for various regions of overlap as a result of the relative motion between *stator coil 1* and *rotor coil 1*.

**Table 4**

Variation of permeance coefficient between *stator coil 1* and *rotor coil 1* due to relative motion

Region			Mutual Permeance Coefficient
	from	to	
1	0	$\tau_c^S - \tau_c^R$	$\frac{1}{\delta'} \alpha \tau_c^R$
2	$\tau_c^S - \tau_c^R$	$\tau_c^S$	$\frac{1}{\delta'} [\tau_c^S - (1-\alpha)\tau_c^R - \chi]$
3	$\tau_c^S$	$\Gamma^S - \tau_c^R$	$-\frac{1}{\delta'} (1-\alpha)\tau_c^R$
4	$\Gamma^S - \tau_c^R$	$\Gamma^S$	$\frac{1}{\delta'} [\alpha \tau_c^R - \Gamma^S + \chi]$

The preceding considerations form the basis of mutual inductance calculations between any stator coil and rotor coil as the rotor moves relative to the stator. Figure 53 alludes to this by illustrating the simultaneous variation of m.m.f. linkage between *rotor coil 1* and all stator coils. For instance, the m.m.f. linkage between *stator coil 2* and *rotor coil 1* is seen to be lagging behind the m.m.f. linkage between *stator coil 1* and *rotor coil 1* by the circumferential distance between *stator coil 1* and *stator coil 2*, which in this case is equal to the stator coil pitch. It follows that the m.m.f. linkage between the  $j^{\text{th}}$  stator coil and rotor coil 1 can be given, region by region, as below.

Region 1  $(j-1) \kappa^S \leq \chi < (j-1) \kappa^S + \Delta\tau_c$

$$\mathbf{F}_{j,1}^{S,R}(\chi) \Big|_{\text{Region 1}} = \alpha \mathbf{F}_1^S \quad (415)$$

Region 2  $(j-1) \kappa^S + \Delta\tau_c \leq \chi < (j-1) \kappa^S + \tau_c^S$

$$\mathbf{F}_{j,1}^{S,R}(\chi) \Big|_{\text{Region 2}} = \frac{\mathbf{F}_1^S}{\tau_c^R} \left[ (j-1) \kappa^S + \tau_c^S - (1-\alpha)\tau_c^R - \chi \right] \quad (416)$$

Region 3  $(j-1) \kappa^S + \tau_c^S \leq \chi < (j-1) \kappa^S + \Gamma^S - \tau_c^R$

$$\mathbf{F}_{j,1}^{S,R}(\chi) \Big|_{\text{Region 3}} = -(1-\alpha)\mathbf{F}_1^S \quad (417)$$

Region 4  $(j-1) \kappa^S + \Gamma^S - \tau_c^R \leq \chi < (j-1) \kappa^S + \Gamma^S$

$$\mathbf{F}_{j,1}^{S,R}(\chi) \Big|_{\text{Region 4}} = \frac{\mathbf{F}_1^S}{\tau_c^R} \left[ \alpha\tau_c^R - (j-1) \kappa^S - \Gamma^S + \chi \right] \quad (418)$$

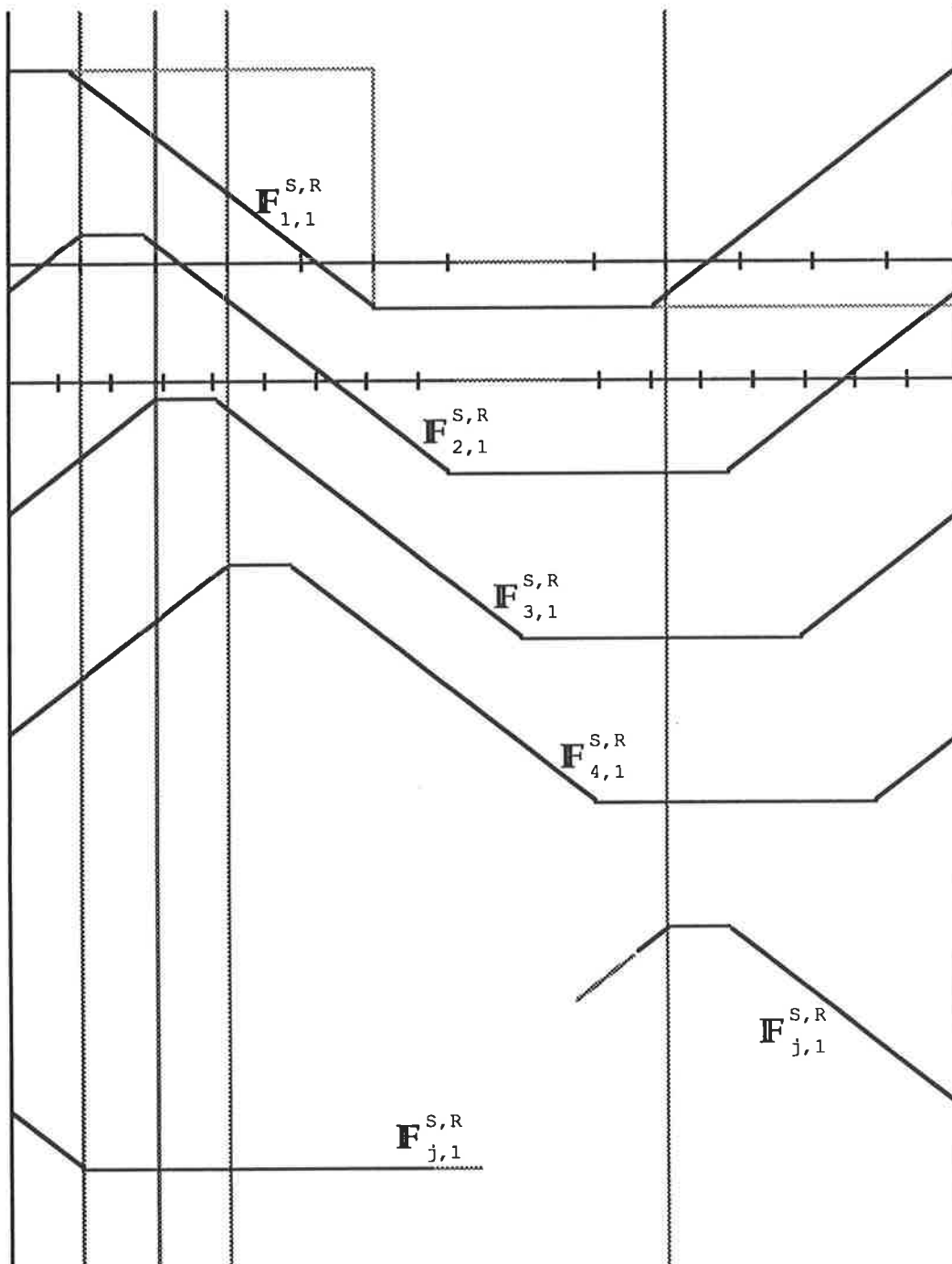


Figure 53

Variation of m.m.f. linkage between stator coils and *rotor coil 1*



The corresponding permeance coefficients are listed in Table 5. The mutual inductance between *rotor coil 1* and the  $j^{\text{th}}$  stator coil can consequently be calculated using

$$L_{\delta,j,1}^{S,R}(\chi) = N_j^S N_1^R \mu_0 l_c \lambda_{\delta,j,1}^{S,R} \quad (419)$$

$\Delta\tau_c$  in Equations (415) and (416) as well as in Table 5 below represents the difference between the stator coil pitch and the rotor coil pitch.

**Table 5**

Variation of permeance coefficient between *rotor coil 1* and the  $j^{\text{th}}$  stator coil due to relative motion

Region			Mutual Permeance Coefficient
	from	to	
1	$(j-1)\kappa^S$	$(j-1)\kappa^S + \Delta\tau_c$	$\frac{1}{\delta'} \alpha\tau_c^R$
2	$(j-1)\kappa^S + \Delta\tau_c$	$(j-1)\kappa^S + \tau_c^S$	$\frac{1}{\delta'} [(j-1)\kappa^S + \tau_c^S - (1-\alpha)\tau_c^R - \chi]$
3	$(j-1)\kappa^S + \tau_c^S$	$(j-1)\kappa^S + \Gamma^S - \tau_c^R$	$-\frac{1}{\delta'} (1-\alpha)\tau_c^R$
4	$(j-1)\kappa^S + \Gamma^S - \tau_c^R$	$(j-1)\kappa^S + \Gamma^S$	$\frac{1}{\delta'} [\alpha\tau_c^R - \Gamma^S - (j-1)\kappa^S + \chi]$

The above can be generalised to obtain the mutual inductance between the  $j^{\text{th}}$  stator coil and the  $k^{\text{th}}$  rotor coil during motion by considering the relative position of the two coils as shown in Figure 54. The  $k^{\text{th}}$  rotor coil is depicted as having travelled a distance  $\chi'$  from the datum. Evidently, the m.m.f. linkage variation between this rotor coil and the  $j^{\text{th}}$  stator coil will be identical to that of *rotor coil 1* with the  $j^{\text{th}}$  stator coil, except that there will be a shift between the two variations as depicted in Figure 54. Once again, the regions of overlap determining the m.m.f. linkage between the two coils are identified below for clarity.

Region 1     $\mathbf{X}_1 \leq \chi < \mathbf{X}_2$

$$\mathbf{F}_{j,k}^{S,R}(\chi) \Big|_{\text{Region 1}} = \alpha \mathbf{F}_j^S \quad (420)$$

Region 2     $\mathbf{X}_2 \leq \chi < \mathbf{X}_3$

$$\mathbf{F}_{j,k}^{S,R}(\chi) \Big|_{\text{Region 2}} = \frac{\mathbf{F}_j^S}{\tau_c^R} \left[ (j-1) \kappa^S + \tau_c^S - (1-\alpha)\tau_c^R - \chi \right] \quad (421)$$

Region 3     $\mathbf{X}_3 \leq \chi < \mathbf{X}_4$

$$\mathbf{F}_{j,k}^{S,R}(\chi) \Big|_{\text{Region 3}} = -(1-\alpha)\mathbf{F}_j^S \quad (422)$$

Region 4     $\mathbf{X}_4 \leq \chi < \mathbf{X}_1$

$$\mathbf{F}_{j,k}^{S,R}(\chi) \Big|_{\text{Region 4}} = \frac{\mathbf{F}_j^S}{\tau_c^R} \left[ \alpha\tau_c^R - (j-1) \kappa^S - \Gamma^S + \chi \right] \quad (423)$$

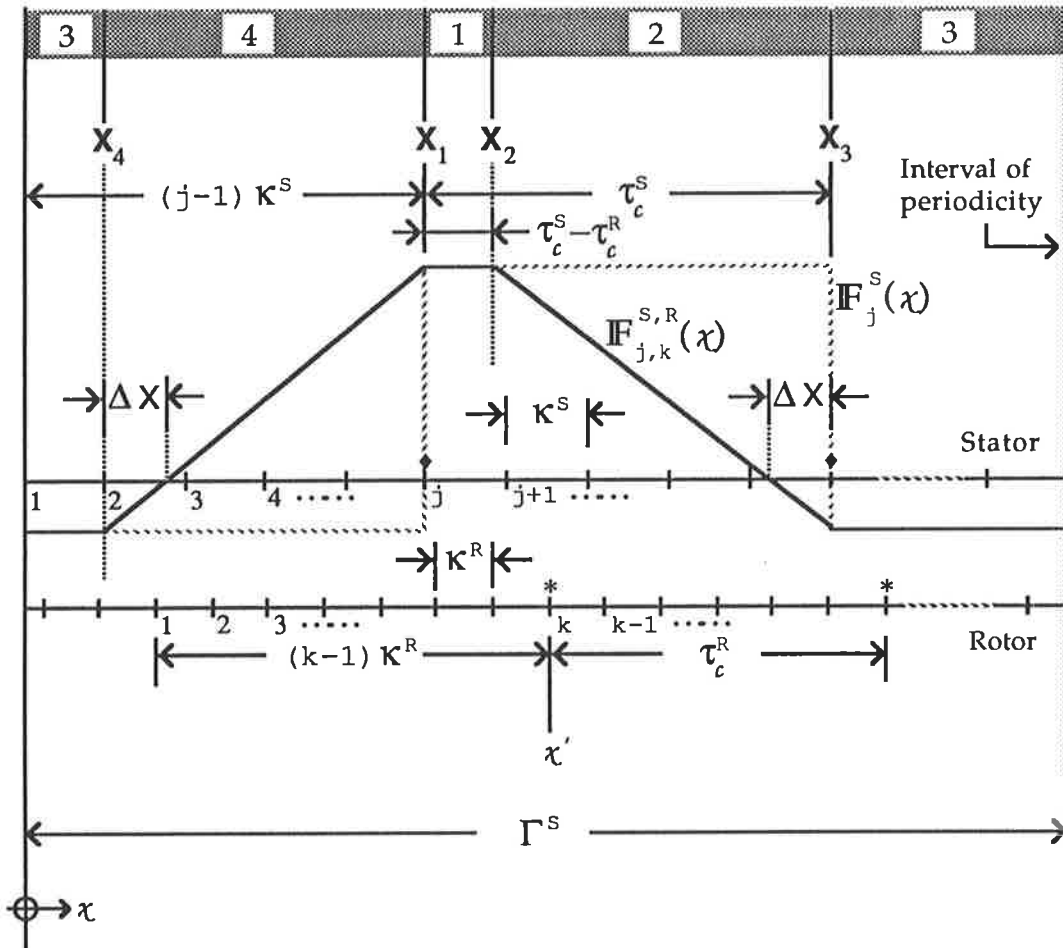


Figure 54  
 m.m.f. linkage between  $j^{\text{th}}$  stator coil and  $k^{\text{th}}$  rotor coil

The above equations show that the m.m.f. linkage between the  $j^{\text{th}}$  stator coil and the  $k^{\text{th}}$  rotor coil varies exactly in the same way as the m.m.f. linkage between the  $j^{\text{th}}$  stator coil and *rotor coil 1* except that there is a lag corresponding to the physical position of the  $k^{\text{th}}$  rotor coil as measured with reference to *rotor coil 1*. The equations can be generalised as

$$\mathbf{F}_{j,k}^{S,R}(\chi) = \begin{cases} \alpha \mathbf{F}_j^S & \text{if } \mathbf{X}_1 \leq \chi < \mathbf{X}_2 \\ -\frac{\mathbf{F}_j^S}{\tau_c^R} [\chi - (\mathbf{X}_3 - \Delta\mathbf{X})] & \text{if } \mathbf{X}_2 \leq \chi < \mathbf{X}_3 \\ (1-\alpha)\mathbf{F}_j^S & \text{if } \mathbf{X}_3 \leq \chi < \mathbf{X}_4 \\ \frac{\mathbf{F}_j^S}{\tau_c^R} [\chi - (\mathbf{X}_4 + \Delta\mathbf{X})] & \text{if } \mathbf{X}_4 \leq \chi < \mathbf{X}_1 \end{cases} \quad (424)$$

and

$$\mathbf{F}_{j,k}^{S,R}(\chi) = \mathbf{F}_{j,k}^{S,R}(\chi + \Gamma^S) \quad (425)$$

where

$$\mathbf{X}_1 = (j-1)\kappa^S \quad (426)$$

$$\mathbf{X}_2 = (j-1)\kappa^S + \Delta\tau_c \quad (427)$$

$$\mathbf{X}_3 = (j-1)\kappa^S + \tau_c^S \quad (428)$$

$$\mathbf{X}_4 = (j-1)\kappa^S + \Gamma^S - \tau_c^R \quad (429)$$

$$\Delta\mathbf{X} = (1-\alpha)\tau_c^R \quad (430)$$

$$\Delta\tau_c = \tau_c^S - \tau_c^R \quad (431)$$

Once the m.m.f. variation for various regions of overlap is known, the corresponding mutual inductances can be found as

$$L_{\delta,j,k}^{S,R}(\chi) = N_j^S N_k^R \mu_0 l_c \lambda_{\delta,j,k}^{S,R}(\chi) \quad (432)$$

where the mutual permeance coefficient for each region is as shown in Table 6.

**Table 6**

Variation of permeance coefficient between  $j^{\text{th}}$  stator coil and  $k^{\text{th}}$  rotor coil due to relative motion

Region			Mutual Permeance Coefficient
	from	to	
1	$X_1$	$X_2$	$\frac{1}{\delta'} \alpha \tau_c^R$
2	$X_2$	$X_3$	$\frac{1}{\delta'} [(j-1)\kappa^S + \tau_c^S - (1-\alpha)\tau_c^R - \chi]$
3	$X_3$	$X_4$	$-\frac{1}{\delta'} (1-\alpha)\tau_c^R$
4	$X_4$	$X_1$	$\frac{1}{\delta'} [\alpha\tau_c^R - \Gamma^S - (j-1)\kappa^S + \chi]$

For a **cage rotor**, the situation is similar. Figure 55 illustrates the relationship between *stator coil 1* and *rotor mesh 1* for the datum position. The m.m.f. linkage remains constant from this position until the leading bar of *rotor mesh 1* is aligned with the right hand coil side of *stator coil 1*. As the rotor continues to move in the same sense of rotation, a transitional period follows as alluded to in Figure 56. During transition, the m.m.f. linkage varies to reach a negative maximum when the lagging bar of *rotor mesh 1* is aligned with the right hand coil side of *stator coil 1*. This maximum negative m.m.f. linkage is maintained until the leading bar of the mesh coincides with left hand coil side of *stator coil 1*. Between this position and the next, when the lagging bar of the mesh is aligned with the left hand coil side of stator coil 1, m.m.f. linkage experiences another transition, this time from a negative maximum to the initially held positive maximum.

Figure 57 illustrates the variation of the m.m.f. linkage between any stator coil and any rotor mesh. Analytical expressions for the m.m.f. linkage variation between the  $j^{\text{th}}$  stator coil and the  $k^{\text{th}}$  rotor mesh can again be derived by considering the regions of overlap.

Region 1     $\mathbf{X}_1 \leq \chi < \mathbf{X}_2$

$$\mathbf{F}_{j,k}^{s,R}(\chi) \Big|_{\text{Region 1}} = \alpha \mathbf{F}_j^s \quad (433)$$

Region 2     $\mathbf{X}_2 \leq \chi < \mathbf{X}_3$

$$\mathbf{F}_{j,k}^{s,R}(\chi) \Big|_{\text{Region 2}} = \frac{\mathbf{F}_j^s}{\tau_c^R} \left[ (j-1) \kappa^S - (1-\alpha) \kappa^R + \tau_c^S - \chi \right] \quad (434)$$

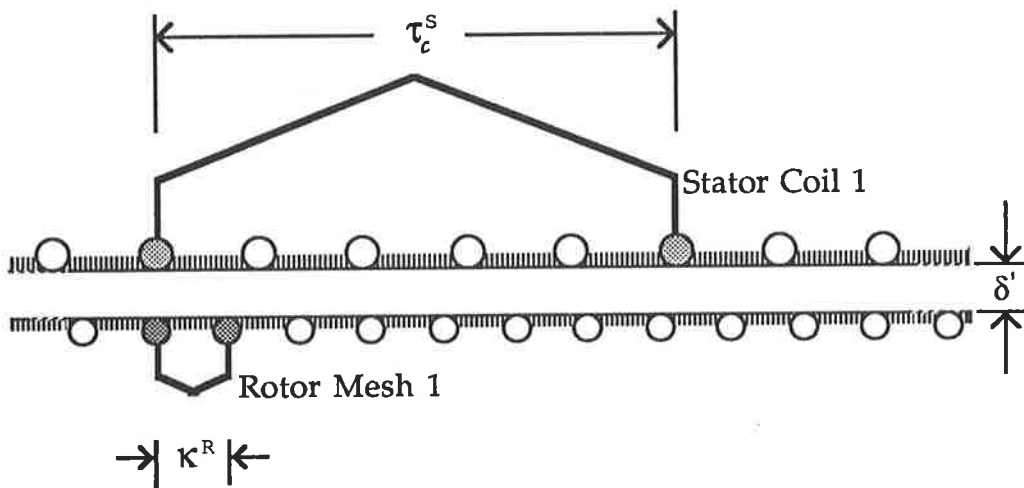


Figure 55

Developed schematic diagram showing relationship between a stator coil and a rotor mesh





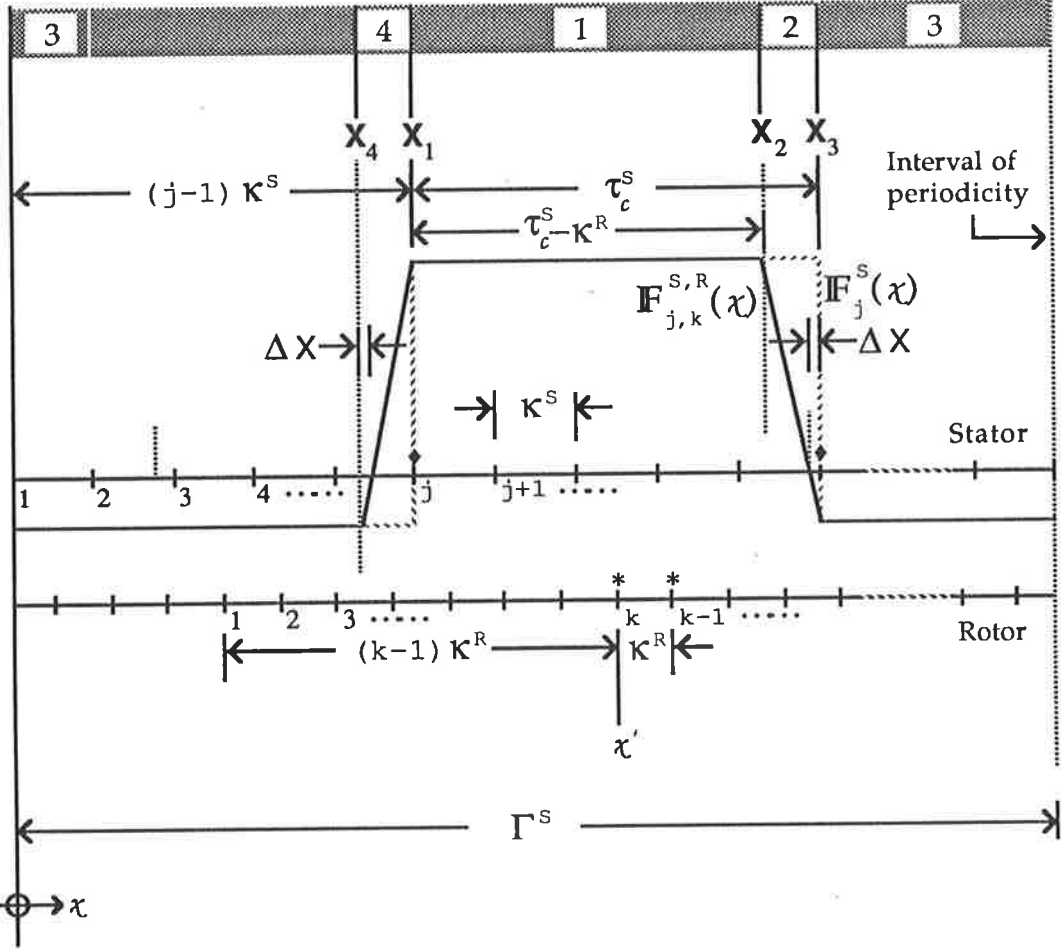


Figure 57  
m.m.f. linkage between  $j^{\text{th}}$  stator coil and  $k^{\text{th}}$  rotor mesh

Region 3  $\mathbf{X}_3 \leq \chi < \mathbf{X}_4$

$$\mathbf{F}_{j,k}^{S,R}(\chi) \Big|_{\text{Region 3}} = -(1-\alpha)\mathbf{F}_j^S \quad (435)$$

Region 4  $\mathbf{X}_4 \leq \chi < \mathbf{X}_1$

$$\mathbf{F}_{j,k}^{S,R}(\chi) \Big|_{\text{Region 4}} = \frac{\mathbf{F}_j^S}{\tau_c^R} \left[ -(j-1)\kappa^S + \alpha\kappa^R - \Gamma^S + \chi \right] \quad (436)$$

The regional m.m.f. expressions of Equations (433) to (436) can be generalised with the use of the regional boundaries and the interval  $\Delta\mathbf{X}$  identified in Figure 57. The resulting expressions, shown below, are compact and reflect the symmetry implicit in the underlying machine topology. As can be expected, these equations closely resemble those describing the m.m.f. linkages in the case of an induction machine with a wound rotor. In fact, if a rotor mesh is viewed to represent a single-turn coil with its coil pitch being equal to the rotor slot pitch, then the expressions are identical.

$$\mathbf{F}_{j,k}^{S,R}(\chi) = \begin{cases} \alpha\mathbf{F}_j^S & \text{if } \mathbf{X}_1 \leq \chi < \mathbf{X}_2 \\ -\frac{\mathbf{F}_j^S}{\kappa^R} \left[ \chi - (\mathbf{X}_3 - \Delta\mathbf{X}) \right] & \text{if } \mathbf{X}_2 \leq \chi < \mathbf{X}_3 \\ (1-\alpha)\mathbf{F}_j^S & \text{if } \mathbf{X}_3 \leq \chi < \mathbf{X}_4 \\ \frac{\mathbf{F}_j^S}{\kappa^R} \left[ \chi - (\mathbf{X}_4 + \Delta\mathbf{X}) \right] & \text{if } \mathbf{X}_4 \leq \chi < \mathbf{X}_1 \end{cases} \quad (437)$$

and

$$\mathbf{F}_{j,k}^{S,R}(\chi) = \mathbf{F}_{j,k}^{S,R}(\chi + \Gamma^S) \quad (438)$$

where

$$\mathbf{X}_1 = (j-1)\kappa^S \quad (439)$$

$$\mathbf{X}_2 = (j-1)\kappa^S - \kappa^R + \tau_c^S \quad (440)$$

$$\mathbf{X}_3 = (j-1)\kappa^S + \tau_c^S \quad (441)$$

$$\mathbf{X}_4 = (j-1)\kappa^S - \kappa^R + \Gamma^S \quad (442)$$

$$\Delta\mathbf{X} = (1-\alpha)\kappa^R \quad (443)$$

As before, the corresponding inductances are to be obtained from permeance considerations. Thus, the mutual inductance between the  $j^{\text{th}}$  stator coil and the  $k^{\text{th}}$  rotor mesh can be found using

$$L_{\delta,j,k}^{S,R}(\chi) = 1 \times \frac{\mathbf{F}_{j,k}^{S,R}(\chi) \Lambda_{\delta,j,k}^{S,R}}{I_j^S} \quad (444)$$

which reduces to

$$L_{\delta,j,k}^{S,R}(\chi) = 1 \times N_j^S \mu_0 l_c \lambda_{\delta,j,k}^{S,R}(\chi) \quad (445)$$

Table 7 gives the regional variation of the mutual permeance coefficient  $\lambda_{\delta,j,k}^{S,R}(\chi)$ .

**Table 7**

Regional variation of permeance coefficient between  $j^{\text{th}}$  stator coil and  $k^{\text{th}}$  rotor mesh due to relative motion

Region			Mutual Permeance Coefficient
	from	to	
1	$\mathbf{X}_1$	$\mathbf{X}_2$	$\frac{1}{\delta'} \alpha \kappa^R$
2	$\mathbf{X}_2$	$\mathbf{X}_3$	$\frac{1}{\delta'} [\chi + (\mathbf{X}_3 - \Delta \mathbf{X})]$
3	$\mathbf{X}_3$	$\mathbf{X}_4$	$-\frac{1}{\delta'} (1 - \alpha) \kappa^R$
4	$\mathbf{X}_4$	$\mathbf{X}_1$	$\frac{1}{\delta'} [\chi - (\mathbf{X}_4 + \Delta \mathbf{X})]$

So far in the analysis it has been assumed that the slots are not skewed. However, skewing of either stator slots or rotor slots or both is a commonly adopted measure in induction machine design practice in order to overcome certain aspects of parasitic behaviour. If skewing is present, the permeance expressions developed above require modification.

Figure 58 depicts the practically important case of **rotor skewing**. In Figure 59 a skewed rotor mesh is superimposed on the projected m.m.f. distribution due to current flowing in the  $j^{\text{th}}$  stator coil to illustrate the interaction. As can be seen, the transitional regions are no longer solely defined by the alignment with stator coil sides of the leading and lagging bars of rotor meshes; three subregions come into existence as alluded to in Figure 60. The m.m.f. variation is linear in the middle subregion whereas the outer subregions are now characterised by a non-linear variation resulting in a smooth and continuous transition into the adjoining constant m.m.f. regions. Evidently, the amount of skewing affects both the width of the subregions and the shape of the transitional m.m.f. within the subregions.

The general expressions for m.m.f. linkage between the  $j^{\text{th}}$  stator coil and the skewed  $k^{\text{th}}$  rotor mesh can be developed with the aid of Figure 60. In doing so, attention needs to be given to the amount of skewing; the transitional m.m.f. distribution for a rotor slot skew,  $\kappa$ , less than that corresponding to one rotor slot pitch is different from that exceeding one rotor slot pitch. The following deliberations will differentiate between these two cases.

The analytical expressions for the m.m.f. linkage variation will be once again obtained region by region.

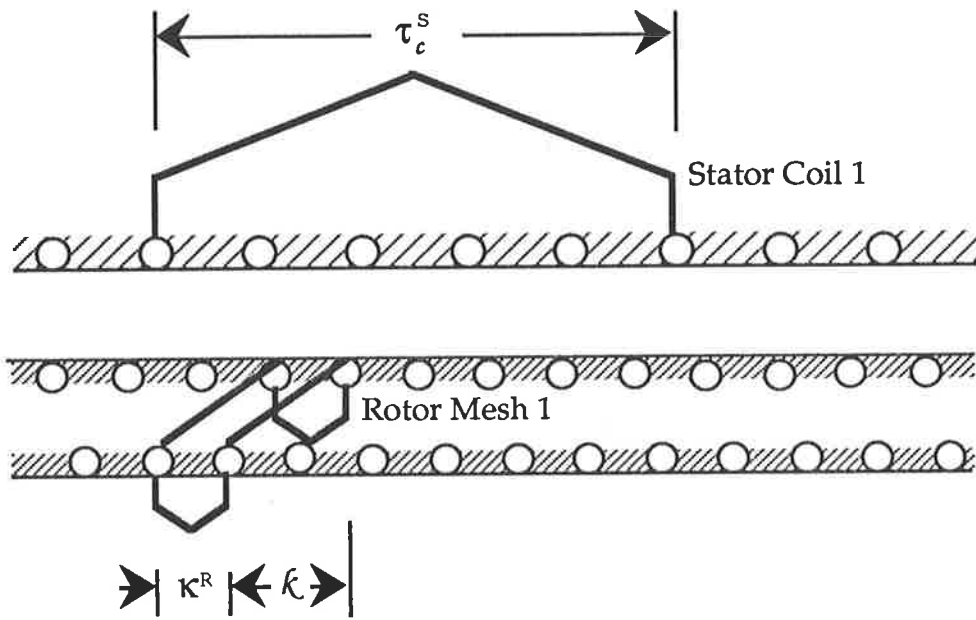


Figure 58

Developed schematic diagram depicting the relationship between a stator coil and a skewed rotor mesh

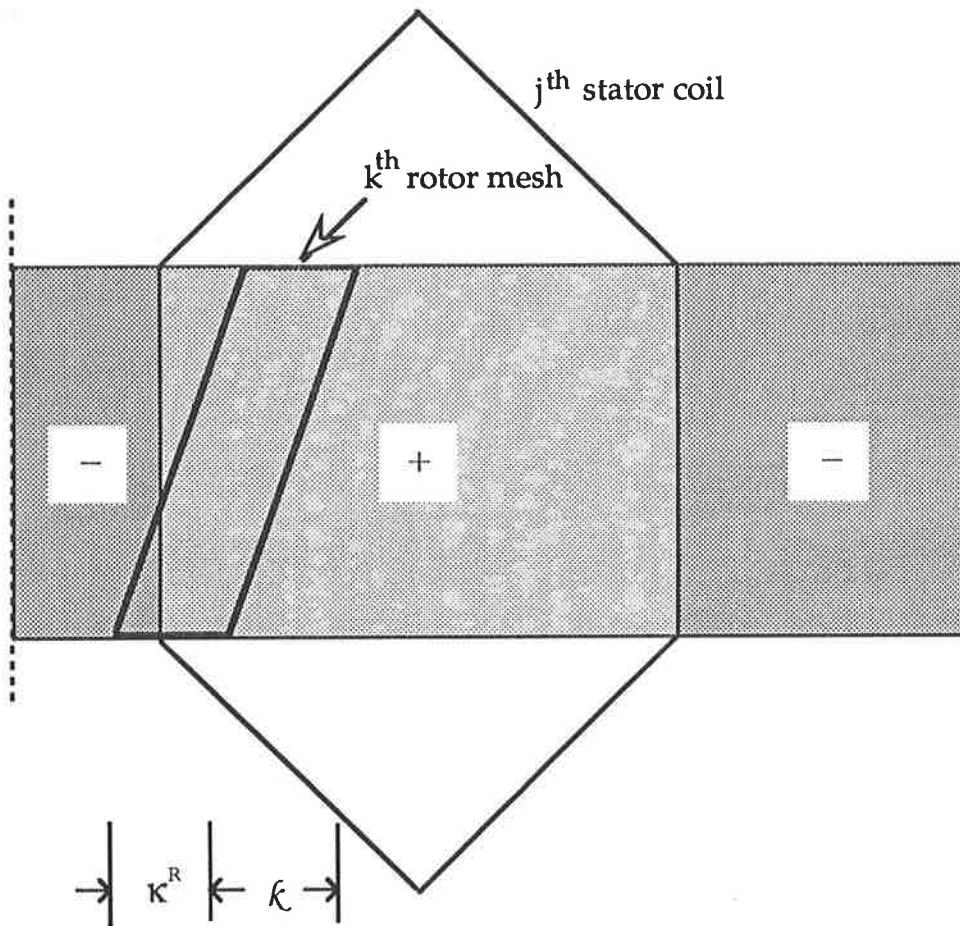


Figure 59

Projected view of a skewed rotor mesh linking with a stator coil  
m.m.f.

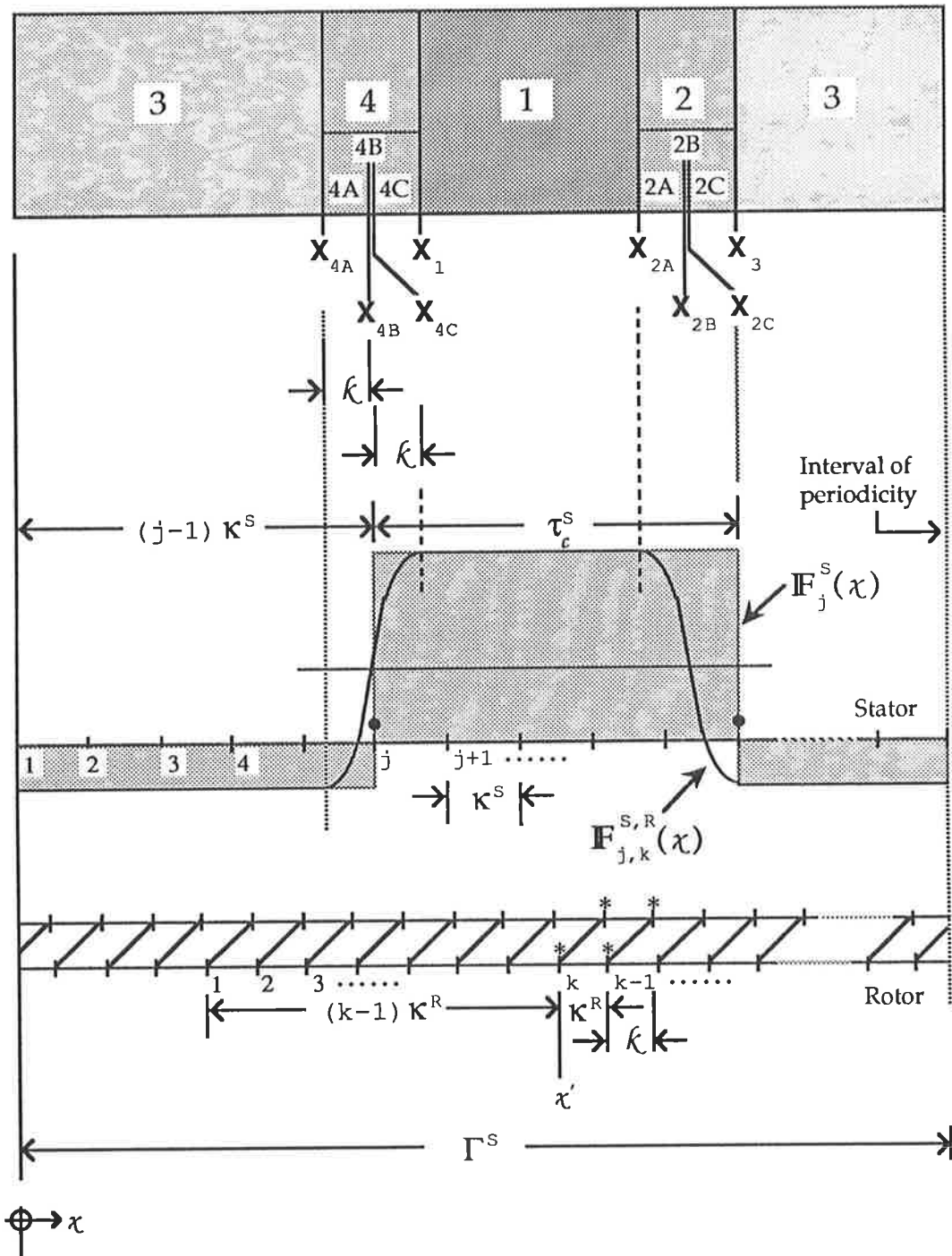


Figure 60

m.m.f. linkage between  $j^{\text{th}}$  stator coil and skewed  $k^{\text{th}}$  rotor mesh



**Case 1**  $\kappa \leq \kappa^R$

If the rotor slot skew is equal to or less than a rotor slot pitch, the following regional m.m.f. expressions apply.

**Region 1**  $X_1 \leq \chi < X_{2A}$

$$\mathbf{F}_{j,k}^{s,R}(\chi) \Big|_{\text{Region 1}} = \alpha \mathbf{F}_j^s \quad (446)$$

**Region 2**  $X_{2A} \leq \chi < X_3$

**Region 2A**  $X_{2A} \leq \chi < X_{2B}$

$$\mathbf{F}_{j,k}^{s,R}(\chi) \Big|_{\text{Region 2A}} = \alpha \mathbf{F}_j^s \left[ 1 - \frac{(\chi - X_{2B} + \kappa)^2}{2 \alpha \kappa^R \kappa} \right] \quad (447)$$

**Region 2B**  $X_{2B} \leq \chi < X_{2C}$

$$\mathbf{F}_{j,k}^{s,R}(\chi) \Big|_{\text{Region 2B}} = \alpha \mathbf{F}_j^s \left[ 1 - \frac{2(\chi - X_{2B}) + \kappa}{2 \alpha \kappa^R} \right] \quad (448)$$

**Region 2C**  $X_{2C} \leq \chi < X_3$

$$\mathbf{F}_{j,k}^{s,R}(\chi) \Big|_{\text{Region 2C}} = \alpha \mathbf{F}_j^s \left[ \frac{\alpha - 1}{\alpha} - \frac{(X_3 - \chi)^2}{2 \alpha \kappa^R \kappa} \right] \quad (449)$$

**Region 3**  $X_3 \leq \chi < X_{4A}$

$$\mathbf{F}_{j,k}^{s,R}(\chi) \Big|_{\text{Region 3}} = -(1 - \alpha) \mathbf{F}_j^s \quad (450)$$

**Region 4**  $X_{4A} \leq \chi < X_{4C} + \Gamma^s$

**Region 4A**  $X_{4A} \leq \chi < X_{4B}$

$$\mathbf{F}_{j,k}^{s,R}(\chi) \Big|_{\text{Region 4A}} = \alpha \mathbf{F}_j^s \left[ \frac{\alpha - 1}{\alpha} + \frac{(\chi - X_{4B} + \kappa)^2}{2 \alpha \kappa^R \kappa} \right] \quad (451)$$

Region 4B  $\mathbf{X}_{4B} \leq \chi < \mathbf{X}_{4C}$

$$\mathbf{F}_{j,k}^{s,R}(\chi) \Big|_{\text{Region 4B}} = \alpha \mathbf{F}_j^s \left[ \frac{\alpha-1}{\alpha} - \frac{2(\chi - \mathbf{X}_{4B}) + \ell}{2\alpha\kappa^R} \right] \quad (452)$$

Region 4C  $\mathbf{X}_{4C} \leq \chi < \mathbf{X}_{4C} + \Gamma^S$

$$\mathbf{F}_{j,k}^{s,R}(\chi) \Big|_{\text{Region 4C}} = \alpha \mathbf{F}_j^s \left[ 1 - \frac{(\mathbf{X}_{4C} - \chi + \ell)^2}{2\alpha\kappa^R\ell} \right] \quad (453)$$

Evidently,  $\Gamma^S$  again constitutes the interval of periodicity, resulting in

$$\mathbf{F}_{j,k}^{s,R}(\chi) = \mathbf{F}_{j,k}^{s,R}(\chi + \Gamma^S) \quad (454)$$

whereas the regional boundaries of Equations (446) to (453) are defined as

$$\mathbf{X}_1 = (j-1)\kappa^S \quad (455)$$

$$\mathbf{X}_{2A} = (j-1)\kappa^S - \kappa^R + \tau_c^S - \ell \quad (456)$$

$$\mathbf{X}_{2B} = (j-1)\kappa^S + \tau_c^S - \kappa^R \quad (457)$$

$$\mathbf{X}_{2C} = (j-1)\kappa^S + \tau_c^S - \ell \quad (458)$$

$$\mathbf{X}_3 = (j-1)\kappa^S + \tau_c^S \quad (459)$$

$$\mathbf{X}_{4A} = (j-1)\kappa^S - \kappa^R + \Gamma^S - \ell \quad (460)$$

$$\mathbf{X}_{4B} = (j-1)\kappa^S - \kappa^R + \Gamma^S \quad (461)$$

$$\mathbf{X}_{4C} = (j-1)\kappa^S + \Gamma^S - \ell \quad (462)$$

**Case 2**  $\ell > \kappa^R$

If the rotor slot skew is larger than a rotor slot pitch, m.m.f. expressions for various regions differ from those developed above as shown below.

**Region 1**  $X_1 \leq \chi < X_{2A}$

$$\mathbf{F}_{j,k}^{S,R}(\chi) \Big|_{\text{Region 1}} = \alpha \mathbf{F}_j^S \quad (463)$$

**Region 2**  $X_{2A} \leq \chi < X_3$

**Region 2A**  $X_{2A} \leq \chi < X_{2B}$

$$\mathbf{F}_{j,k}^{S,R}(\chi) \Big|_{\text{Region 2A}} = \alpha \mathbf{F}_j^S \left[ 1 - \frac{(\chi - X_{2B} + \kappa^R)^2}{2 \alpha \kappa^R \ell} \right] \quad (464)$$

**Region 2B**  $X_{2B} \leq \chi < X_{2C}$

$$\mathbf{F}_{j,k}^{S,R}(\chi) \Big|_{\text{Region 2B}} = \alpha \mathbf{F}_j^S \left[ 1 - \frac{2(\chi - X_{2C} + \ell) - \kappa^R}{2 \alpha \ell} \right] \quad (465)$$

**Region 2C**  $X_{2C} \leq \chi < X_3$

$$\mathbf{F}_{j,k}^{S,R}(\chi) \Big|_{\text{Region 2C}} = \alpha \mathbf{F}_j^S \left[ \frac{\alpha - 1}{\alpha} + \frac{(X_3 - \chi)^2}{2 \alpha \kappa^R \ell} \right] \quad (466)$$

**Region 3**  $X_3 \leq \chi < X_{4A}$

$$\mathbf{F}_{j,k}^{S,R}(\chi) \Big|_{\text{Region 3}} = -(1 - \alpha) \mathbf{F}_j^S \quad (467)$$

**Region 4**  $\mathbf{X}_{4A} \leq \chi < \mathbf{X}_{4C} + \Gamma^S$

**Region 4A**  $\mathbf{X}_{4A} \leq \chi < \mathbf{X}_{4B}$

$$\mathbf{F}_{j,k}^{S,R}(\chi) \Big|_{\text{Region 4A}} = \alpha \mathbf{F}_j^S \left[ 1 - \frac{\left[ 2 \ell \kappa^R - \left\{ \chi - \mathbf{X}_{4B} + \kappa^R \right\} \right]^2}{2 \alpha \kappa^R \ell} \right] \quad (468)$$

**Region 4B**  $\mathbf{X}_{4B} \leq \chi < \mathbf{X}_{4C}$

$$\mathbf{F}_{j,k}^{S,R}(\chi) \Big|_{\text{Region 4B}} = \alpha \mathbf{F}_j^S \left[ 1 + \frac{2(\chi - \mathbf{X}_{4C}) - \kappa^R}{2 \alpha \kappa^R} \right] \quad (469)$$

**Region 4C**  $\mathbf{X}_{4C} \leq \chi < \mathbf{X}_{4C} + \Gamma^S$

$$\mathbf{F}_{j,k}^{S,R}(\chi) \Big|_{\text{Region 4C}} = \alpha \mathbf{F}_j^S \left[ 1 - \frac{(\mathbf{X}_{4C} - \chi + \kappa^R)^2}{2 \alpha \kappa^R \ell} \right] \quad (470)$$

Due to the periodicity of the m.m.f. distribution

$$\mathbf{F}_{j,k}^{S,R}(\chi) = \mathbf{F}_{j,k}^{S,R}(\chi + \Gamma^S) \quad (471)$$

The regional boundaries are given by

$$\mathbf{X}_1 = (j-1)\kappa^S \quad (472)$$

$$\mathbf{X}_{2A} = (j-1)\kappa^S - \kappa^R + \tau_c^S - \ell \quad (473)$$

$$\mathbf{X}_{2B} = (j-1)\kappa^S + \tau_c^S - \ell \quad (474)$$

$$\mathbf{X}_{2C} = (j-1)\kappa^S + \tau_c^S - \kappa^R \quad (475)$$

$$\mathbf{X}_3 = (j-1)\kappa^S + \tau_c^S \quad (476)$$

$$\mathbf{X}_{4A} = (j-1)\kappa^S - \kappa^R + \Gamma^S - \ell \quad (477)$$

$$\mathbf{X}_{4B} = (j-1)\kappa^S + \Gamma^S - \ell \quad (478)$$

$$\mathbf{X}_{4C} = (j-1)\kappa^S + \Gamma^S - \kappa^R \quad (479)$$

The mutual inductance variation within each of the above regions can once again found using the m.m.f. expression for the specific region as

$$L_{\delta,j,k}^{S,R}(\chi, \ell) = 1 \times \frac{\mathbf{F}_{j,k}^{S,R}(\chi, \ell) \Lambda_{\delta,j,k}^{S,R}}{I_j^S} \quad (480)$$

which can also be expressed in terms of a regional permeance coefficient in the form

$$L_{\delta,j,k}^{S,R}(\chi, \ell) = 1 \times N_j^S \mu_0 \ell_c \lambda_{\delta,j,k}^{S,R}(\chi, \ell) \quad (481)$$

Tables 8 and 9 show the expressions for the skew-dependent permeance coefficient,  $\lambda_{\delta,j,k}^{S,R}(\chi, \ell)$ , for each of the regions identified above for the two cases discussed.

**Table 8**

Regional variation of permeance coefficient between  $j^{\text{th}}$  stator coil and skewed  $k^{\text{th}}$  rotor mesh due to relative motion ( $\ell \leq \kappa^R$ )

Region			Mutual Permeance Coefficient	
	from	to		
1	$\mathbf{X}_1$	$\mathbf{X}_{2A}$	$\frac{1}{\delta'} \alpha \kappa^R$	
2	2A	$\mathbf{X}_{2A}$	$\mathbf{X}_{2B}$	$\frac{1}{\delta'} \alpha \kappa^R \left[ 1 - \frac{(\chi - \mathbf{X}_{2B} + \ell)^2}{2 \alpha \kappa^R \ell} \right]$
	2B	$\mathbf{X}_{2B}$	$\mathbf{X}_{2C}$	$\frac{1}{\delta'} \alpha \kappa^R \left[ 1 - \frac{2(\chi - \mathbf{X}_{2B}) + \ell}{2 \alpha \kappa^R} \right]$
	2C	$\mathbf{X}_{2C}$	$\mathbf{X}_3$	$\frac{1}{\delta'} \alpha \kappa^R \left[ \frac{\alpha - 1}{\alpha} - \frac{(\mathbf{X}_3 - \chi)^2}{2 \alpha \kappa^R \ell} \right]$
3	$\mathbf{X}_3$	$\mathbf{X}_{4A}$	$-\frac{1}{\delta'} (1 - \alpha) \kappa^R$	
4	4A	$\mathbf{X}_{4A}$	$\mathbf{X}_{4B}$	$\frac{1}{\delta'} \alpha \kappa^R \left[ \frac{\alpha - 1}{\alpha} + \frac{(\chi - \mathbf{X}_{4B} + \ell)^2}{2 \alpha \kappa^R \ell} \right]$
	4B	$\mathbf{X}_{4B}$	$\mathbf{X}_{4C}$	$\frac{1}{\delta'} \alpha \kappa^R \left[ \frac{\alpha - 1}{\alpha} - \frac{2(\chi - \mathbf{X}_{4B}) + \ell}{2 \alpha \kappa^R} \right]$
	4C	$\mathbf{X}_{4C}$	$\mathbf{X}_3$	$\frac{1}{\delta'} \alpha \kappa^R \left[ 1 - \frac{(\mathbf{X}_{4C} - \chi + \ell)^2}{2 \alpha \kappa^R \ell} \right]$

**Table 9**

Regional variation of permeance coefficient between  $j^{\text{th}}$  stator coil and skewed  $k^{\text{th}}$  rotor mesh due to relative motion ( $\ell > \kappa^R$ )

Region			Mutual Permeance Coefficient	
	from	to		
1	$\mathbf{X}_1$	$\mathbf{X}_{2A}$	$\frac{1}{\delta'} \alpha \kappa^R$	
2	2A	$\mathbf{X}_{2A}$	$\mathbf{X}_{2B}$	$\frac{1}{\delta'} \alpha \kappa^R \left[ 1 - \frac{(\chi + \kappa^R - \mathbf{X}_{2B})^2}{2 \alpha \kappa^R \ell} \right]$
	2B	$\mathbf{X}_{2B}$	$\mathbf{X}_{2C}$	$\frac{1}{\delta'} \alpha \kappa^R \left[ 1 - \frac{2(\chi + \ell - \mathbf{X}_{2C}) - \kappa^R}{2 \alpha \kappa^R} \right]$
	2C	$\mathbf{X}_{2C}$	$\mathbf{X}_3$	$\frac{1}{\delta'} \alpha \kappa^R \left[ \frac{\alpha - 1}{\alpha} + \frac{(\mathbf{X}_3 - \chi)^2}{2 \alpha \kappa^R \ell} \right]$
3	$\mathbf{X}_3$	$\mathbf{X}_{4A}$	$-\frac{1}{\delta'} (1 - \alpha) \kappa^R$	
4	4A	$\mathbf{X}_{4A}$	$\mathbf{X}_{4B}$	$\frac{1}{\delta'} \alpha \kappa^R \left[ 1 - \frac{2\kappa^R - (\chi - \mathbf{X}_{4B} + \kappa^R)^2}{2 \alpha \kappa^R \ell} \right]$
	4B	$\mathbf{X}_{4B}$	$\mathbf{X}_{4C}$	$\frac{1}{\delta'} \alpha \kappa^R \left[ 1 + \frac{2(\chi - \mathbf{X}_{4C}) - \kappa^R}{2 \alpha \ell} \right]$
	4C	$\mathbf{X}_{4C}$	$\mathbf{X}_3$	$\frac{1}{\delta'} \alpha \kappa^R \left[ 1 - \frac{(\mathbf{X}_{4C} - \chi + \kappa^R)^2}{2 \alpha \kappa^R \ell} \right]$

#### 4.4 Terminal Voltage Equations

The circuit model parameters obtained thus far can now be used to obtain the machine terminal voltage equations based on

$$[\mathbf{u}(t)] = [\mathbf{z}(\chi, t)] [\mathbf{i}(t)] \quad (482)$$

Figure 61 conceptualises the corresponding discrete circuit model for an induction machine with a double layer winding in the stator and a single cage in the rotor. The circuit parameters are representative of the entire discrete circuit, but are shown distributed over the sides of their respective circuit for simplicity. It must be emphasised that the inductive parameters account, not only for self inductances, but also for mutual inductances with all other circuits within the machine. For generality, each stator coil constituting a circuit is shown as having its own supply. The terminal voltage equation for the  $j^{\text{th}}$  stator coil can thus be written as

$$\mathbf{u}_j^S = \mathbf{R}_j^S \mathbf{i}_j^S + p \sum_{\bar{l}=1}^m L_{j,\bar{l}}^S \mathbf{i}_{\bar{l}}^S + p \sum_{\bar{\omega}=1}^n L_{j,\bar{\omega}}^{S,R} \mathbf{i}_{\bar{\omega}}^R \quad (483)$$

Similarly, the terminal voltage equation for the  $k^{\text{th}}$  rotor mesh becomes

$$\mathbf{u}_k^R = \mathbf{R}_k^R \mathbf{i}_k^R + p \sum_{\bar{\omega}=1}^n L_{\delta,k,\bar{\omega}}^R \mathbf{i}_{\bar{\omega}}^R + p \sum_{\bar{l}=1}^m L_{\delta,j,\bar{l}}^{R,S} \mathbf{i}_{\bar{l}}^S \quad (484)$$

Evidently

$$j \in \{m\} \quad (485)$$

$$k \in \{n\} \quad (486)$$



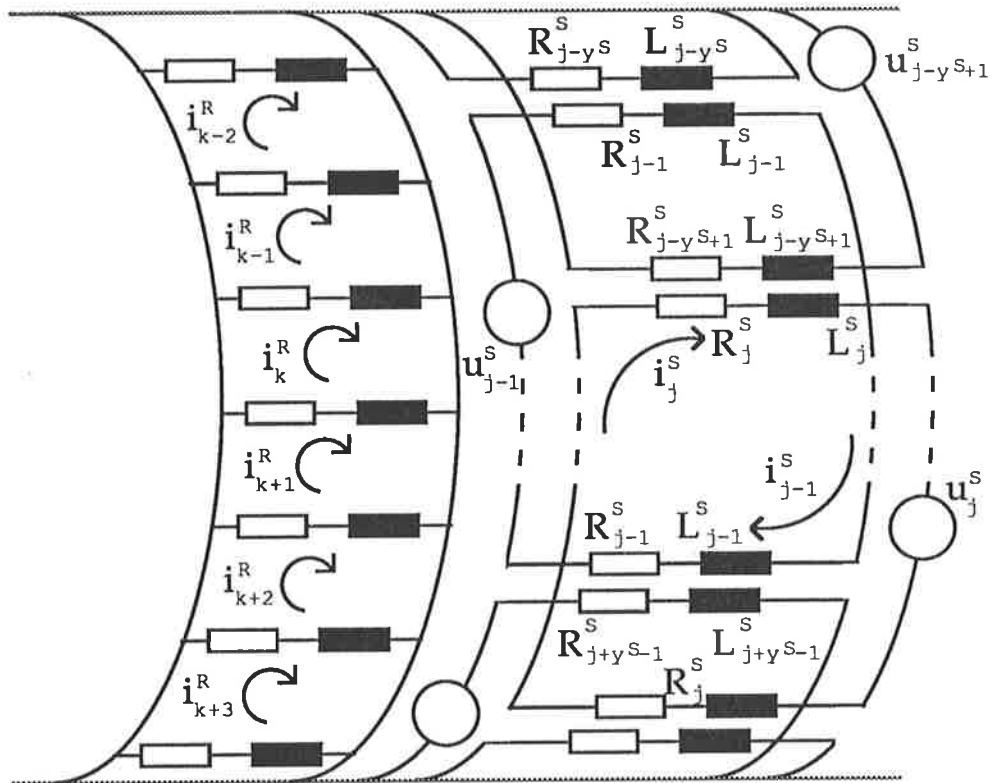


Figure 61

Conceptual discrete circuit model for an induction machine with a double layer stator winding and a single cage rotor

Equations (483) and (484) can be extended to all other stator and rotor circuits. The resulting terminal voltage equations can generally be represented in matrix notation as

$$[\mathbf{u}^S] = [\mathbf{R}^S][\mathbf{i}^S] + [\mathbf{L}^S] p[\mathbf{i}^S] + p[\mathbf{L}^S][\mathbf{i}^S] + [\mathbf{L}^{S,R}] p[\mathbf{i}^R] + p[\mathbf{L}^{S,R}][\mathbf{i}^R] \quad (487)$$

$$[\mathbf{u}^R] = [\mathbf{L}^{R,S}] p[\mathbf{i}^S] + p[\mathbf{L}^{R,S}][\mathbf{i}^S] + [\mathbf{R}^R][\mathbf{i}^R] + [\mathbf{L}^R] p[\mathbf{i}^R] + p[\mathbf{L}^R][\mathbf{i}^R] \quad (488)$$

where

$$[\mathbf{L}^{R,S}] = [\mathbf{L}^{S,R}]^T \quad (489)$$

or

$$[\mathbf{u}^S] = [\mathbf{R}^S + \mathbf{L}^S p + p\mathbf{L}^S][\mathbf{i}^S] + [\mathbf{L}^{S,R} p + p\mathbf{L}^{S,R}][\mathbf{i}^R] \quad (490)$$

$$[\mathbf{u}^R] = [\mathbf{L}^{R,S} p + p\mathbf{L}^{R,S}][\mathbf{i}^S] + [\mathbf{R}^R + \mathbf{L}^R p + p\mathbf{L}^R][\mathbf{i}^R] \quad (491)$$

Equations (487) to (491) allow for the variation of self inductance as a function of the relative position between the stator and the rotor, as would be the case with slotted airgap boundaries. If the assumption of smooth airgap boundaries is justifiable, as indicated by the adoption of a modified airgap distance a la Carter, Equations (490) and (491) simplify to

$$[\mathbf{u}^S] = [\mathbf{R}^S + \mathbf{L}^S p][\mathbf{i}^S] + [\mathbf{L}^{S,R} p + p\mathbf{L}^{S,R}][\mathbf{i}^R] \quad (492)$$

$$[\mathbf{u}^R] = [\mathbf{L}^{R,S} p + p\mathbf{L}^{R,S}][\mathbf{i}^S] + [\mathbf{R}^R + \mathbf{L}^R p][\mathbf{i}^R] \quad (493)$$

In terms of Laplace transforms with zero initial conditions, Equations (492) and (493) become

$$[\mathbf{u}^S(s)] = [\mathbf{R}^S + s\mathbf{L}^S] [\mathbf{i}^S(s)] + [s\mathbf{L}^{S,R} + \omega \frac{\partial \mathbf{L}^{S,R}}{\partial \theta}] [\mathbf{i}^R(s)] \quad (494)$$

$$[\mathbf{u}^R(s)] = [s\mathbf{L}^{R,S} + \omega \frac{\partial \mathbf{L}^{R,S}}{\partial \theta}] [\mathbf{i}^S(s)] + [\mathbf{R}^R + s\mathbf{L}^R] [\mathbf{i}^R(s)] \quad (495)$$

This latter form is convenient in analysing the constant speed behaviour of the machine.

Alternatively, Equations (487) and (488) can be written in state variable form as

$$p \begin{bmatrix} [\mathbf{L}^S] & [\mathbf{L}^{S,R}] \\ [\mathbf{L}^{S,R}]^T & [\mathbf{L}^R] \end{bmatrix} \begin{bmatrix} [\mathbf{i}^S] \\ [\mathbf{i}^R] \end{bmatrix} = \begin{bmatrix} [\mathbf{u}^S] \\ [\mathbf{u}^R] \end{bmatrix} - \begin{bmatrix} [\mathbf{R}^S] & 0 \\ 0 & [\mathbf{R}^R] \end{bmatrix} \begin{bmatrix} [\mathbf{i}^S] \\ [\mathbf{i}^R] \end{bmatrix} \quad (496)$$

The state variable formulation has computational advantages when numerical integration techniques are employed in obtaining time variant solutions for the currents.

In above equations, voltages and currents for the stator and the rotor are given by column matrices as

$$[\mathbf{u}^S] = \begin{bmatrix} u_1^S \\ u_2^S \\ u_3^S \\ \dots \\ \dots \\ u_j^S \\ \dots \\ \dots \\ u_m^S \end{bmatrix} \quad [\mathbf{i}^S] = \begin{bmatrix} i_1^S \\ i_2^S \\ i_3^S \\ \dots \\ \dots \\ i_j^S \\ \dots \\ \dots \\ i_m^S \end{bmatrix} \quad (497)$$

$$[\mathbf{u}^R] = \begin{bmatrix} u_1^R \\ u_2^R \\ u_3^R \\ \dots \\ \dots \\ u_k^R \\ \dots \\ \dots \\ u_n^R \end{bmatrix} \quad [\mathbf{i}^R] = \begin{bmatrix} i_1^R \\ i_2^R \\ i_3^R \\ \dots \\ \dots \\ i_k^R \\ \dots \\ \dots \\ i_n^R \end{bmatrix} \quad (498)$$

The above equations constitute the most general form of voltages and currents for the machine. If, however, several coils are connected in series to form a coil group, as is normally the case, the same current flows in all coils within the group. In this case, the use of a *connection matrix* becomes necessary as demonstrated later in Section 5.2.

For a singly excited induction machine, the rotor voltage matrix becomes a *null matrix*.

The stator resistance matrix  $[R^S]$  is a diagonal matrix, as illustrated conceptually in Figure 62 for a winding with 18 identical coils. The same applies for a wound rotor. In the case of a cage rotor, however, the principal diagonal contains the total mesh resistances, whereas the matrix elements on both sides of the principal diagonal and at both corners of the secondary diagonal represent the shared branch resistances between contiguous meshes. With the current flow convention adopted in Figure 61, these resistances appear with a negative sign. All other matrix elements are zero. Figure 63 illustrates this for a single cage with 22 rotor bars.

The inductance matrices  $[L^S]$  and  $[L^R]$  are to be obtained according to Section 4.3.5 as

$$[L^S] = \begin{pmatrix} L_{1,1}^S & L_{1,2}^S & L_{1,3}^S & \dots & L_{1,m-1}^S & L_{1,m}^S \\ L_{2,1}^S & L_{2,2}^S & L_{2,3}^S & \dots & L_{2,m-1}^S & L_{2,m}^S \\ L_{3,1}^S & L_{3,2}^S & L_{3,3}^S & \dots & L_{3,m-1}^S & L_{3,m}^S \\ \dots & \dots & \dots & \dots & \dots & \dots \\ \dots & \dots & \dots & \dots & \dots & \dots \\ L_{j,1}^S & L_{j,2}^S & L_{j,3}^S & \dots & L_{j,m-1}^S & L_{j,m}^S \\ \dots & \dots & \dots & \dots & \dots & \dots \\ \dots & \dots & \dots & \dots & \dots & \dots \\ L_{m,1}^S & L_{m,2}^S & L_{m,3}^S & \dots & L_{m,m-1}^S & L_{m,m}^S \end{pmatrix} \quad (499)$$

and

$$\mathbf{[L^R]} = \begin{pmatrix} L_{1,1}^R & L_{1,2}^R & L_{1,3}^R & \dots & L_{1,n-1}^R & L_{1,n}^R \\ L_{2,1}^R & L_{2,2}^R & L_{2,3}^R & \dots & L_{2,n-1}^R & L_{2,n}^R \\ L_{3,1}^R & L_{3,2}^R & L_{3,3}^R & \dots & L_{1,n-1}^R & L_{3,n}^R \\ \dots & \dots & \dots & \dots & \dots & \dots \\ \dots & \dots & \dots & \dots & \dots & \dots \\ L_{k,1}^R & L_{k,2}^R & L_{k,3}^R & \dots & L_{1,n-1}^R & L_{k,n}^R \\ \dots & \dots & \dots & \dots & \dots & \dots \\ \dots & \dots & \dots & \dots & \dots & \dots \\ L_{n,1}^R & L_{n,2}^R & L_{n,3}^R & \dots & L_{1,n-1}^R & L_{n,n}^R \end{pmatrix} \quad (500)$$

Mutual inductances between the stator and the rotor are given by an  $m \times n$  matrix as explained previously, viz.

$$\mathbf{[L^{SR}]} = \begin{pmatrix} L_{1,1}^{S,R} & L_{1,2}^{S,R} & L_{1,3}^{S,R} & \dots & L_{1,k}^{S,R} & \dots & L_{1,n-1}^{S,R} & L_{1,n}^{S,R} \\ L_{2,1}^{S,R} & L_{2,2}^{S,R} & L_{2,3}^{S,R} & \dots & L_{2,k}^{S,R} & \dots & L_{2,n-1}^{S,R} & L_{2,n}^{S,R} \\ L_{3,1}^{S,R} & L_{3,2}^{S,R} & L_{3,3}^{S,R} & \dots & L_{3,k}^{S,R} & \dots & L_{3,n-1}^{S,R} & L_{3,n}^{S,R} \\ \dots & \dots & \dots & \dots & \dots & \dots & \dots & \dots \\ \dots & \dots & \dots & \dots & \dots & \dots & \dots & \dots \\ L_{j,1}^{S,R} & L_{j,2}^{S,R} & L_{j,3}^{S,R} & \dots & L_{j,k}^{S,R} & \dots & L_{j,n-1}^{S,R} & L_{j,n}^{S,R} \\ \dots & \dots & \dots & \dots & \dots & \dots & \dots & \dots \\ \dots & \dots & \dots & \dots & \dots & \dots & \dots & \dots \\ L_{m,1}^R & L_{m,2}^R & L_{m,3}^R & \dots & L_{m,k}^{S,R} & \dots & L_{m,n-1}^R & L_{m,n}^R \end{pmatrix} \quad (501)$$

where the matrix elements are defined by Equations (432) or (445) for a wound rotor induction machine or a cage induction machine respectively.

	1	2	3	4	5	6	7	8	9	10	11	12	13	14	15	16	17	18
1	◆	0	0	0	0	0	0	0	0	0	0	0	0	0	0	0	0	0
2	0	◆	0	0	0	0	0	0	0	0	0	0	0	0	0	0	0	0
3	0	0	◆	0	0	0	0	0	0	0	0	0	0	0	0	0	0	0
4	0	0	0	◆	0	0	0	0	0	0	0	0	0	0	0	0	0	0
5	0	0	0	0	◆	0	0	0	0	0	0	0	0	0	0	0	0	0
6	0	0	0	0	0	◆	0	0	0	0	0	0	0	0	0	0	0	0
7	0	0	0	0	0	0	◆	0	0	0	0	0	0	0	0	0	0	0
8	0	0	0	0	0	0	0	◆	0	0	0	0	0	0	0	0	0	0
9	0	0	0	0	0	0	0	0	◆	0	0	0	0	0	0	0	0	0
10	0	0	0	0	0	0	0	0	0	◆	0	0	0	0	0	0	0	0
11	0	0	0	0	0	0	0	0	0	0	◆	0	0	0	0	0	0	0
12	0	0	0	0	0	0	0	0	0	0	0	◆	0	0	0	0	0	0
13	0	0	0	0	0	0	0	0	0	0	0	0	◆	0	0	0	0	0
14	0	0	0	0	0	0	0	0	0	0	0	0	0	◆	0	0	0	0
15	0	0	0	0	0	0	0	0	0	0	0	0	0	0	◆	0	0	0
16	0	0	0	0	0	0	0	0	0	0	0	0	0	0	0	◆	0	0
17	0	0	0	0	0	0	0	0	0	0	0	0	0	0	0	0	◆	0
18	0	0	0	0	0	0	0	0	0	0	0	0	0	0	0	0	0	◆

Figure 62

Conceptual resistance matrix for a stator winding with 18 identical coils

	1	2	3	4	5	6	7	8	9	10	11	12	13	14	15	16	17	18	19	20	21	22	
1	*	+	0	0	0	0	0	0	0	0	0	0	0	0	0	0	0	0	0	0	0	0	+
2	+	*	+	0	0	0	0	0	0	0	0	0	0	0	0	0	0	0	0	0	0	0	0
3	0	+	*	+	0	0	0	0	0	0	0	0	0	0	0	0	0	0	0	0	0	0	0
4	0	0	+	*	+	0	0	0	0	0	0	0	0	0	0	0	0	0	0	0	0	0	0
5	0	0	0	+	*	+	0	0	0	0	0	0	0	0	0	0	0	0	0	0	0	0	0
6	0	0	0	0	+	*	+	0	0	0	0	0	0	0	0	0	0	0	0	0	0	0	0
7	0	0	0	0	0	+	*	+	0	0	0	0	0	0	0	0	0	0	0	0	0	0	0
8	0	0	0	0	0	0	+	*	+	0	0	0	0	0	0	0	0	0	0	0	0	0	0
9	0	0	0	0	0	0	0	+	*	+	0	0	0	0	0	0	0	0	0	0	0	0	0
10	0	0	0	0	0	0	0	0	+	*	+	0	0	0	0	0	0	0	0	0	0	0	0
11	0	0	0	0	0	0	0	0	0	+	*	+	0	0	0	0	0	0	0	0	0	0	0
12	0	0	0	0	0	0	0	0	0	0	+	*	+	0	0	0	0	0	0	0	0	0	0
13	0	0	0	0	0	0	0	0	0	0	0	+	*	+	0	0	0	0	0	0	0	0	0
14	0	0	0	0	0	0	0	0	0	0	0	0	+	*	+	0	0	0	0	0	0	0	0
15	0	0	0	0	0	0	0	0	0	0	0	0	0	+	*	+	0	0	0	0	0	0	0
16	0	0	0	0	0	0	0	0	0	0	0	0	0	0	+	*	+	0	0	0	0	0	0
17	0	0	0	0	0	0	0	0	0	0	0	0	0	0	0	+	*	+	0	0	0	0	0
18	0	0	0	0	0	0	0	0	0	0	0	0	0	0	0	0	+	*	+	0	0	0	0
19	0	0	0	0	0	0	0	0	0	0	0	0	0	0	0	0	0	+	*	+	0	0	0
20	0	0	0	0	0	0	0	0	0	0	0	0	0	0	0	0	0	0	+	*	+	0	0
21	0	0	0	0	0	0	0	0	0	0	0	0	0	0	0	0	0	0	0	+	*	+	0
22	+	0	0	0	0	0	0	0	0	0	0	0	0	0	0	0	0	0	0	0	0	+	*

Figure 63

Conceptual resistance matrix for a cage rotor with 22 bars



## 4.5 Torque Equation

A generally applicable torque equation for an induction machine with  $m$  stator coils and  $n$  rotor circuits can be developed from the consideration of energy balance and the principle of virtual work [133]. In differential form, the energy balance equation can be expressed as

$$dE_{mech} = dE_{elec} - dE_{magn} - dE_{loss} \quad (502)$$

where

$$dE_{mech} = T d\phi \quad (503)$$

The electric energy term on the right hand side of Equation (502) can be found from

$$dE_{elec} = dE_{elec}^S + dE_{elec}^R \quad (504)$$

where the sub-terms  $dE_{elec}^S$  and  $dE_{elec}^R$ , for the stator and the rotor respectively, are obtained as

$$dE_{elec}^S = \sum_{j=1}^m u_j^S i_j^S dt \quad (505)$$

$$dE_{elec}^R = \sum_{k=1}^n u_k^R i_k^R dt \quad (506)$$

$u_j^S$  and  $u_k^R$  are as given by Equations (483) and (484) previously. Substituting these into Equations (505) and (506) and rearranging yields the electric energy differential sub-terms as

$$dE_{elec}^S = \sum_{j=1}^m \sum_{k=1}^n \left( R_j^S i_j^S dt + L_{j,j}^S i_j^S di_j^S + i_j^S dL_{j,j}^S + L_{j,k}^{S,R} i_j^S di_k^R + i_j^S i_k^R L_{j,k}^{S,R} \right) \quad (507)$$

and

$$dE_{elec}^R = \sum_{k=1}^n \sum_{j=1}^m \left( R_k^R i_k^R dt + L_{k,k}^R i_k^R di_k^R + i_k^R dL_{k,k}^R + L_{k,j}^{R,S} i_k^R di_j^S + i_k^R i_j^S L_{k,j}^{R,S} \right) \quad (508)$$

Equation (504) can also be expressed in matrix form, as

$$dE_{elec} = [\mathbf{i}]^T [\mathbf{u}] dt \quad (509)$$

in which case the voltage and current matrices  $[\mathbf{u}]$  and  $[\mathbf{i}]$  are given by

$$[\mathbf{u}] = \begin{bmatrix} [\mathbf{u}^S] \\ [\mathbf{u}^R] \end{bmatrix} \quad [\mathbf{i}] = \begin{bmatrix} [\mathbf{i}^S] \\ [\mathbf{i}^R] \end{bmatrix} \quad (510)$$

The sub-matrices in Equation (510) are defined by Equations (497) and (498) respectively.

The differential magnetic energy term, on the other hand, can be obtained generally as

$$dE_{magn} = i d\Psi \quad (511)$$

If the assumption of a linear core is justifiable, the expression becomes

$$dE_{magn} = \frac{1}{2} (i d\Psi + \Psi di) \quad (512)$$

Regionalising the differential magnetic energy term as

$$dE_{magn} = dE_{magn}^S + dE_{magn}^R \quad (513)$$

the sub-terms for a stator with  $m$  coils and for a rotor with  $n$  circuits can be given as

$$dE_{magn}^S =$$

$$\frac{1}{2} \sum_{j=1}^m \sum_{k=1}^n \left( 2L_{j,j}^S i_j^S di_j^S + i_j^{S^2} dL_{j,j}^S + L_{j,k}^{S,R} i_j^S di_k^R + L_{j,k}^{S,R} i_k^R di_j^S + i_j^S i_k^R dL_{j,k}^{S,R} \right)$$

$$(514)$$

and

$$dE_{magn}^R = \frac{1}{2} \sum_{k=1}^n \sum_{j=1}^m \left( 2L_{k,k}^R i_k^R di_k^R + i_k^{R^2} dL_{k,k}^R + L_{k,j}^{R,S} i_k^R di_j^S + L_{k,j}^{R,S} i_j^R di_k^S + i_k^R i_j^S dL_{k,j}^{R,S} \right) \quad (515)$$

The magnetic energy term can alternatively be expressed in matrix form as

$$E_{magn} = \frac{1}{2} [\mathbf{i}]^T [\mathbf{L}] [\mathbf{i}] \quad (516)$$

Substituting Equations (503), (504) and (513) into Equation (502) under consideration of the sub-terms as defined above yields

$$T d\phi = \frac{1}{2} \sum_{j=1}^m \sum_{k=1}^n \left( i_j^{S^2} dL_{j,j}^S + i_k^{R^2} dL_{k,k}^S + i_j^S i_k^R dL_{j,k}^{S,R} \right) \quad (517)$$

from which the electromagnetically produced torque can be extracted.

Evidently, if the assumption of a constant airgap distance is justifiable, Equation (517) reduces to

$$T d\phi = \frac{1}{2} \sum_{j=1}^m \sum_{k=1}^n i_j^S i_k^R dL_{j,k}^{S,R} \quad (518)$$

since

$$\frac{dL_{j,j}^S}{d\phi} = 0 \quad \frac{dL_{k,k}^R}{d\phi} = 0 \quad (519)$$

Thus, the torque produced is given by

$$T = \frac{1}{2} \sum_{j=1}^m \sum_{k=1}^n i_j^S i_k^R \frac{dL_{j,k}^{S,R}}{d\phi} \quad (520)$$

This electromagnetically produced torque can also be expressed in matrix form as

$$T = \frac{1}{2} [i]^T \frac{\partial}{\partial \phi} [L_{j,k}^{S,R}] [i] \quad (521)$$

The complete torque equation can now be written as

$$T = T_L + J \frac{d\omega}{dt} + D\omega + K\phi \quad (522)$$

Equation (522) represents a torque balance equation, where the torque produced,  $T$ , is shown to counteract the load torque  $T_L$  along with the inertial torque and damping torque. The last term on the right hand side of Equation (522) is included to describe the effect of torsional shaft deflection in long shafts with low stiffness.  $K$  is the torsional deflection constant;  $\phi$  represents the angular shaft displacement. In most cases, this term can be safely neglected since short shaft ends with high stiffness are prevalent in induction machine practice.

Equation (522) is generally applicable regardless of the mode of operation of an induction machine, provided the sense of each torque element is accounted for correctly.

#### 4.6 Model Utility

The discrete circuit modelling approach yields a potent tool in the *a priori* analysis of induction machine behaviour. The model utility is high in evaluating the performance of an induction machine generally, including both transient and steady state regimes. The model is sensitive to parameter variations; an indispensable feature for realistic modelling. Applications extend from the analysis of perfectly healthy conventional machines to that of machines with unusual topologies or with faults. These arguably constitute major strengths for the discrete circuit modelling approach since conventional models are void of such capabilities. Evidently computational effort is more extensive than that expected for lumped parameter circuit models. However, if aspects mentioned here are significant and important, the advantages offered by discrete circuit models far outweigh the consequential computational effort. The strengths of discrete circuit models are to be demonstrated in the following chapter.

# 5

## MODEL VERIFICATION

### 5.1 Introduction

The main object of this thesis is dynamic modelling of induction machines; yet, substantial effort has been expended in Chapter 2 on steady-state models. The attention is justified because the basis for the determination of model parameters is common to both the dynamic models and steady-state models. This chapter will demonstrate this commonality by bringing together the two classes of model, namely *lumped parameter circuit models* based on Chapter 2 and *discrete circuit models* based on Chapter 4. The former are particularly popular in the design offices of electrical machine manufacturers; this provides the additional incentive for seizing the opportunity to demonstrate the effectiveness of *high fidelity models in a priori* performance prediction. The main part that follows will systematically validate the discrete circuit modelling approach by exemplifying the various possible uses of such models. Experimental results are presented to verify both modelling approaches.

## 5.2 Test Results

### 5.2.1 Test Results - Machine I

A series of tests was conducted on a commercial machine, here designated **Machine I**, for the purpose of validating the high fidelity modelling approach solicited in Chapter 2 of this thesis. The tests included no-load and load tests as well as the measurement of the complete quasi-dynamic torque-speed characteristic in the first quadrant. The name plate details of the machine are supplied in Appendix A.2, Section A.2.1. The following is an overview of the salient test results.

Table 10 gives the test results for three different operating conditions: rated load, no-load and blocked rotor. It should be noted that the blocked rotor test was conducted at reduced voltage and wye-connection. Figure 64 shows the magnetisation characteristic. Figure 65 illustrates the segregation of mechanical losses from core losses; curve fitting was effected using a fifth order polynomial. Both Figure 64 and Figure 65 were obtained with the machine operating as a motor, which should explain the relative increase in the no-load current, accompanying the decrease in the terminal voltage. In Figure 65, the voltage axis is quadratic in an attempt to increase the accuracy in determining the mechanical losses by extrapolation.

Figures 66 to 68 show the variation of line current, efficiency and power factor as a function of shaft load. A spline is fitted in each case to the early part of the characteristic to indicate the trend of the characteristic.

Figure 69 delineates the torque-speed characteristic in the first quadrant. A spline is fitted to the region between 1600-3000 rpm to emphasise the trend.



The characteristic was obtained by extrapolation from measurements made at the reduced line-to-line voltage of 220V and with wye-connection. This was necessitated due to the limitations of the test facilities. All other tests were done at rated voltage.

Of considerable interest is the low speed region, characterised by the presence of substantial parasitic torques. As will be shown, it is impossible to predict the nature and the magnitude of such parasitic behaviour if conventional low order circuit models, such as the "exact"-equivalent circuit, are employed for design .

Figure 69 also depicts additional measurements within the parasitic torque region. These measurements were made with delta-connected windings at a reduced line-to-line voltage of 128V which gives the same airgap flux as for the wye-connection; the object was to assess the effect of winding connections on the production of parasitic torques. These additional measurements reveal that the parasitic torque formation is by no means insensitive to the winding connection, as is well known from the literature [133, 134, 135, 136].

**Table 10**

Test results for Machine I

	U (V)	f (Hz)	I (A)	P <sub>in</sub> (W)	cosφ	T (Nm)	n (rpm)	P <sub>out</sub> (W)	χ (%)
Rated Load	380	50	251	152220	0.922	451	2970	140300	92.2
No-Load	380	50	47.8	5120	0.103	0	~3000	0	0
Blocked Rotor	220	50	342	40150	0.309	451	0	0	0

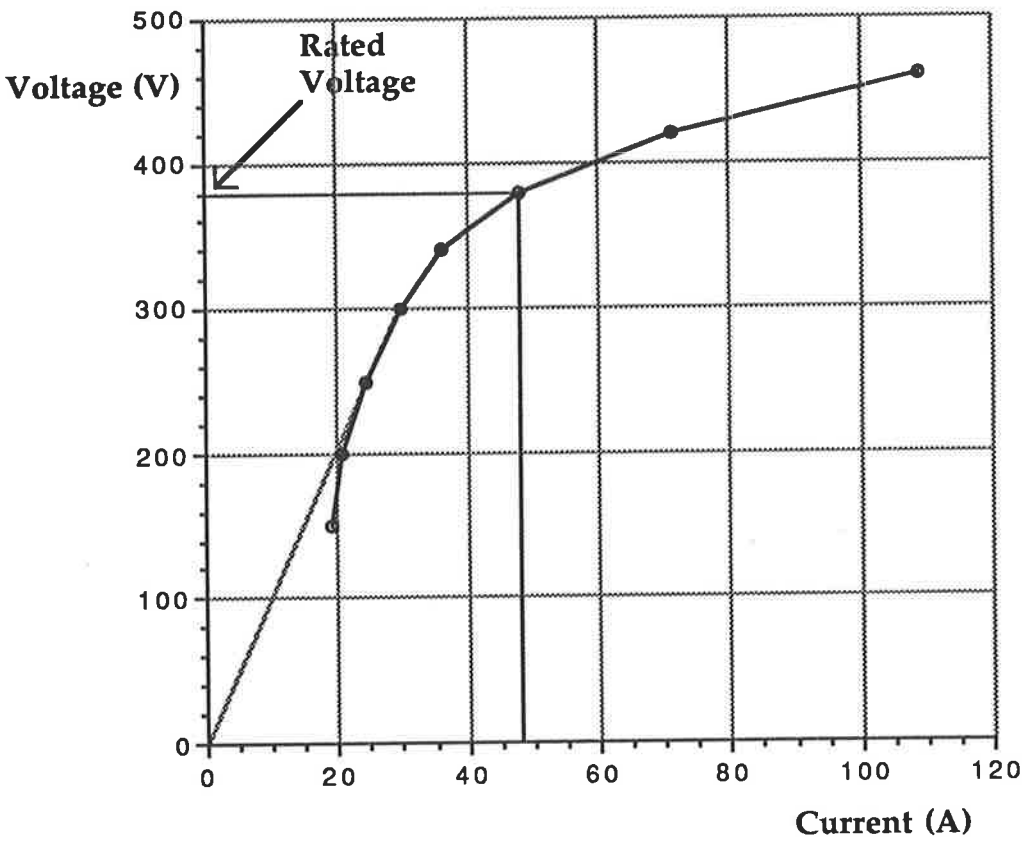


Figure 64  
Magnetisation characteristic of Machine I  
(measured)

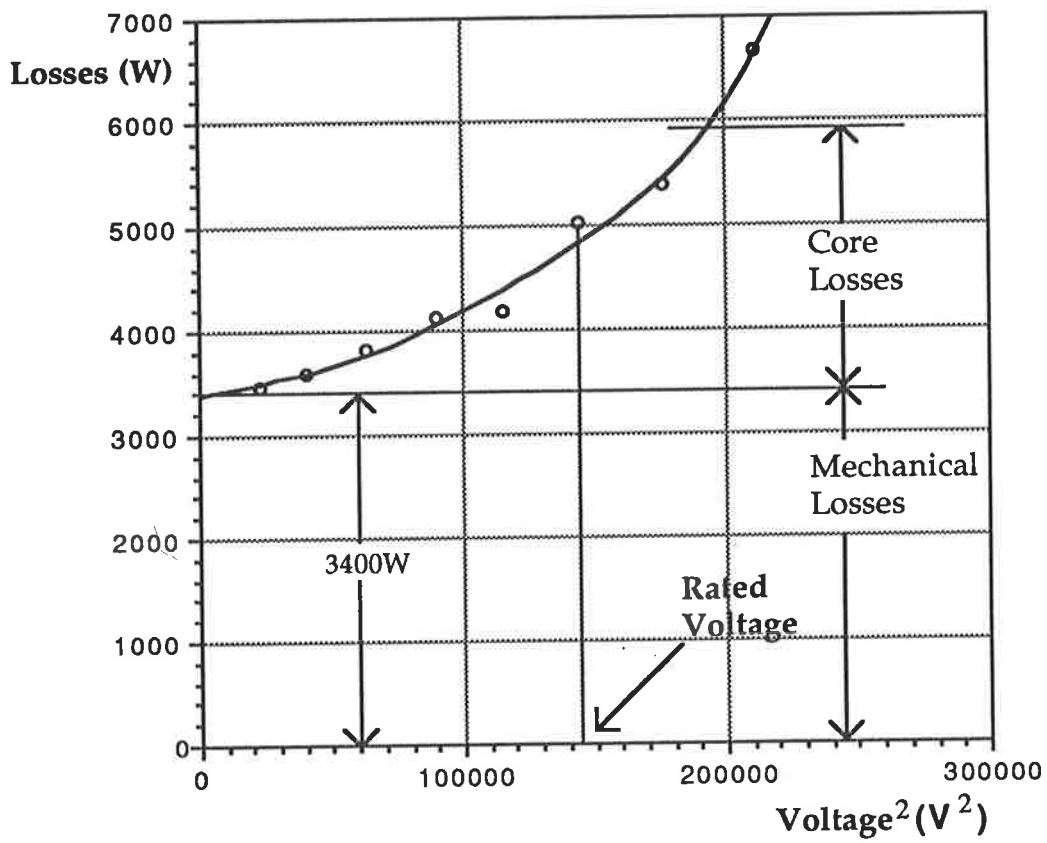


Figure 65

Mechanical losses and core losses for Machine I  
(measured)

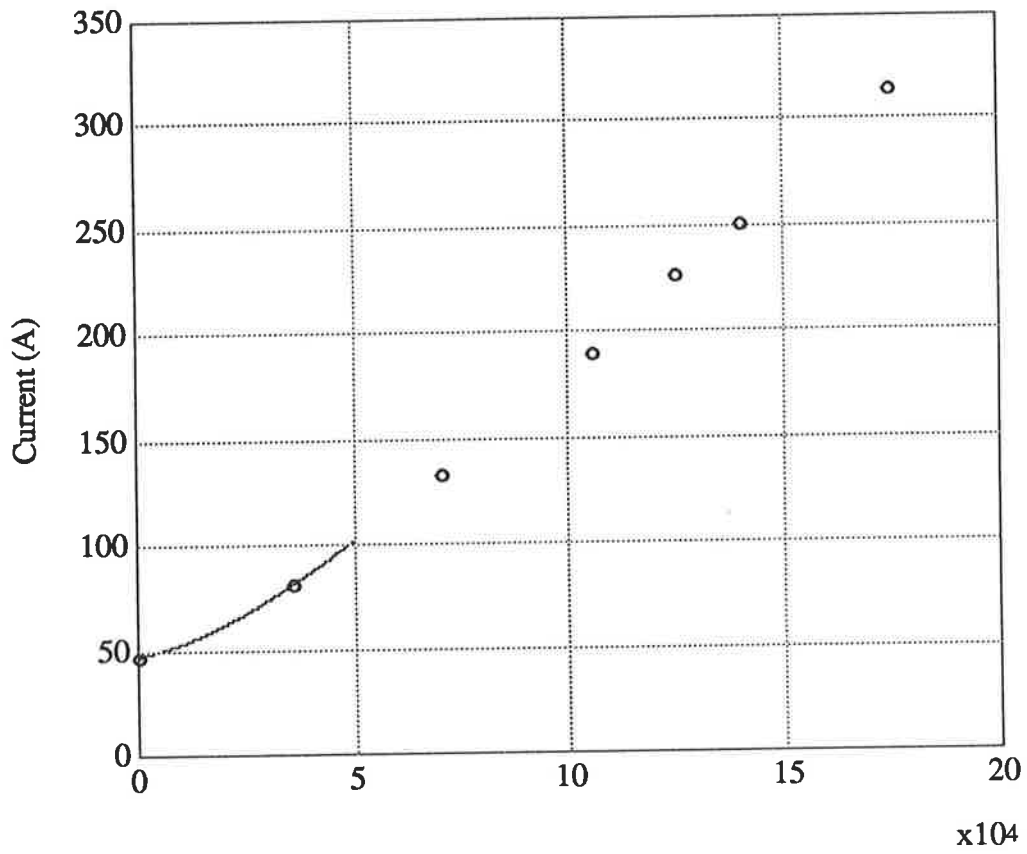


Figure 66

Line current as a function of shaft power for Machine I  
(measured)

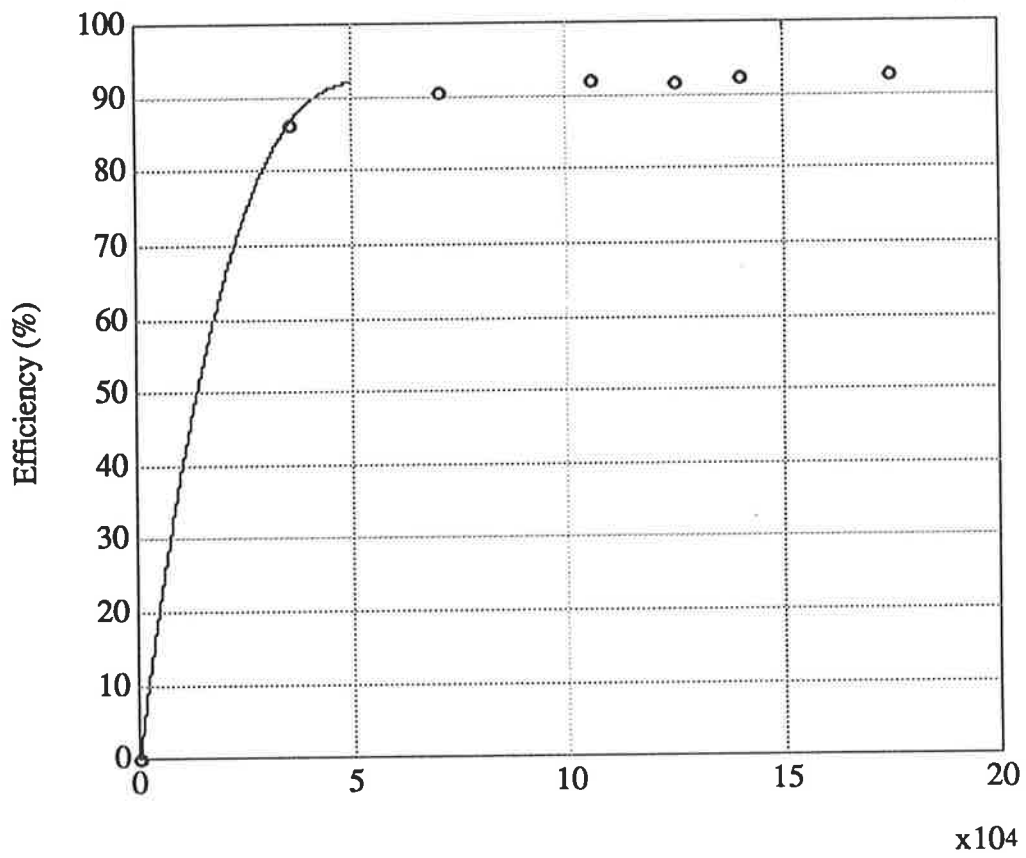


Figure 67

Efficiency as a function of shaft load for Machine I  
(measured)

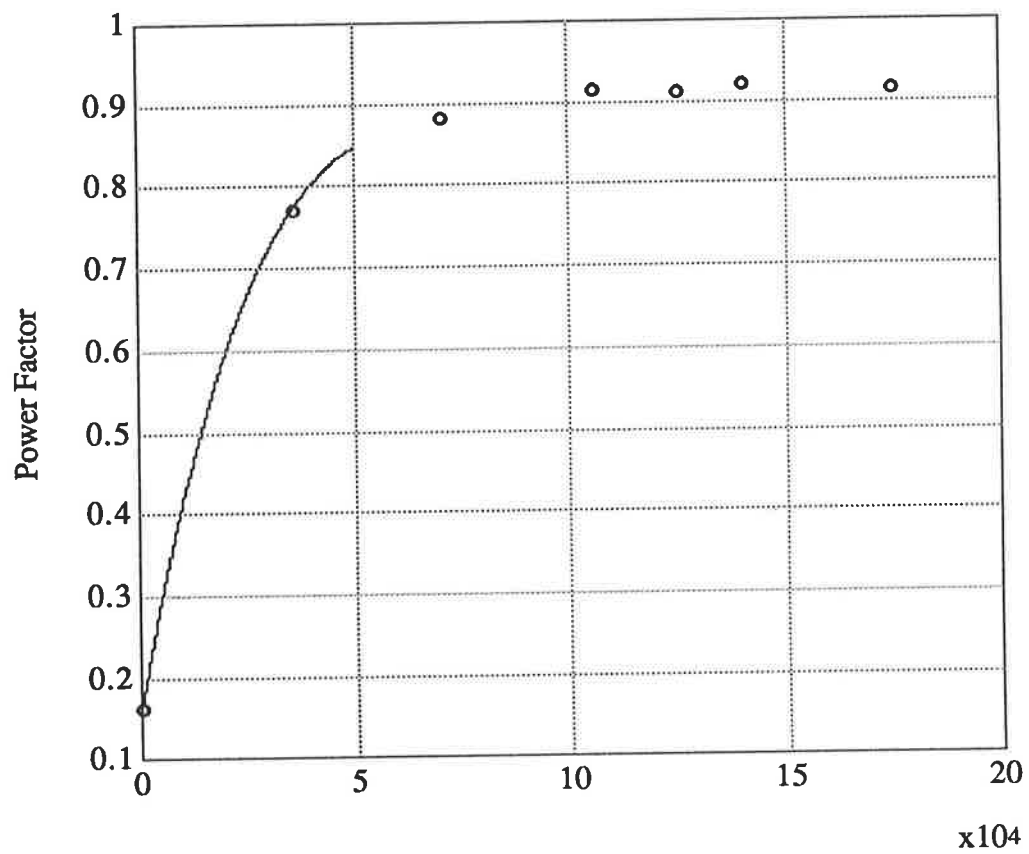


Figure 68

Power factor as a function of shaft load for Machine I  
(measured)

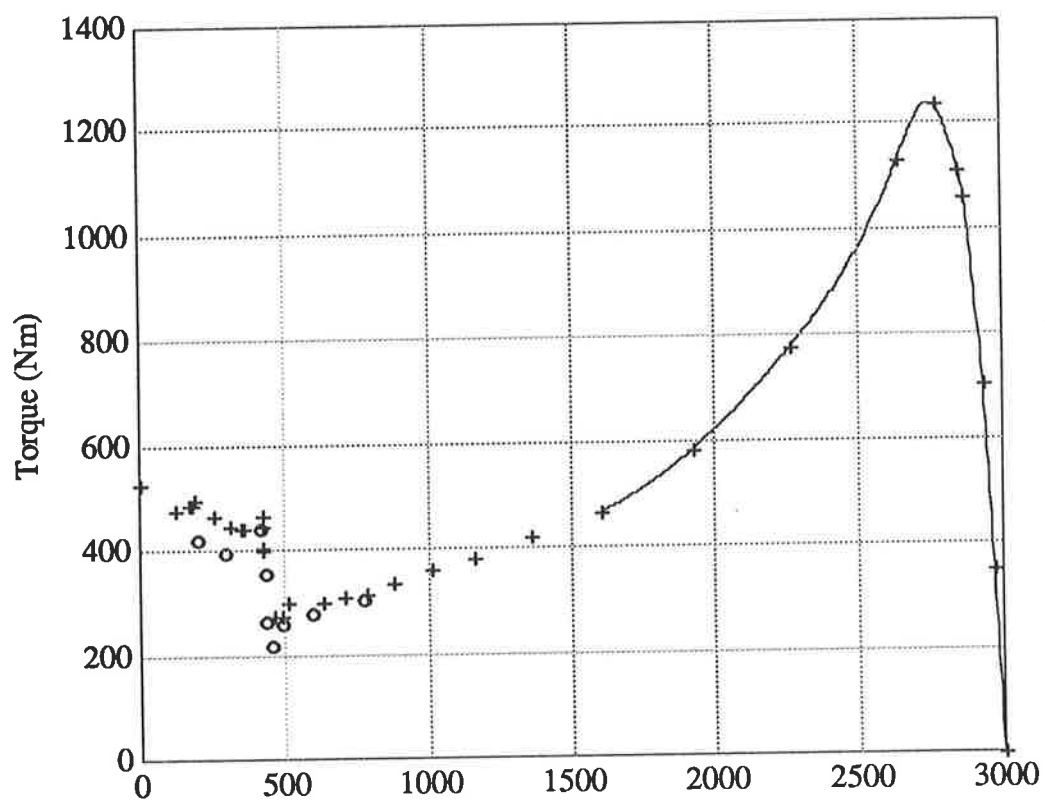


Figure 69

Torque-speed characteristic for Machine I

(measured)

+ + + wye-connected

o o o delta-connected

## 5.2.2 Test Results - Machine II

A laboratory test machine, here designated **Machine II**, was used to provide experimental back-up for the discrete circuit modelling approach. Tests conducted included the conventional parameter identification tests along with retardation tests and transient performance tests. The test machine is a swinging frame machine coupled to a d.c. machine; the d.c. machine was used to load or drive the test machine. Both machines are mounted on trunnion bearings so that the reaction torque can be measured. There is also a flywheel on the shaft of the test machine. The shaft speed was measured using a tachometer mounted on the shaft of the d.c. machine. The torque was measured using the torque transducer attached to the swinging frame of the test machine; the transducer consists of a tapered cantilever torque arm with a strain-gauge bridge.

Table 11 lists the measured parameters obtained from the blocked rotor test with rated current and from the no-load test with rated voltage for 2-pole configuration. Appendix A.3.4 gives the measured values of the polar moment of inertia,  $J$ , and the damping coefficient,  $D$ , which were obtained from retardation tests and loss measurements.

**Table 11**

Measured conventional model parameters for Machine II (2 pole)

<b>Stator</b>	Resistance	$R_1$	1.417 $\Omega$
	Leakage Reactance	$X_{l1}$	2.300 $\Omega$
<b>Rotor</b>	Resistance	$R_2$	1.457 $\Omega$
	Leakage Reactance	$X_{l2}$	2.300 $\Omega$
<b>Magnetisation</b>	Core loss resistance	$R_c$	612 $\Omega$
	Magnetising Reactance	$X_m$	95 $\Omega$



Figures 70 to 73 give the results of transient tests conducted on the test machine; these represent the direct-on-line starting in 2-pole configuration. Figure 70 depicts the current in Phase A during the start-up. Figures 71 and 72 give the torque and speed as a function of time respectively, whereas Figure 73 shows the resultant dynamic torque-speed characteristic.

The above set of tests was repeated with the machine connected in 4-pole configuration. This was done to validate the expectation that the presence of parallel paths in the winding when it is connected in the four-pole mode would have a discernible effect on the nature of the transient torque-speed characteristic, a point mentioned previously. Figure 74 is the measured stator current. Figures 75 and 76 show the torque and speed as a function of time, on the basis of which the transient torque-speed characteristic of Figure 77 was obtained. Figure 77 confirms the above expectation. It should be noted that the natural frequencies of the swinging frame of the test machine augments the electromagnetically produced torque, considerably magnifying it over the range 0 to 50 rad/s.

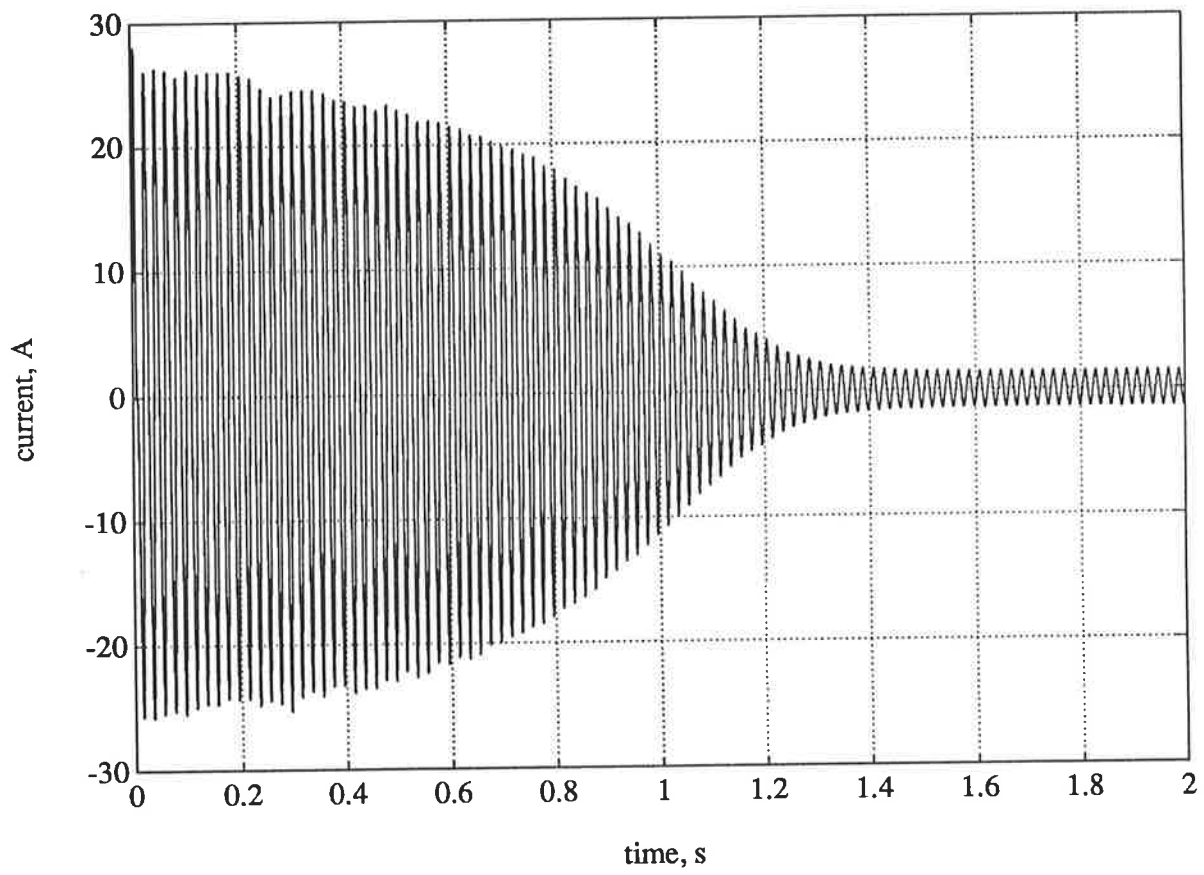


Figure 70

Measured stator current during start-up for Machine II (2-pole)

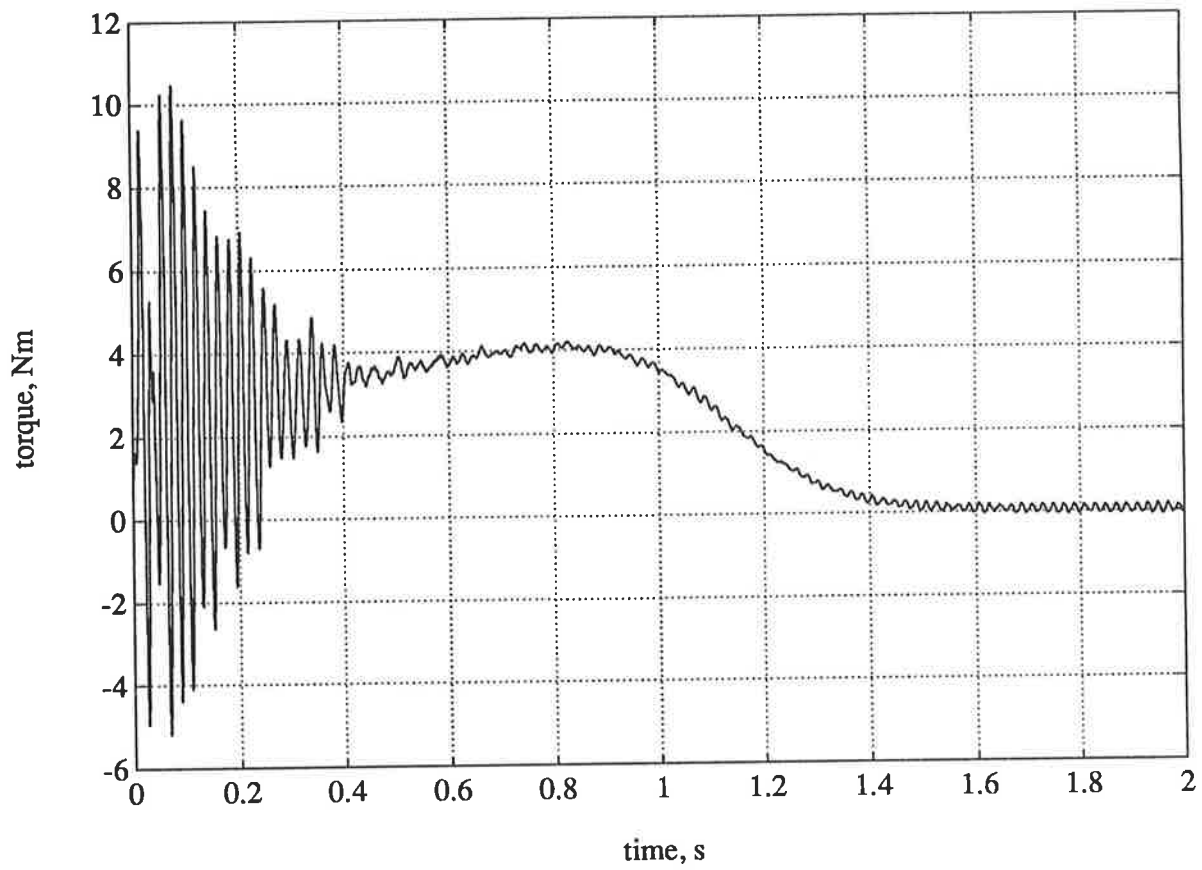


Figure 71

Measured torque during start-up for Machine II (2-pole)

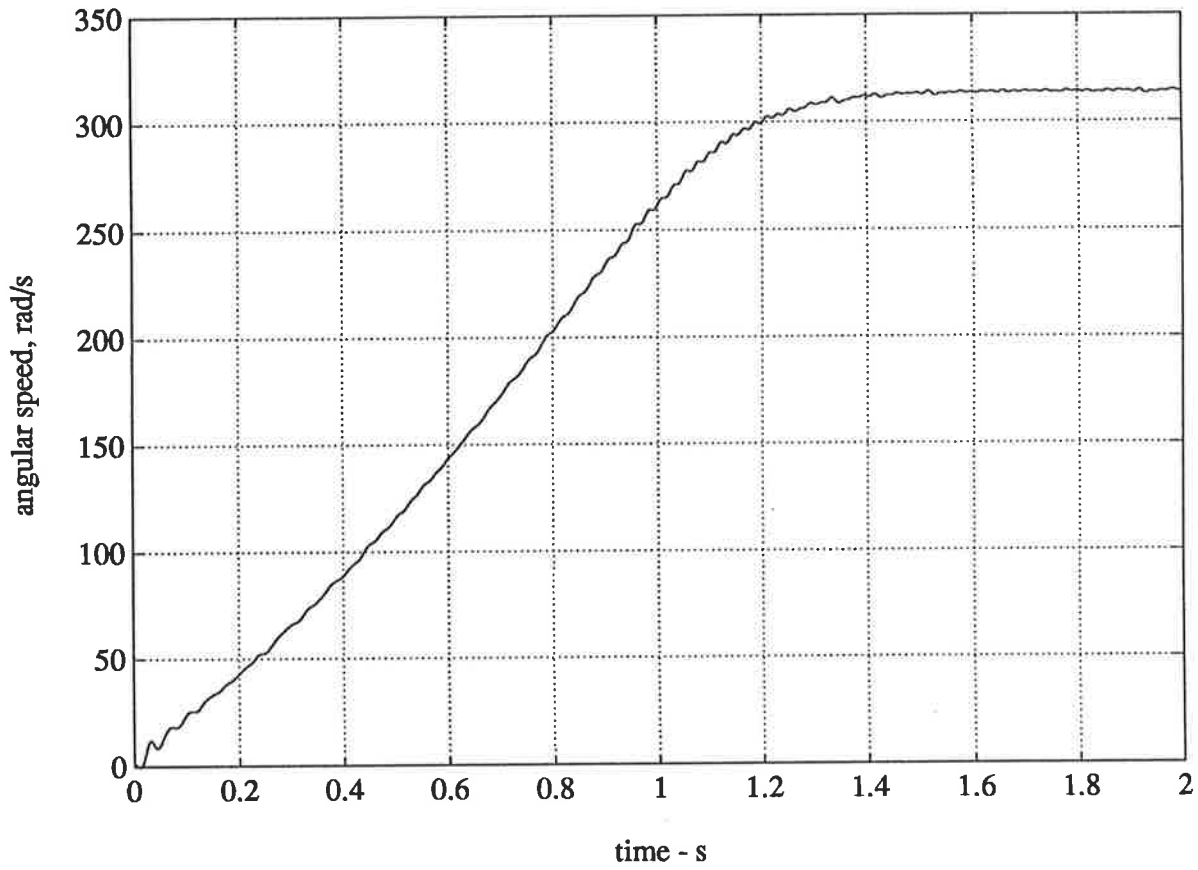


Figure 72

Measured speed during start-up for Machine II (2-pole)

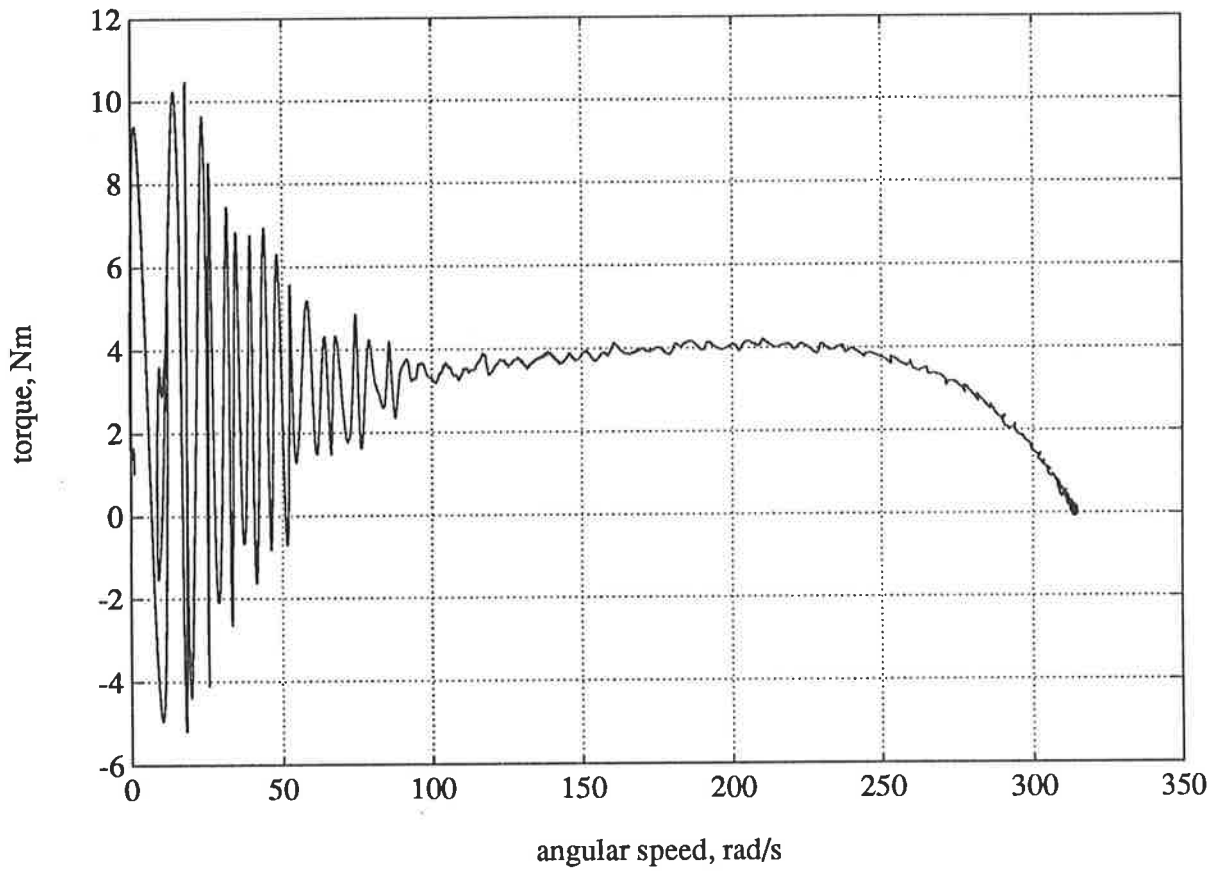


Figure 73

Measured dynamic torque-speed characteristic for Machine II  
(2-pole)

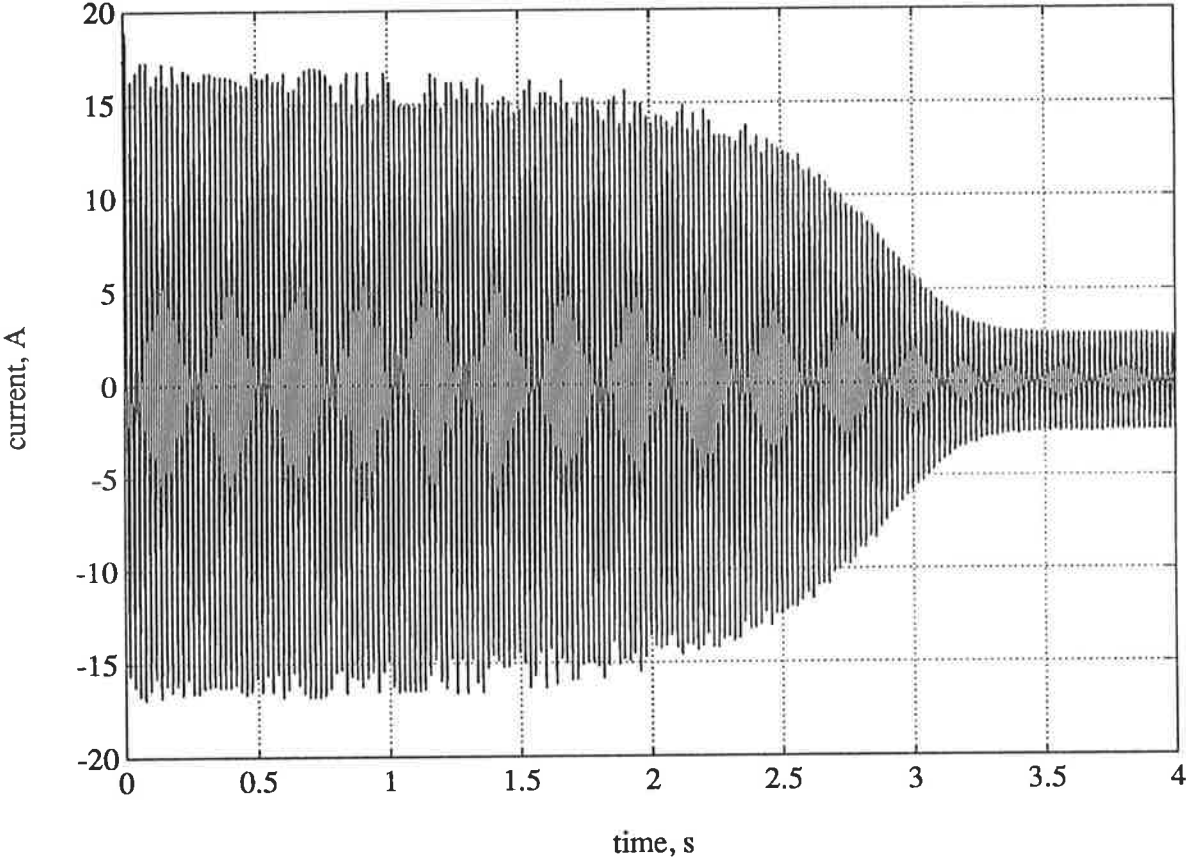


Figure 74  
Measured stator current during start-up for Machine II (4-pole)

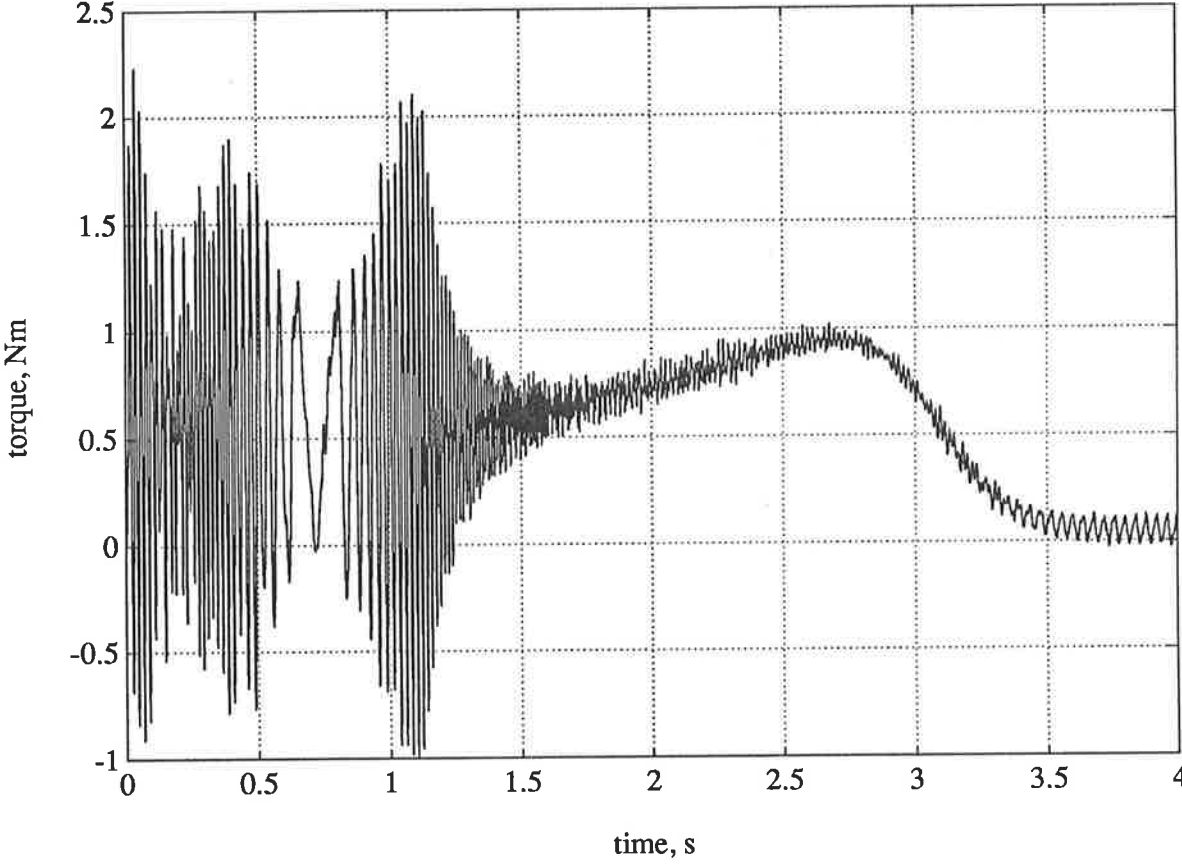


Figure 75  
Measured torque during start-up for Machine II (4-pole)

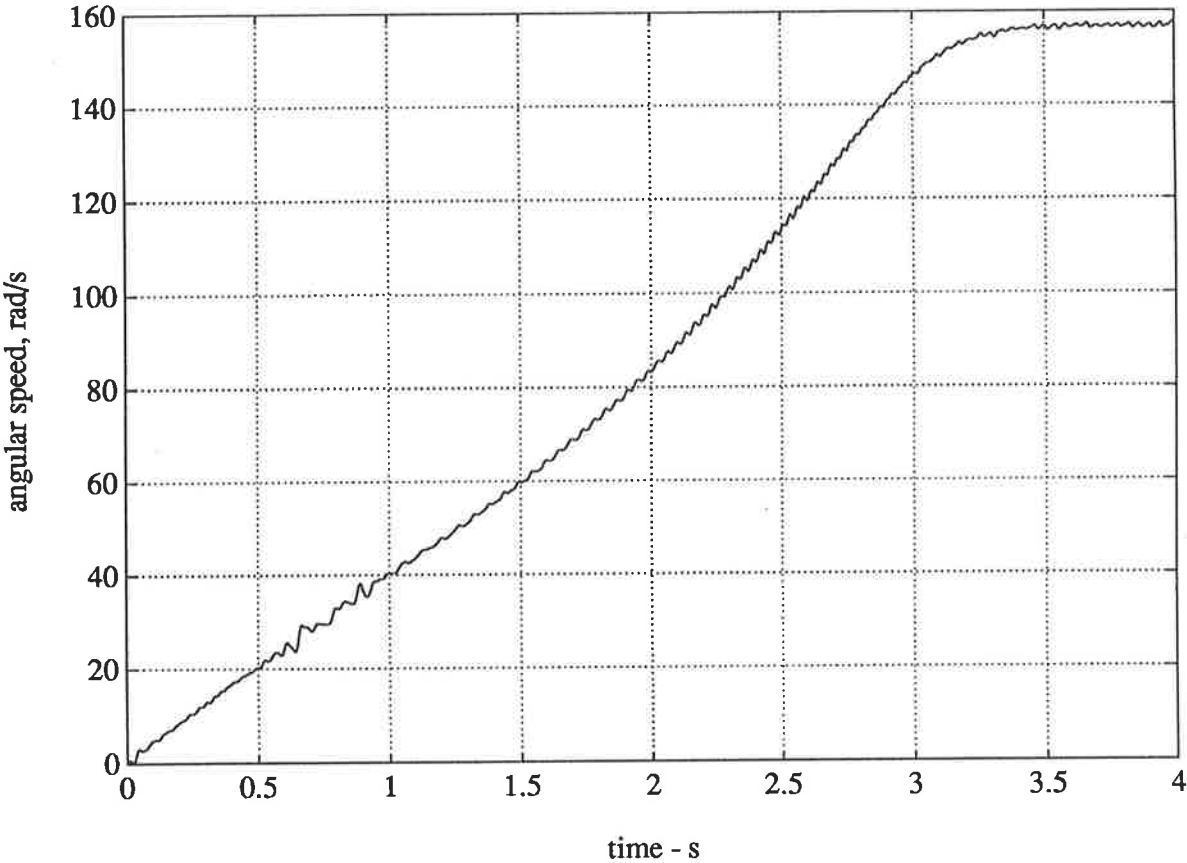


Figure 76  
Measured speed during start-up for Machine II (4-pole)



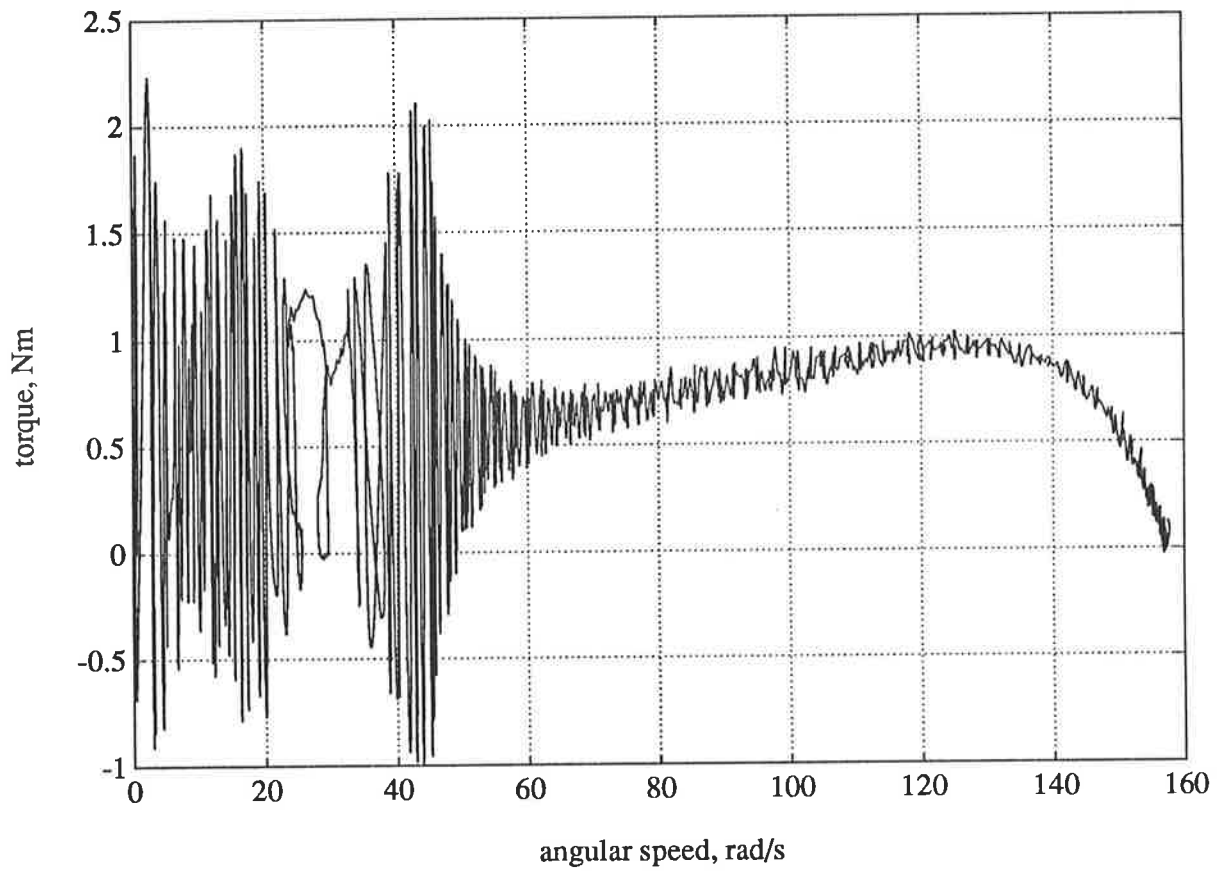


Figure 77

Measured dynamic torque-speed characteristic for **Machine II**  
(4-pole)

### 5.3 High Fidelity Harmonic Circuit Model

The validity of the high fidelity harmonic circuit modelling approach will be demonstrated below for a three-phase, deep-bar cage induction motor driven from a sinusoidal voltage source. The details of the machine, designated **Machine I** in the following, are presented in Appendix A.2, Sections A.2.1 to A.2.4.

To illustrate the gains to be made by the use of high fidelity circuit models, performance predictions below will be based progressively on the following set of models:

- a Conventional circuit model ("exact" equivalent circuit)
- b Conventional circuit model enhanced by the inclusion of current displacement effects
- c Conventional circuit model enhanced by the inclusion of saturation
- d Conventional circuit model enhanced by the inclusion of both current displacement effects and saturation
- e A high fidelity circuit model

As will be shown, accounting for either current displacement or saturation reduces the error in the prediction of starting characteristics, without necessarily improving the prediction accuracy elsewhere. If both current displacement and saturation are included in the model, prediction of starting characteristic becomes acceptably accurate. However, if space harmonics are significant as in this case, the prediction accuracy remains unsatisfactory except for standstill and the normal operating region, unless

space harmonics are also accounted for. When finally the effect of space harmonics is also introduced into the model, the prediction accuracy is dramatically improved.

Results of tests conducted on the test machine, a deep-bar squirrel-cage motor, were presented in Section 5.2.1 earlier in the chapter. In the discussion to follow, performance predictions based on the use of the above various models will be progressively compared with the actually measured results to demonstrate the effects of accounting for various different phenomena in model formation.

### 5.3.1 Performance Prediction Using " 'Exact' Equivalent Circuit"

Figure 78 represents an '*exact*' *equivalent circuit* model, which will be adopted here to initially predict the performance of Machine I. This conventional low order model is typical of the lumped parameter circuit models, commonly used to project the performance of induction machines. In line with the common practice, all space harmonics are included as leakage in both the stator and rotor leakage reactances. Model parameters are listed in Table 12. Figures 79 and 80 depict the torque-speed characteristic and the stator current locus obtained using the model. Figure 81 gives the current as a function of speed. The measured characteristic is superimposed in each case to facilitate comparison. Correlation is seen to be acceptable within the normal operating region up to about twice the rated load. Thus, this simple model is seen to be quite satisfactory for use in performance prediction if the interest is confined to this region. Outside the operating region, the '*exact*' *equivalent circuit* proves inadequate, yielding grossly erroneous results. These observations apply equally to all other performance characteristics not shown here.

In this context, it needs to be emphasised that parameters for this low-order model were determined directly from aspects of core topology and the knowledge of material properties, without accounting for other physically relevant phenomena, such as current displacement and discrete winding distribution. In conventional design practice, empirical factors are often introduced to compensate for these omissions. In this case, the parameters were obtained purposely without recourse to such corrective action; firstly to show that a limited consideration of geometry and material properties is not entirely adequate for reliable performance prediction; secondly to demonstrate that performance prediction can be improved with proper incorporation in this base model of the relevant phenomena. It is submitted that this constitutes a substantially more systematic approach to modelling, far superior to the somewhat arbitrary use of empirical factors in an attempt to improve prediction accuracy.

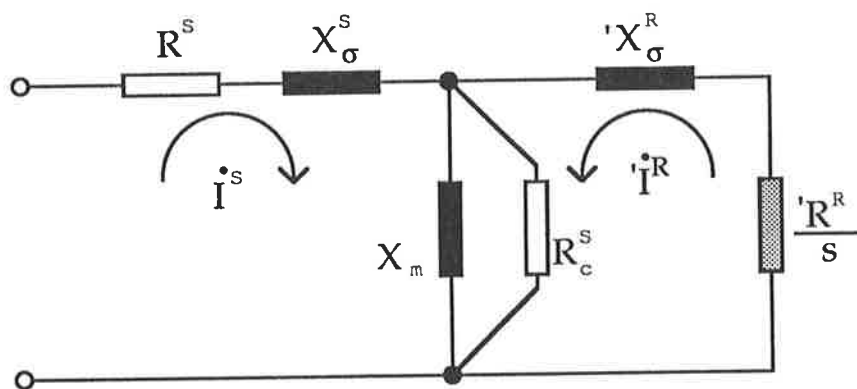


Figure 78

Typical low order circuit model for a three-phase deep-bar cage induction machine

(for model parameters, see Table 12)

**Table 12**

Model Parameters for the " 'Exact' Equivalent Circuit of Figure 105

Stator Resistance	$R^S$	0.055 $\Omega$
Rotor Resistance Referred to Stator	' $R^R$	0.034 $\Omega$
Magnetising Reactance	$X_m$	12.120 $\Omega$
Core Loss Resistance	$R_c$	92.024 $\Omega$
Stator Leakage Reactance	$X_\sigma^S$	0.254 $\Omega$
Rotor Leakage Reactance Referred to Stator	' $X_\sigma^R$	0.162 $\Omega$

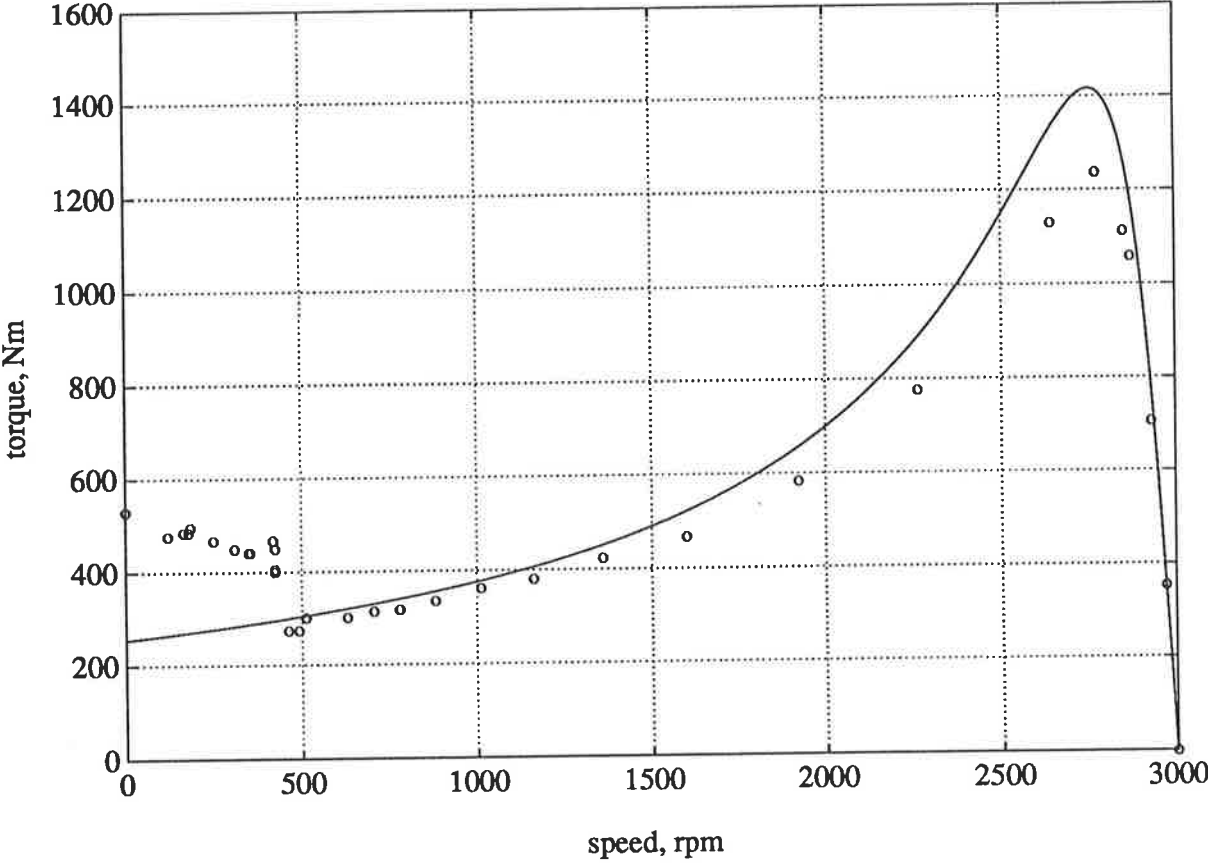


Figure 79

Torque-speed characteristic for Machine I

— Predicted using low order model of Figure 105

o o o Measured

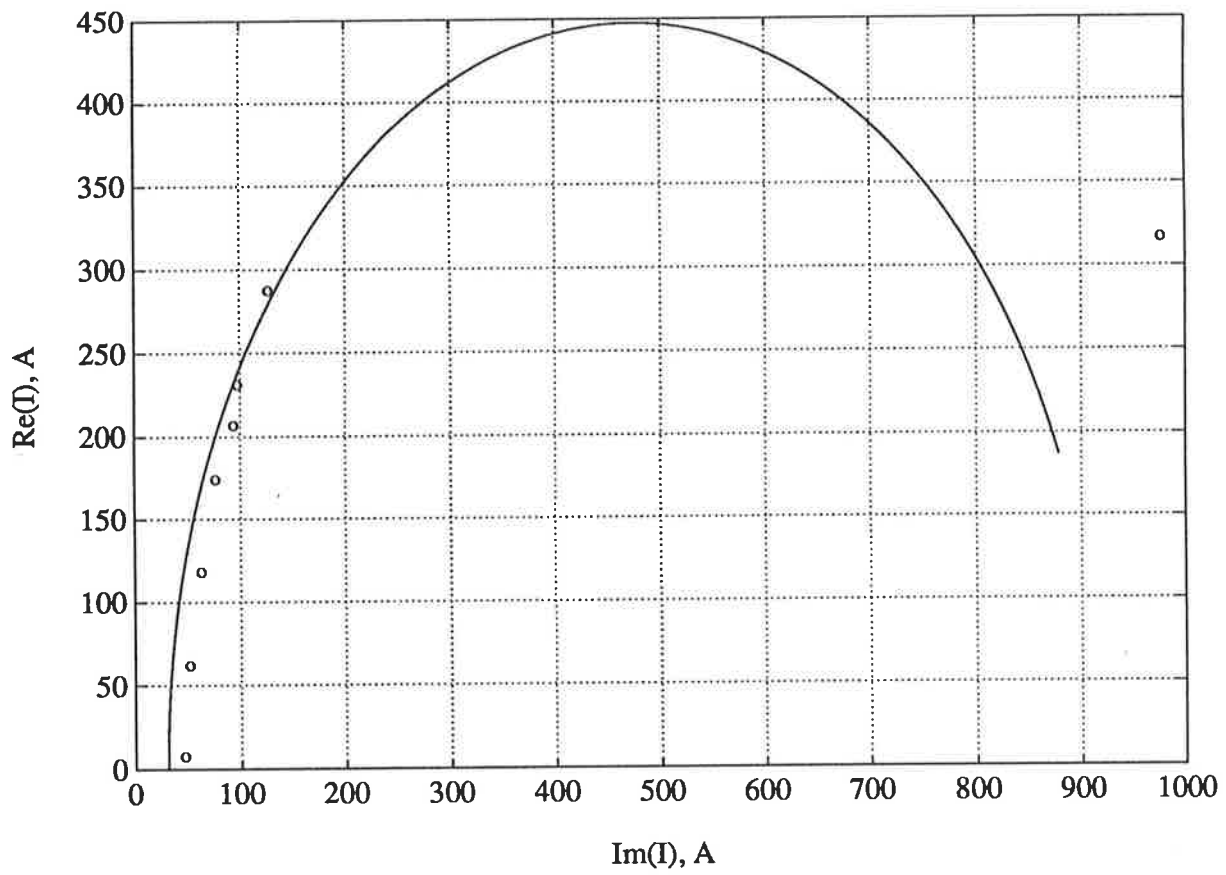


Figure 80

Current locus for Machine I

— Predicted using low order model of Figure 105

o o o Measured

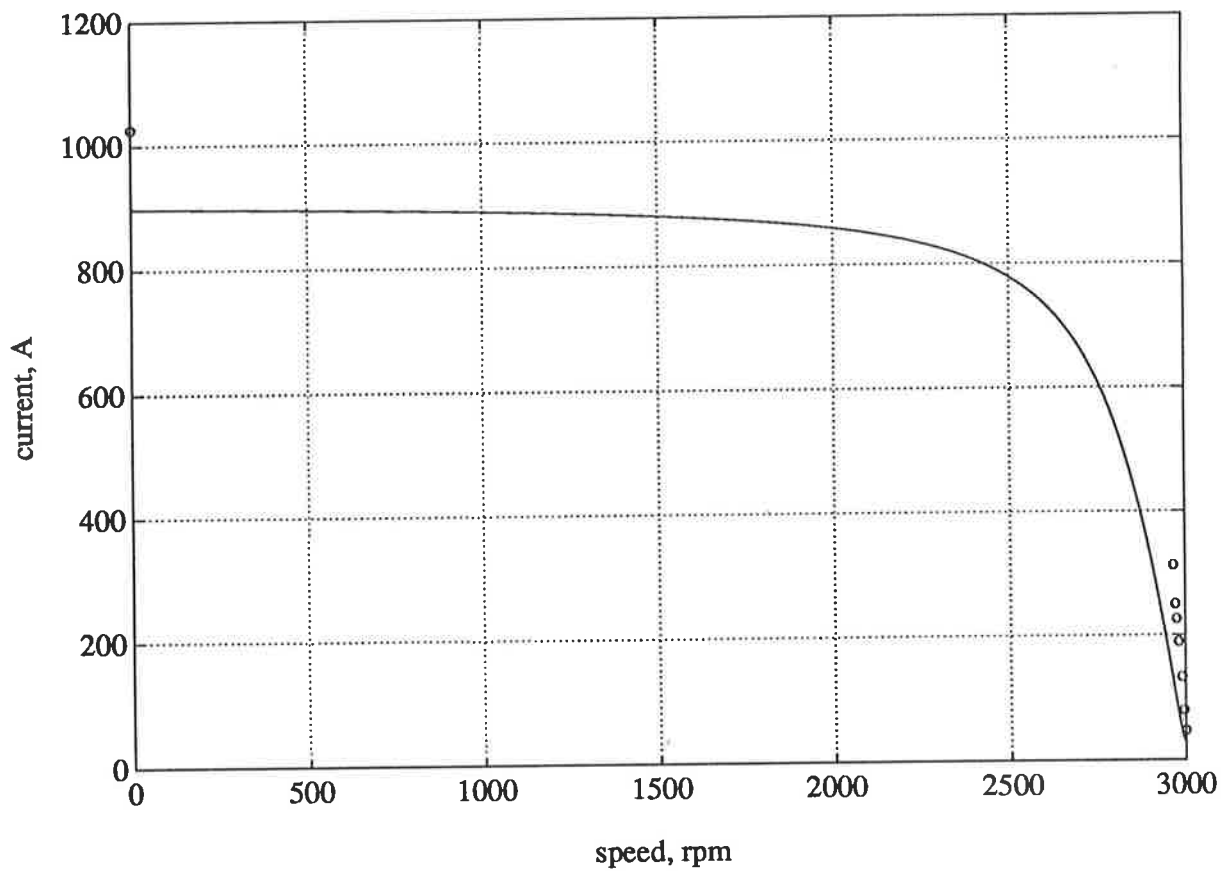


Figure 81

Current versus speed characteristic for Machine I

— Predicted using low order model of Figure 105

o o o Measured



### 5.3.2 Performance Prediction with Enhanced Low-Order Models

It will now be shown that the low-order base model of Figure 78 can be enhanced by the inclusion of other physically relevant phenomena toward yielding a more accurate performance prediction. Firstly, the effect of **saturation** will be included. Secondly, **current displacement** will be accounted for. Thirdly, the effect of incorporating in the base model of both saturation and current displacement will be demonstrated.

Figure 82 depicts the saturation-enhanced low-order circuit model for Machine I. The leakage reactances  $X_{\sigma}^S$  and  $X_{\sigma}^R$  of Figure 78 are broken down into their constituent components to emphasise the components affected by saturation. Saturation affected parameters are evidently the magnetising reactance, the slot leakage reactances and the differential leakage reactances. Effect of saturation is modelled with the aid of the apparent slot opening width,  $w'_o$ , substituting the actual slot opening width,  $w_o$ , as explained in Section 2.5. For instance, the stator slot leakage reactance is now obtained as

$$X_s^S = \omega N^{S2} \mu_0 l_c \left( \frac{h_c}{3w_s} + \frac{\pi^2}{16} + \frac{h_o}{3w'_o} \right) \quad (523)$$

$w'_o$  is to replace  $w_o$  in every other instance.  $w'_o$  is procured, using the shearing method, from Equation (156).

Figures 83 to 85 give the torque-speed characteristic, the stator current locus and the current versus speed characteristic respectively, predicted using the saturation-enhanced low-order model of Figure 78. The predictions from the low-order model of Figure 78 and measured values are superimposed

for ease of comparison. As can be seen, the prediction of the starting torque is somewhat improved by the inclusion of the effect of saturation. Yet, the maximum torque is still too high and prediction accuracy elsewhere leaves much to be desired with the exception of the operating region. However, one must not hastily conclude that the incorporation of saturation in the model is of no consequence; other phenomena need to be taken into account to improve the accuracy of prediction further. On the other hand, prediction accuracy suffers considerably if saturation effects are not included even if all other physically relevant phenomena may have been represented in the model.

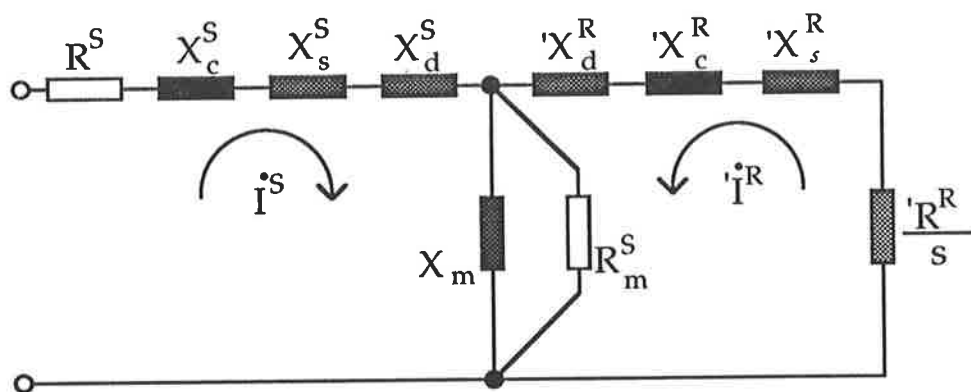


Figure 82

Enhanced low-order circuit model for Machine I  
(accounting for saturation)

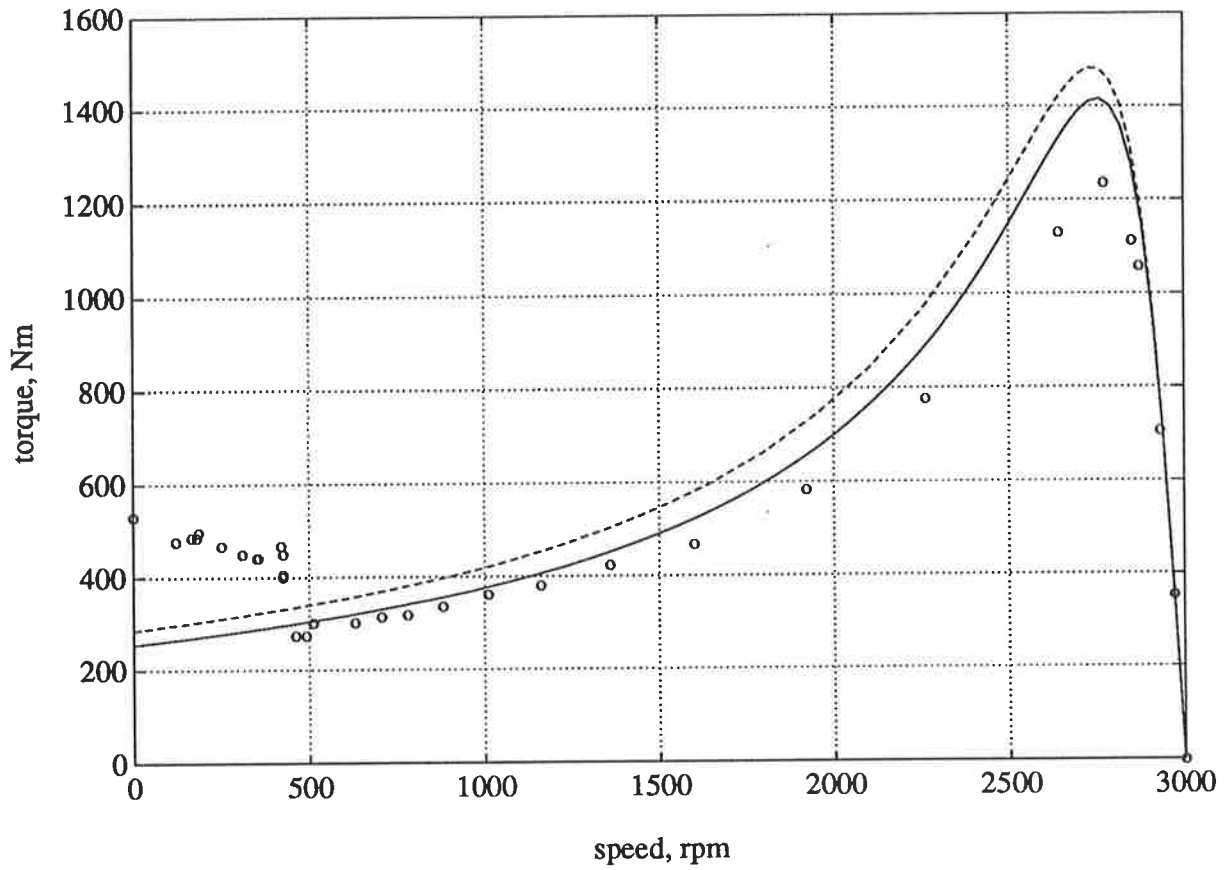


Figure 83

Torque-speed characteristic for Machine I

----- Predicted using enhanced low order model of Figure 82

(includes saturation)

—— Predicted using low order model of Figure 78

o o o Measured

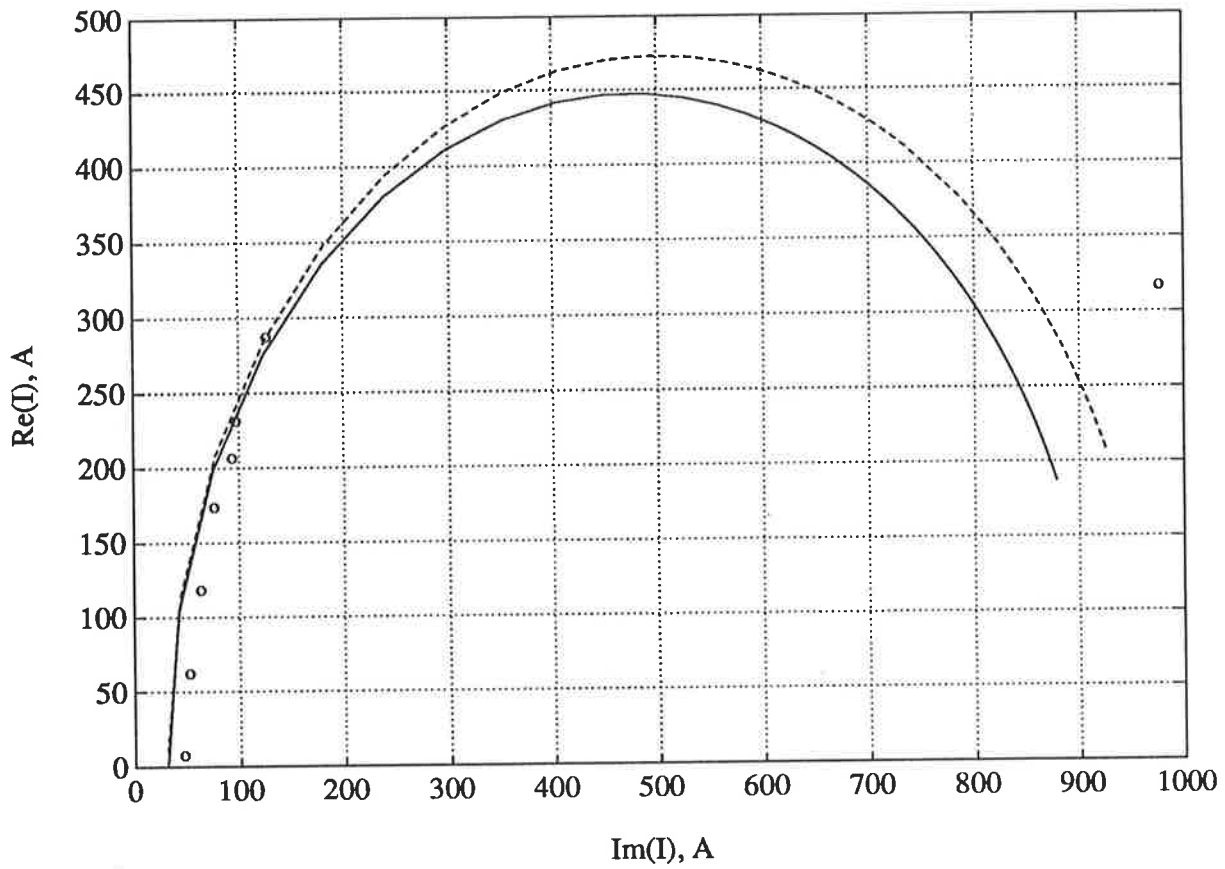


Figure 84

Current locus for Machine I

----- Predicted using enhanced low order model of Figure 82  
(includes saturation)

—— Predicted using low order model of Figure 78

o o o Measured

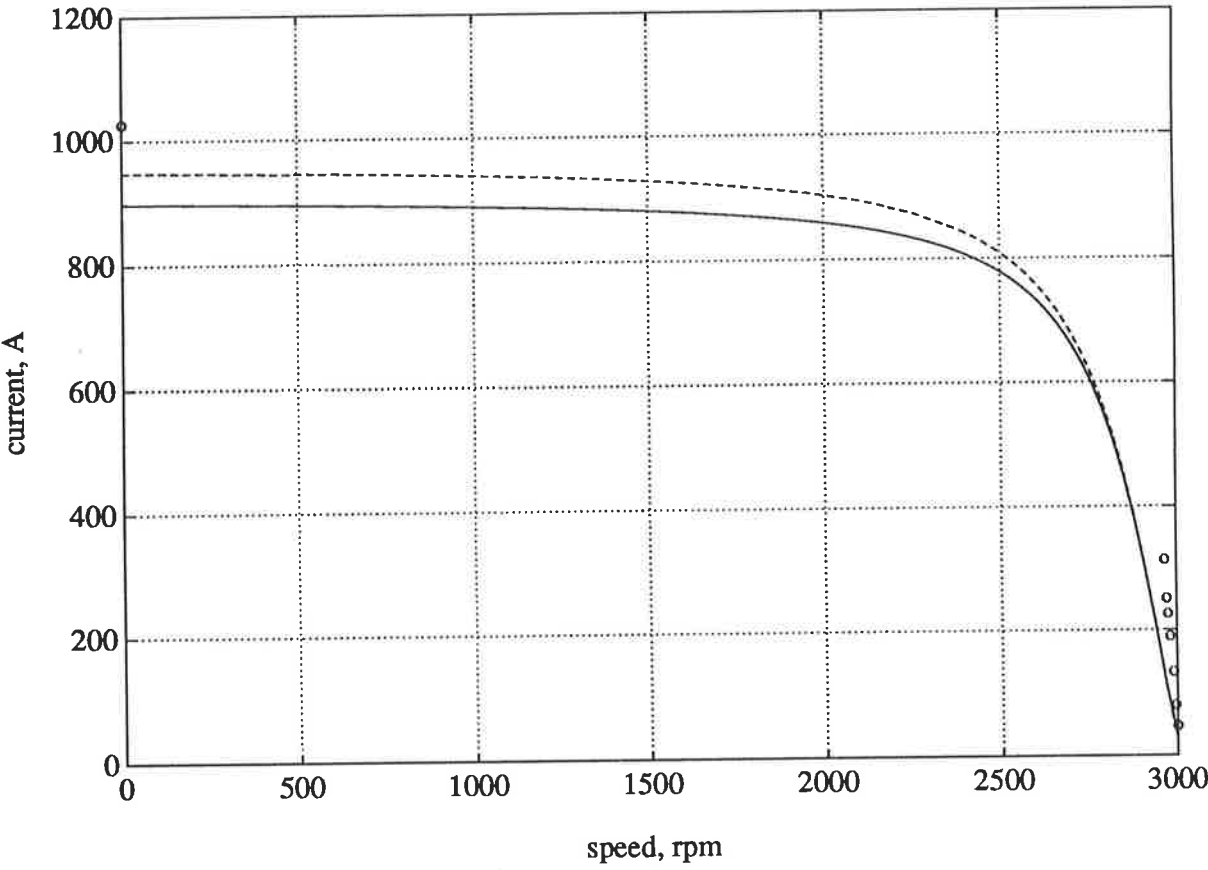


Figure 85

Current versus speed characteristic for Machine I

- Predicted using enhanced low order model of Figure 82  
(includes saturation)
- Predicted using low order model of Figure 78
- o o o Measured

Next, it will be shown what effect the consideration of current displacement has on performance prediction. Figure 86 shows a low order model which is enhanced by the incorporation in the " 'exact' equivalent circuit", given in Figure 78, of model parameters which account for **current displacement** in rotor bars; this time the model does not include saturation effects. The consequential changes in the cage impedance are represented by an incremental series resistance,  $\Delta R_b$ , and a decremental series reactance,  $\Delta X_b$ . The reactive model component  $X_{\sigma-}^R$  represents the portion of the rotor leakage reactance unaffected by current displacement and is evidently given by

$$X_{\sigma-}^R = X_{\sigma}^R - X_s^R \quad (524)$$

where  $X_s^R$  is the rotor slot leakage reactance referred to the stator. Table 13 gives the values for the model parameters. The factors  $c_r^R$  and  $c_x^R$  are to be obtained using Equations (111) and (112) from

$$c_r^R = f_p \left( \frac{h}{\delta_p} \right) - 1 \quad (525)$$

$$c_x^R = 1 - f_Q \left( \frac{h}{\delta_p} \right) \quad (526)$$

Figure 87 shows the torque speed characteristic predicted using this enhanced low-order model. The measured characteristic is again superimposed, along with that predicted using the " 'exact' equivalent circuit" of Figure 78. Figure 88 gives the stator current locus predicted using this model and compares it with both those obtained from the use of the base model of Figure 78 and from measurement. Figure 89 gives the stator current as a function of shaft speed and makes comparisons. It is seen that the prediction of run-up performance is improved compared with predictions when the base model is used.

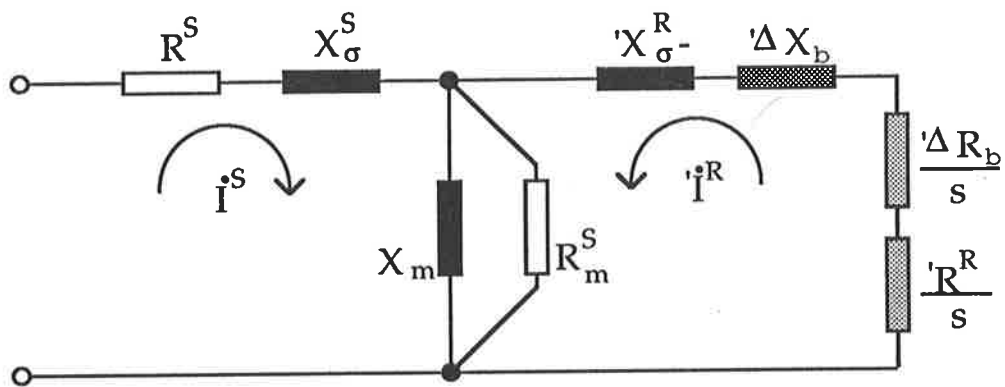


Figure 86

Enhanced low-order circuit model for Machine I

(accounting for current displacement)

(for model parameters, see Table 13)

**Table 13**

Model parameters for the enhanced low-order model of Figure 113

Stator Resistance	$R^S$	$0.055\Omega$
Rotor Resistance <sup>4</sup>	$'R^R$	$0.034\Omega$
Incremental Rotor Resistance <sup>5</sup>	$'\Delta R_b$	$0.015 \times c_T^R \Omega$
Residual Rotor Resistance <sup>6</sup>	$'R^-$	$0.016\Omega$
Core Loss Resistance	$R_c$	$92.024\Omega$
Magnetising Reactance	$X_m$	$12.120\Omega$
Stator Leakage Reactance	$X_\sigma^S$	$0.254\Omega$
Rotor Slot Leakage Reactance <sup>7</sup>	$'X_s^R$	$0.162\Omega$
Decremental Rotor Slot Leakage Reactance <sup>8</sup>	$'\Delta X_b$	$0.071 \times c_x^R \Omega$
Residual Rotor Leakage Reactance <sup>9</sup>	$'X_\sigma^R$	$0.091\Omega$

---

<sup>4</sup> referred to stator

<sup>5</sup> referred to stator

<sup>6</sup> referred to stator

<sup>7</sup> referred to stator

<sup>8</sup> referred to stator

<sup>9</sup> referred to stator



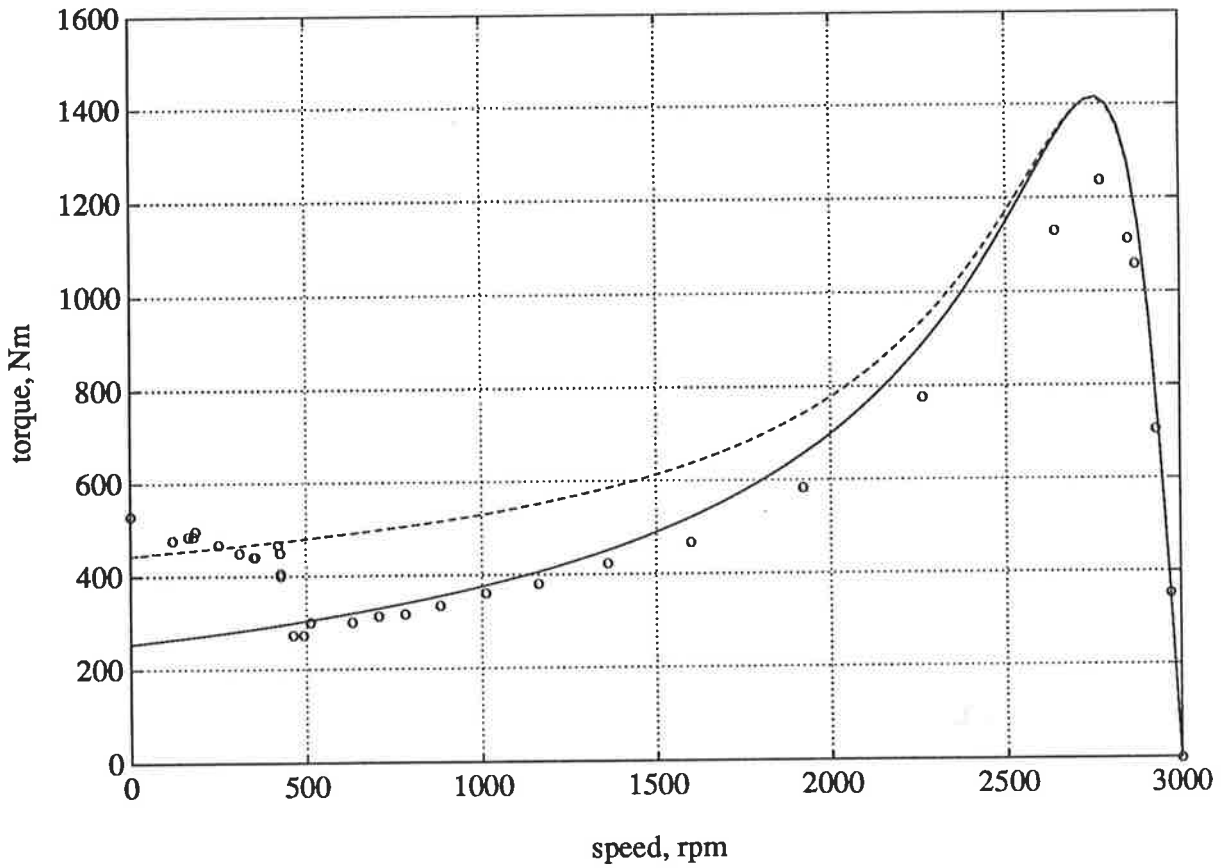


Figure 87

Torque-speed characteristic for Machine I

----- Predicted using enhanced low order model of Figure 86  
(includes current displacement)

—— Predicted using low order model of Figure 78

o o o Measured

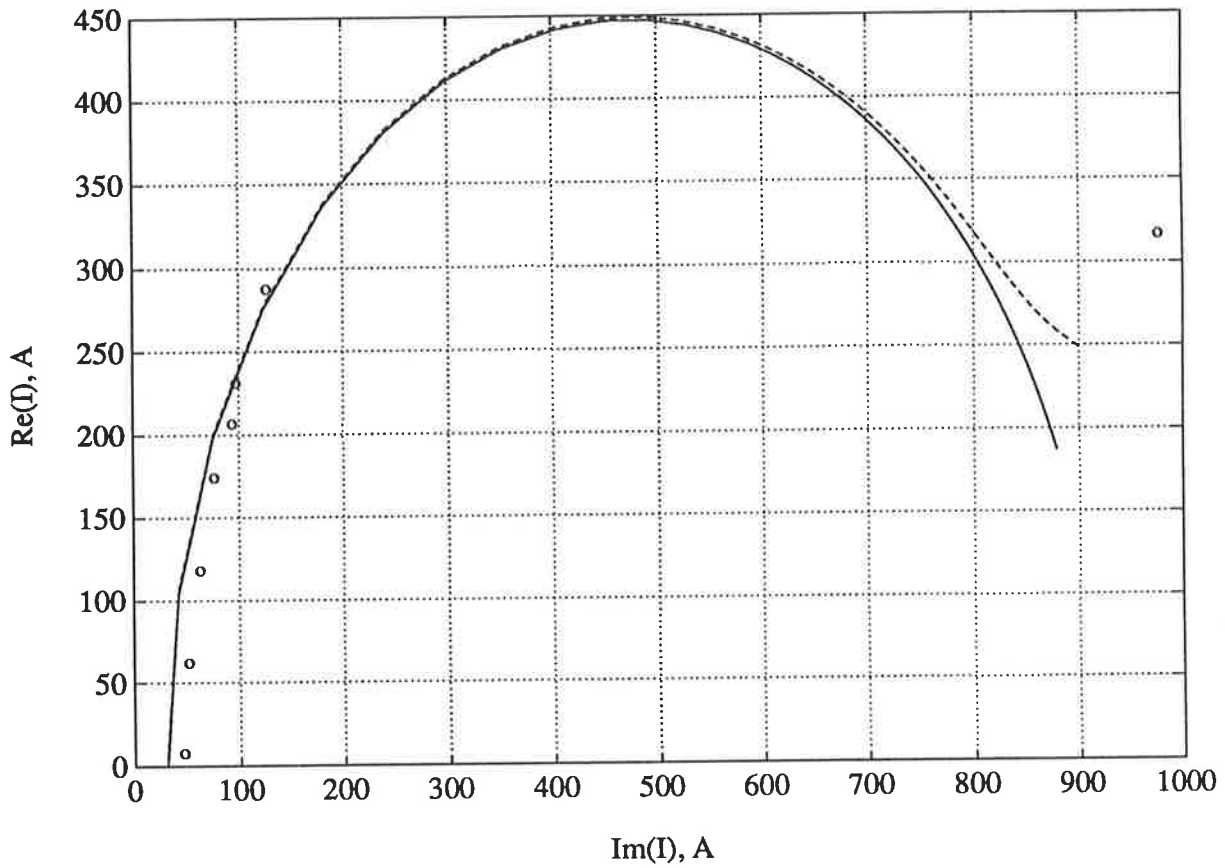


Figure 88

Current locus for Machine I

----- Predicted using enhanced low order model of Figure 86

(includes current displacement)

——— Predicted using low order model of Figure 78

o o o Measured

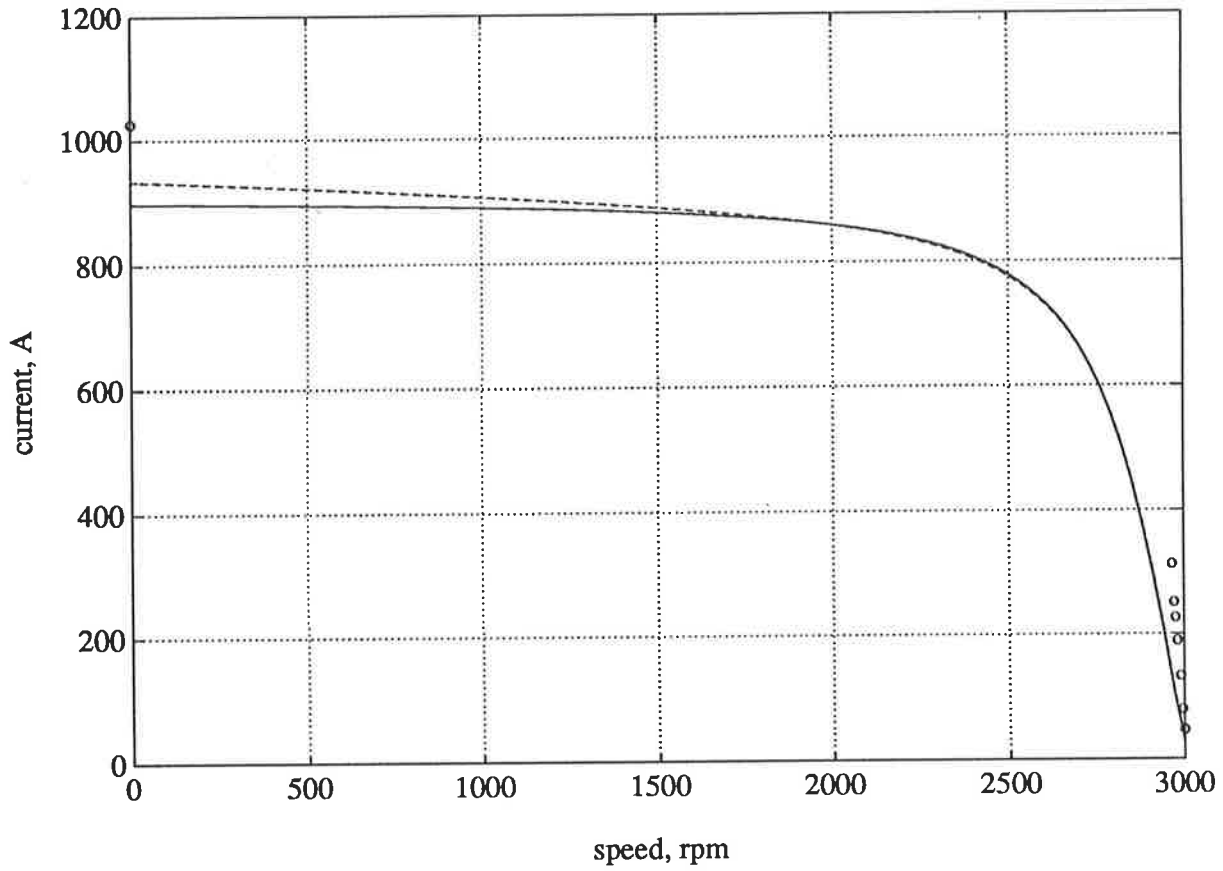


Figure 89

Current versus speed characteristic for Machine I

----- Predicted using enhanced low order model of Figure 86  
(includes current displacement)

———— Predicted using low order model of Figure 78

o o o Measured

Intuitively, one would expect that the improvement in prediction accuracy would be substantial if both the saturation and current displacement are added to the base model, especially for the run-up region. This expectation is seen to be confirmed below. Figure 90 depicts the corresponding modified model. Saturation affected parameters are the magnetising reactance  $X_m$ , the slot leakage reactances  $X_s^S$  and  $'X_s^R$  and the differential leakage reactances  $X_d^S$  and  $'X_d^R$ . The parameters  $'\Delta X_b$  and  $'\Delta R_b$  represent the effect of current displacement as before.

Figures 91 to 93 show the characteristics predicted on the basis of this model. It is evident from these that incorporating the effects of both saturation and current displacement substantially improves the accuracy in predicting the starting characteristics. Again, the improvement does not carry beyond the starting region; for the prediction to improve for the rest of the characteristic, dominant space harmonics need to be included in the model. This will be discussed next.

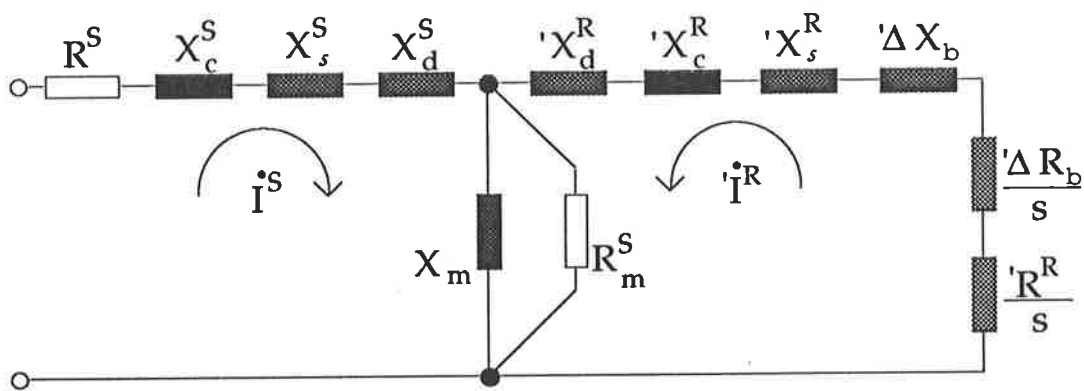


Figure 90

Enhanced low-order circuit model for Machine I

(includes saturation and current displacement effects)

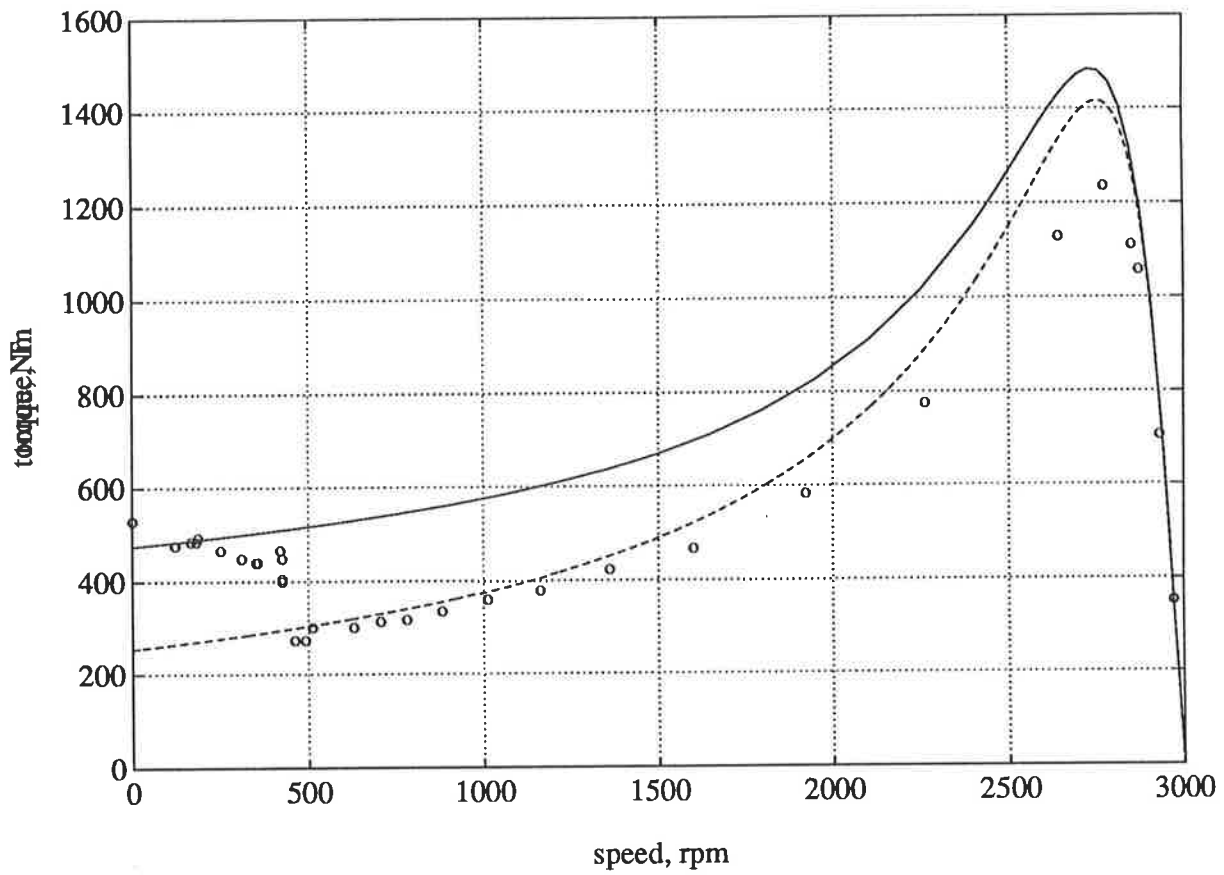


Figure 91

Torque-speed characteristic for Machine I

- Predicted using enhanced low order model of Figure 90  
(includes current displacement and saturation)
- - - Predicted using low order model of Figure 78
- o o o Measured

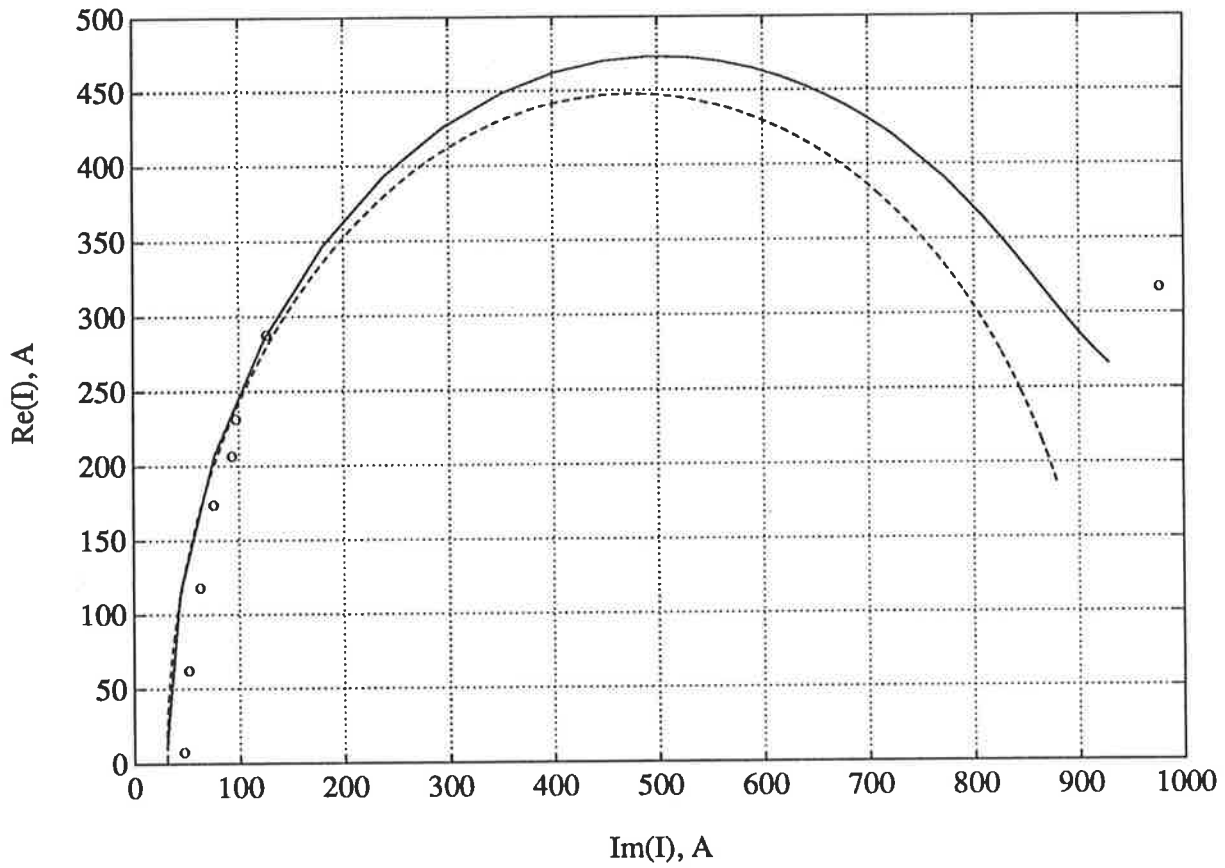


Figure 92

Current locus for Machine I

—— Predicted using enhanced low order model of Figure 90

(includes current displacement and saturation)

----- Predicted using low order model of Figure 78

o o o Measured

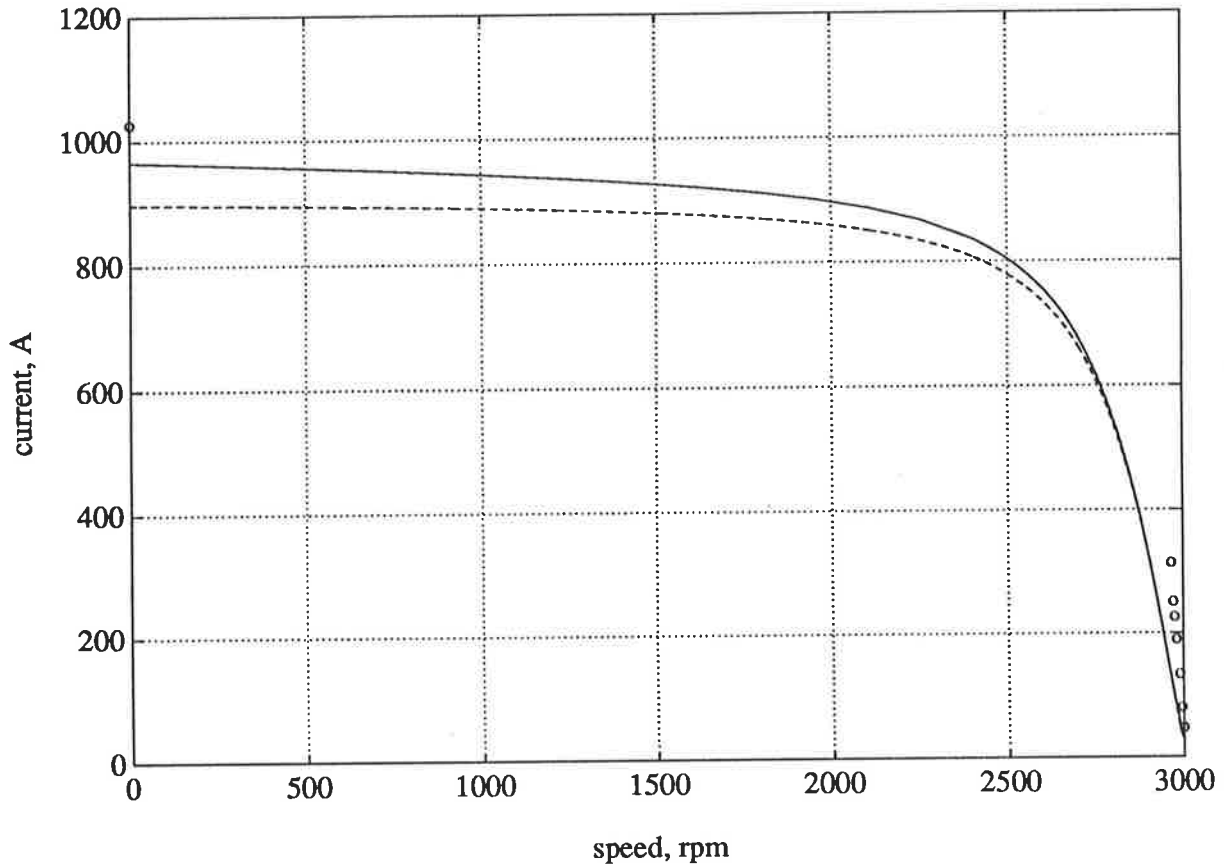


Figure 93

Current versus speed characteristic for Machine I

— Predicted using enhanced low order model of Figure 90

(includes current displacement and saturation)

----- Predicted using low order model of Figure 78

o o o Measured



### 5.3.3 Performance Prediction with High-Fidelity Circuit Models

It will now be shown that the inclusion in the model of space harmonic effects along with other phenomena further improves performance prediction.

It was stated earlier that only the dominant space harmonics need be included in a high order model since these are the ones which significantly affect the machine behaviour. The dominant harmonics can be selected from the spectrum of the airgap flux distribution as represented by the spectrum of the resultant winding factor. As explained previously in Section 2.2.7, the winding factor spectrum constitutes a truncation criterion; invaluable in the selection of harmonics for inclusion in a high fidelity circuit model. Figure 94 shows the winding factor spectrum for the test machine. The fifth and seventh harmonics are seen to be the most dominant.

The third order model of Figure 95 was formed by accounting for the effects on the machine behaviour of the fifth and seventh harmonics in addition to the fundamental. The model also accounts for saturation, stator and rotor core losses and current displacement in the rotor conductors. The torque-speed characteristic of Figure 96 shows that the prediction accuracy is significantly improved over a wider range of speed. For instance, the maximum torque is now predicted accurately and the prediction error for the rest of the characteristic is reduced. In addition, it is now possible to predict the presence of a cusp in the torque-speed characteristic: this is a remarkable achievement which low-order models are unable to produce. It should also be noted that the improvement in the prediction of the maximum torque is solely brought about by the

increase in the model order from *one* to *three* without resorting to the use of any *correction factors*.

Prediction accuracy within the starting region can be improved further by increasing the order of the model from *three* to *five* with the inclusion of the effects of the eleventh and thirteenth harmonics; the most significant harmonics after the fifth and seventh harmonics. However, the anticipated improvement is not considered commensurate with the associated computational effort, since the prediction using the third order model is amply satisfactory.

This case of a deep-bar cage induction motor shows that, in predicting the machine performance in steady state or under quasi-dynamic conditions, dramatic improvements can be achieved by the use of judiciously formed high fidelity circuit models. Such high fidelity per phase models for machines with balanced and symmetrically distributed windings, driven from a balanced supply, constitute an asset for induction machine design, not to be dismissed lightly.

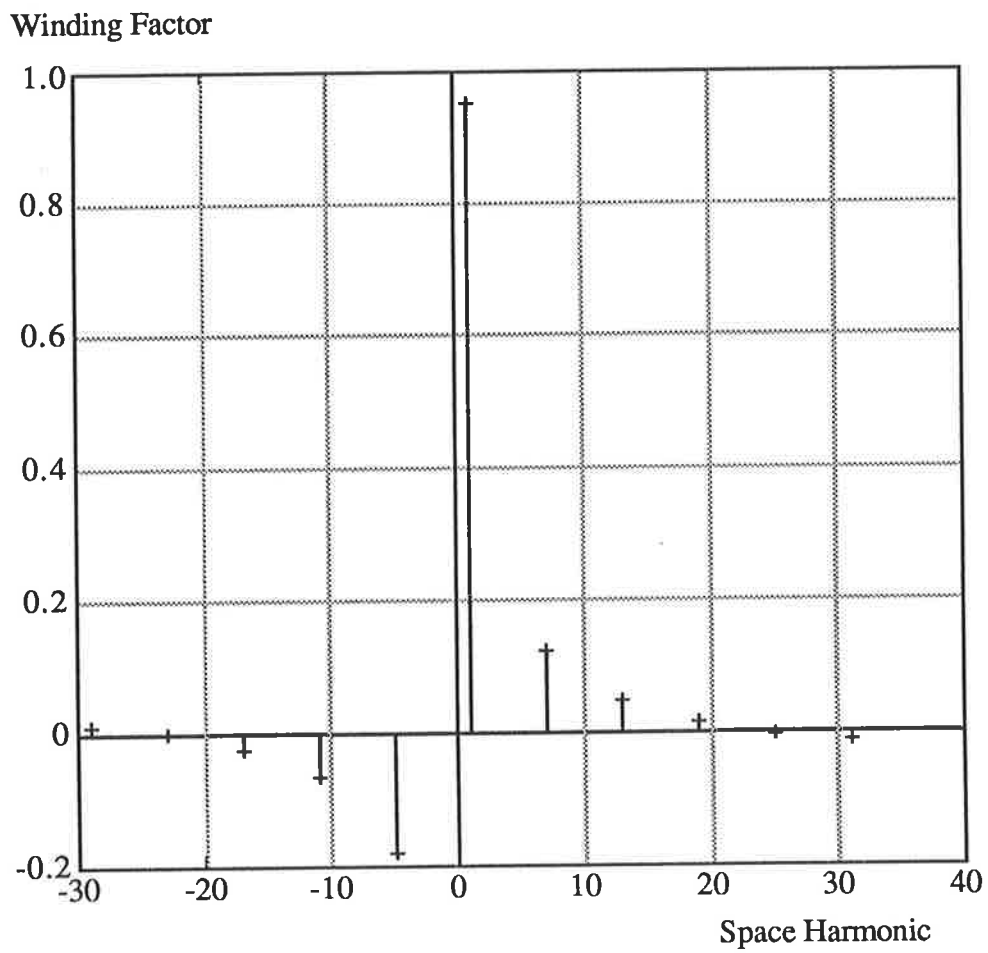


Figure 94

The spectrum of winding factor for Machine I

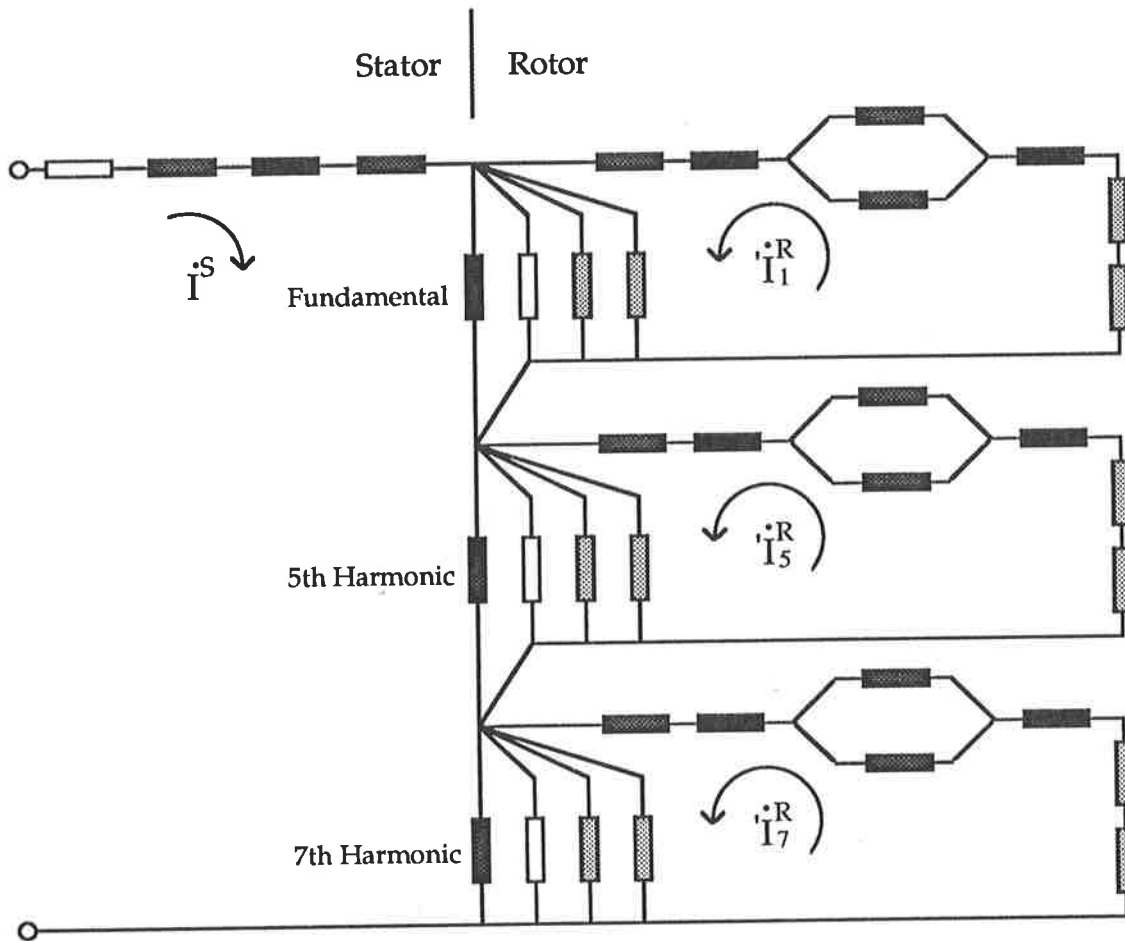


Figure 95

Third-order high fidelity harmonic circuit model for deep-bar cage induction motor

(for model parameters, see Appendix A.2.4)

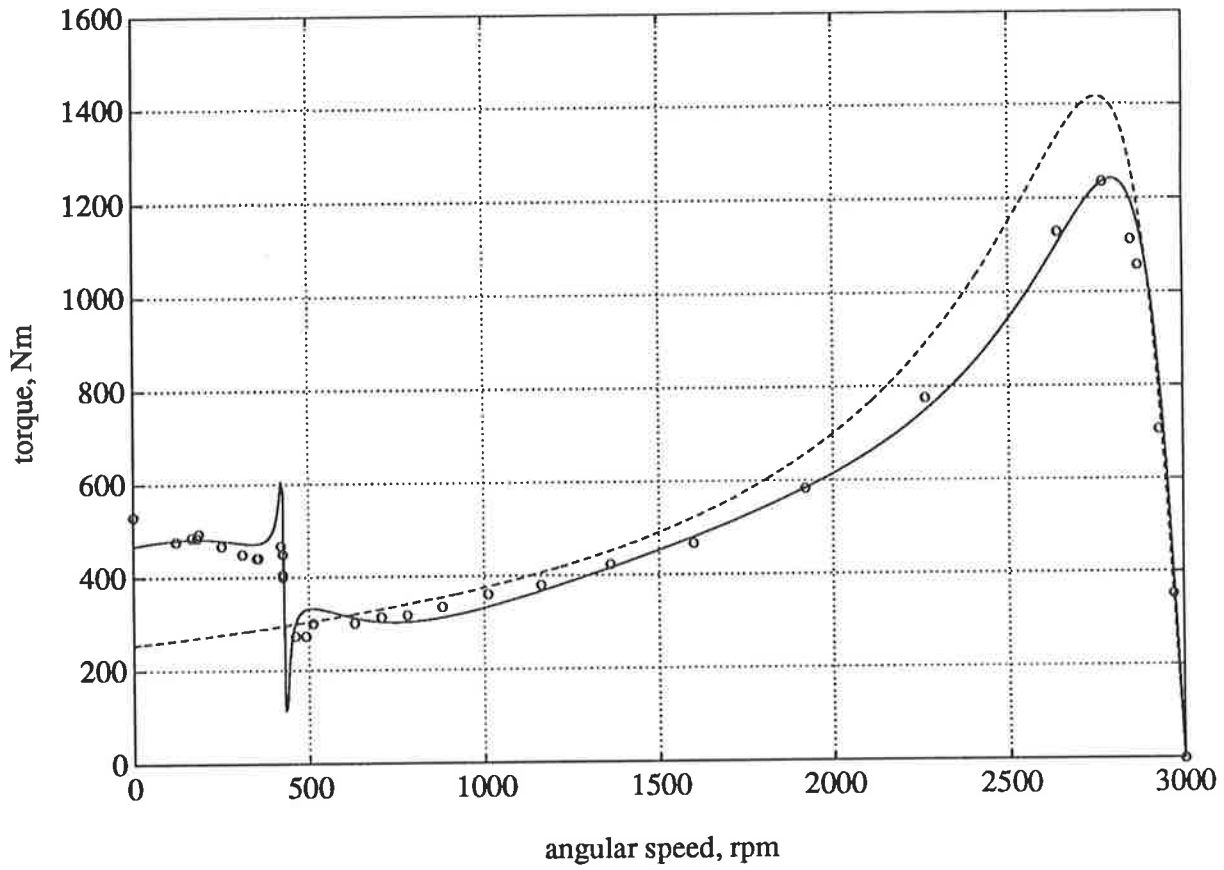


Figure 96

Torque-speed characteristic for Machine I

— Predicted using third-order model of Figure 95  
 (includes current displacement and saturation)

----- Predicted using low order model of Figure 78

o o o Measured

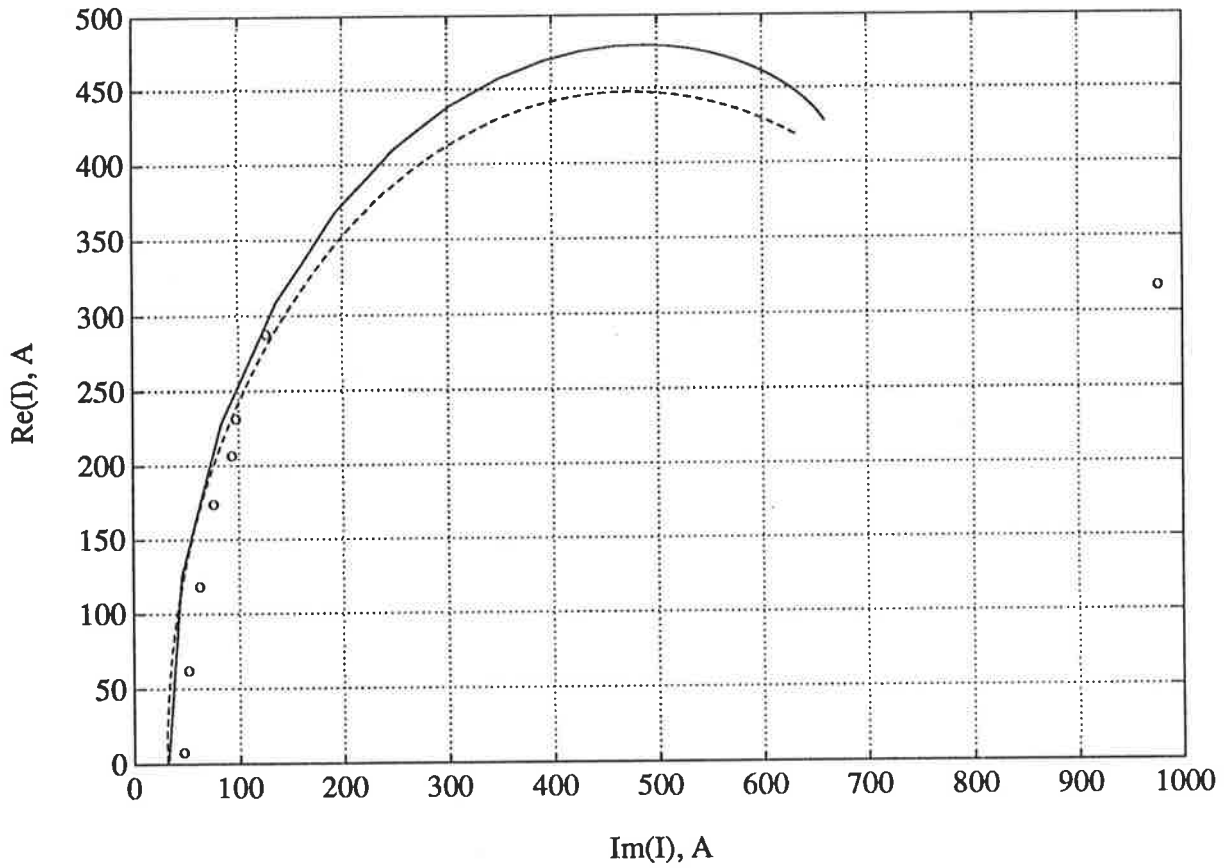


Figure 97

Current locus for Machine I

- Predicted using third-order model of Figure 95  
(includes current displacement and saturation)
- - - Predicted using low order model of Figure 78
- o o o Measured

## 5.4 Dynamic Modelling with Conventional Models

It was stated earlier that lumped parameter circuit models have been popularly used for the dynamic modelling of induction machines. Of these, d-q axis models have been the most prevalent although direct phase circuit models have also found increasing use. The advantage of d-q axis models is that they offer substantial economies in computation time owing to their inherently lucid and compact formulation; however, they are often constrained by the assumption of invariant inductance and fail to give realistic results if inductance variation is significant. Direct phase models overcome this difficulty since the inductance variation is a built-in feature, with the additional advantage that the calculated values are directly related to actually measurable quantities without the need for transformations. However the computation time for direct phase models is considerably longer than for d-q axis models. Compared with these two, space phasor models offer further advantages by way of model compactness and computation time; computation time is even less than that for d-q axis models. Yet, space phasor models are not in general use currently.

All three types of model are to be employed below in predicting the dynamic performance of Machine II. The deliberations are to be confined to the direct-on-line starting conditions since the object is to establish benchmarks for comparison with discrete circuit models. The parameters determined from terminal measurements, as given in Table 11, Section 2.2.2, were used in forming these models on the basis of conventional considerations.

#### 5.4.1 Dynamic Performance Prediction Using Direct Phase Models

Direct phase models for time domain analysis have been considered to be more relevant to the modelling of polyphase induction machines than other types of aggregate circuit models based on transformation techniques. The reasons are twofold. Firstly, directly measurable parameters appear in the model. Secondly, restrictions are often imposed to enable transformation techniques to be applied; this introduces additional error factors into modelling [45,125]. An additional advantage of direct phase models is that they enable such effects as supply unbalance and winding asymmetry to be assessed with relative ease.

The simulation results presented in Figures 98 to 102 were obtained using a direct phase model of Machine II for direct-on-line starting with no load. A comparison with the experimental results given in Figures 70 to 73 reveals that both the stator current and transient torque are considerably over-estimated, which results in a much shorter run-up time for the motor. The predicted speed build-up of Figure 101 is reasonably realistic, although the torque, shown in Figure 100 is excessive. The simulated rotor current is seen to have the correct frequency relationship, which is not the case for models obtained on the basis of transformations where the rotating windings are referred to a stationary reference frame.

Expectably, the detail observed in the measured characteristics is absent, especially in the simulated torque-speed characteristic. The resolution suffers due to the omission of realistic features such as the discrete winding distribution. Thus, direct phase models may not always be relied upon for the prediction of dynamic performance with reasonable accuracy.



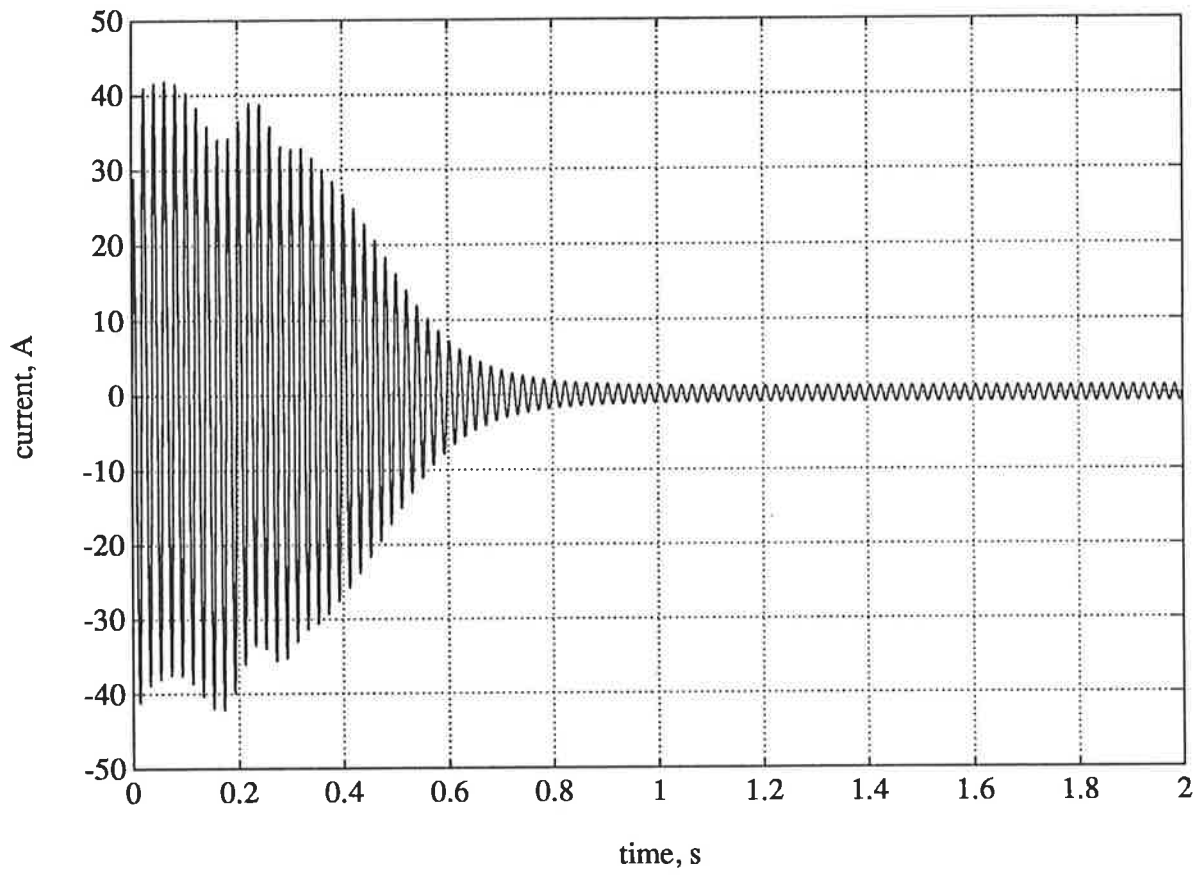


Figure 98

Simulation: Direct phase model

Stator current during start-up for Machine II

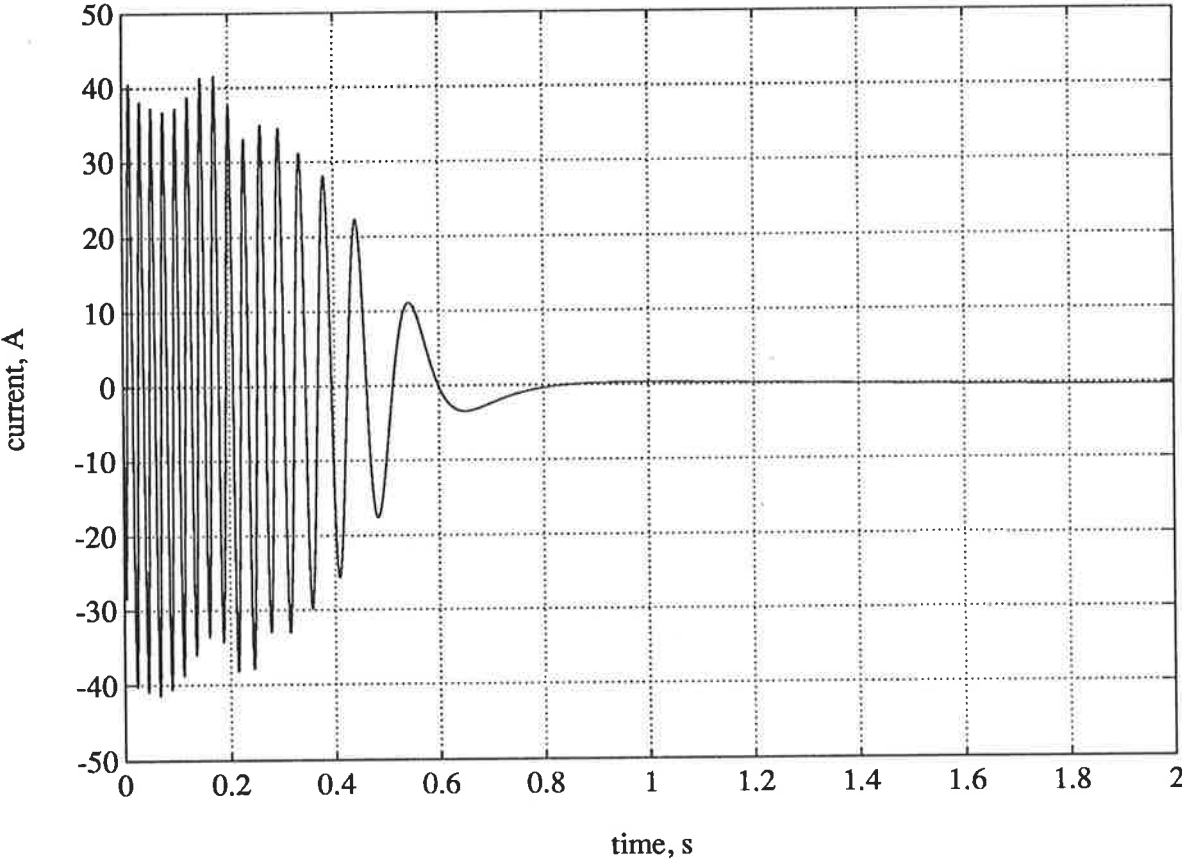


Figure 99

Simulation: Direct phase model

Rotor current during start-up for Machine II

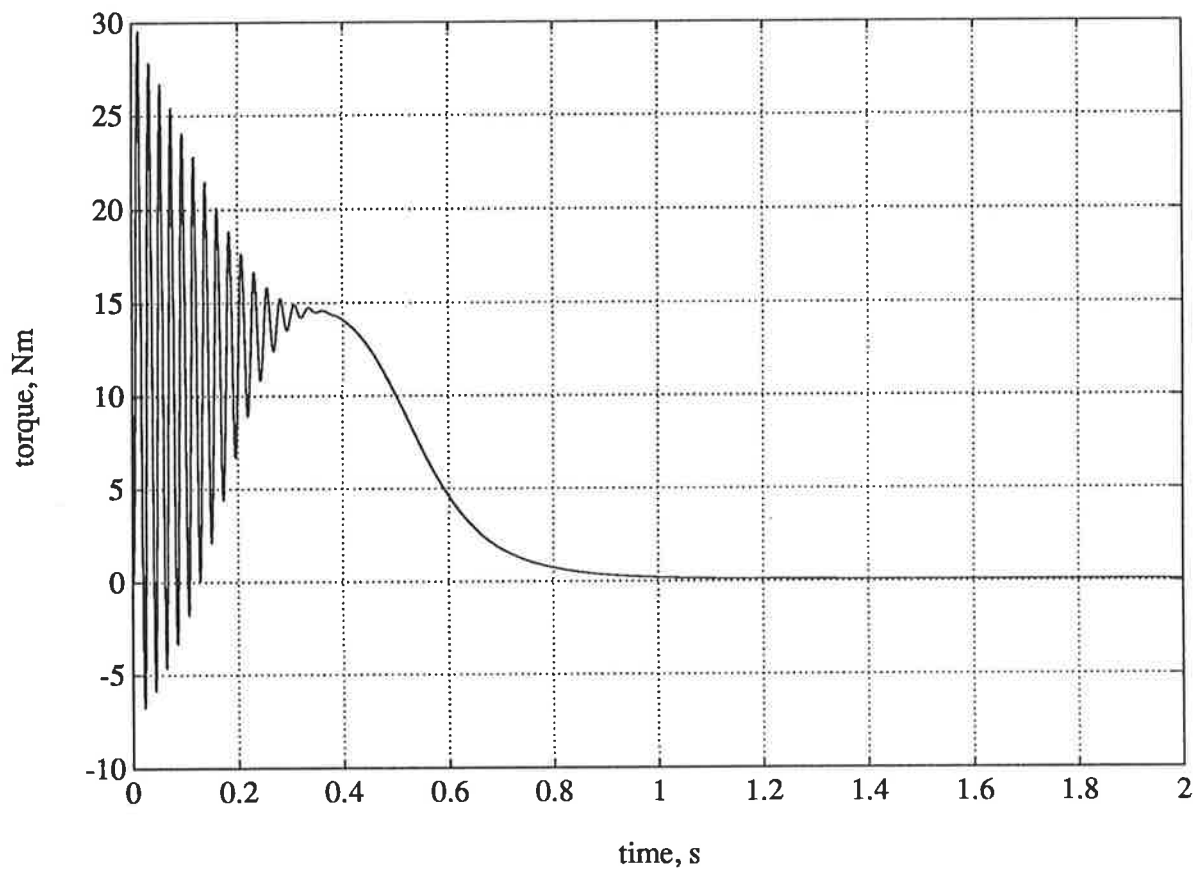


Figure 100

Simulation: Direct phase model

Torque during start-up for Machine II

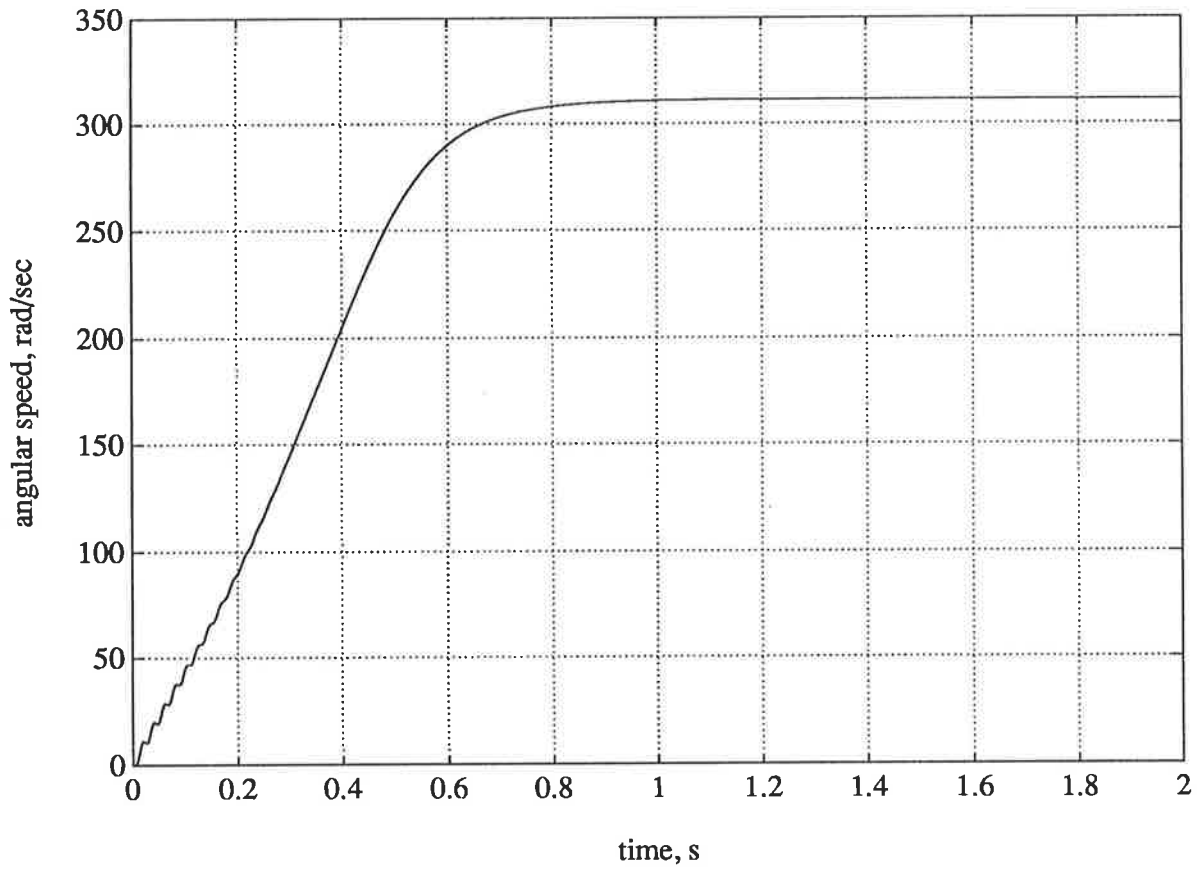


Figure 101

Simulation: Direct phase model

Angular speed during start-up for Machine II

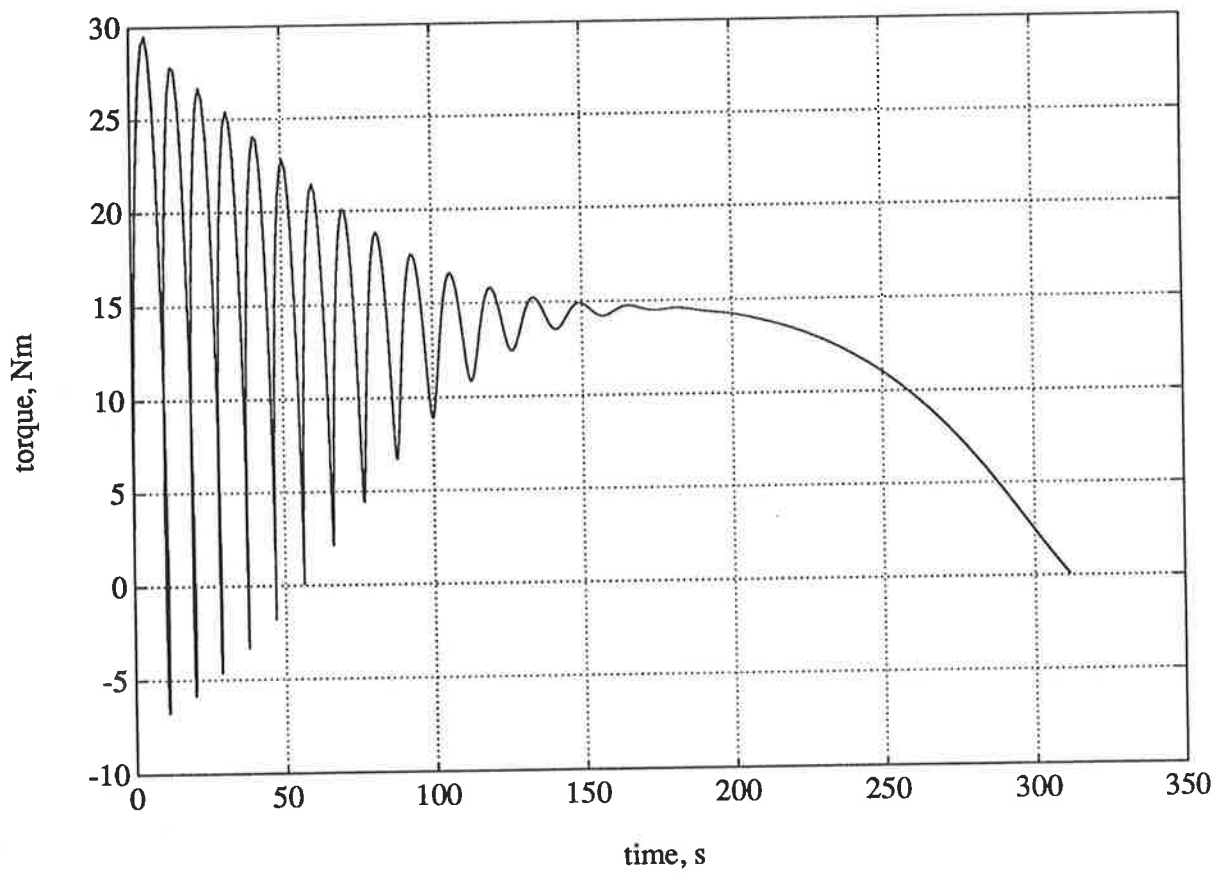


Figure 102

Simulation: Direct phase model

Torque-speed characteristic during start-up for Machine II

#### 5.4.2 Dynamic Performance Prediction Using d-q Models

Circuit models formed on the basis of **d-q** axis transformations have been widely used in simulating transient behaviour of induction machines. They offer distinct computational advantages although their usefulness may be limited due to the idealisations intrinsic in their formation.

The simulation results obtained from a **d-q** model for Machine II are given in Figures 103 to 109. It is seen that the run-up time is predicted with acceptable accuracy. However stator currents are again over-estimated as was the case with the direct phase model. Owing to the transformation technique employed, the rotor currents appear as if they have the same frequency as that of the stator currents, which may lead to some confusion for the unsuspecting observer.

The prediction of the transient torque-speed characteristic, given in Figure 109, is improved considerably; however, the characteristic is void of any parasitic ripple which the actual measurement clearly shows. The same observation applies to the stator and rotor currents shown in Figures 103 to 106; they do not reveal any modulation effects although modulation effects are seen to be present in the measurements. The reason for this lack is obvious: aspects responsible for irregularities such as torque ripple and current modulation are not included in the model. This is a weakness shared with other conventional models as previously observed. The simulation results obtained from **d-q** models can thus be misleading to the unwary.

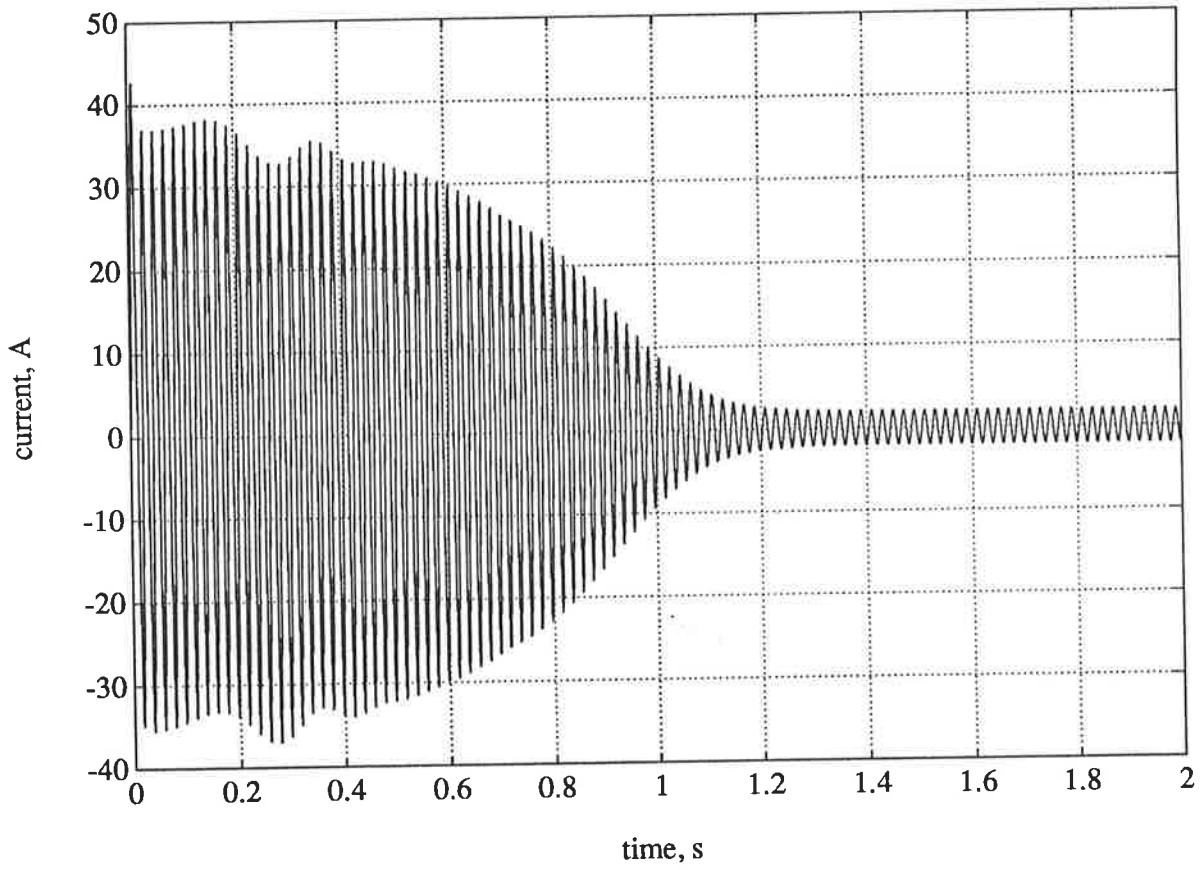


Figure 103

Simulation: **d-q** model

**d**-coil stator current during start-up for Machine II

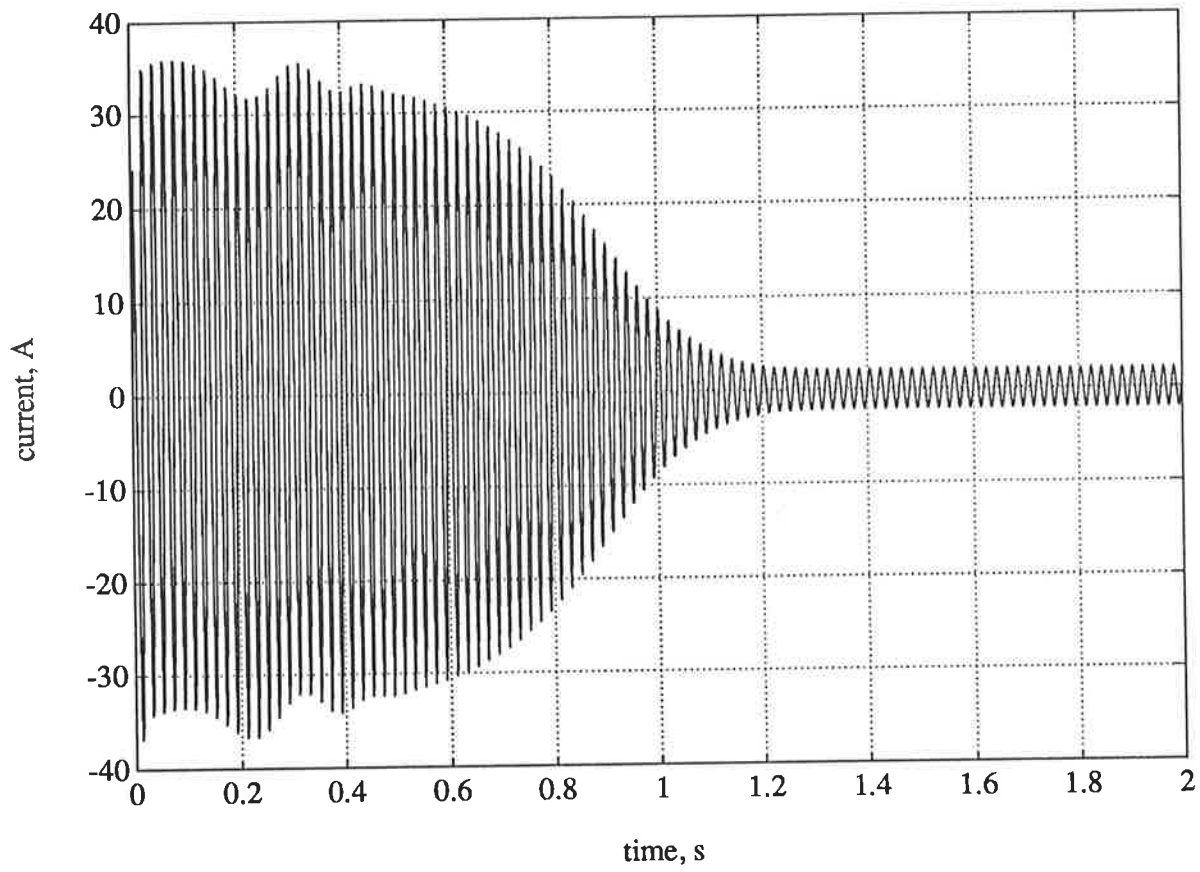


Figure 104

Simulation: d-q model

q-coil stator current during start-up for Machine II



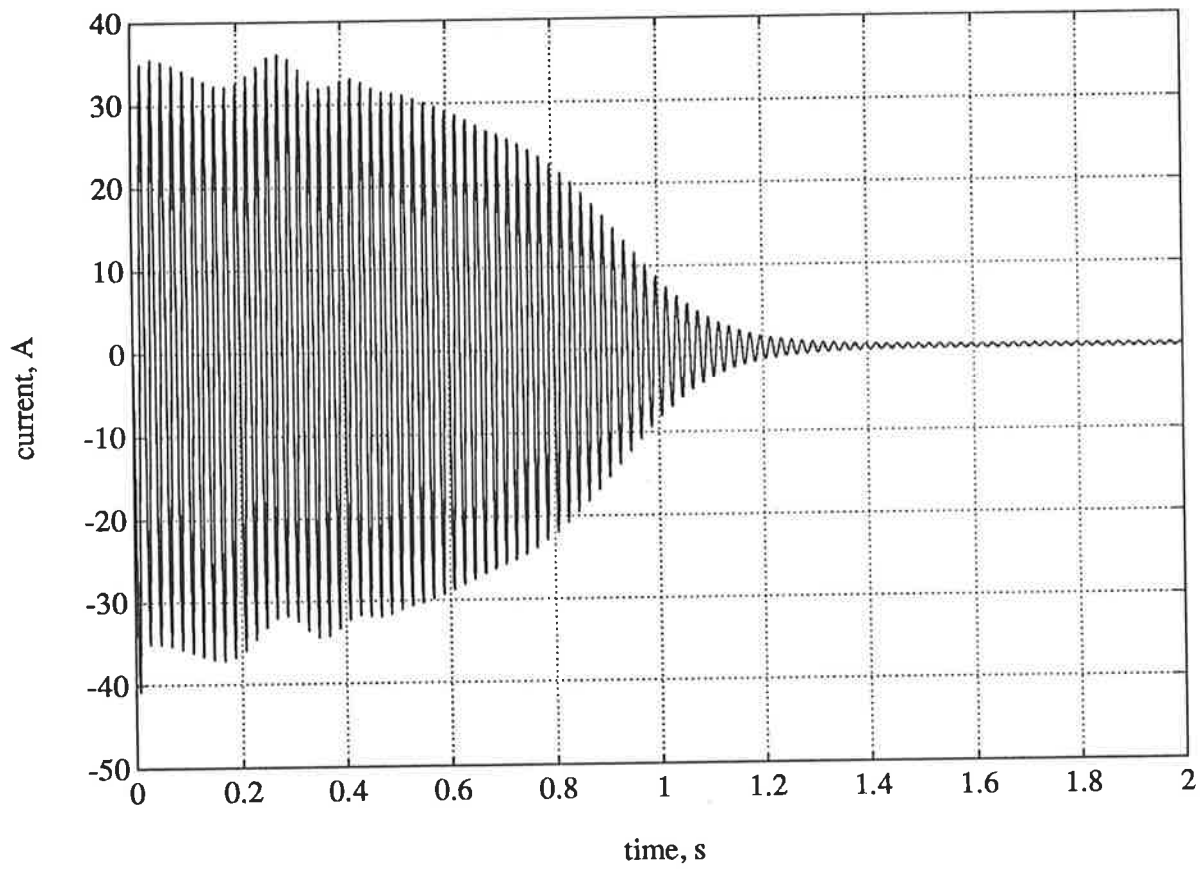


Figure 105

Simulation: **d-q** model

**d**-coil rotor current during start-up for Machine II

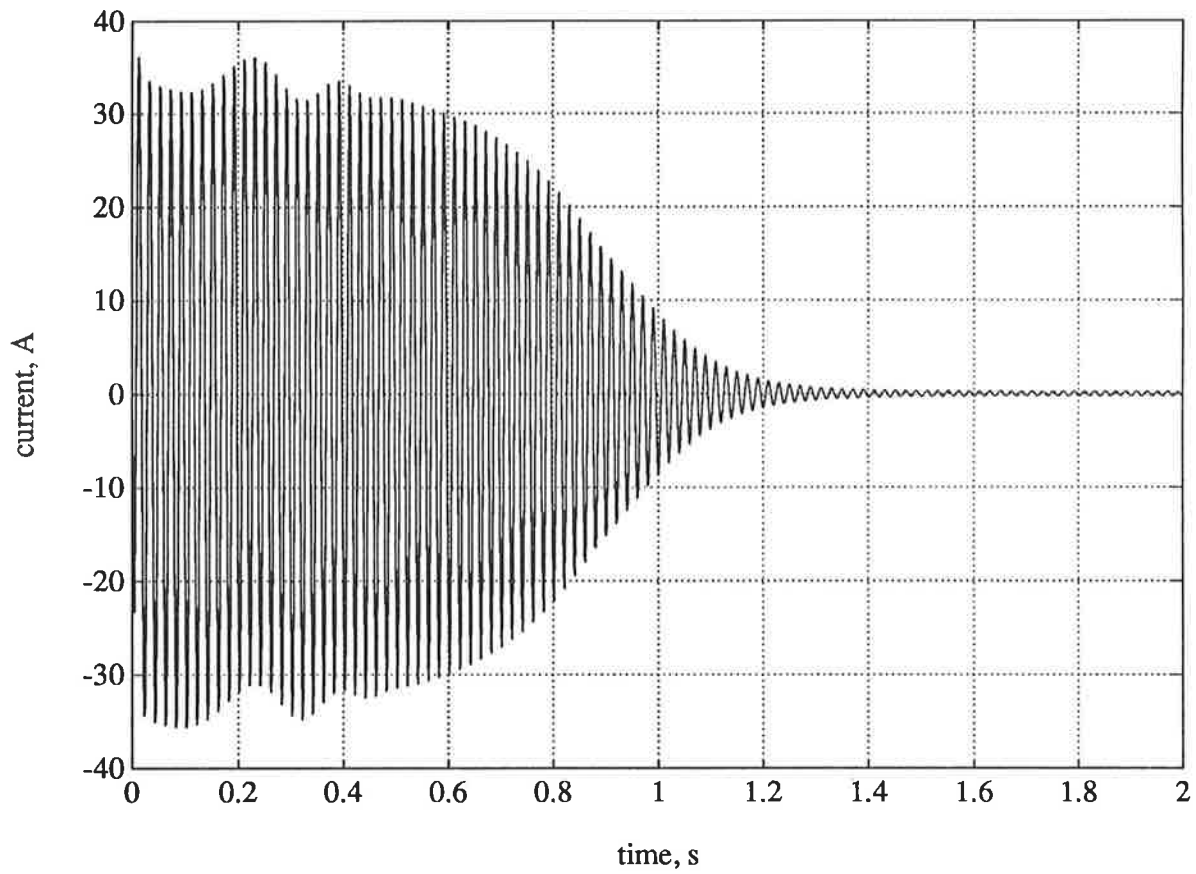


Figure 106

Simulation: **d-q** model

q-coil rotor current during start-up for Machine II

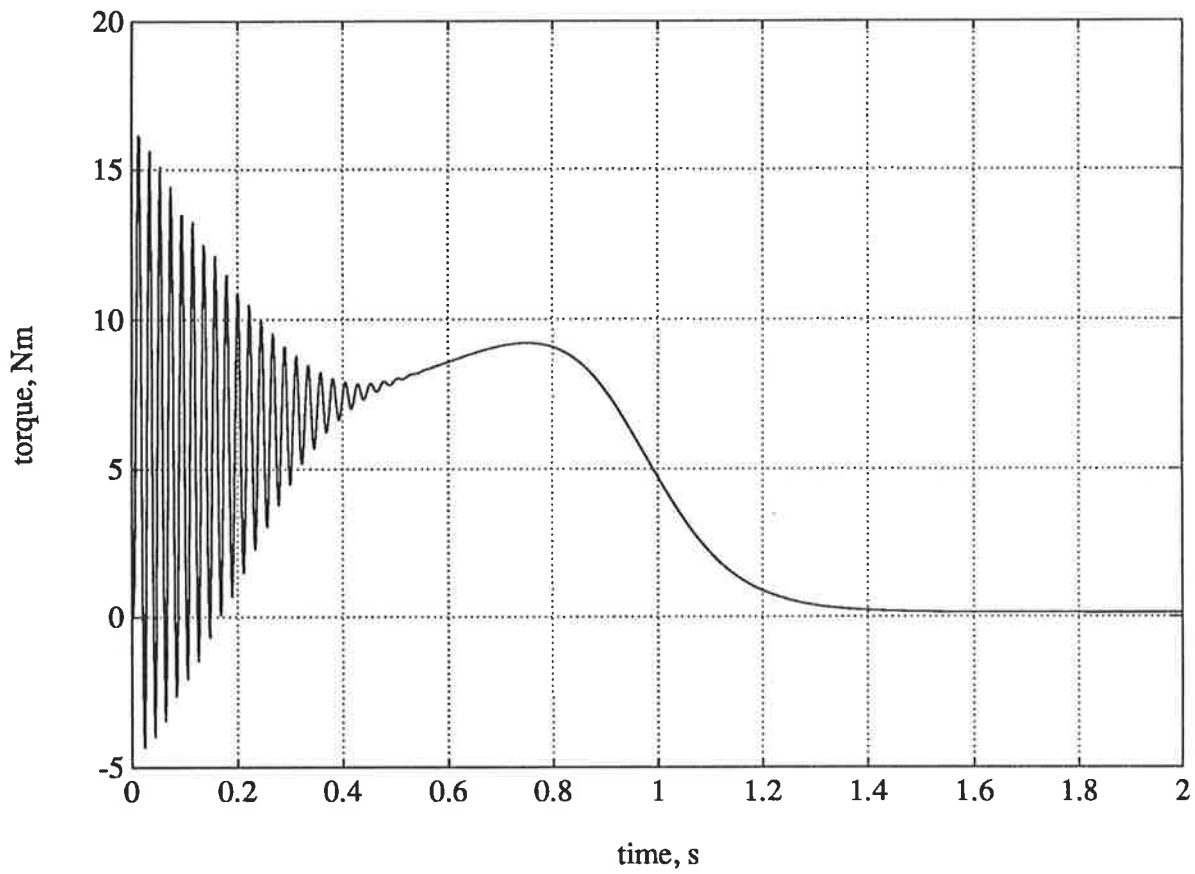


Figure 107

Simulation: **d-q** model

Torque during start-up for Machine II

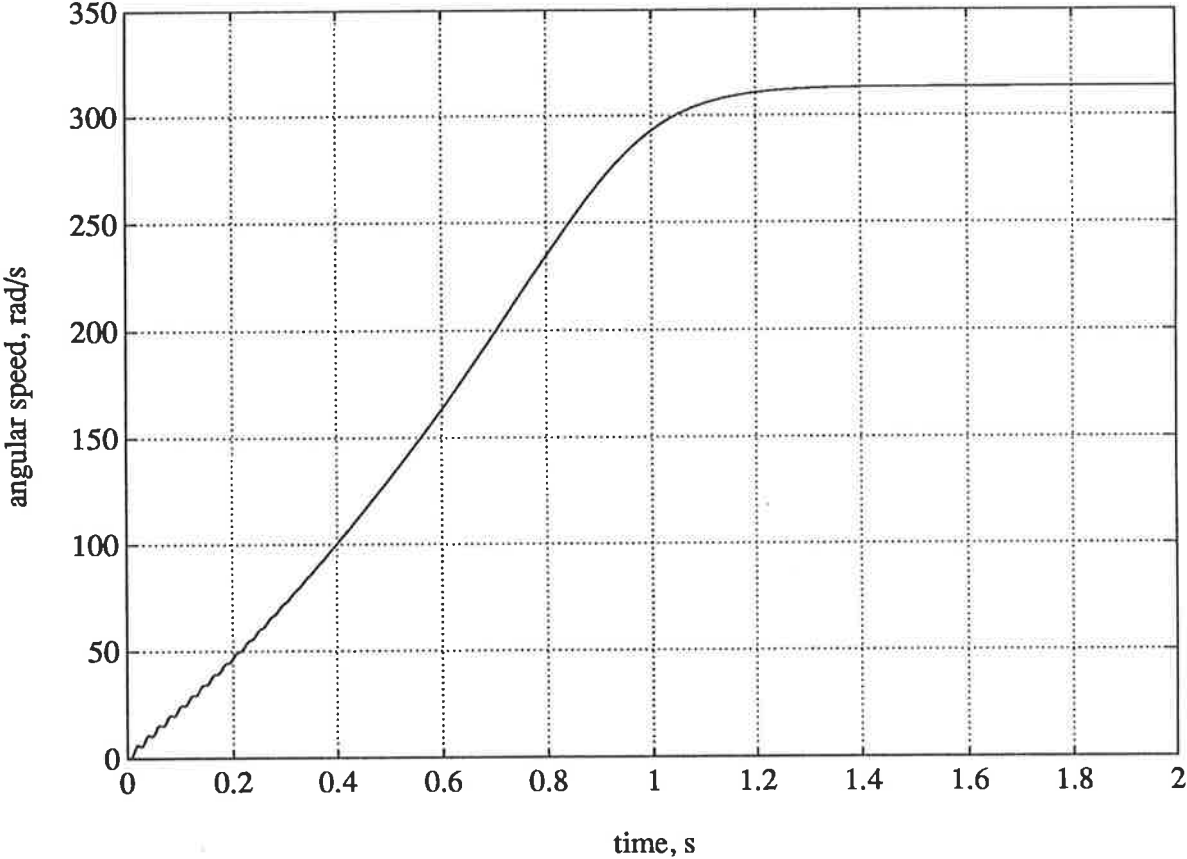


Figure 108

Simulation: **d-q** model

Angular speed during start-up for Machine II

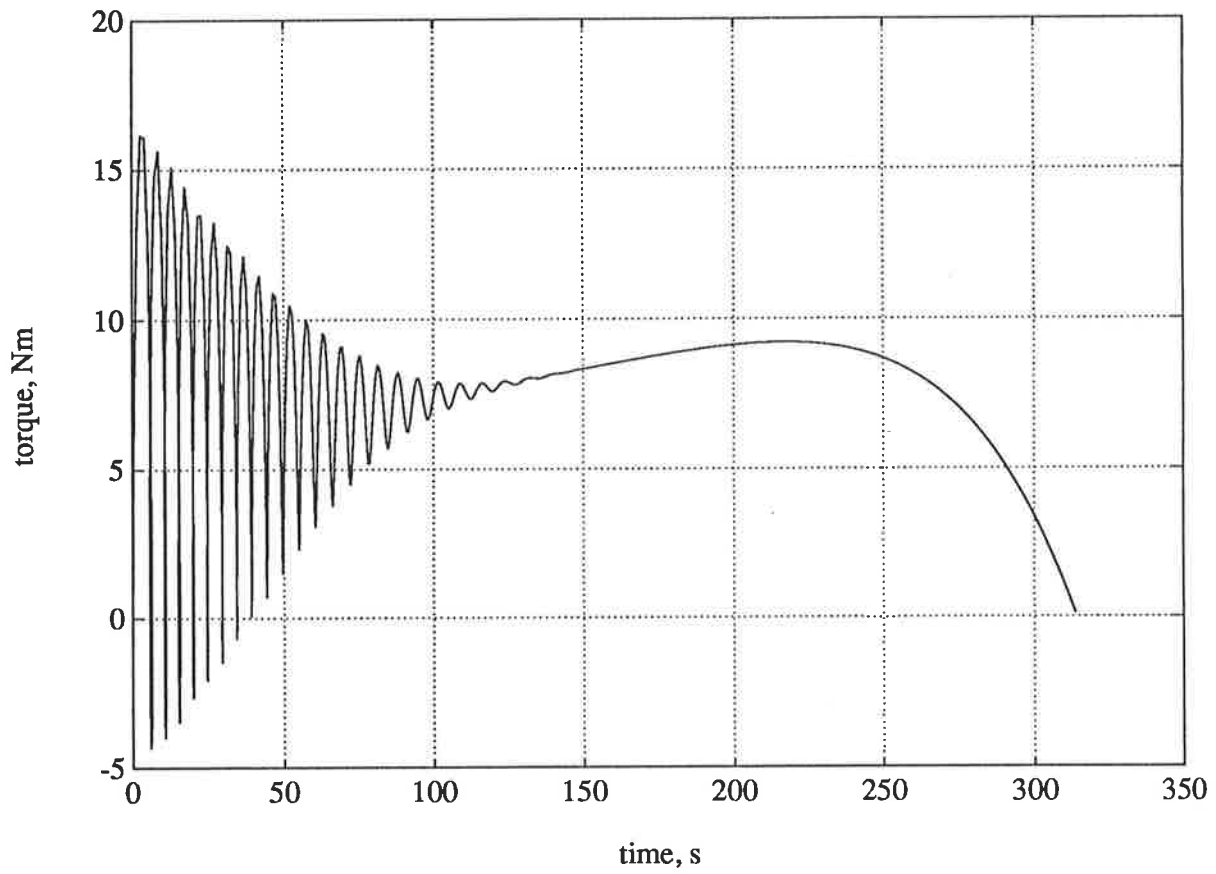


Figure 109

Simulation: **d-q** model

Torque-speed characteristic during start-up for Machine II

### 5.4.3 Dynamic Performance Prediction Using Space-Phasor Models

Space phasor models constitute elegant representations of complex electromagnetic interactions within the machine although they are not as widely used as they deserve. The elegance stems from the representation of spatial relationships with the aid of complex numbers along with time-variant quantities, as explained in Chapter 3, Section 3.6. The need to use complex numbers in numerical integration routines may be construed as a disadvantage of space phasor models compared with other conventional models, however their compactness and computational economies far outweigh this disadvantage in simulating the dynamic behaviour of machines with well behaved performance characteristics. On the other hand, the model compactness may constitute a weakness, especially in predicting the transient performance in cases where discrete effects may be significant. In such cases, the model compactness equates to model coarseness, concealing, for instance, ripple effects which may be present in measured quantities.

Figures 110 to 114 depict the simulation results obtained using a  $\Gamma$ -type space phasor model [134]. In common with other conventional models, the stator current is predicted as being much larger than the measured current. Since the model treats the mutual inductance as being invariant, the rotor current appears to have the same frequency as that of the stator current; a disadvantage shared with the  $d$ - $q$  model. The torque-speed characteristic, shown in Figure 114, is similar to that predicted using the direct phase model and far exceeds the measured values. Qualitative detail observed in the measured characteristic is also absent as was the case with other conventional dynamic models.

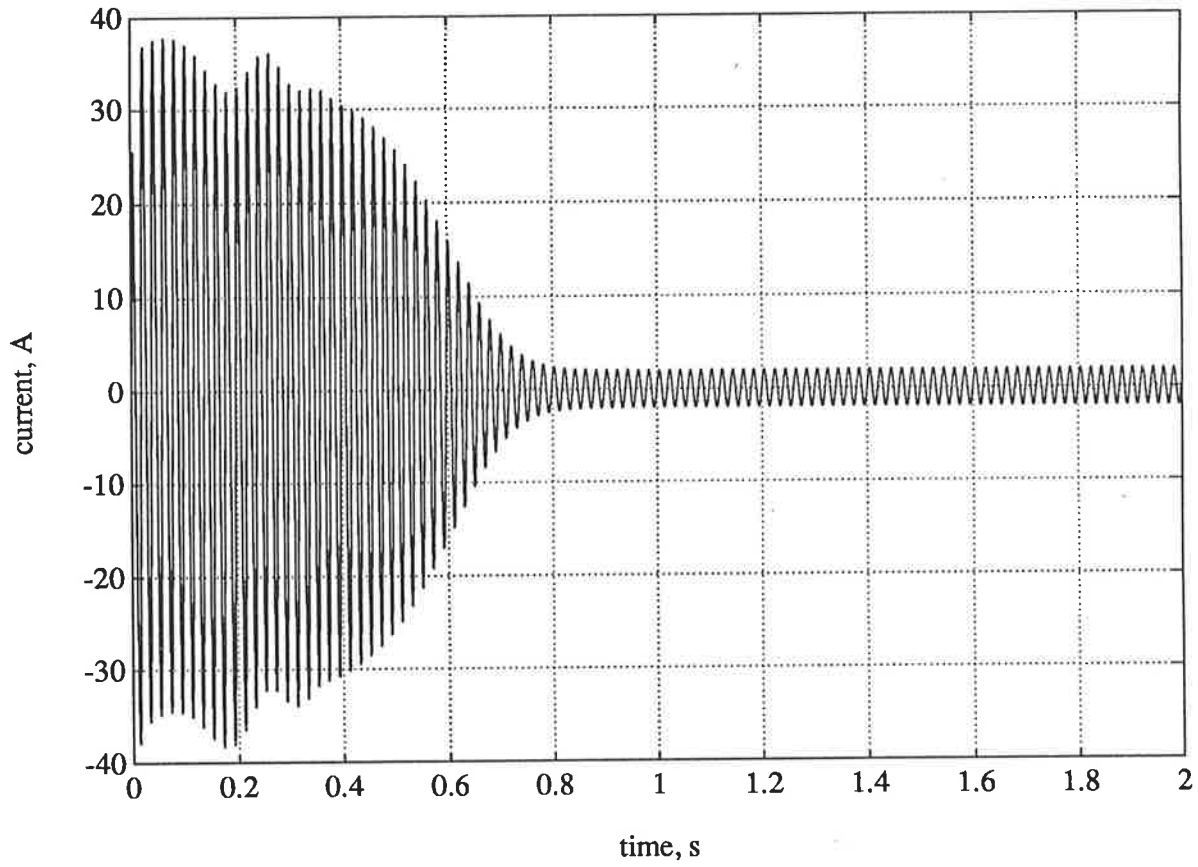


Figure 110

Simulation: space phasor model

Stator current during start-up for Machine II

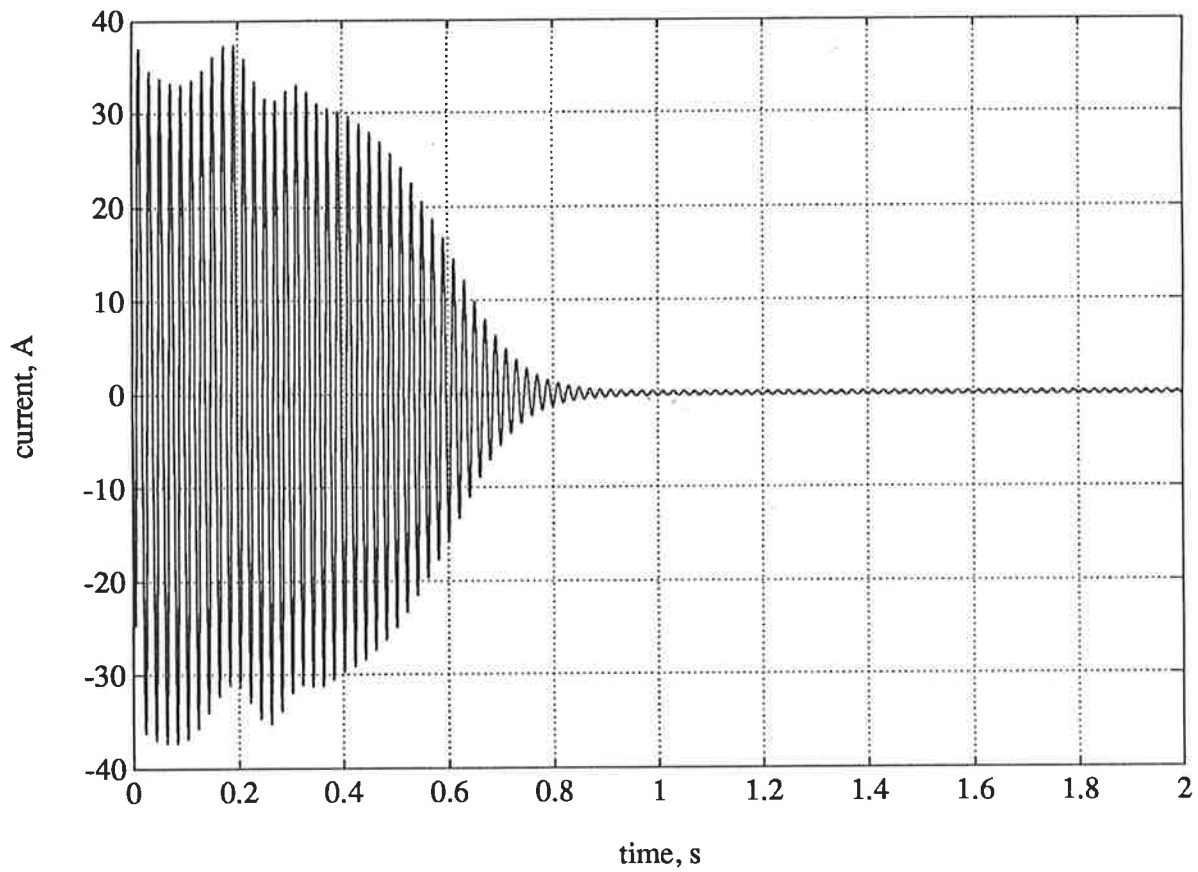


Figure 111

Simulation: space phasor model

Rotor current during start-up for Machine II



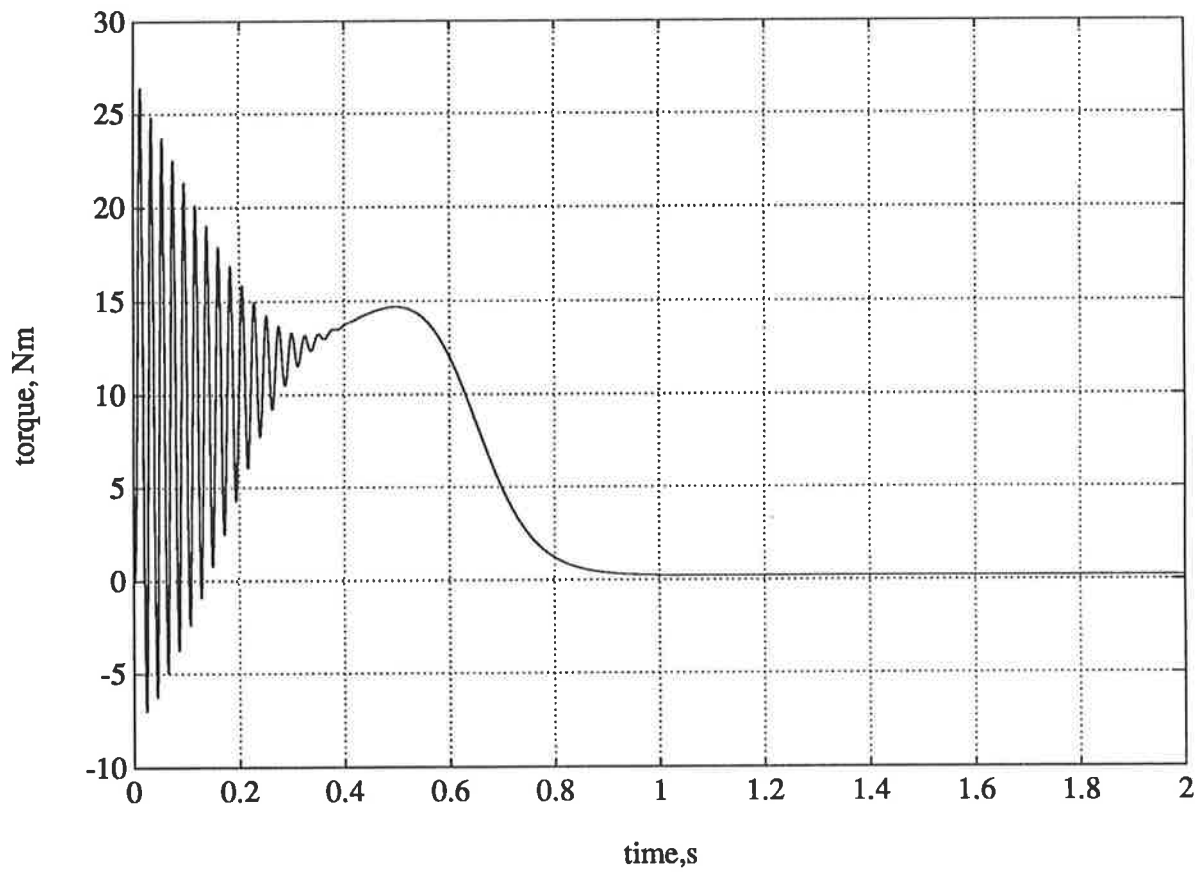


Figure 112

Simulation: space phasor model

Torque during start-up for Machine II

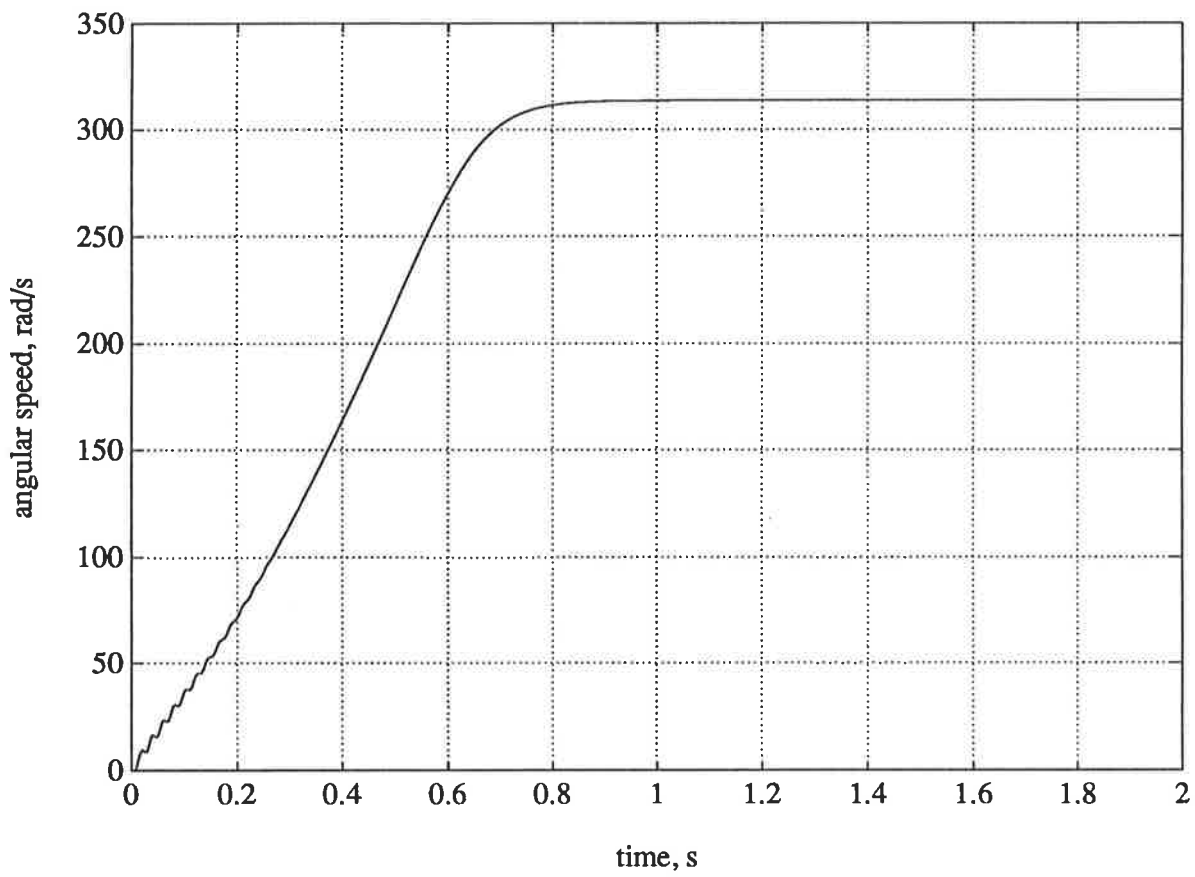


Figure 113

Simulation: space phasor model

Angular speed during start-up for Machine II

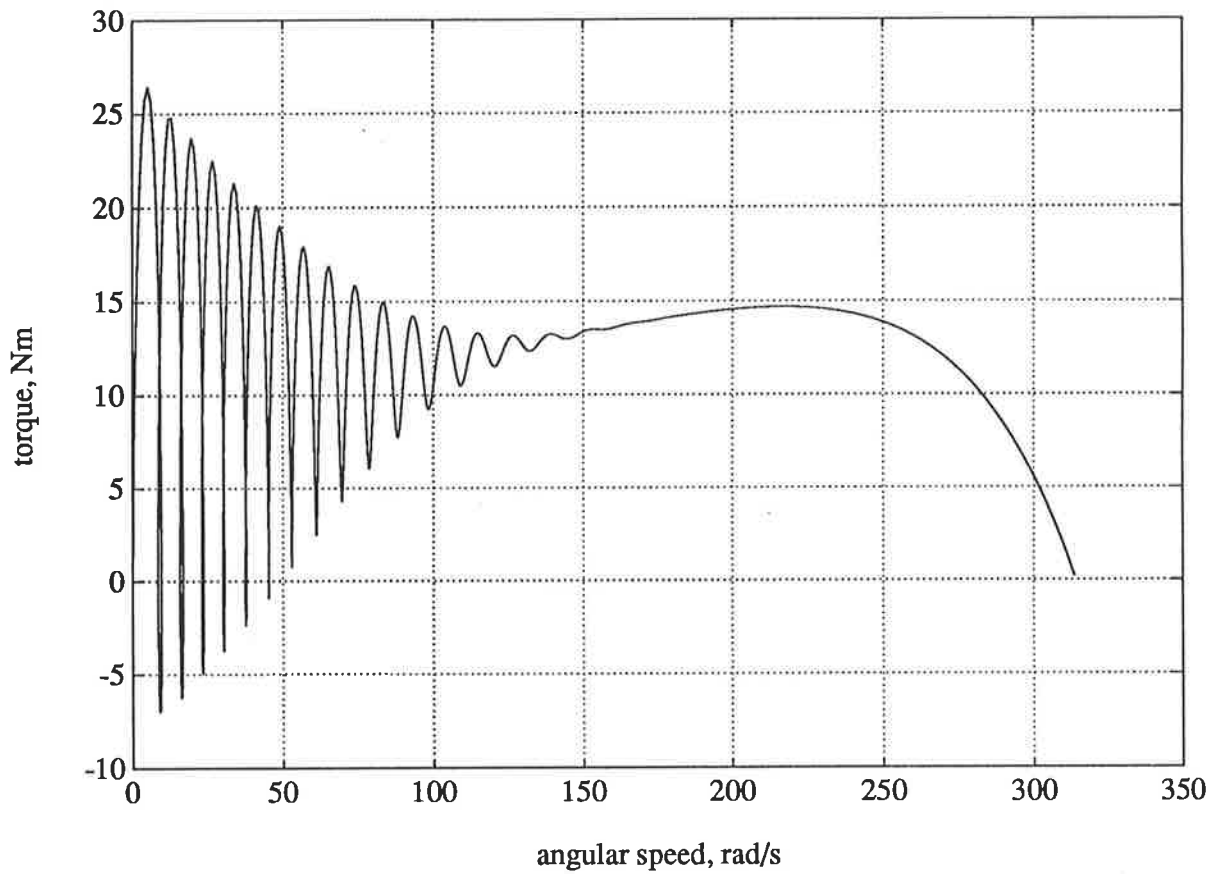


Figure 114

Simulation: space phasor model

Torque-speed characteristic during start-up for Machine II

## 5.5 Dynamic Modelling with Discrete Circuit Model

### 5.5.1 Introduction

The notion of discrete circuit modelling for an induction machine is to be illustrated below for a three-phase cage induction machine with a pole-amplitude-modulated (P.A.M.) winding. The details of the machine, here designated **Machine II**, including core topology and the winding connection diagrams are given in Appendix A.3, Sections A.3.1 to A.3.4. However, it should be noted that the data listed in Appendix A.3 were obtained from a spare machine identical to the test machine, since the test machine belongs to a laboratory set; the only possible way of obtaining the core details and winding information was deemed to be by cutting the spare machine asunder. It was assumed that the test machine had the same data as those obtained from this twin machine.

It was mentioned earlier that winding connections can have a considerable effect on the performance of the machine. This applies especially when parallel paths are present in the phase windings. Discrete circuit models are capable of predicting the performance of an induction machine for any winding configuration. This capability will be demonstrated in Sections 5.5.3 and 5.5.4 for the test machine by simulating its run-up transients by means of connection-specific discrete circuit models: first for the *two-pole* operation and then for the *four-pole* operation of the machine.

The machine used here has skewed rotor slots. However, to demonstrate the suitability of discrete circuit models for sensitivity analysis, in this case assessing the impact on machine performance of skewing, in Section 5.5.3 it will be initially assumed that rotor slots are not skewed. Simulation results obtained when no skewing is assumed will be contrasted with those obtained when skewing is accounted for. It will also be shown that

accounting for current displacement as detailed in Chapter 2 allows for a more realistic prediction to be achieved.

To substantiate the superiority of discrete circuit models, the start-up characteristics for the same conditions will be contrasted with those obtained earlier with the aid of conventional dynamic models. It will be seen that conventional models are unable to match the realism and sensitivity provided by discrete circuit models for performance prediction.

The main forte of the discrete circuit modelling approach is its ability to account for asymmetries in a machine, whether it be due to design features or operating conditions. This feature of discrete circuit models will be demonstrated for the assessment of the effect on machine performance of fault conditions, again using the same machine as above, but this time only in two-pole configuration.

### 5.5.2 Model Formation

A discrete circuit model for Machine II, connected in 2-pole configuration, was formed on the basis of the modelling deliberations of Chapter 4. Model parameters were determined to completely describe the machine electromagnetically in terms of individual stator coils and rotor meshes. A summary of the invariant model parameters is given in Appendix A.3, Section A.3.4. The non-linear model parameters, namely the *angular-position-dependent* mutual inductances between stator coils and rotor meshes were obtained as explained in Section 4.3.5.

The machine was equipped with a P.A.M. winding, a point mentioned earlier. Figure 115 shows the coil group layout for the machine. Appendix A.3, Section A.3.4 gives the winding connections for the two-pole operation of the machine.

1	2	3	4	5	6	7	8	9	10	11	12	13	14	15	16	17	18
A	A	A	B'	B'	B'	C	C	C	A'	A'	A'	B	B	B	C'	C'	C'
B'	B'	C	C	C	A'	A'	A'	B	B	B	C'	C'	C'	A	A	A	B'

Figure 115

Coil group layout for Machine II

The resistive and inductive parameters for the 18 stator coils are both given by 18×18 matrices. The corresponding rotor parameters are described by 66×66 matrices representing 22 rotor bars and a total of 44 end-ring segments joining the rotor bars; this allows for the greatest generality in modelling. The simulation will be initially carried out for identical stator coils and a symmetrical, balanced rotor cage. The complete resistance and the inductance matrices are given as

$$R = \begin{array}{|c|c|} \hline \mathbf{R}^s & \mathbf{0} \\ (18 \times 18) & (18 \times 66) \\ \hline \mathbf{0} & \mathbf{R}^R \\ (66 \times 18) & (66 \times 66) \\ \hline \end{array} \tag{527}$$

$$L = \begin{array}{|c|c|} \hline \mathbf{L}^s & \mathbf{L}^{SR} \\ (18 \times 18) & (18 \times 66) \\ \hline \mathbf{L}^{RS} & \mathbf{L}^R \\ (66 \times 18) & (66 \times 66) \\ \hline \end{array} \tag{528}$$

If driven from a balanced and sinusoidal three-phase supply, the supply voltages are

$$u_{UV}(t) = U \cos \omega t \quad (529)$$

$$u_{VW}(t) = U \cos \left( \omega t - \frac{2\pi}{3} \right) \quad (530)$$

$$u_W(t) = U \cos \left( \omega t + \frac{2\pi}{3} \right) \quad (531)$$

Figure 116 depicts the **star-connected** stator coil groups in the **two-pole** configuration. Considering the direction of current flow, as alluded to by the dot notation, the coil currents can be expressed, in terms of the mesh currents, as

$$i_1^S(t) = i_2^S(t) = i_3^S(t) = i_{UV}(t) - i_{WU}(t) \quad (532)$$

$$i_4^S(t) = i_5^S(t) = i_6^S(t) = i_{VW}(t) - i_{UV}(t) \quad (533)$$

$$i_7^S(t) = i_8^S(t) = i_9^S(t) = i_{WU}(t) - i_{UV}(t) \quad (534)$$

$$i_{10}^S(t) = i_{11}^S(t) = i_{12}^S(t) = - [i_{UV}(t) - i_{WU}(t)] \quad (535)$$

$$i_{13}^S(t) = i_{14}^S(t) = i_{15}^S(t) = - [i_{VW}(t) - i_{UV}(t)] \quad (536)$$

$$i_{16}^S(t) = i_{17}^S(t) = i_{18}^S(t) = - [i_{WU}(t) - i_{UV}(t)] \quad (537)$$



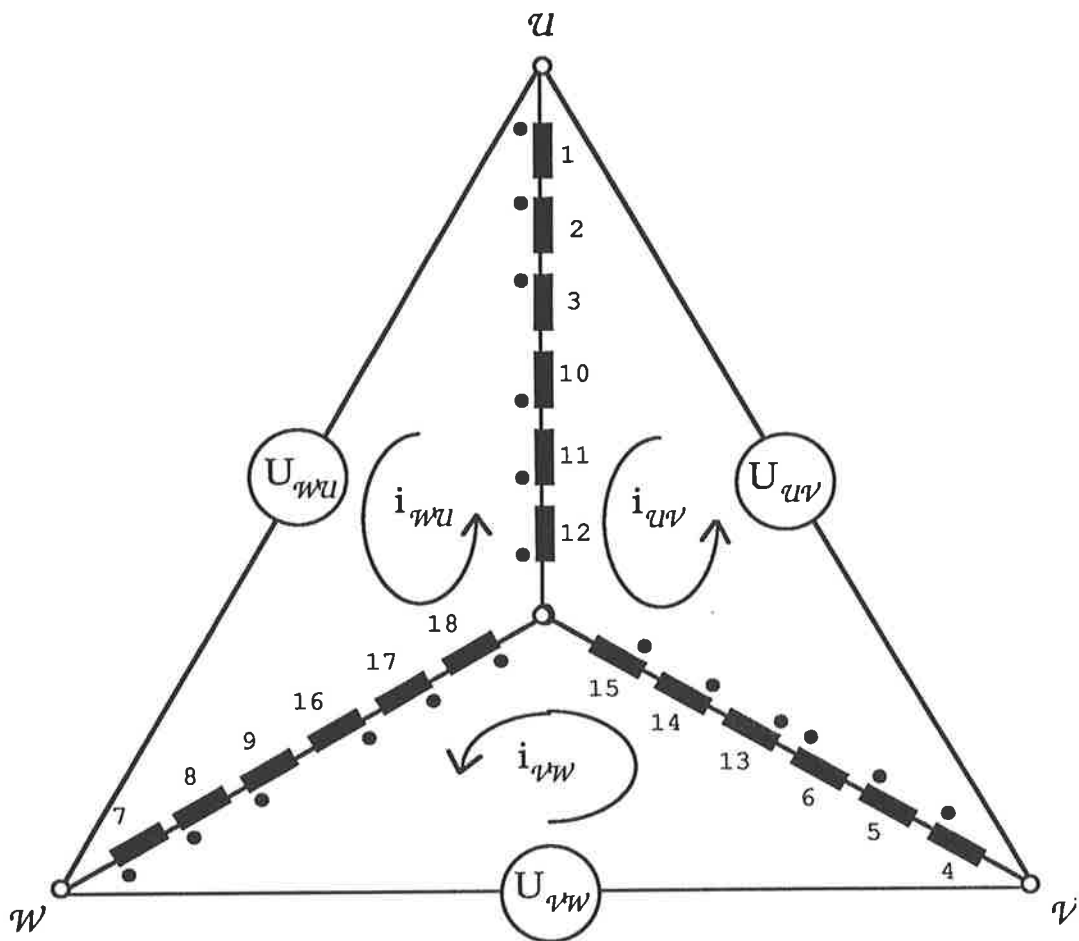


Figure 116

Two-pole wye-connection of coil groups for an 18-coil P.A.M. winding

The current relationships of Equations (532) to (537) can be *forced* by the use of a connection matrix as mentioned earlier. In this case, the 18×3 connection matrix for the **star-connected** stator winding in **2-pole** configuration is obtained as

$$C^s = \begin{array}{c} \begin{array}{c} 1 \\ 2 \\ 3 \\ 4 \\ 5 \\ 6 \\ 7 \\ 8 \\ 9 \\ 10 \\ 11 \\ 12 \\ 13 \\ 14 \\ 15 \\ 16 \\ 17 \\ 18 \end{array} \begin{array}{ccc} i_{uv} & i_{vw} & i_{wu} \\ \hline 1 & & -1 \\ 1 & & -1 \\ 1 & & -1 \\ -1 & -1 & \\ -1 & -1 & \\ -1 & -1 & \\ & 1 & 1 \\ & 1 & 1 \\ & 1 & 1 \\ -1 & & 1 \\ -1 & & 1 \\ -1 & & 1 \\ 1 & 1 & \\ 1 & 1 & \\ 1 & 1 & \\ & -1 & -1 \\ & -1 & -1 \\ & -1 & -1 \end{array} \end{array} \quad (538)$$

where  $i_{uv}$ ,  $i_{vw}$ , and  $i_{wu}$  represent the stator mesh currents affecting the three series-connected coil groups depicted in Figure 116. The rotor connection matrix is a 66×24 matrix. The dimensions arise from the 22 rotor bars, the 44 end-ring segments on both cage ends, joining the rotor

bars on the one hand and two end-rings on the other hand. The end-ring segments are included separately to allow the model to be used later when fault conditions are to be assessed generally by the use of the model. The complete connection matrix is obtained by combining the connection matrix of the stator with that of the rotor as

$$C = \begin{array}{|c|c|} \hline \begin{array}{c} C^S \\ (18 \times 3) \end{array} & \begin{array}{c} 0 \\ (18 \times 24) \end{array} \\ \hline \begin{array}{c} 0 \\ (66 \times 3) \end{array} & \begin{array}{c} C^R \\ (66 \times 24) \end{array} \\ \hline \end{array} \quad (539)$$

The preceding deliberations apply to the test machine in a two-pole configuration. If the machine were to be connected in a four-pole configuration, coil currents would have to be ascertained on the basis of a series/parallel combination of the coils as necessitated by the pole-amplitude modulation. Figure 117 illustrates this **double-star-connection** of the stator coil groups of the same machine in a **four-pole** configuration. Again, with the dot notations indicated, the coil currents can now be expressed, in terms of the mesh currents, as

$$i_1^S(t) = i_2^S(t) = i_3^S(t) = i_{uv}(t) - i_{vu}(t) \quad (540)$$

$$i_4^S(t) = i_5^S(t) = i_6^S(t) = i_{vw}(t) - i_{wv}(t) \quad (541)$$

$$i_7^S(t) = i_8^S(t) = i_9^S(t) = i_{wu}(t) - i_{uw}(t) \quad (542)$$

$$i_{10}^S(t) = i_{11}^S(t) = i_{12}^S(t) = i_{uv}(t) - i_{vu}(t) \quad (543)$$

$$i_{13}^S(t) = i_{14}^S(t) = i_{15}^S(t) = i_{vw}(t) - i_{wv}(t) \quad (544)$$

$$i_{16}^S(t) = i_{17}^S(t) = i_{18}^S(t) = (i_{vw}(t) - i_{wv}(t)) \quad (545)$$

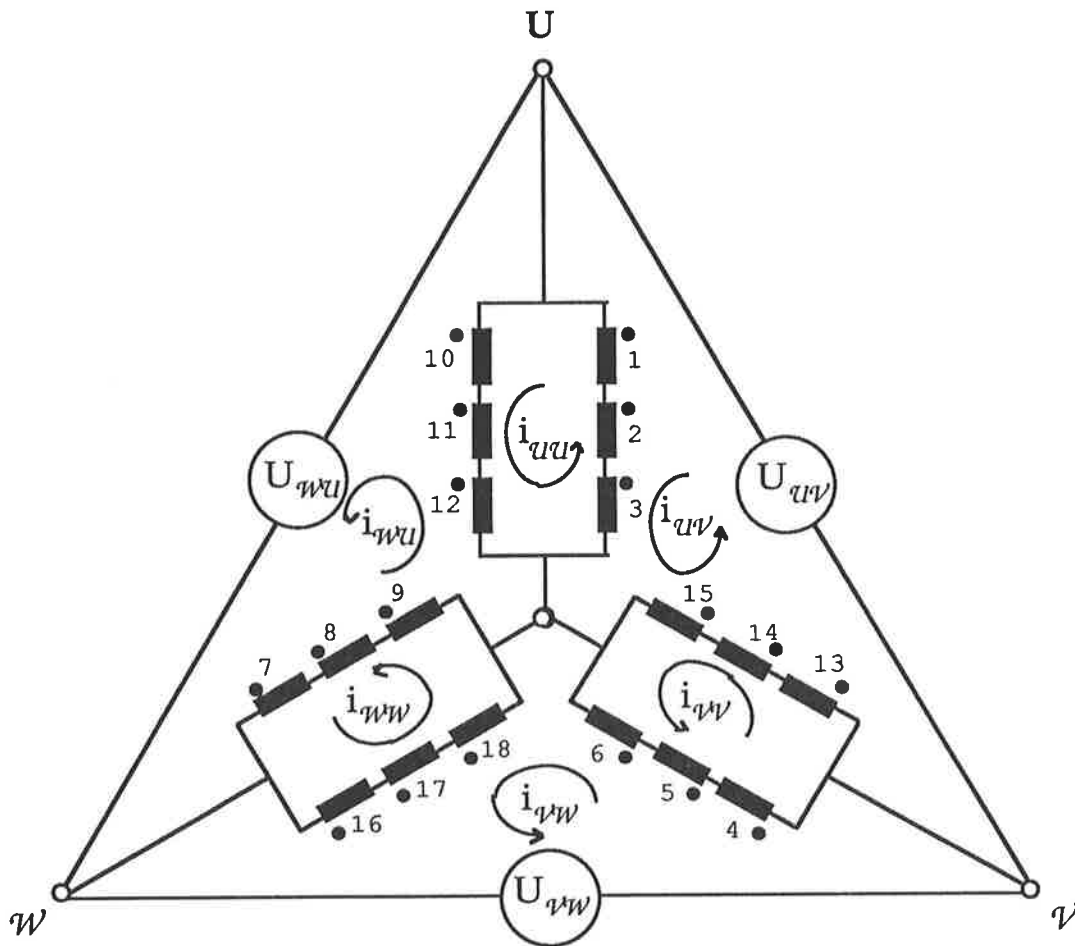


Figure 117

Four-pole connection of coil groups for an 18-coil P.A.M. winding



$$C = \begin{array}{|c|c|} \hline C^S & 0 \\ (18 \times 6) & (18 \times 24) \\ \hline 0 & C^R \\ (66 \times 6) & (66 \times 24) \\ \hline \end{array} \quad (547)$$

For both winding configurations, the simulation can now be carried out using the state variable formulation of the machine model in the form

$$p\mathbf{x} = \mathbf{A}\mathbf{x} + \mathbf{B}\mathbf{u} \quad (548)$$

where  $\mathbf{A}$  and  $\mathbf{B}$  represent the Bashkow  $\mathbf{A}$  matrix and the constant matrix as discussed previously.

The following sections are to illustrate the power of the discrete circuit modelling approach by applying the above to various operating conditions of an induction machine. In these, Equation (548) is solved numerically using a fourth-order Runge-Kutta method with fixed step-size. In all simulations, initial conditions are set to zero unless otherwise stated, implying zero initial value for the currents, the rotor angular position and the rotor angular velocity. This implies, among other things, that at rest the rotor datum coincides with the stator-bound reference datum and switching occurs at the instance when the terminal voltage for Phase A is at its maximum. However, these conditions were not adhered to during

the actual measurements on Machine II, since the objective was deemed to be the authentication of the ability of a discrete circuit model to deliver detail which coarse models are unable to match. The randomness of the initial rotor position during measurement and the point-on-wave on the voltage waveforms at the instance of switching should explain the phase and magnitude differences between the simulated and measured results.

In the simulations to follow in Section 5.5.3, a discrete circuit model will be used progressively in three stages to substantiate the model sensitivity to parameter variations. *Firstly*, it will be assumed that the rotor slots are unskewed to show what effect unskewed rotor slots have on the machine performance. *Secondly*, current displacement effects will be included in the model, still assuming no skewing. *Thirdly*, skewing will be included in addition to current displacement effects; as will be seen, the improvement in the prediction accuracy is remarkable when both these physically relevant aspects are introduced into the model. In all other cases presented in the sections to follow, both current displacement and skewing will be accounted for in the models.

Section 5.5.4 will show that the presence of parallel connections within the winding groups has a distinct effect on the performance of the machine; this will be demonstrated for the start-up transient of Machine II in four-pole mode. Section 5.5.5 will demonstrate the suitability of the discrete circuit model in simulating the behaviour of a machine with rotor faults. Section 5.5.6 will examine further uses of the discrete circuit model; this will include the transient blocked rotor behaviour, the reswitching transients and the quasi steady-state regime.

### 5.5.3 Simulation of Start-Up Transients (2-pole)

Direct-on-line starting of an induction motor constitutes a most severe transient and is of utmost importance in practice due to its wide-spread use. Discrete circuit models as postulated above constitute an effective means of assessing the performance of a machine under such transient conditions. This is to be demonstrated below by simulating the direct-on-line start-up transients of Machine II for the 2-pole connection of the P.A.M. winding.

Unskewed slots have long been recognised as the source of parasitic behaviour in induction machines; that is why electrical machine manufacturers resort to skewing as a preventive measure, although the cause-effect relationship has not been established that well. The discrete circuit models solicited in this thesis are sensitive to the amount of skewing and hence are capable of assessing the impact skewing has on the machine behaviour. In what follows, this outstanding feature of the discrete circuit model is to be demonstrated in three successive steps: first with a model which assumes no skew as well as uniform current density distribution in the rotor throughout, then with a model which assumes no skew but allows for current displacement effects in the rotor and finally with a model which accounts for both skew and current displacement.

Simulation results, when no skew is assumed, are presented in the suite of Figures 118 to 124. As can be seen, the test machine would be subject to severe parasitic behaviour if the rotor slots were not to be skewed. Furthermore, the machine suffers from marginal instability in the operating region. Figure 118 shows the stator current for Phase A during the start-up obtained from the simulation. Figure 119 gives all phase



currents for the first 100ms of the simulation to illustrate the phase relationships and the magnitudes of the starting currents. The simulated rotor bar current is given in Figure 120. Figure 121 shows all bar currents as a cascade plot for the first 100ms of the simulation. Figures 122 and 123 illustrate the torque and speed build-up during starting. Figure 124 gives the dynamic torque-speed characteristic. These simulations amply prove that the absence of skewing would be grossly detrimental to the transient performance of Machine II.

The next suite of simulation results, presented in Figures 125 to 131, shows the impact of accounting for the current displacement effects in the rotor bars; the envelopes of the characteristics are affected, but the parasitic behaviour remains. Again, the conclusion is that skewing is the crucial parameter in controlling the parasitic behaviour.

The above conclusion is supported by the next set of simulation results given in Figures 132 to 138. This time, both skewing and the current displacement are taken into account. The improvement in the performance of the machine is remarkable; parasitic behaviour is almost entirely eliminated and the machine is no longer subject to marginal instability in the operating region as was the case before.

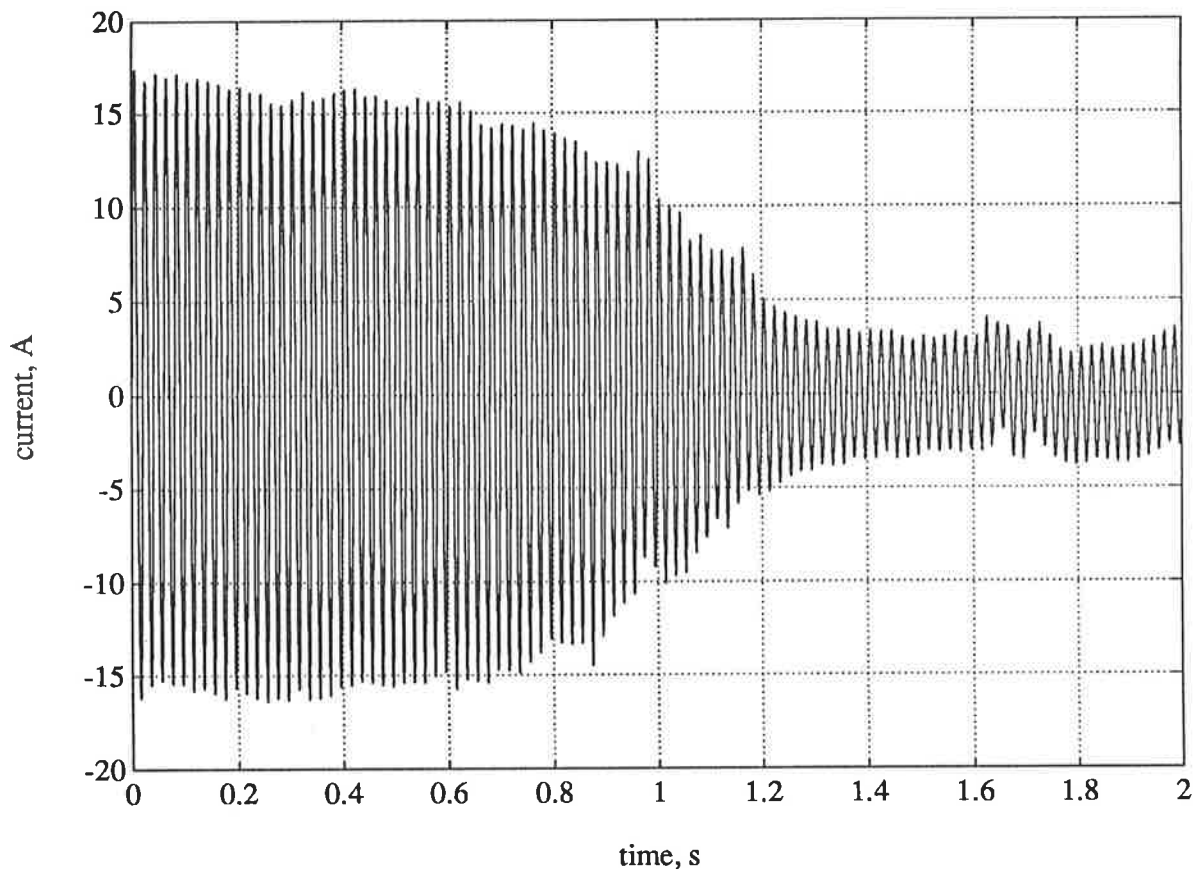


Figure 118

Simulated stator current during start-up for Machine II (2-pole)

(no skew, uniform current density in rotor)

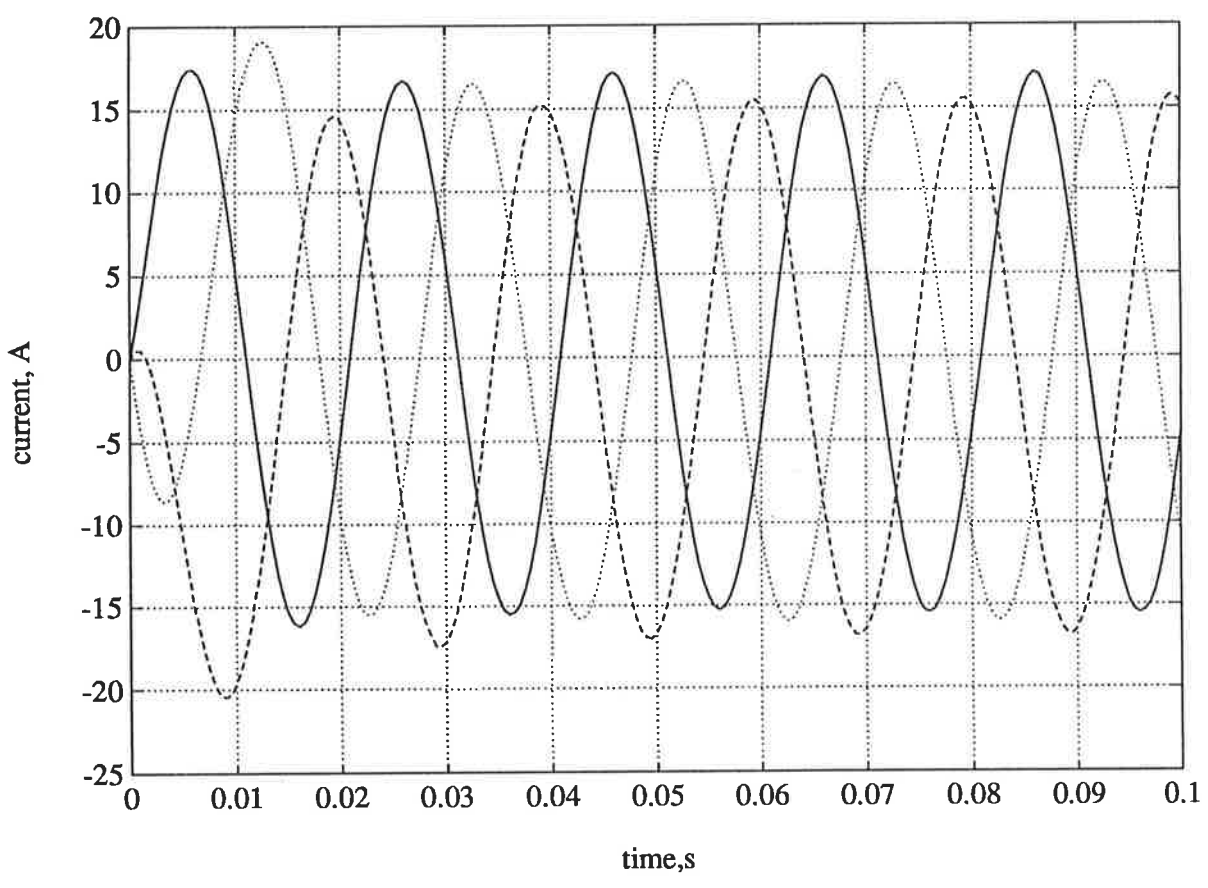


Figure 119  
Simulated stator currents for the first 100ms for Machine II  
(2-pole)  
(no skew, uniform current density in rotor)

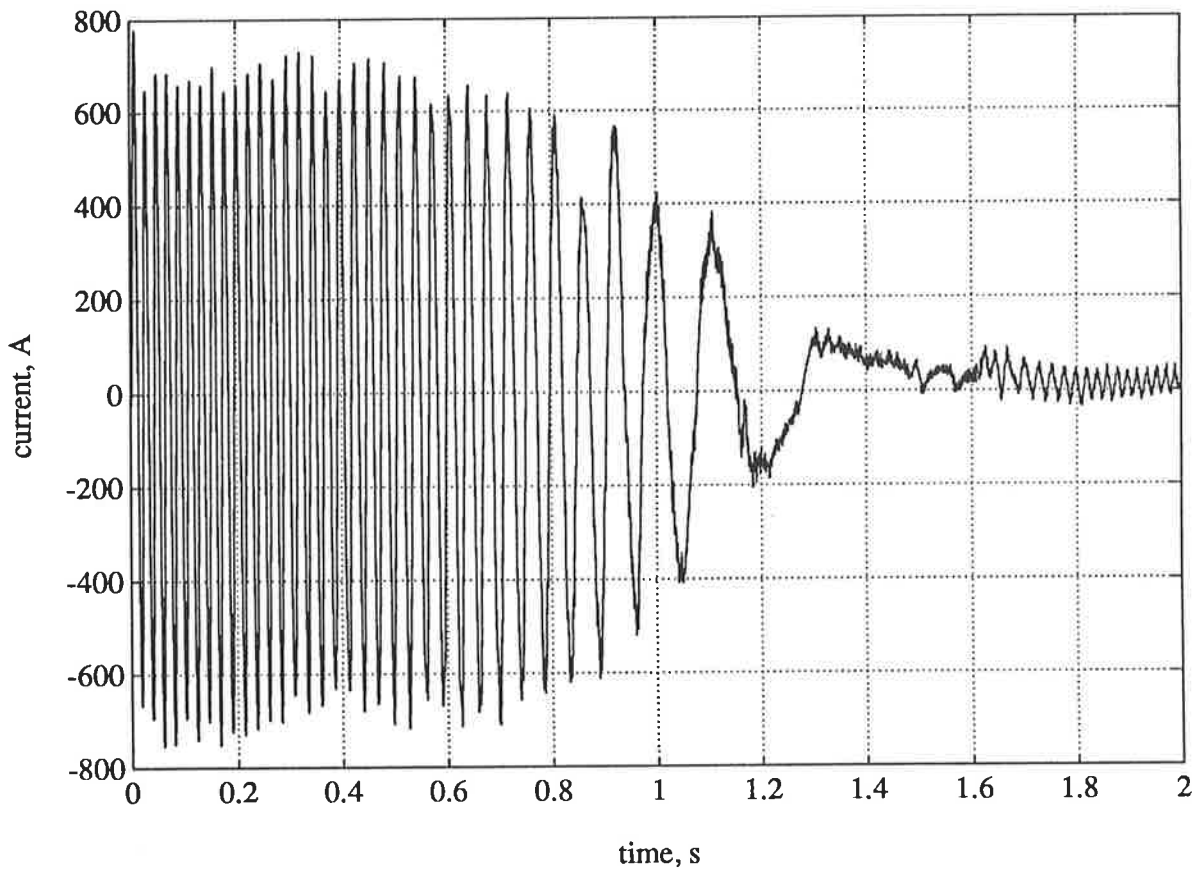


Figure 120

Simulated rotor bar current during start-up for Machine II

(2-pole)

(no skew, uniform current density in rotor)

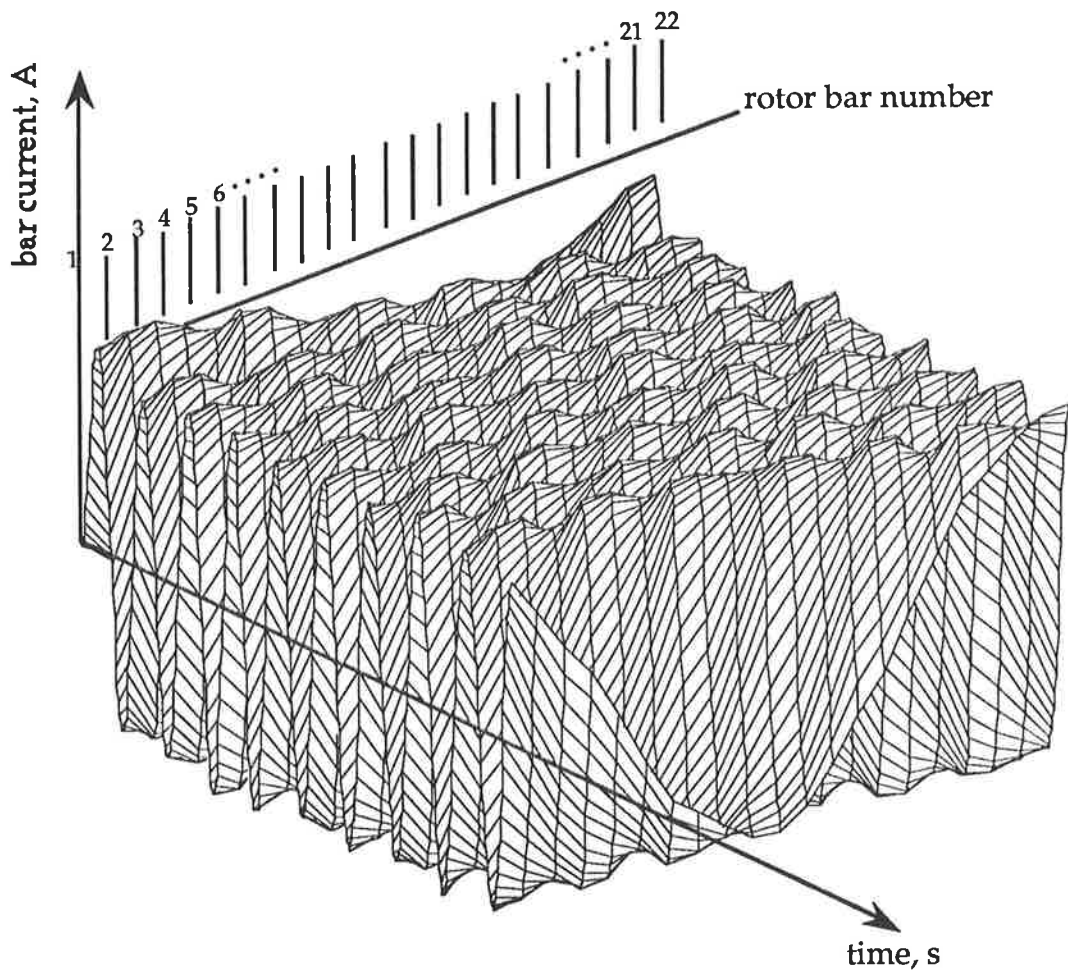


Figure 121

Simulated rotor bar currents for the first 100ms for Machine II

(2-pole)

(no skew, uniform current density in rotor)

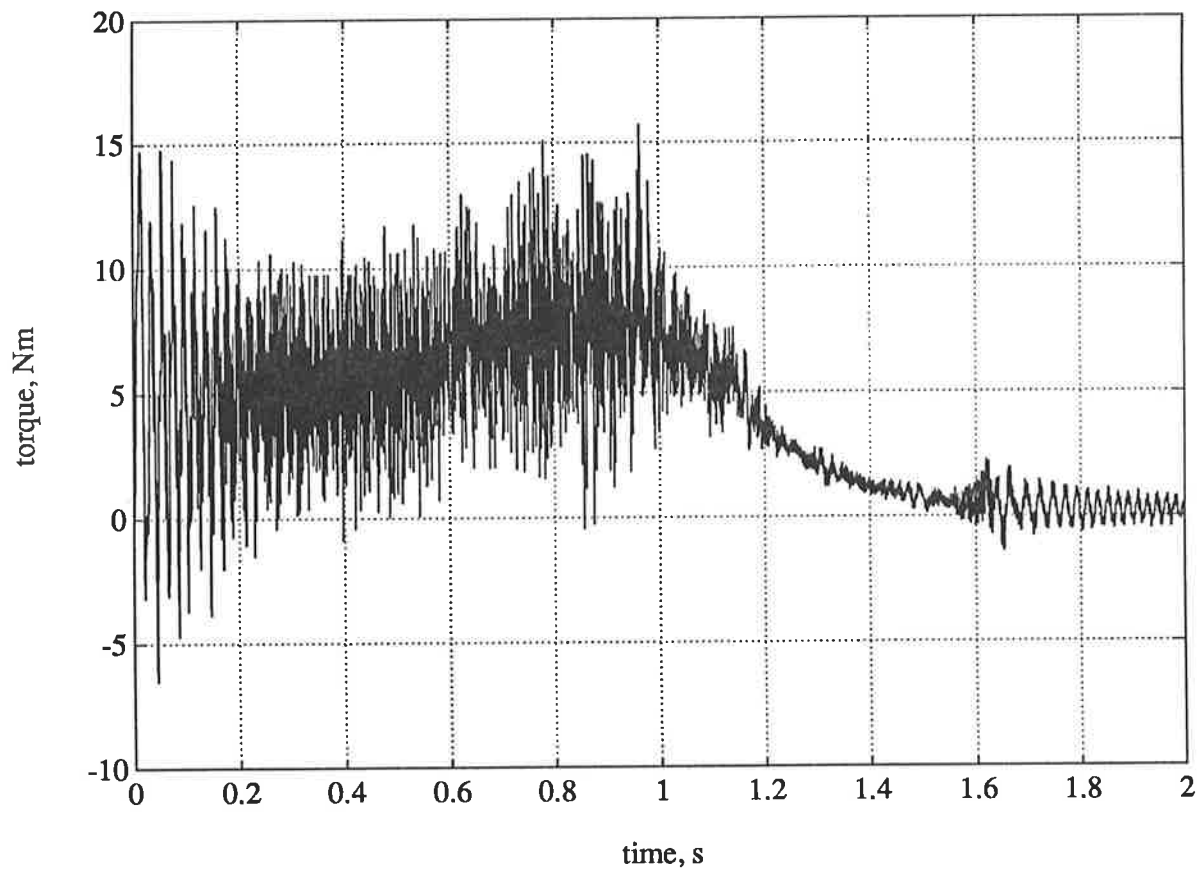


Figure 122

Simulated torque during start-up for Machine II (2-pole)

(no skew, uniform current density in rotor)

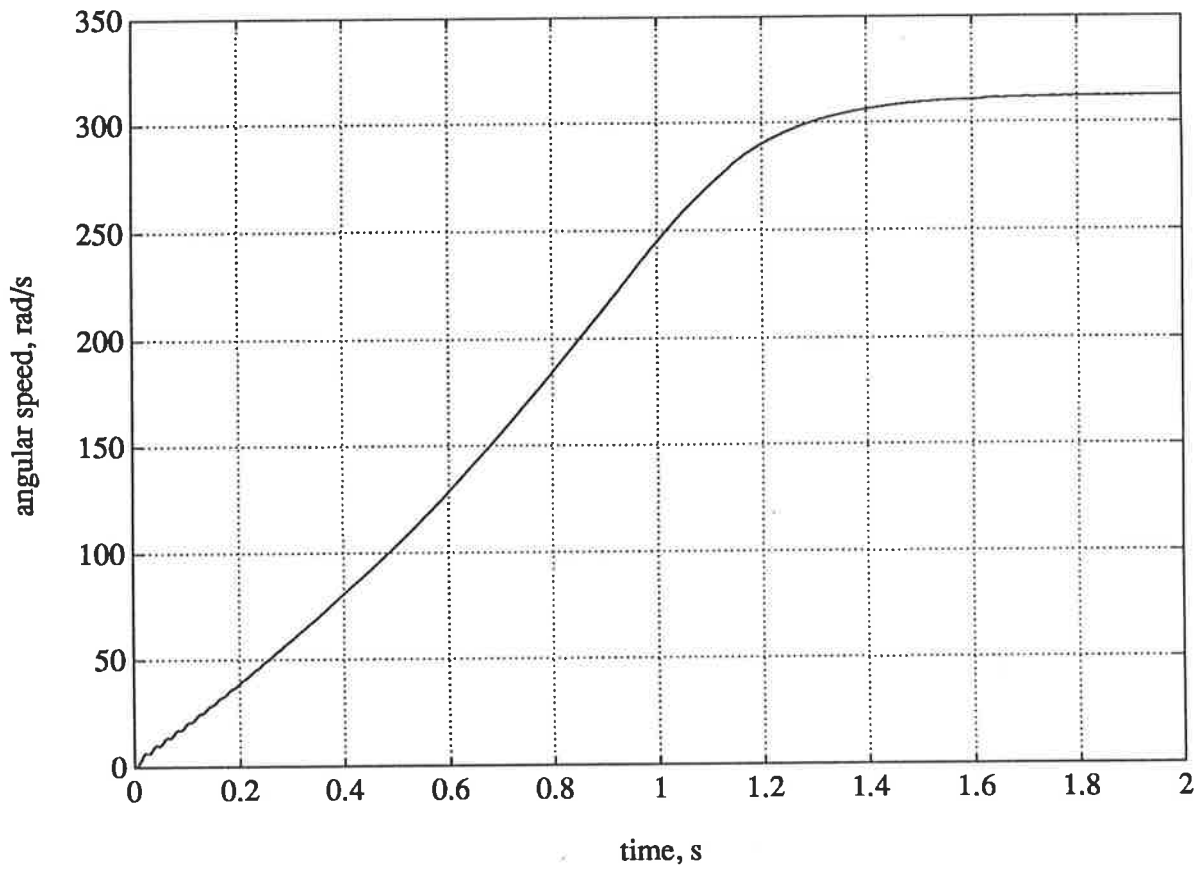


Figure 123

Simulated speed during start-up for Machine II (2-pole)

(no skew, uniform current density in rotor)

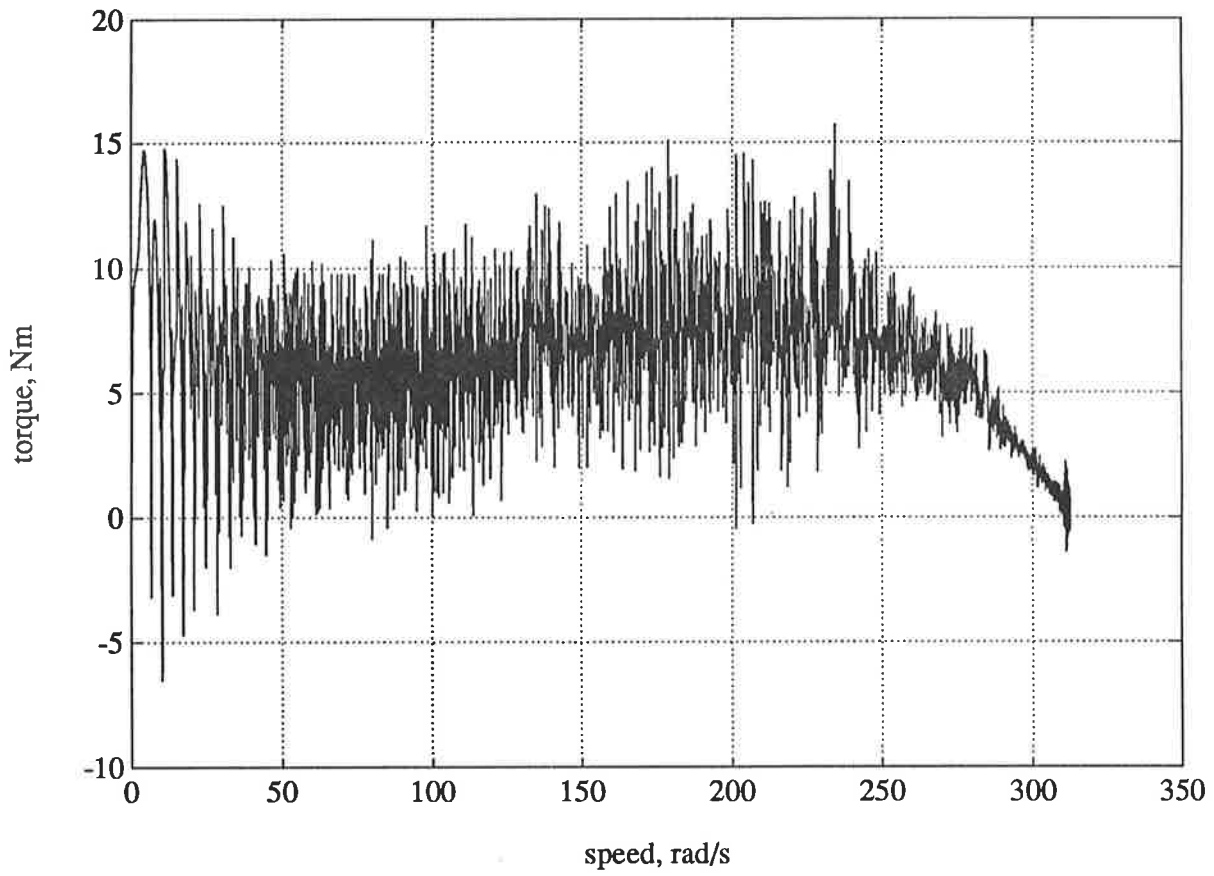


Figure 124

Simulated dynamic torque-speed characteristic for Machine II

(2-pole)

(no skew, uniform current density in rotor)



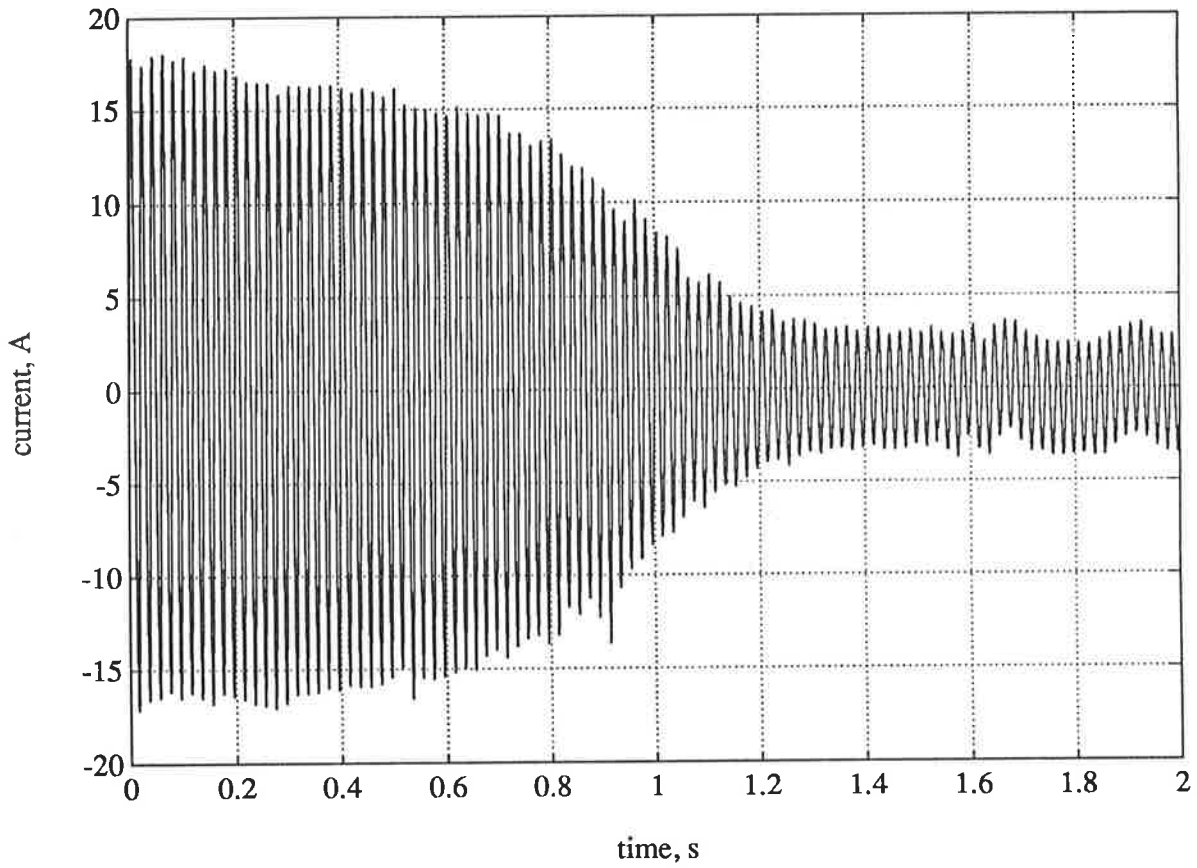


Figure 125

Simulated stator current during start-up for Machine II (2-pole)  
(accounting for current displacement, but assuming no skew)

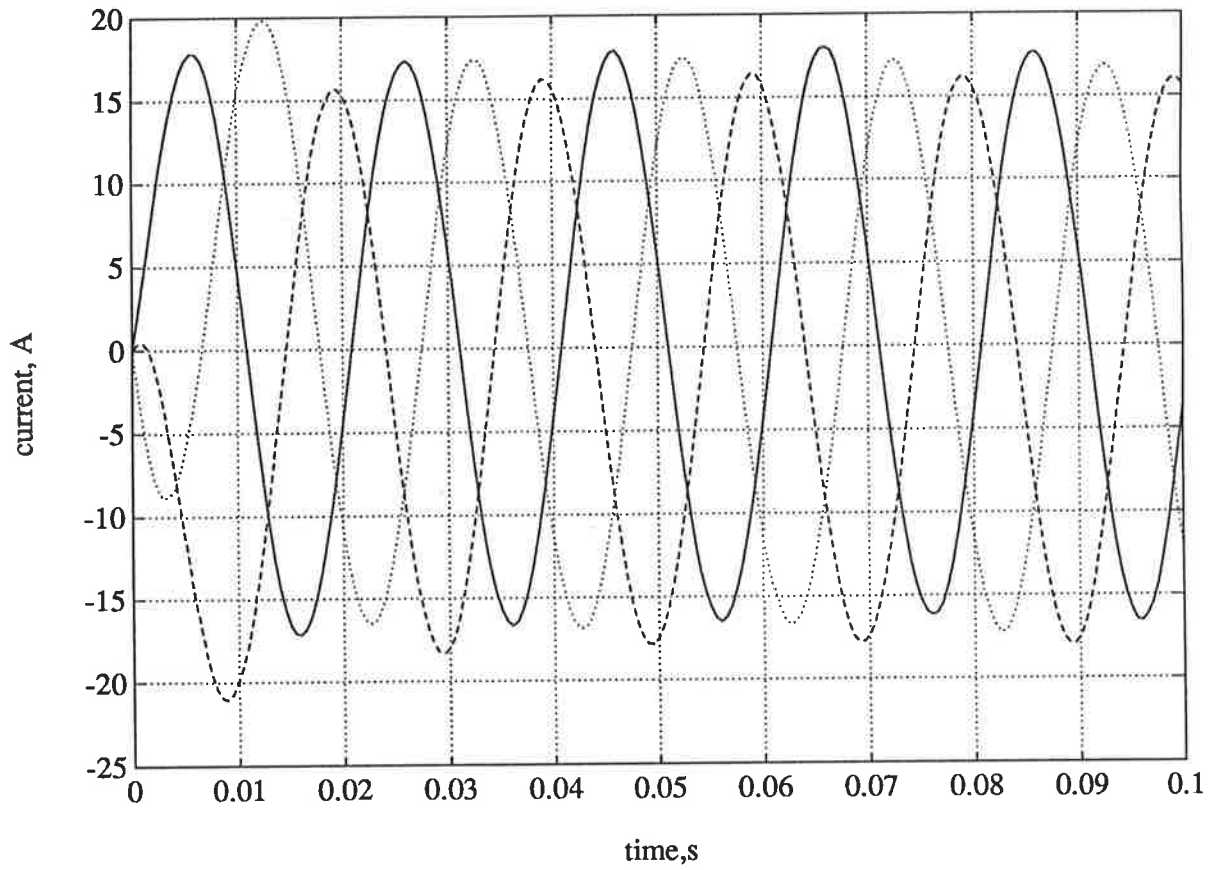


Figure 126

Simulated stator currents for the first 100ms for Machine II

(2-pole)

(accounting for current displacement, but assuming no skew)

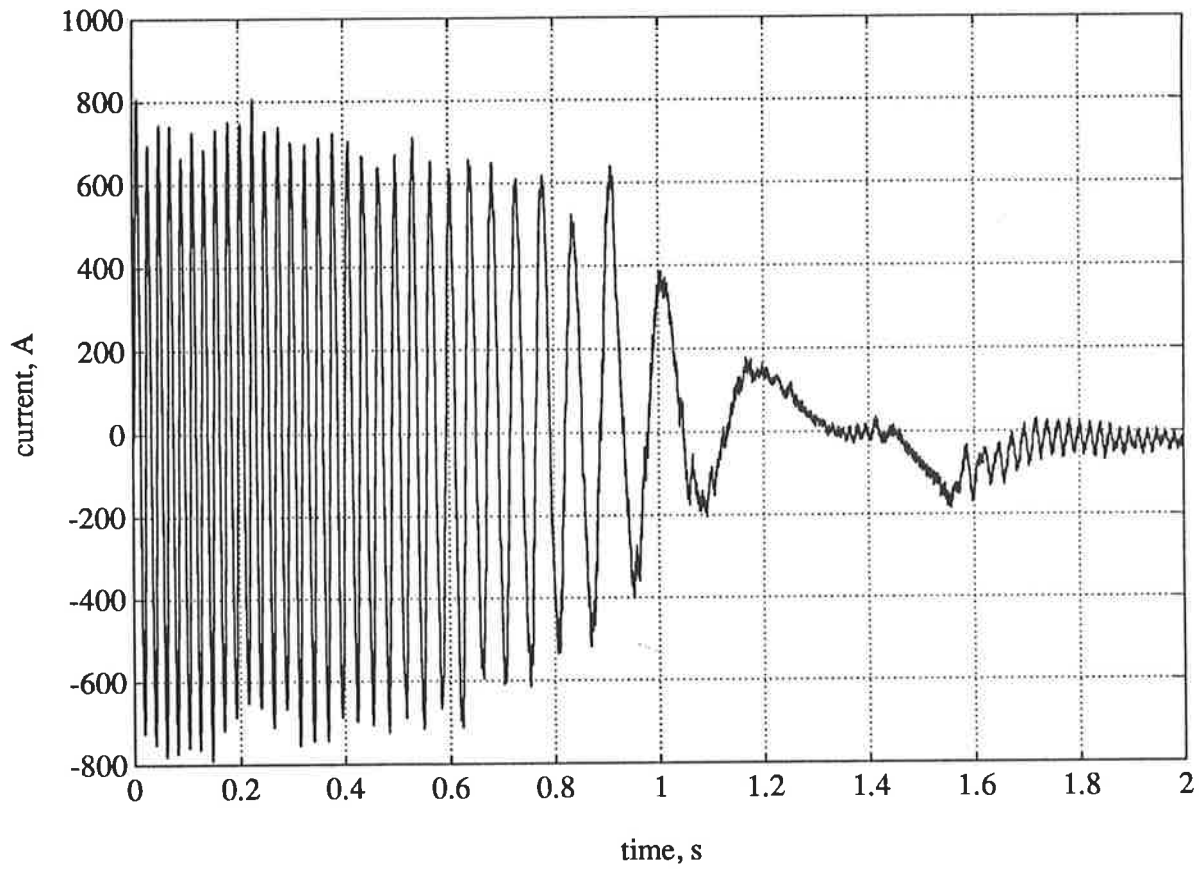


Figure 127

Simulated rotor current during start-up for Machine II (2-pole)  
(accounting for current displacement, but assuming no skew)

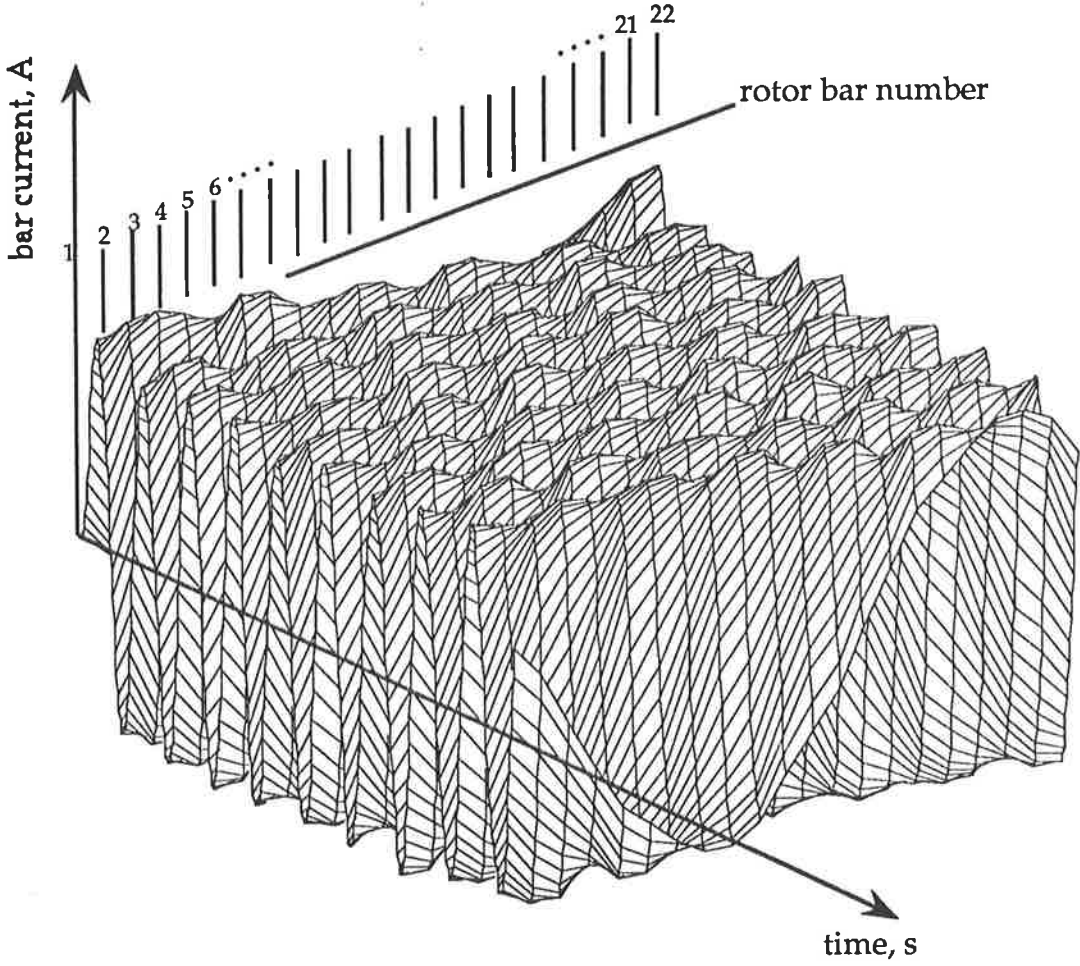


Figure 128  
Simulated rotor bar currents for the first 100ms for Machine II  
(2-pole)  
(accounting for current displacement, but assuming no skew)

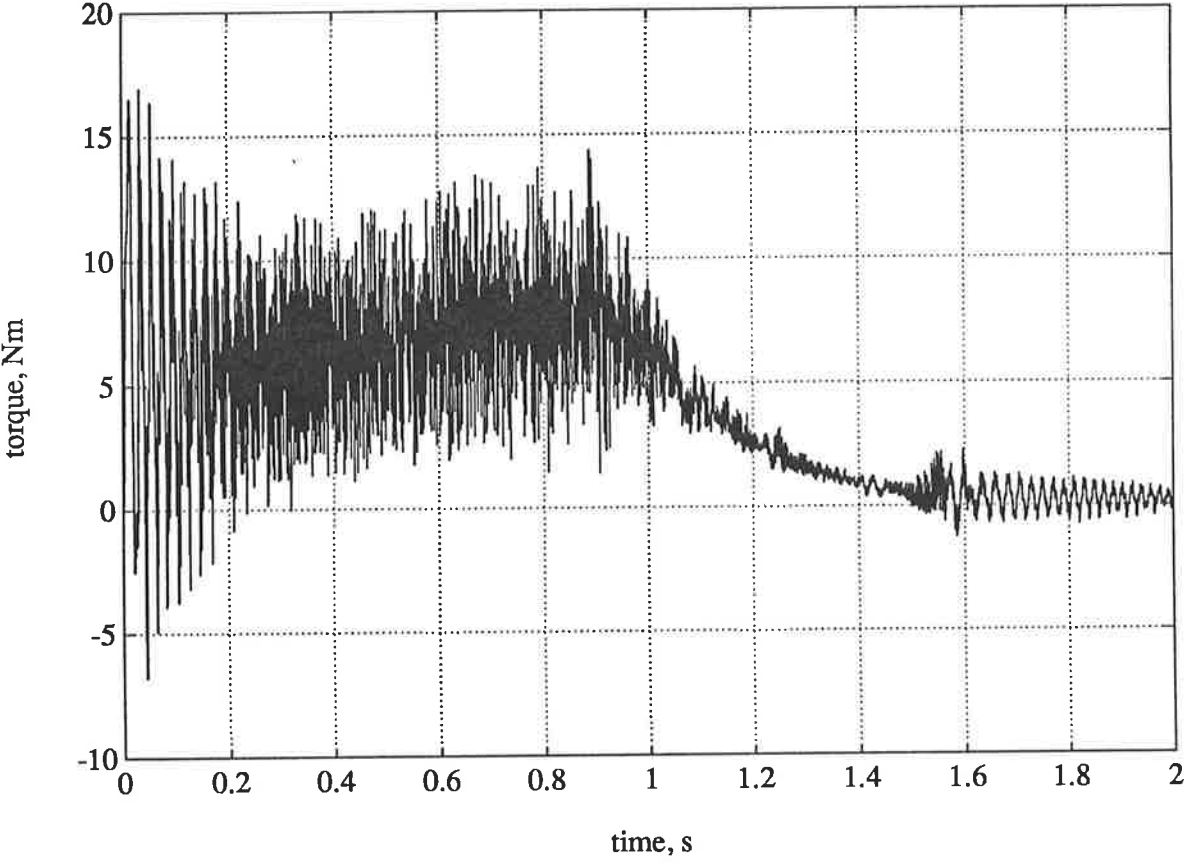


Figure 129  
Simulated torque during start-up for Machine II (2-pole)  
(accounting for current displacement, but assuming no skew)

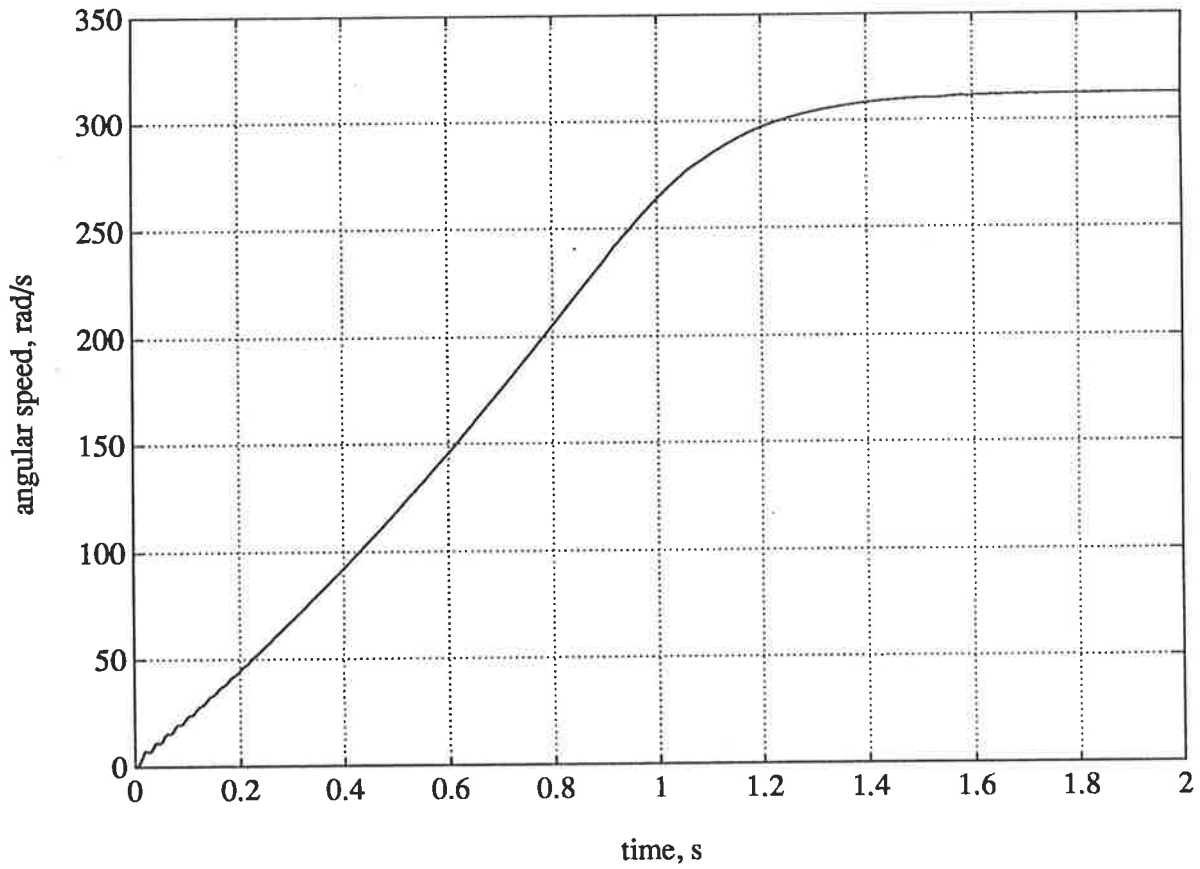


Figure 130

Simulated speed during start-up for Machine II (2-pole)

(accounting for current displacement, but assuming no skew)

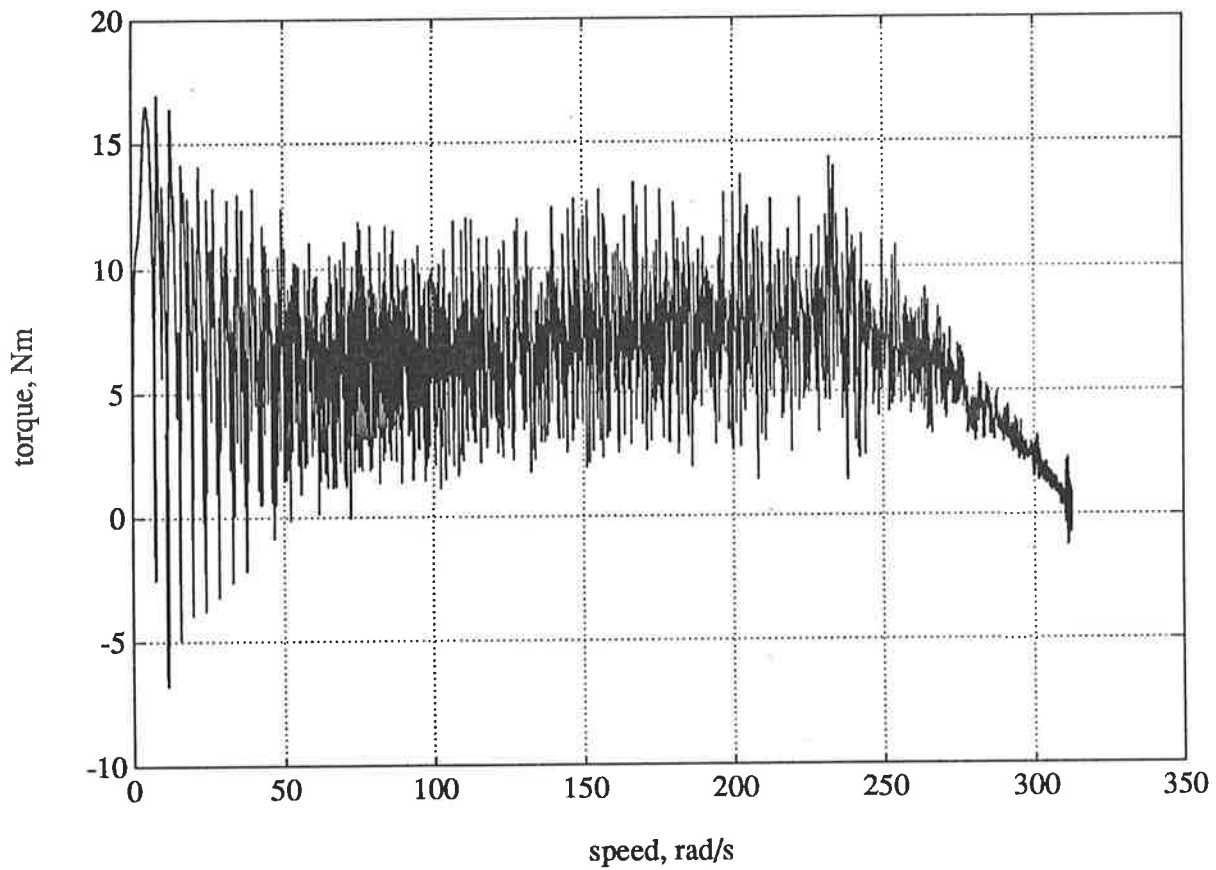


Figure 131

Simulated dynamic torque-speed characteristic for Machine II

(2-pole)

(accounting for current displacement, but assuming no skew)

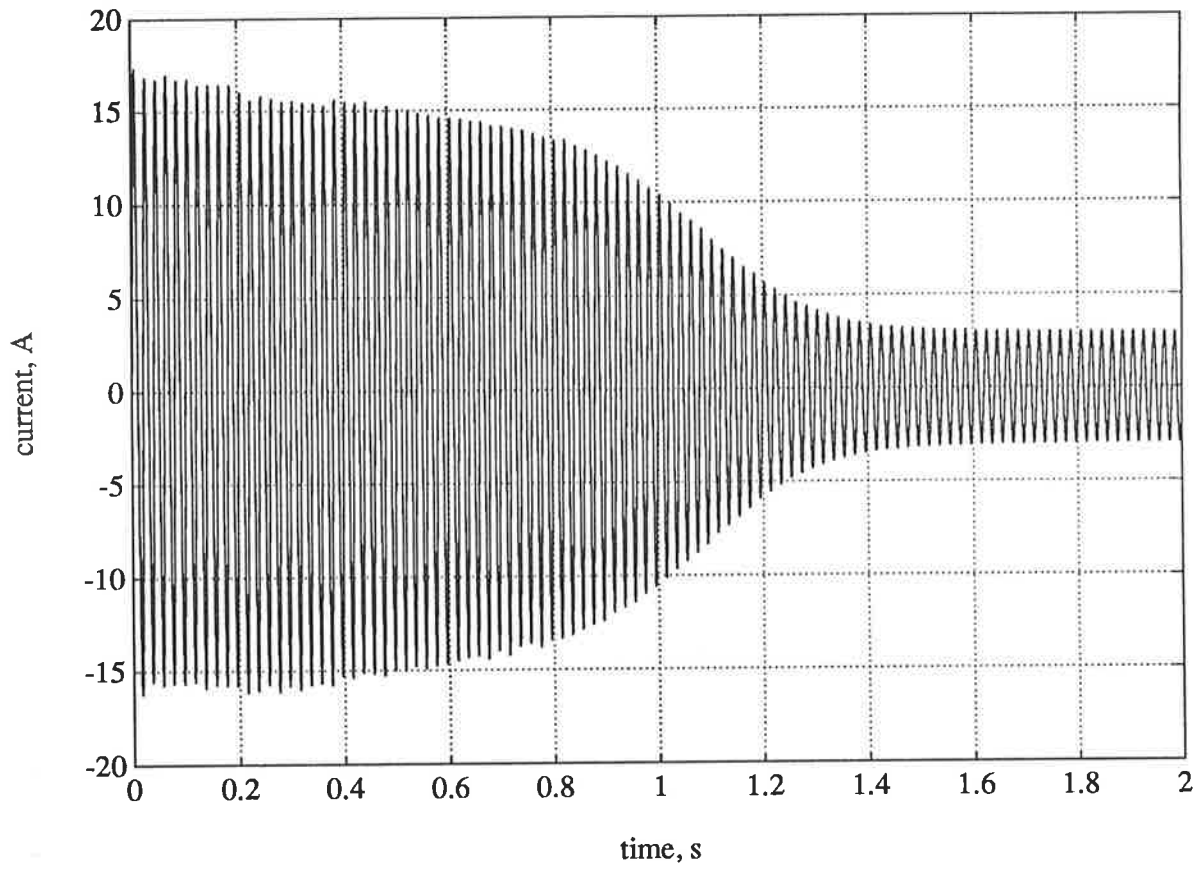


Figure 132

Simulated stator current during start-up for Machine II (2-pole)  
(accounting for both skew and current displacement)



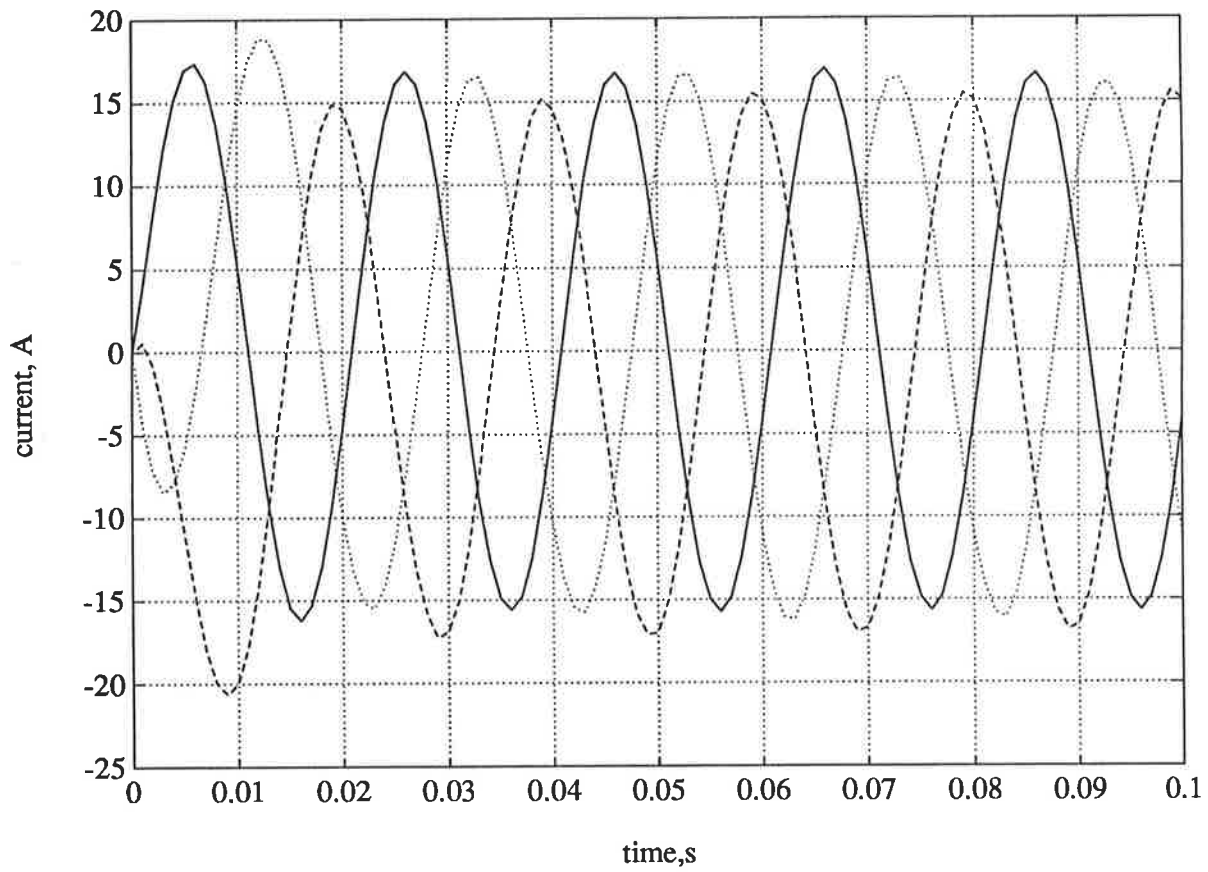


Figure 133

Simulated stator currents for the first 100ms for Machine II

(2-pole)

(accounting for both skew and current displacement)

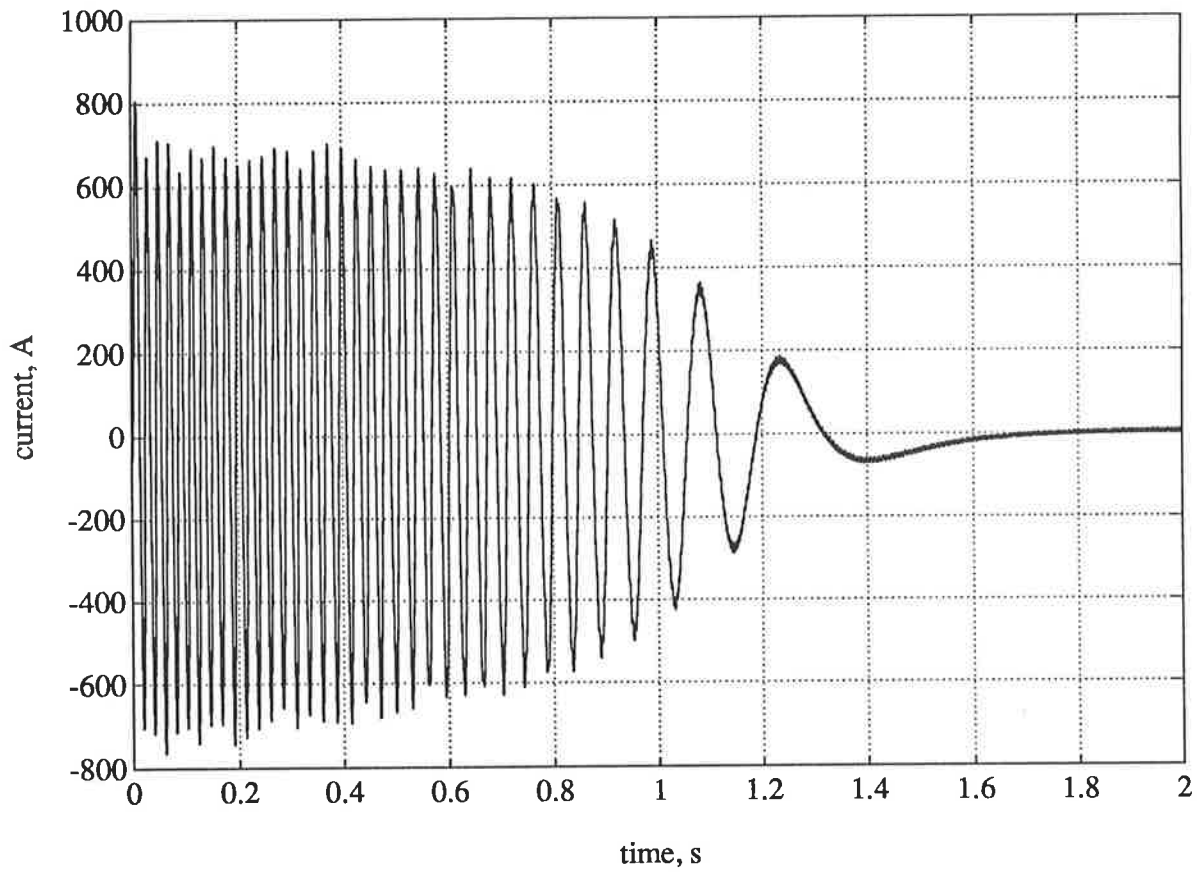


Figure 134

Simulated rotor bar current during start-up for Machine II

(2-pole)

(accounting for both skew and current displacement)

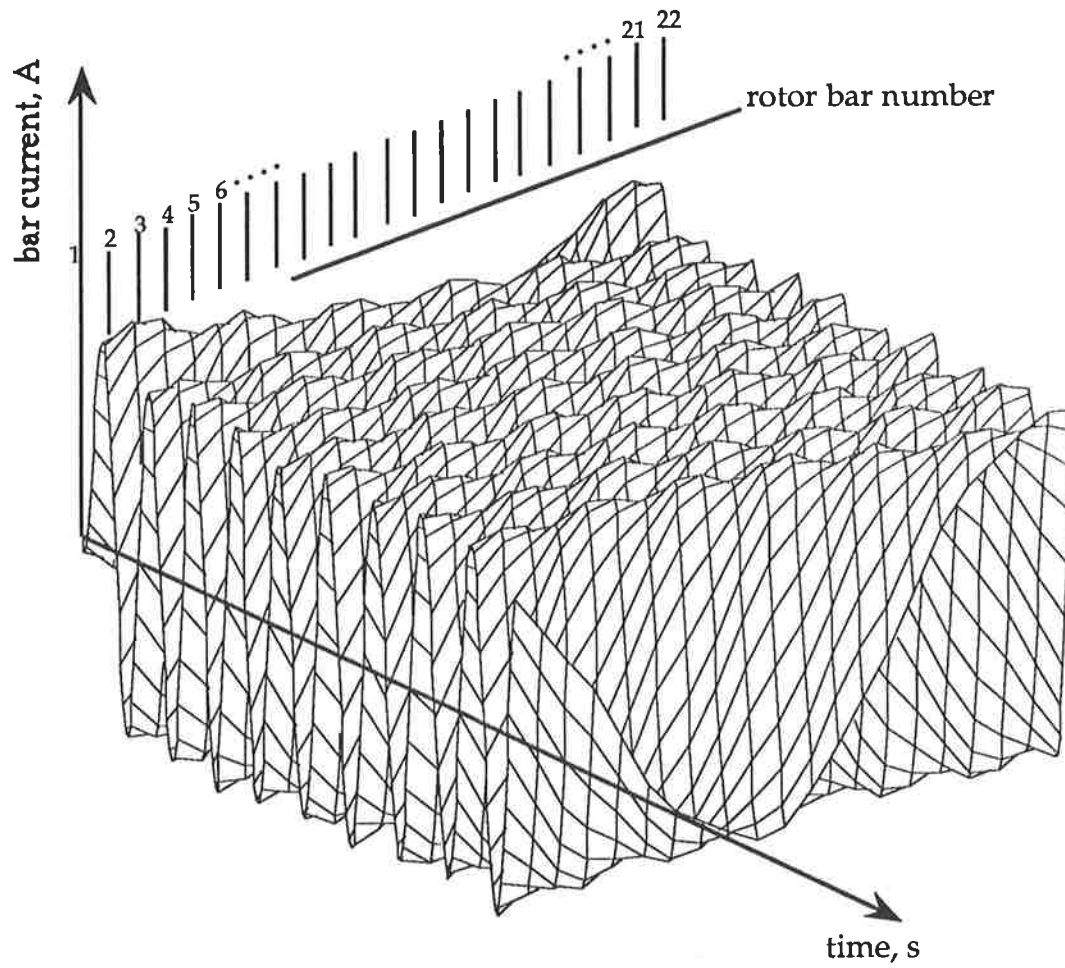


Figure 135

Simulated rotor currents for the first 100ms for Machine II

(2-pole)

(accounting for both skew and current displacement)

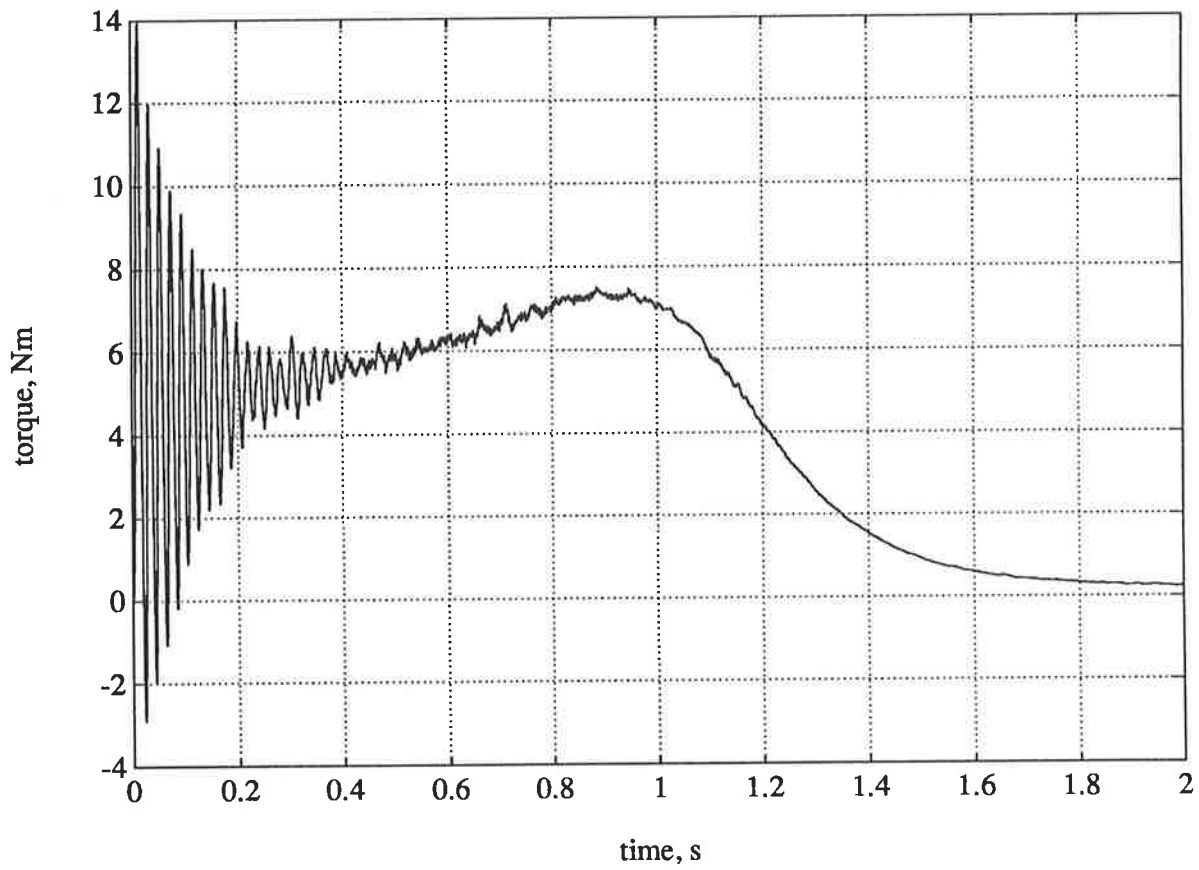


Figure 136

Simulated torque during start-up for Machine II (2-pole)  
(accounting for both skew and current displacement)

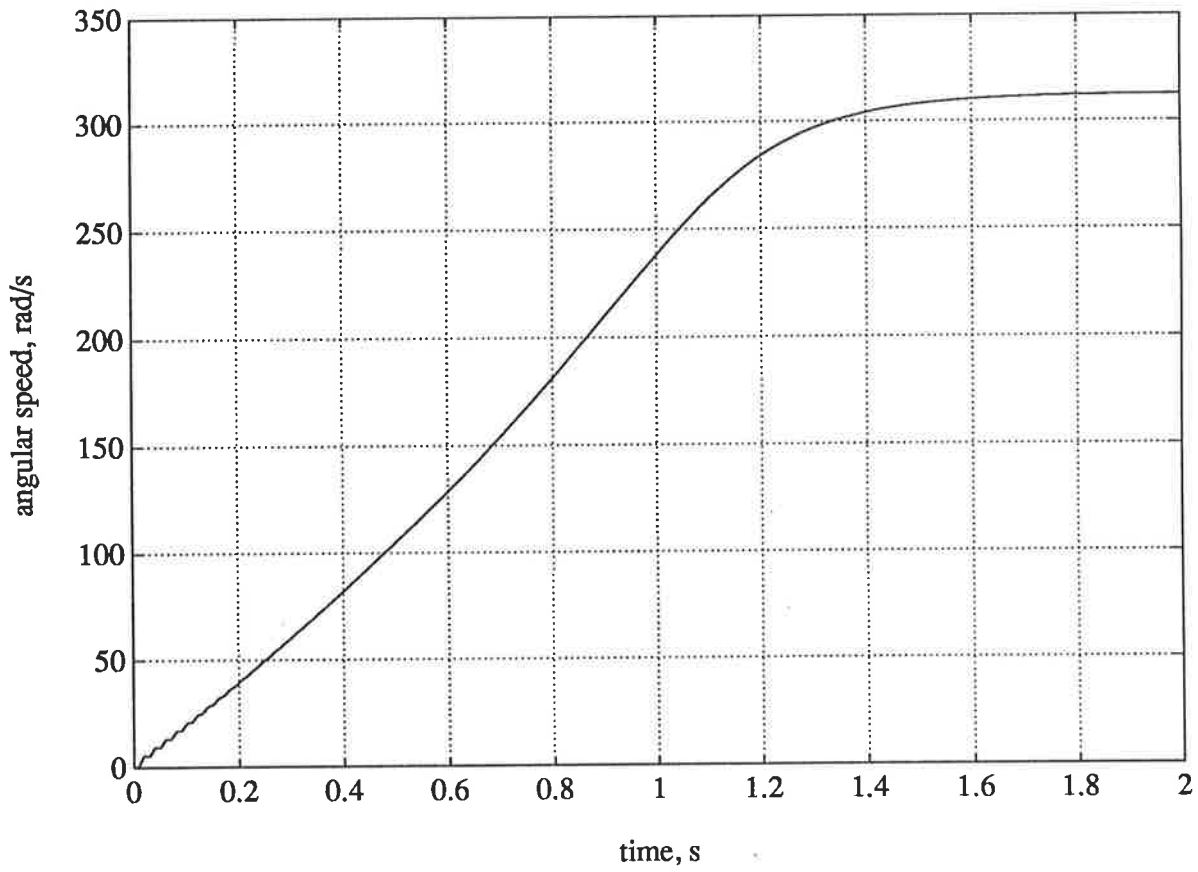


Figure 137

Simulated speed during start-up for Machine II (2-pole)  
(accounting for both skew and current displacement)

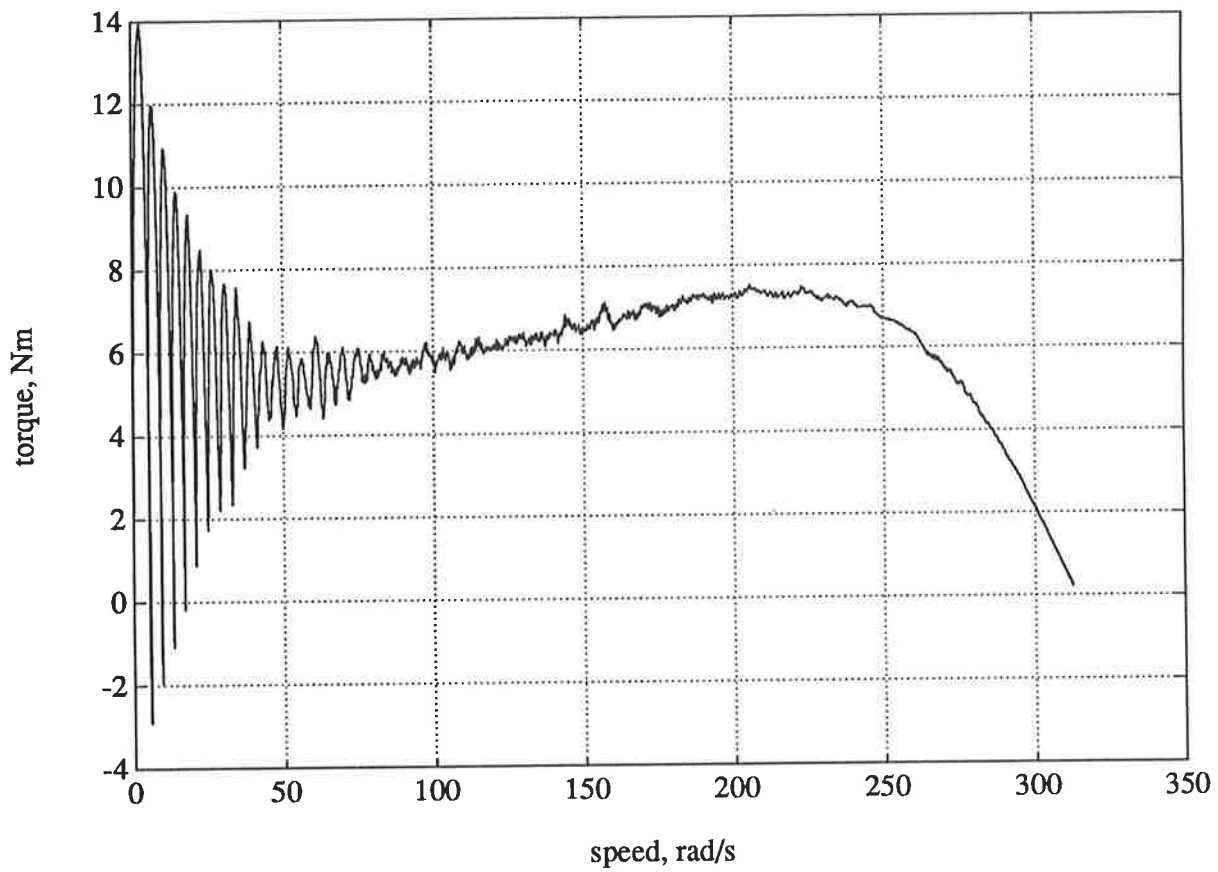


Figure 138

Simulated dynamic torque-speed characteristic for Machine II

(2-pole)

(accounting for both skew and current displacement)

#### 5.5.4 Effect of Parallel Connections on Start-Up Transients

Although not appreciated generally, it has long been established that the type of winding connection can substantially affect the performance of a machine [135,136,137,138]. This applies to all variations including wye or delta connection and winding configurations which incorporate parallel connected winding segments; the so-called parallel paths.

Discrete circuit models, by their very nature, are intrinsically capable of accounting for the effects of winding connections. The modelling approach is explained in Section 5.5.2 for the **double-star-connection** of the stator coil groups of the test machine in 4-pole configuration. The following simulations, presented in Figures 139 to 145, are based on the ensuing discrete circuit model of Machine II. Current displacement and skewing are included in the model. As can be seen, under the direct-on-line starting conditions, the overall behaviour of the machine is distinctly different from that of the wye-connected machine with series winding paths. Of particular interest is the angular velocity range between 20 to 40 rad/s of Figure 145, which displays the same characteristic pattern as in the measured torque-speed curve of Figure 77. The discrepancy in magnitude between the simulated and measured torque largely stems from the natural frequency of the swinging frame of the test machine which coincides with the region in question.

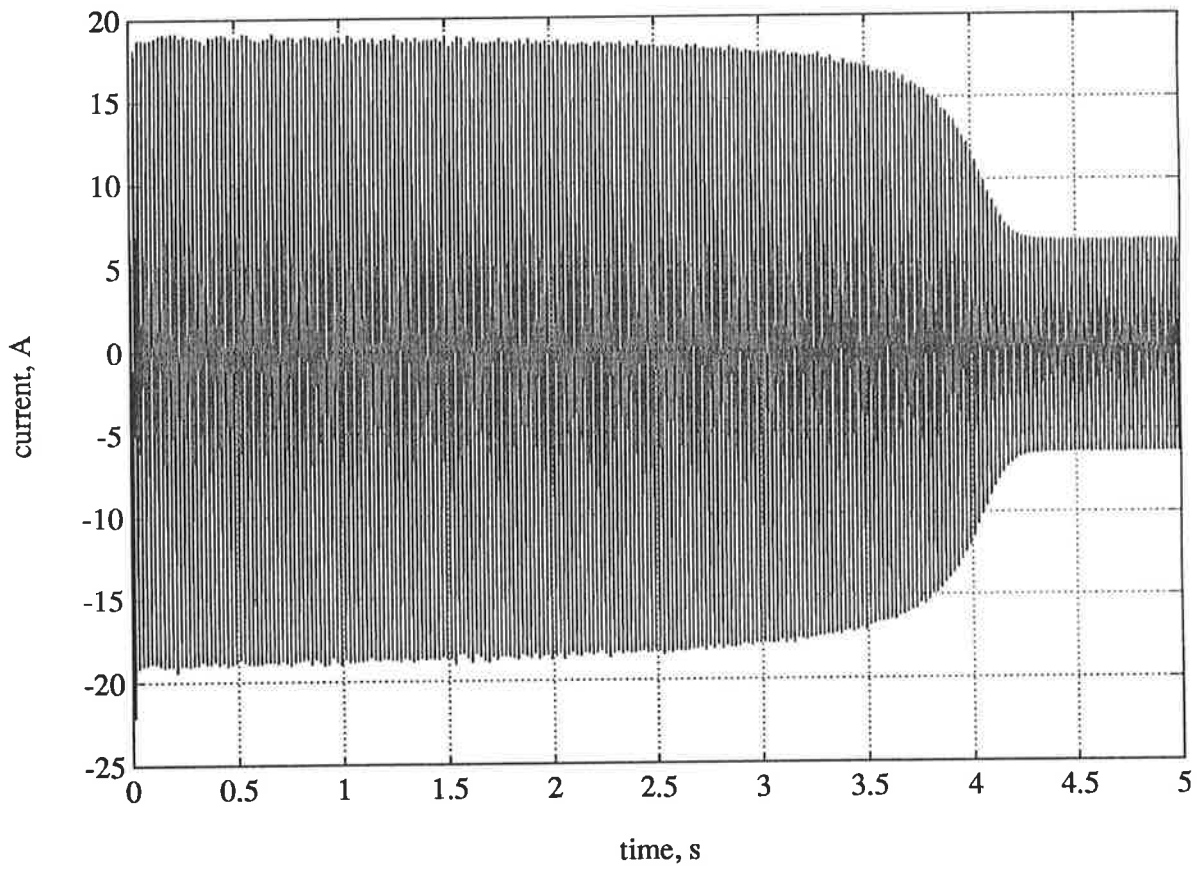


Figure 139

Simulated stator current during start-up for Machine II (4-pole)  
(accounting for both skew and current displacement)



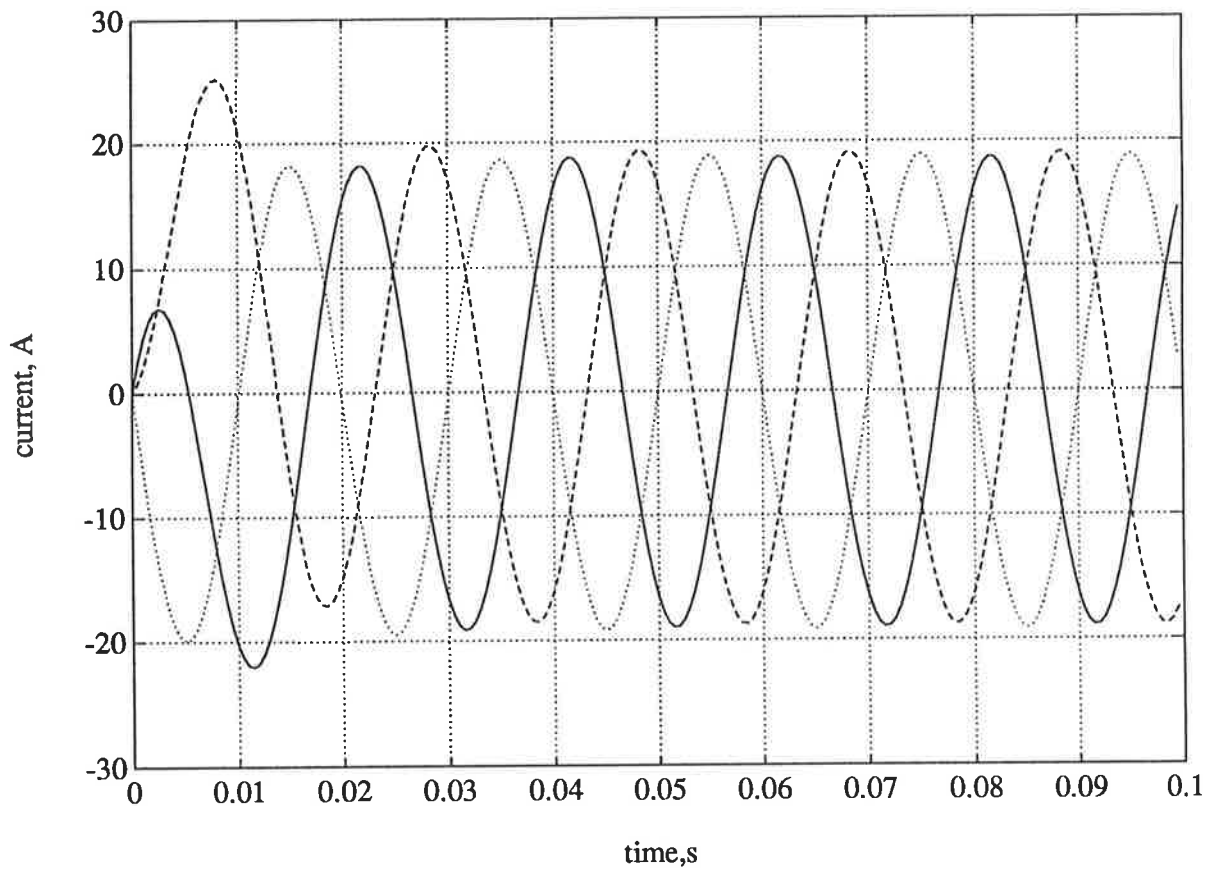


Figure 140

Simulated stator currents for the first 100ms for Machine II

(4-pole)

(accounting for both skew and current displacement)

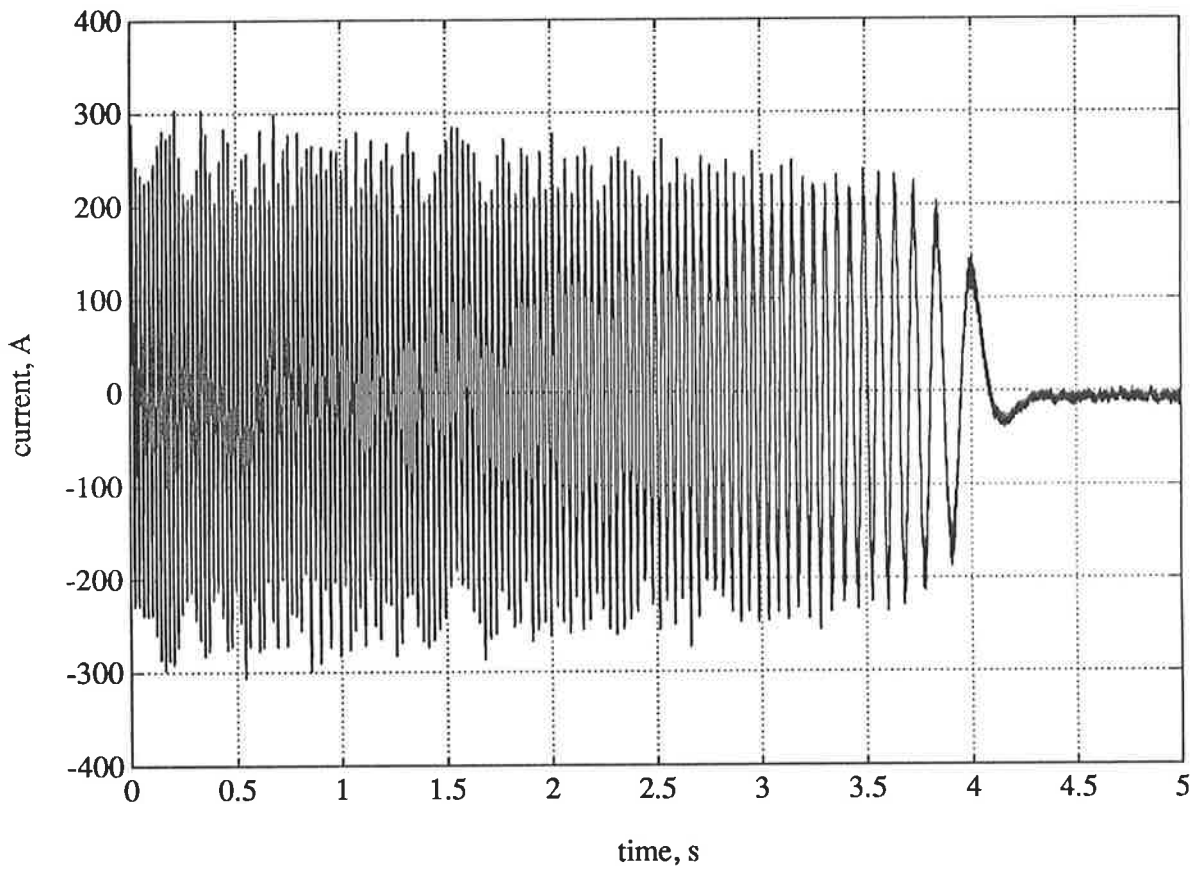


Figure 141

Simulated rotor bar current during start-up for Machine II

(4-pole)

(accounting for both skew and current displacement)

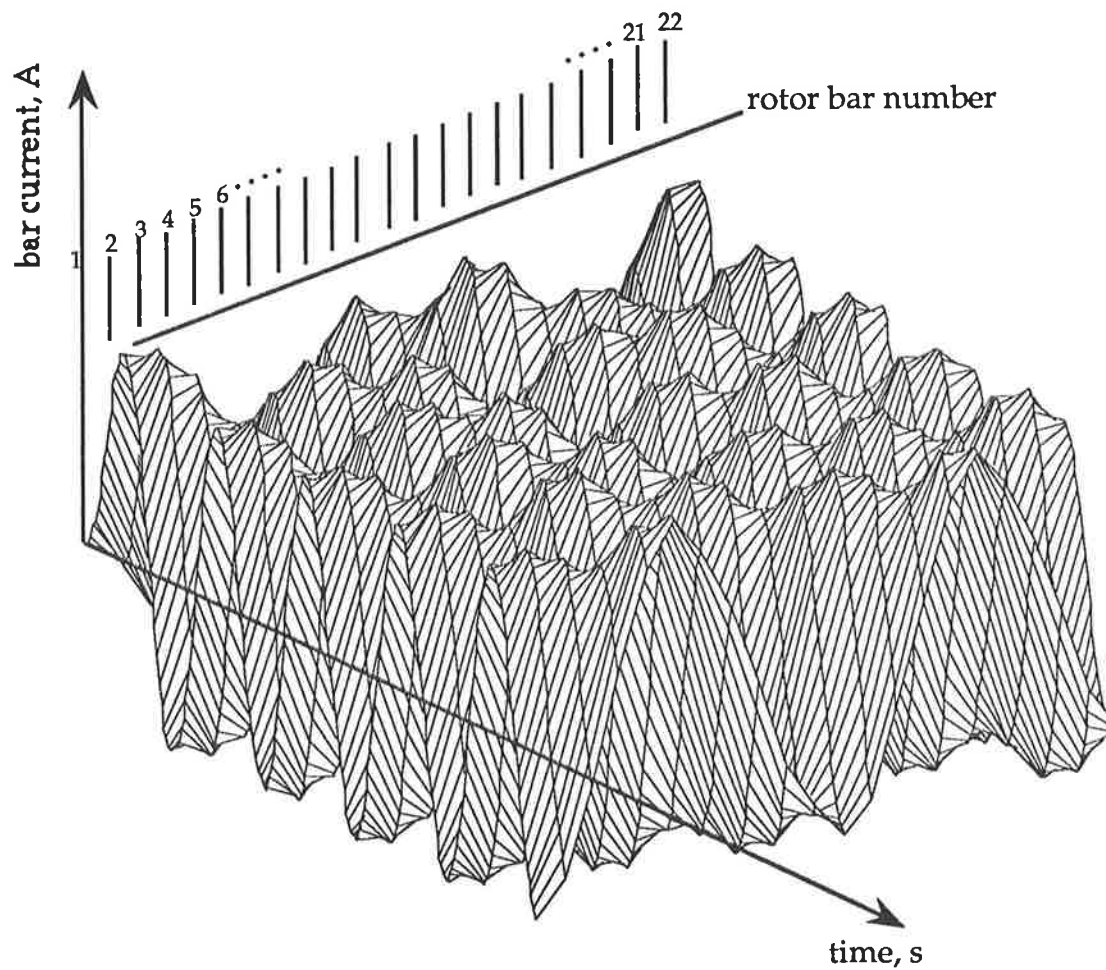


Figure 142

Simulated rotor currents for the first 100ms for Machine II

(4-pole)

(accounting for both skew and current displacement)

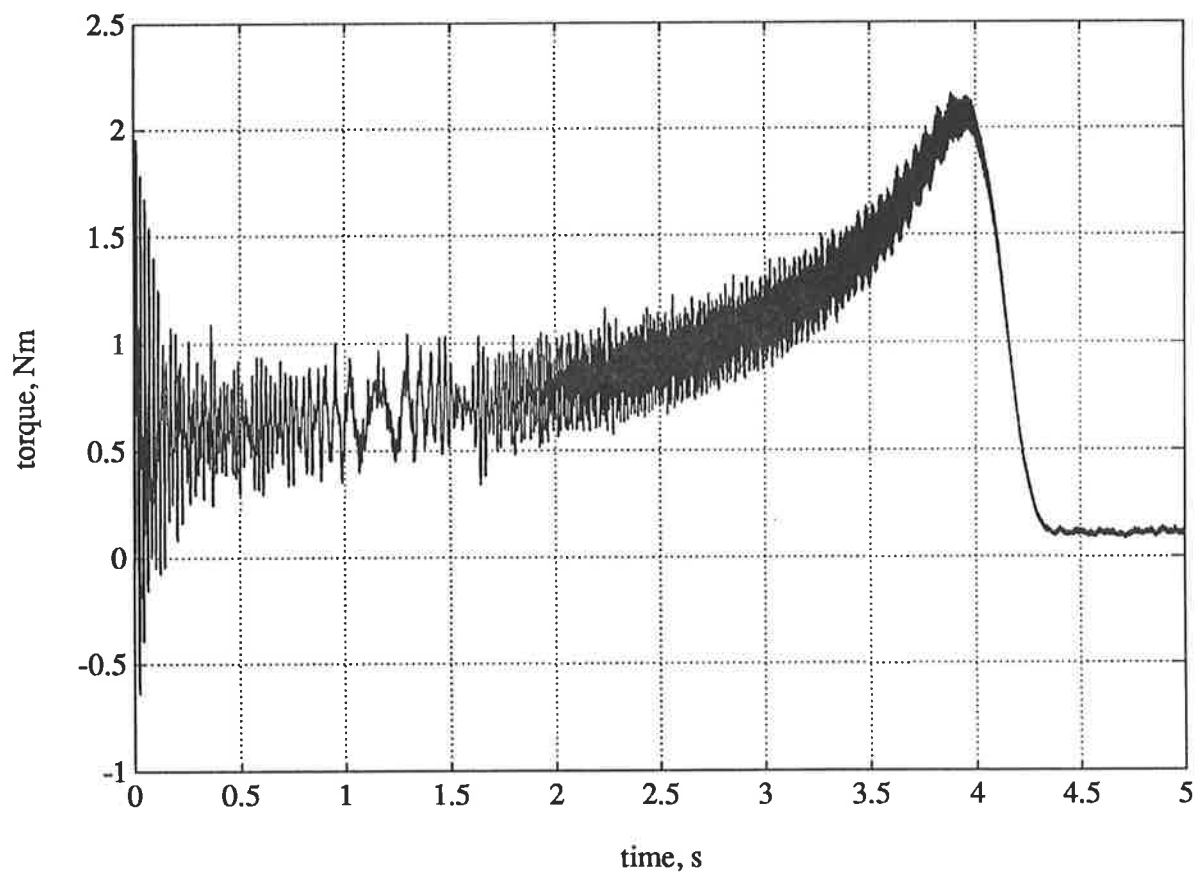


Figure 143

Simulated torque during start-up for Machine II (4-pole)  
(accounting for both skew and current displacement)

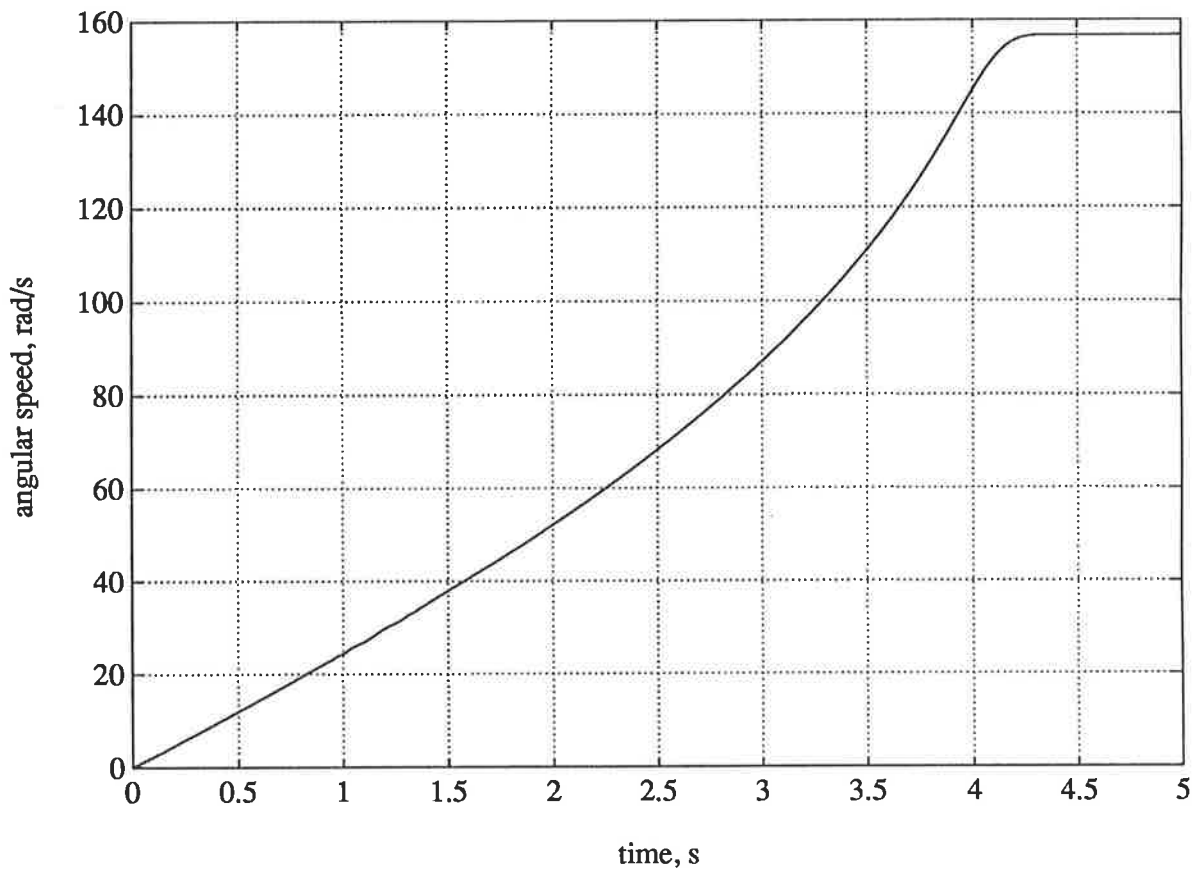


Figure 144

Simulated speed during start-up for Machine II (4-pole)

(accounting for both skew and current displacement)

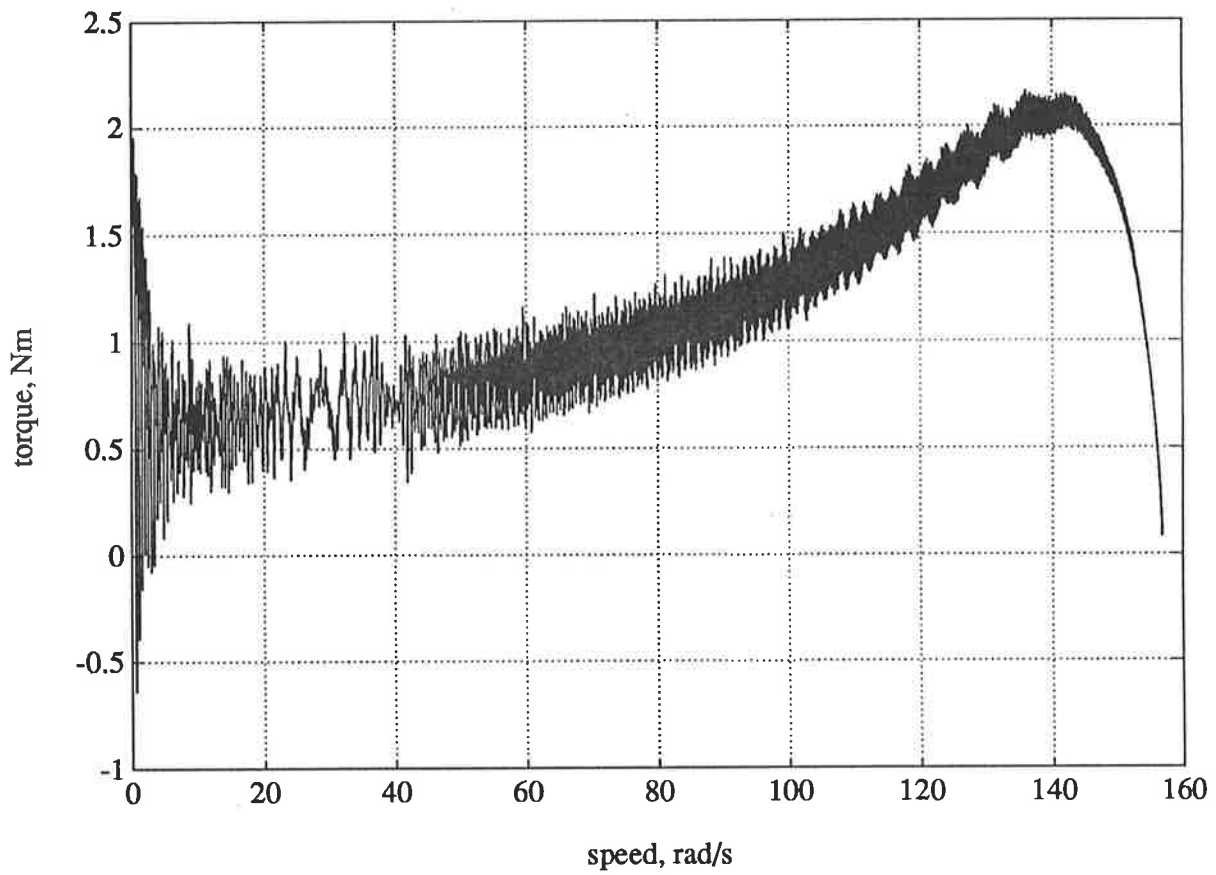


Figure 145

Simulated dynamic torque-speed characteristic for Machine II

(4-pole)

(accounting for both skew and current displacement)

### 5.5.5 Simulation of Rotor Discontinuities

Conventional models of induction machines are incapable of assessing the effects on the machine performance of asymmetries which may be present in the machine either due to the design features or because of operating conditions. Discrete circuit models are naturally capable of analysing the behaviour of machines with asymmetries. This capability will be demonstrated below for the case of rotor asymmetries. Such constitute a common fault and may arise, for instance, from void formation during the manufacture of die-cast rotors or from stress related fracturing of rotor bars during operation.

In the following simulations it will be assumed that two contiguous rotor bars, designated 3 and 4, are fractured. First, the transient start-up performance of the machine with faulty bars will be presented; a constant shaft torque of 2Nm is assumed to be applied during this regime. Next, the dynamic behaviour of the machine under steady state conditions with the same shaft torque will be considered. The latter will establish the cause-effect relationship between rotor faults and their effect on the line current, which has been used to diagnose such faults by external measurement.

Figure 146 shows the stator current during start-up with load. As can be seen, the machine behaves sluggishly, taking more than twice the time to reach the operating speed. During this time, the current is heavily modulated. The modulation continues into the operating region at twice the slip frequency.

Figure 147 gives all three currents for the stator during the first 100 ms of the simulation. Figure 148 depicts the rotor bar current which is also modulated heavily, similar to the stator current. Figure 149 gives all rotor bar currents during the first 100 ms of the run-up. The effect on the rest of

the bar currents is most pronounced, the current amplitudes in the bars adjacent to the fault zone rising considerably. These effects have been previously observed and are known to exacerbate the fault progression in the rotor cage [61]. The transient start-up torque of Figure 150 gives evidence to the detrimental effect of this type of rotor fault on the performance; the machine labours to reach the operating regime. Furthermore it is subject to marginal instability in the operating region. The speed build-up of Figure 151 underlines this. Figure 152 gives the resultant torque-speed characteristic.

If the load on the machine is increased, the modulation effects are amplified. This is demonstrated in Figure 153 which shows the modulation in the steady-state stator current when the load is increased to 4Nm. Figure 154 typifies the corresponding rotor bar currents. In practice, this modulation of the stator current under load is observable by a characteristic swing in the deflection of the needle of switchboard ammeters. Methods of diagnosis based on current modulation have been proposed. In such methods the power spectrum of the line current reveals sidebands the frequency of which is determined by the slip,  $s$ . Although these methods recognise the link between rotor faults and the ensuing sideband effects in the current spectrum, the cause-effect relationships are not established. This is where the discrete circuit models possess an indisputable advantage in that such cause-effect relationships are systematically embedded in the model. Figure 155 shows a window of the power spectrum of the stator current; sidebands are clearly observable on both sides of the fundamental according to the relationship  $(1 \pm 2s)f$ . Figure 156 gives the power spectrum of the stator current for the same machine without any rotor faults; sidebands are absent. This confirms the aptness of sideband detection as a means of diagnosing rotor faults.



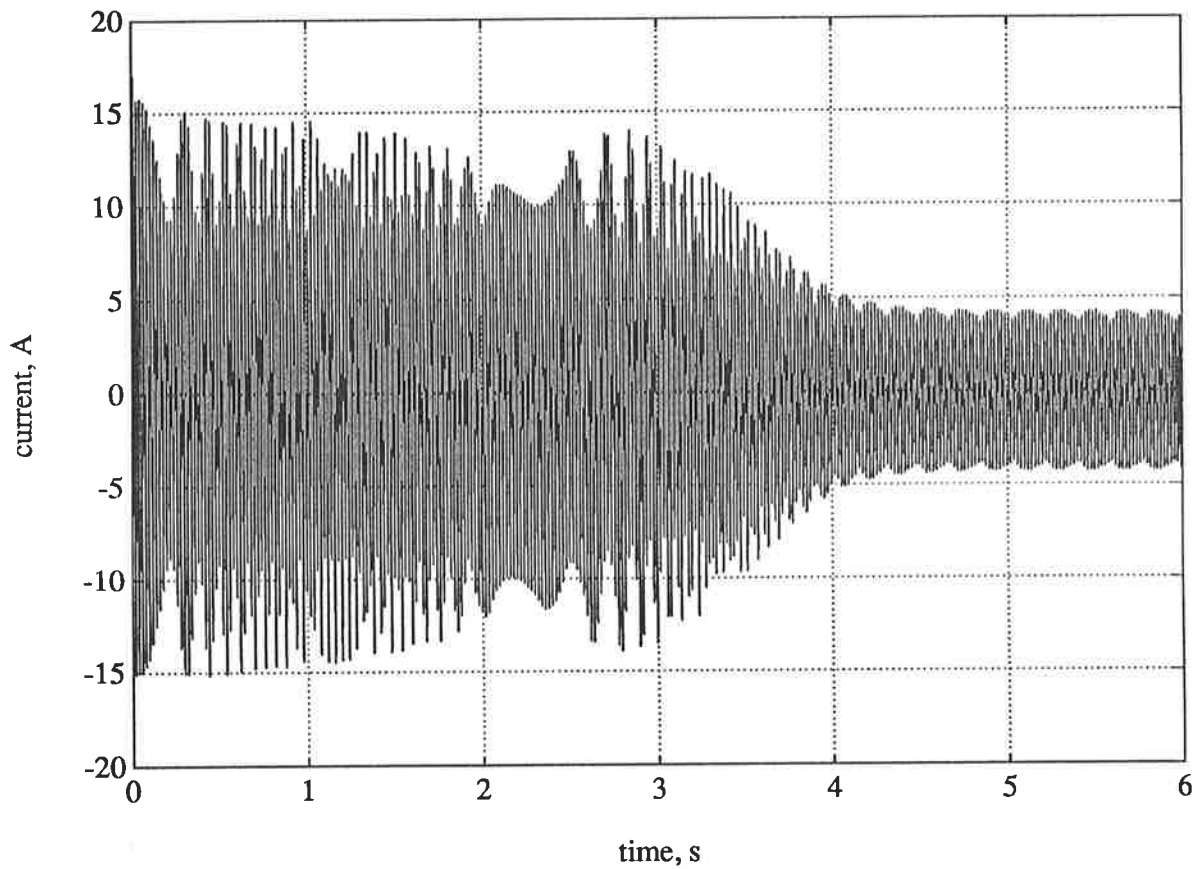


Figure 146

Simulated stator current during start-up for Machine II (2-pole)

- rotor bars 3 and 4 faulty
- skew and current displacement included

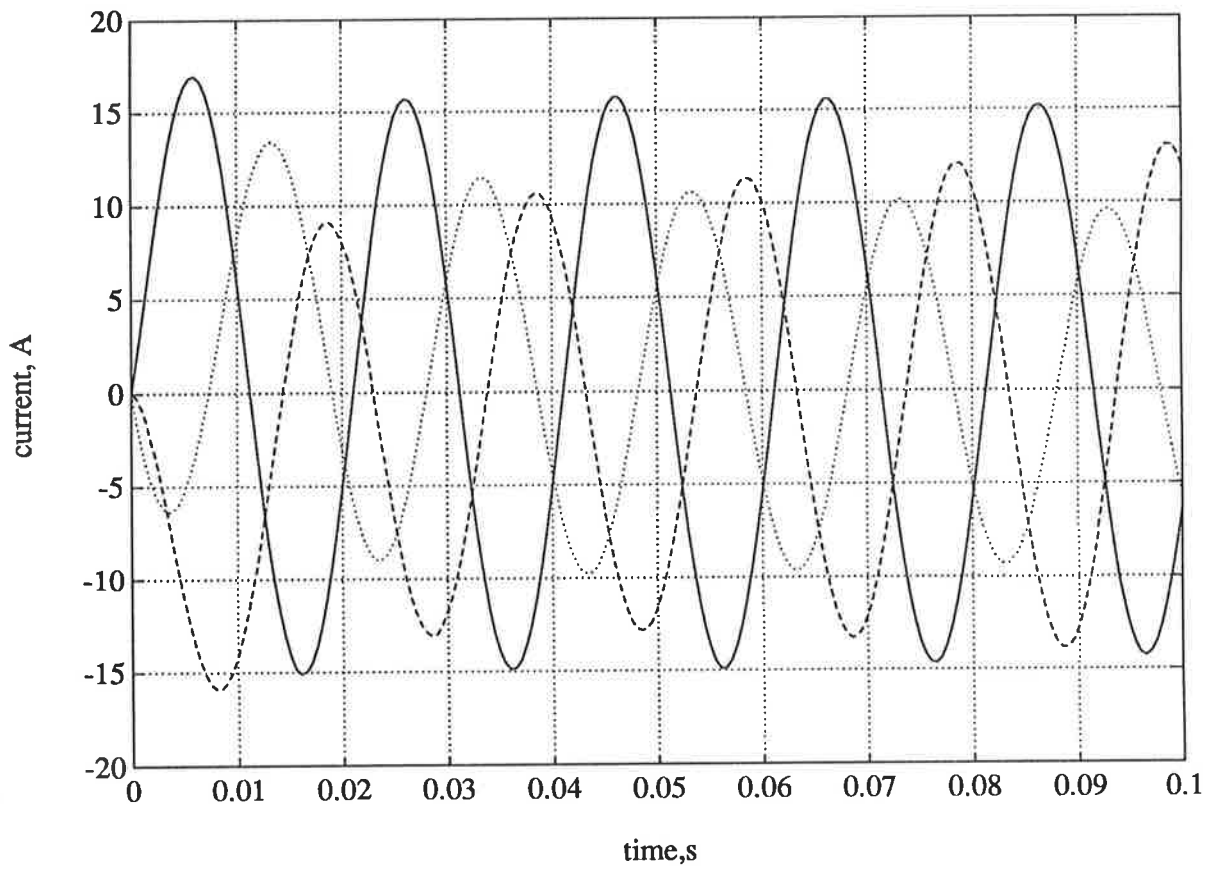


Figure 147

Simulated stator currents for the first 100ms during start-up for  
Machine II (2-pole)

- rotor bars 3 and 4 faulty
- skew and current displacement included

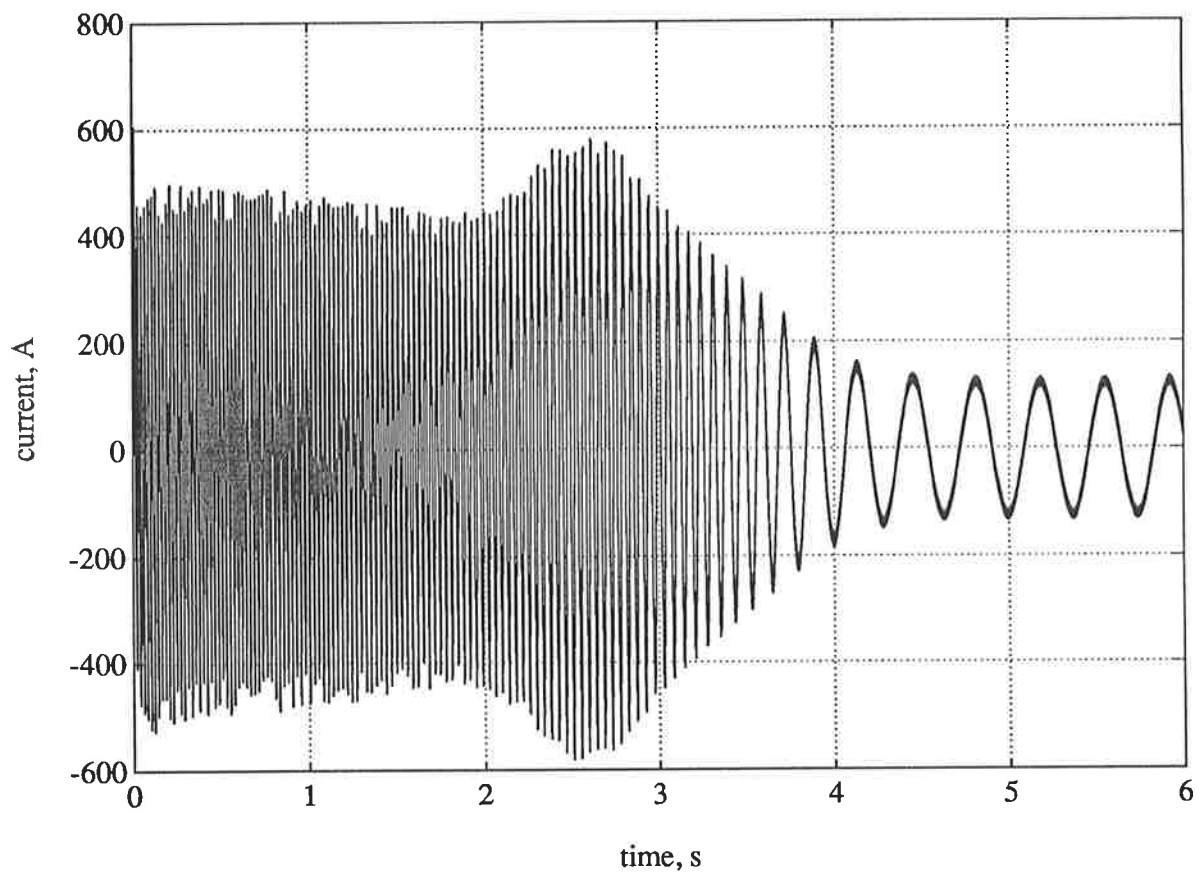


Figure 148

Simulated rotor bar current during start-up for Machine II

(2-pole)

- rotor bars 3 and 4 faulty
- skew and current displacement included

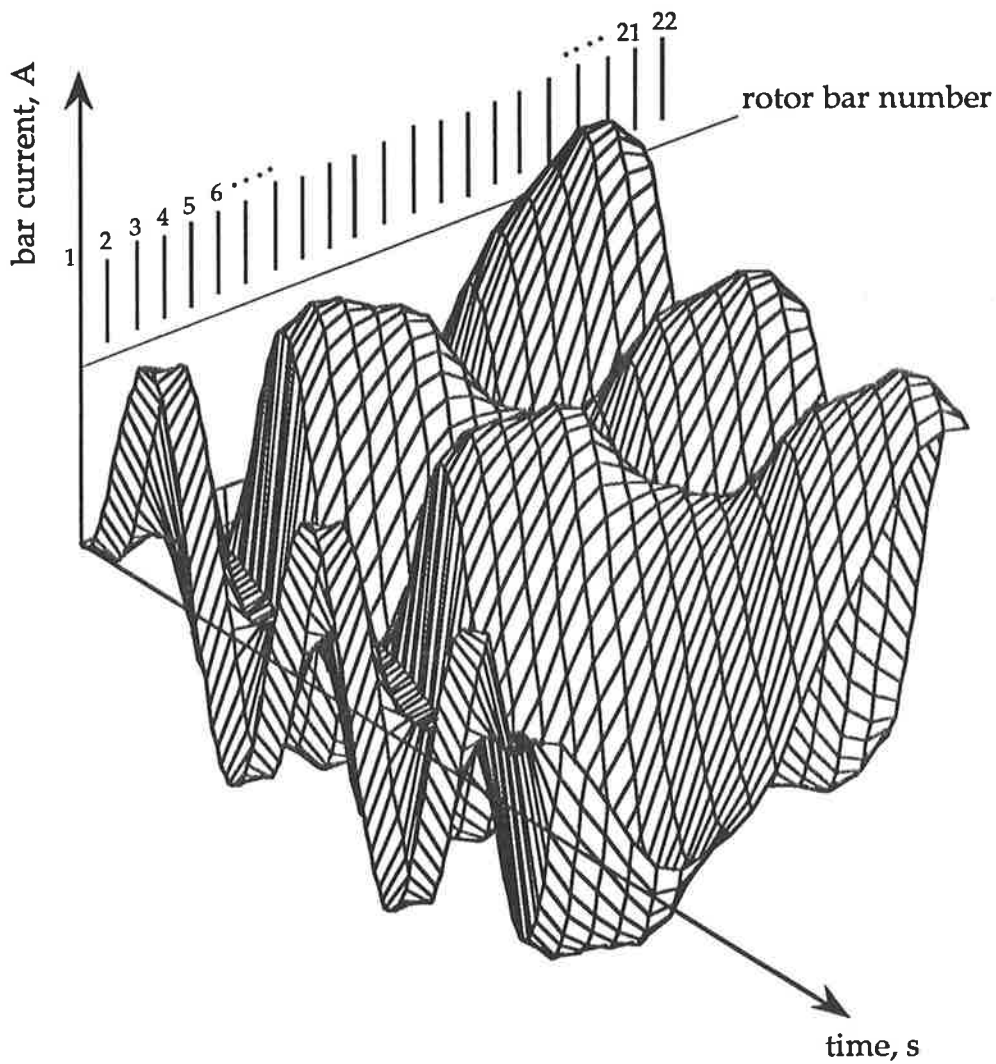


Figure 149

Simulated rotor bar currents for the first 100ms during start-up for Machine II (2-pole)

- rotor bars 3 and 4 faulty
- skew and current displacement included

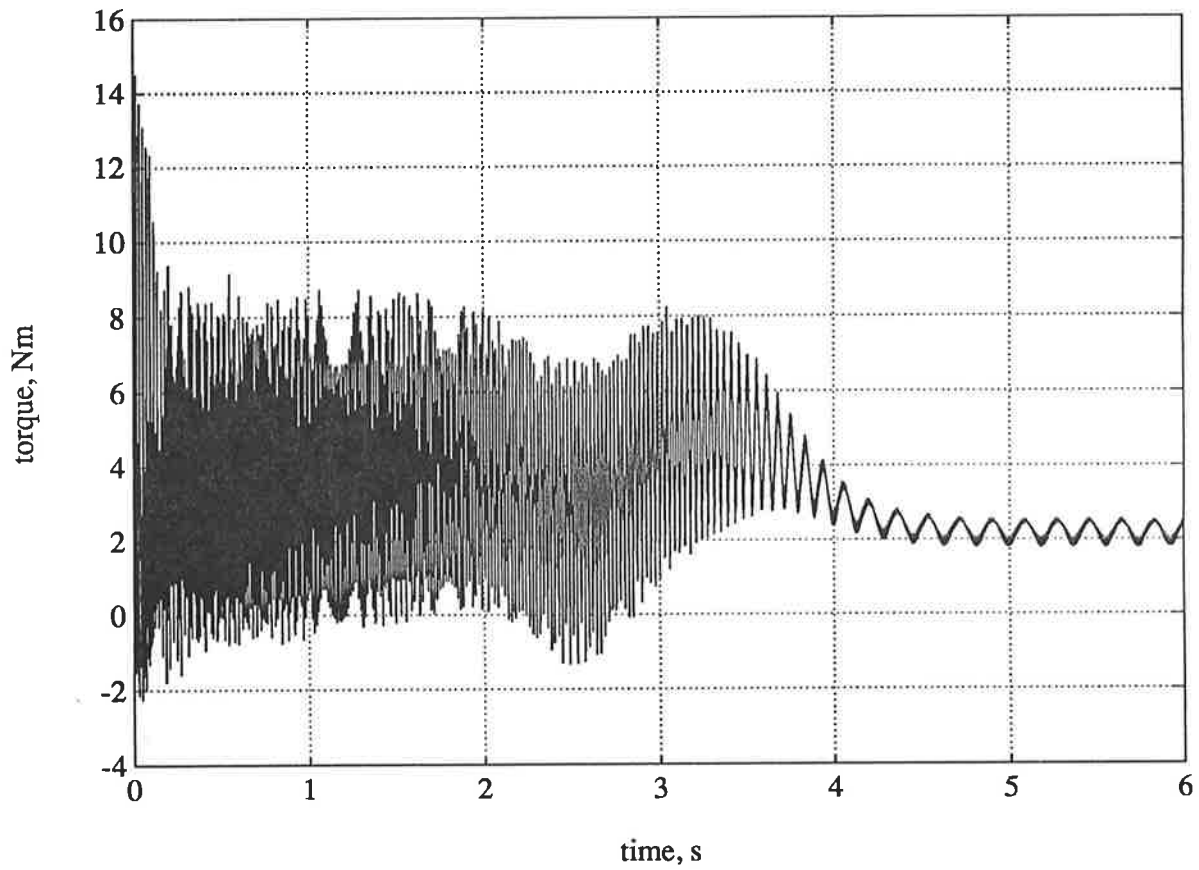


Figure 150

Transient start-up torque for faulty rotor (2-pole)

- rotor bars 3 and 4 faulty
- skew and current displacement included

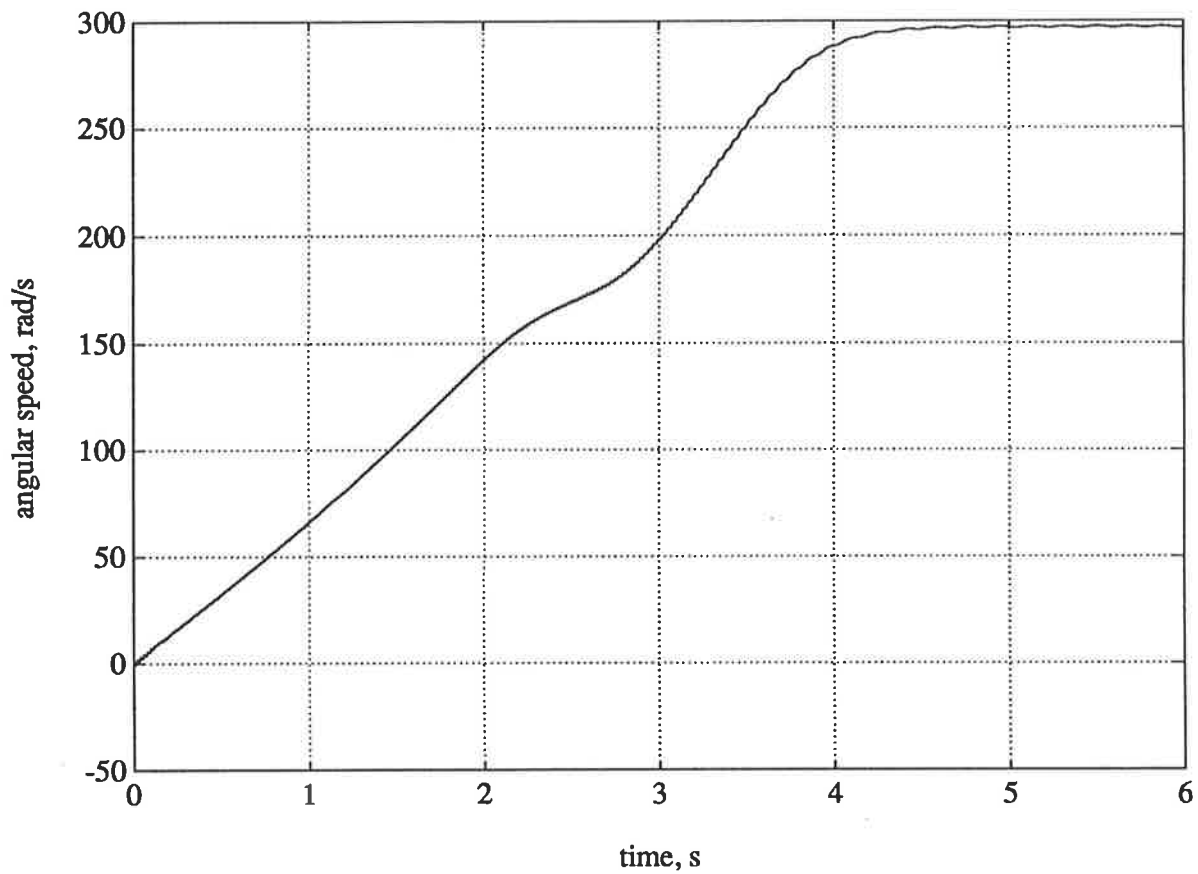


Figure 151

Simulated speed during start-up for Machine II (2-pole)

- rotor bars 3 and 4 faulty
- skew and current displacement included

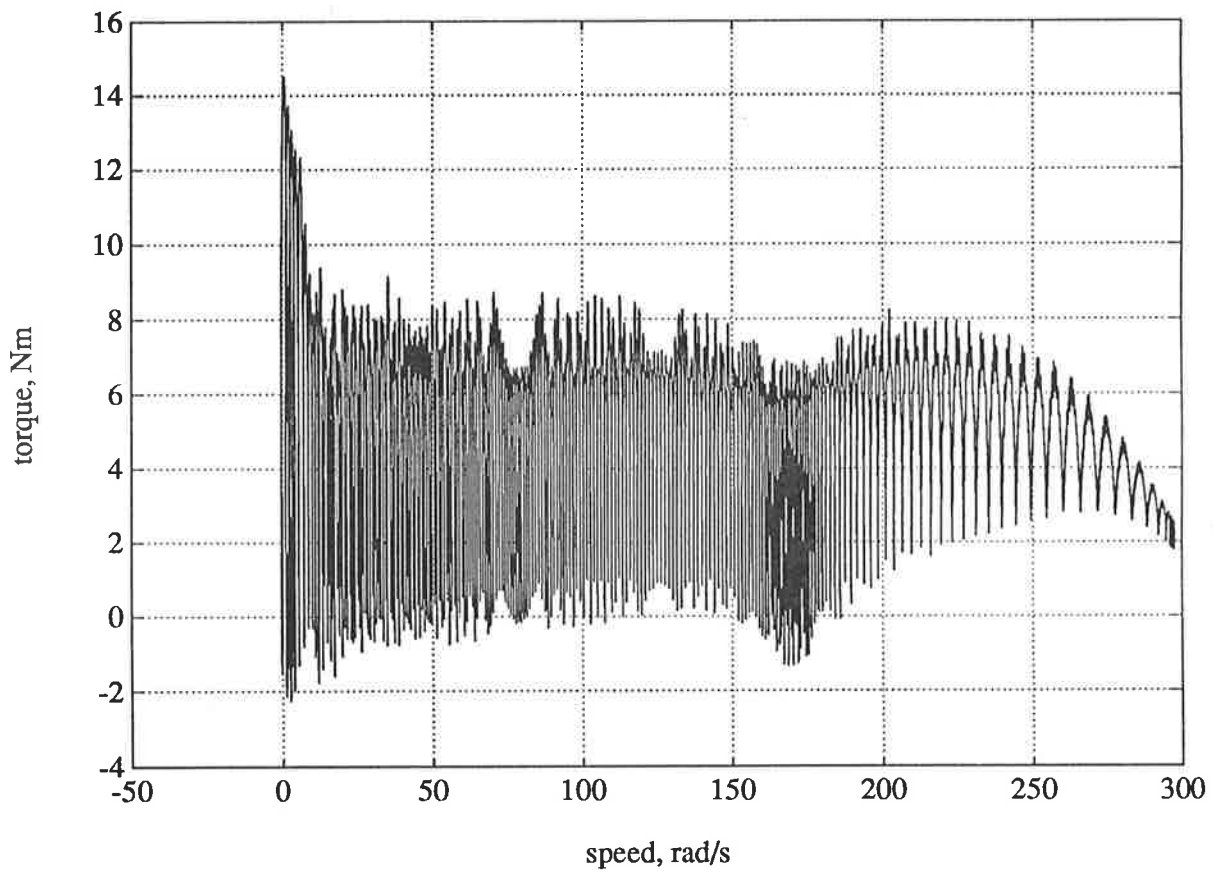


Figure 152

Simulated transient torque-speed during start-up for Machine II

(2-pole)

- rotor bars 3 and 4 faulty
- skew and current displacement included

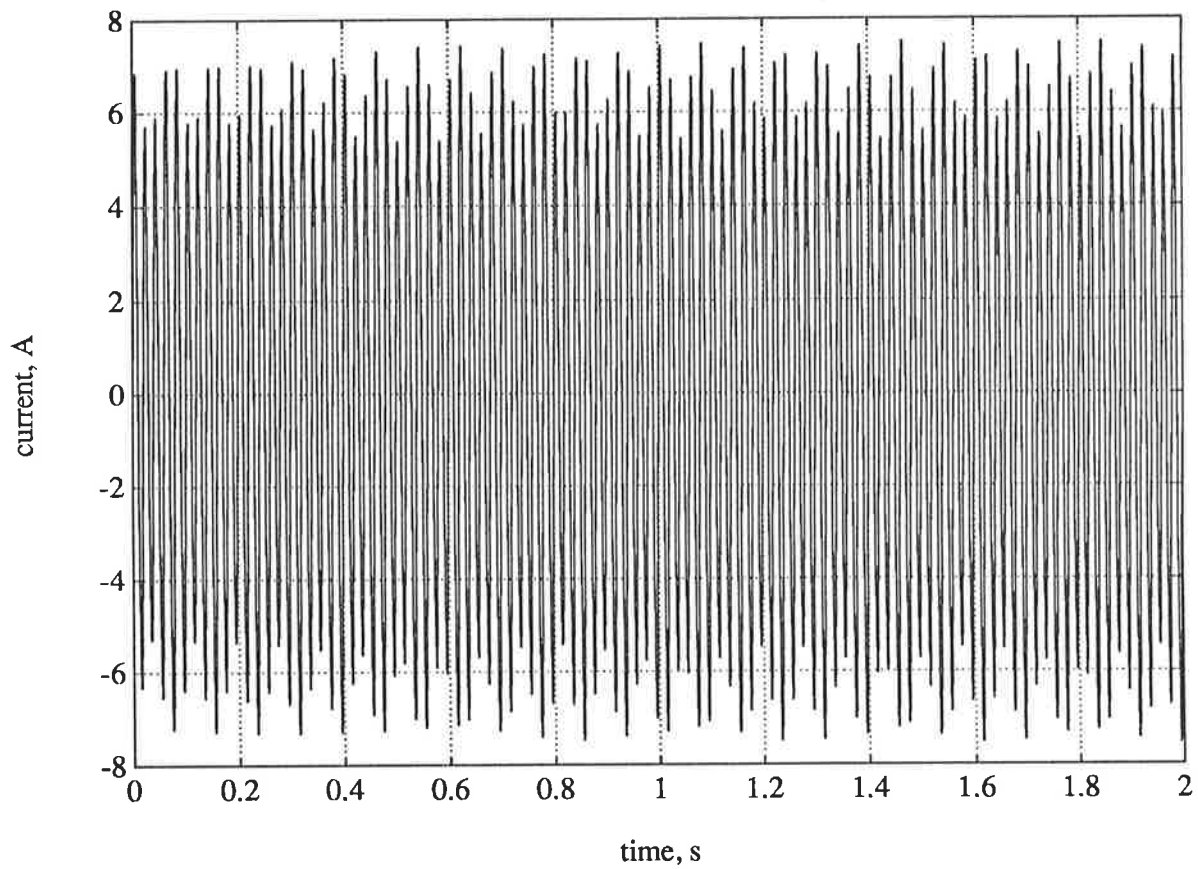


Figure 153

Simulated steady state stator current at 4Nm for Machine II

(2-pole)

- rotor bars 3 and 4 faulty
- skew and current displacement included



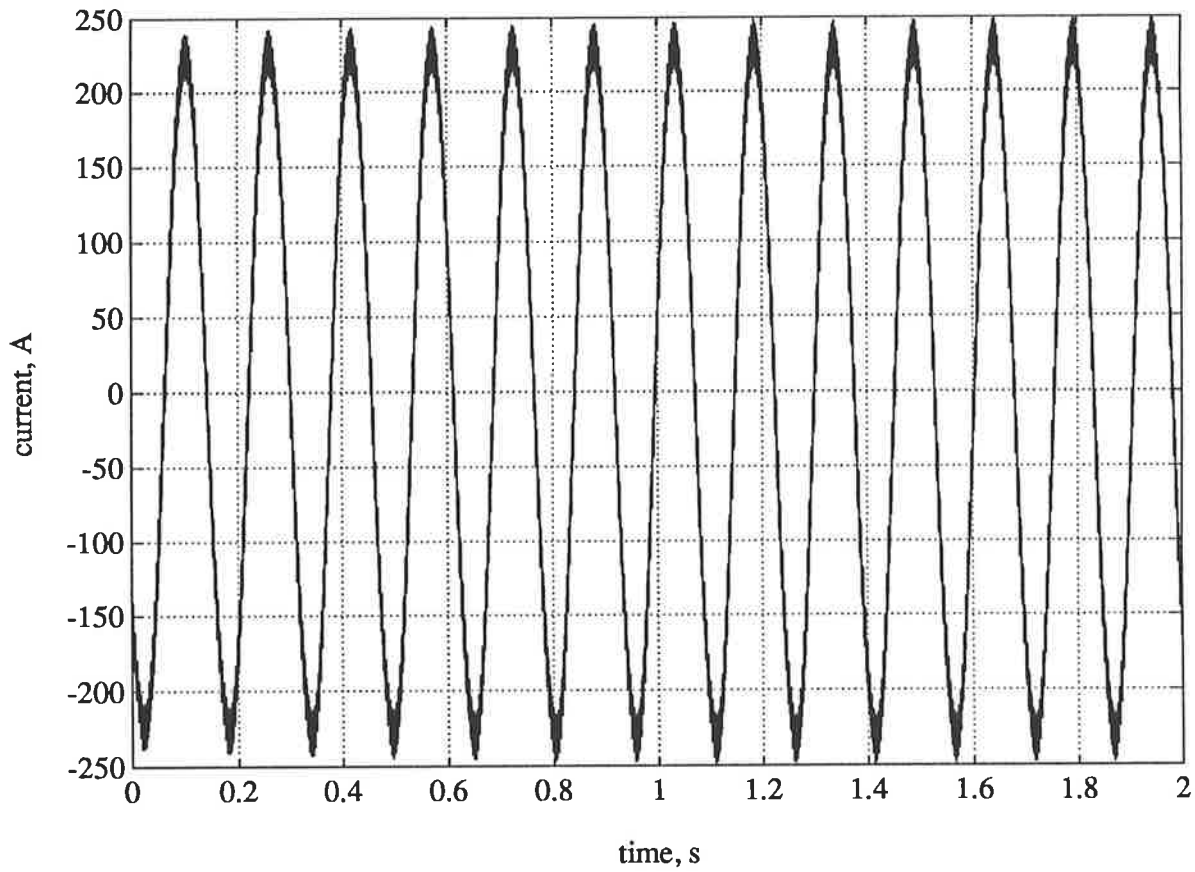


Figure 154

Simulated steady state rotor current at 4Nm for Machine II

(2-pole)

- rotor bars 3 and 4 faulty
- skew and current displacement included

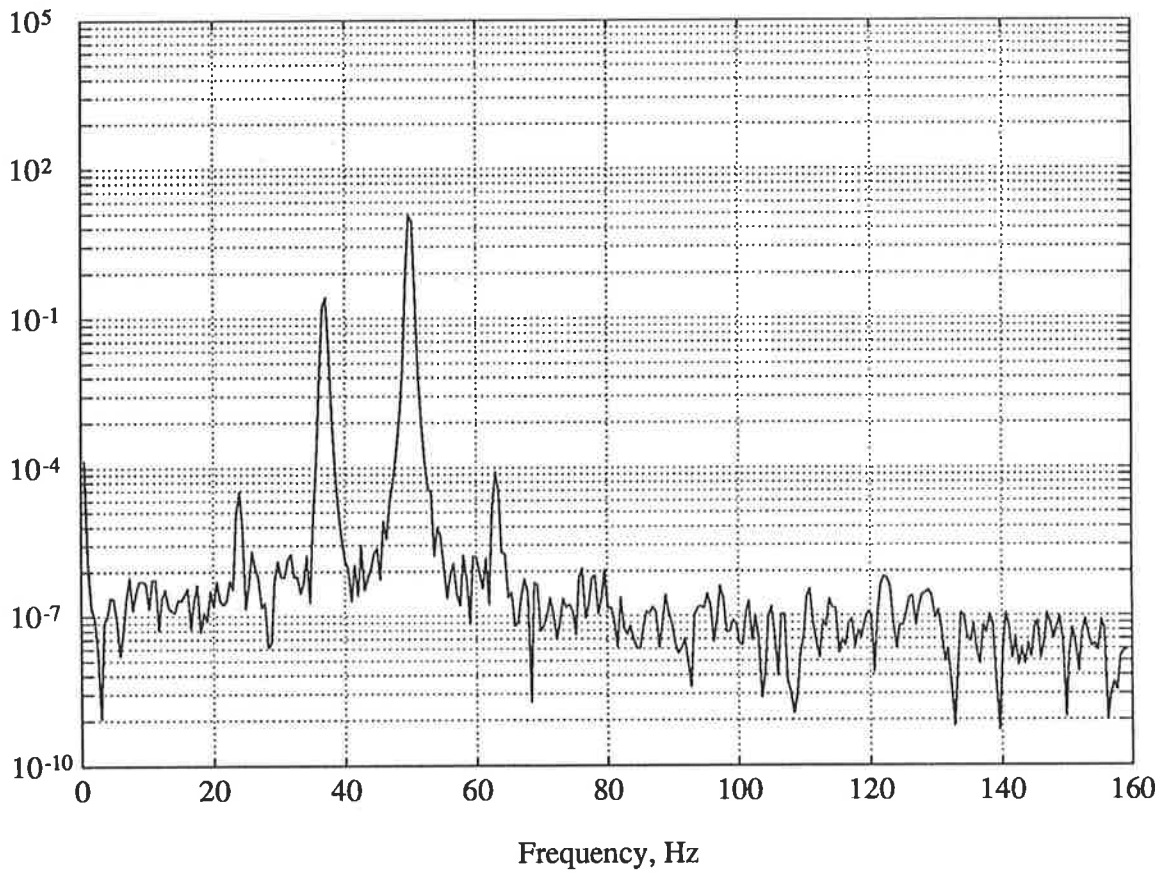


Figure 155

Power spectrum of stator current at 4Nm for Machine II  
(2-pole) (simulated)

- rotor bars 3 and 4 faulty
- skew and current displacement included

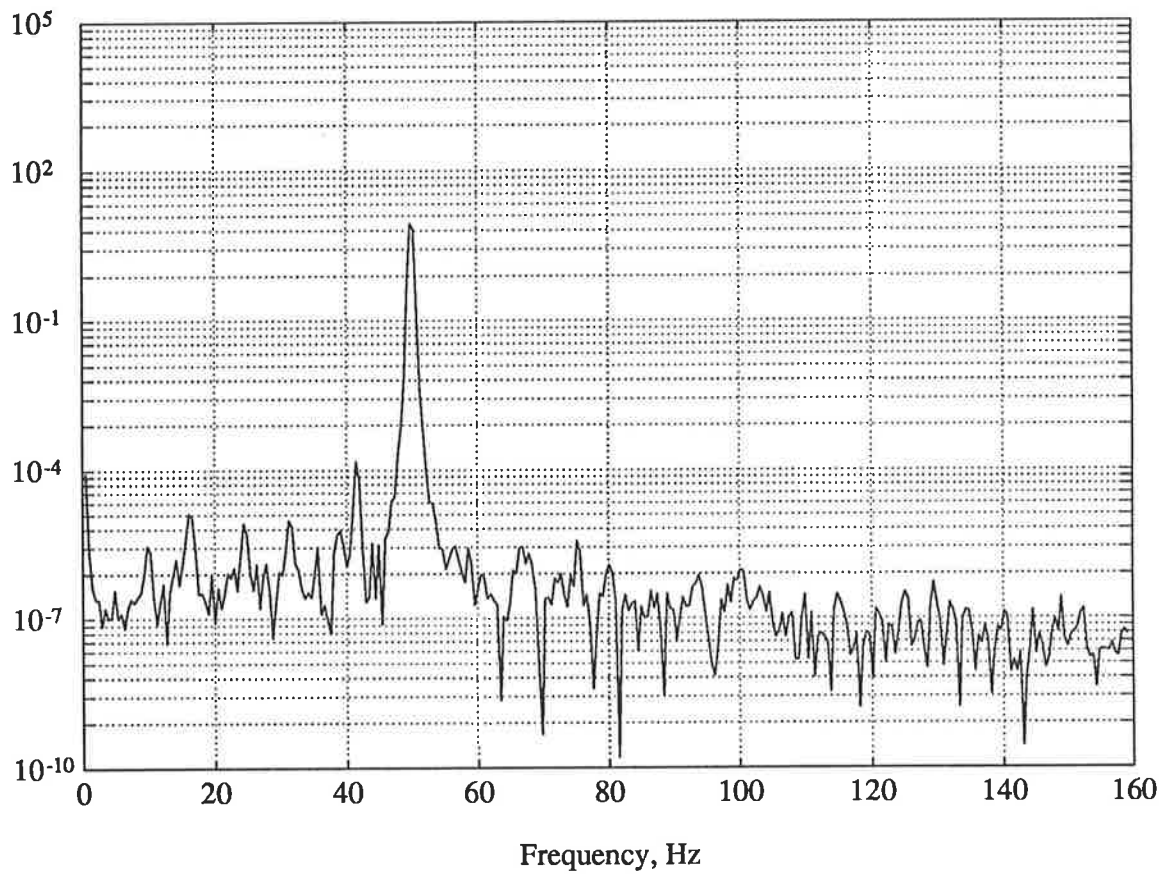


Figure 156

Power spectrum of stator current at 4Nm for Machine II  
(2-pole) (simulated)

- "healthy" rotor
- skew and current displacement included

### 5.5.6 Other Uses of Discrete Circuit Models

In previous sections it has been demonstrated that discrete circuit models can be used successfully in simulating the performance of an induction machine under a variety of operating conditions, ranging from direct-on-line starting of healthy machines to continuous operation of machines with faults. It should be noted that the widely used low order models for dynamic simulation fail completely in providing the level of detail in performance predictions that discrete circuit models are capable of providing. Evidently, the usefulness of discrete circuit models is not limited to the cases discussed; other aspects of behaviour can be readily simulated. These include winding faults, various types of supply fault, reswitching transients and the effect on machine behaviour of non-sinusoidal supply conditions, to name a few. In addition, discrete circuit models are especially well suited to the *a priori* assessment of machine performance in the case of unusual designs. These various possible uses of discrete circuit models will be exemplified here by the simulation of the following three cases:

- a transient blocked rotor behaviour
- b reswitching transients
- c quasi steady-state performance

All cases will be demonstrated using Machine II in the 2-pole connected mode. Furthermore, it will be assumed that the rotor cage is "healthy",

implying identical rotor bars interconnected with identical end-ring segments and the machine is driven from a balanced three-phase sinusoidal supply. Evidently, the effect of skewing of rotor bars and current displacement will be accounted for.

The first simulation is that of the **blocked rotor** condition of Machine II. The machine is connected directly across the supply with the same initial conditions stipulated elsewhere in the thesis. Figures 157 and 158 show the stator current and rotor current respectively. As would be expected, in both the stator windings and the rotor cage an initial in-rush current is observed which settles down to a steady swing. Of greater interest is the behaviour of the torque shown in Figure 159; torque is seen to be subject to a transient modulation following the energisation of the windings before it settles to a sinusoidal swing at twice the supply frequency. This behaviour compares remarkably well with blocked rotor transient torques reported in the literature [23] and encountered in practice.

The second simulation pertains to that of **reswitching** of the machine in the operating region; the machine is started direct-on-line, allowed to reach the operating regime and, while in this mode, the supply is turned off for three cycles, to be restored at the end of the three cycles. Figures 160 and 161 show the stator current and the rotor current respectively; the reswitching currents are seen to be in excess of the starting current. Figure 162 depicts the transient torques arising at reswitching. Figure 163 shows the speed variation during reswitching. Figure 164 presents all rotor bar currents in cascade format during reswitching.

A general model such as the discrete circuit model ought to be capable to predict machine performance not only under transient operating conditions as has been demonstrated so far, but also when the machine is operating under steady state conditions. This capability is to be demonstrated next. The suite of Figures 165 to 170 was obtained by running up the machine to full speed without load, allowing it to settle and then applying a gradually increasing load to brake the machine. The machine was brought to a standstill and forced into the second quadrant. Figures 165 and 166 give the variation of currents in stator and rotor during this process. Figures 167 and 168 depict the variation of torque and angular speed for the run-up and deceleration. Figure 169 is the resultant torque-speed characteristic during the operation. Figure 170 is extracted from Figure 169 and represents the quasi steady-state torque-speed characteristic of the machine. What is remarkable is the ability of the discrete circuit model to pinpoint parasitic torques without the use of harmonic modelling techniques.

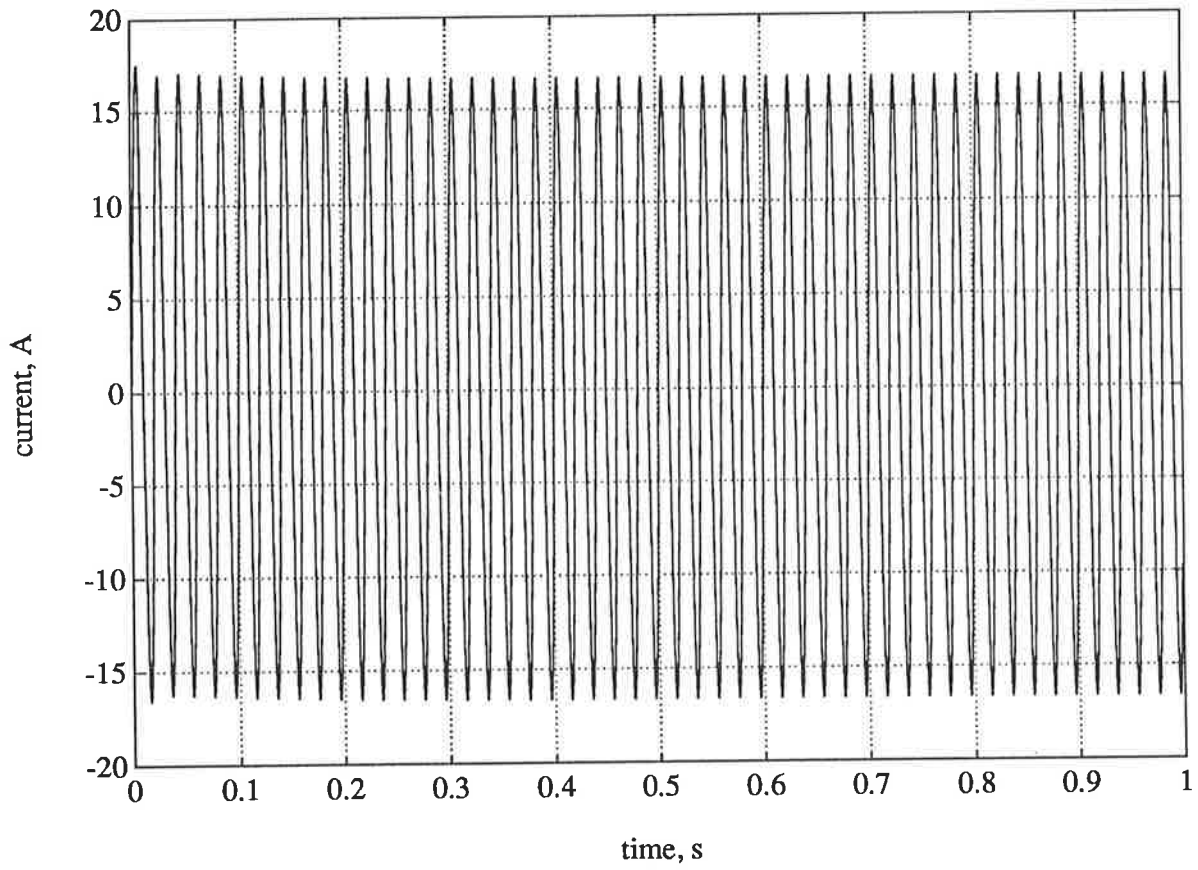


Figure 157

Simulated stator current with blocked rotor for Machine II

(2-pole)

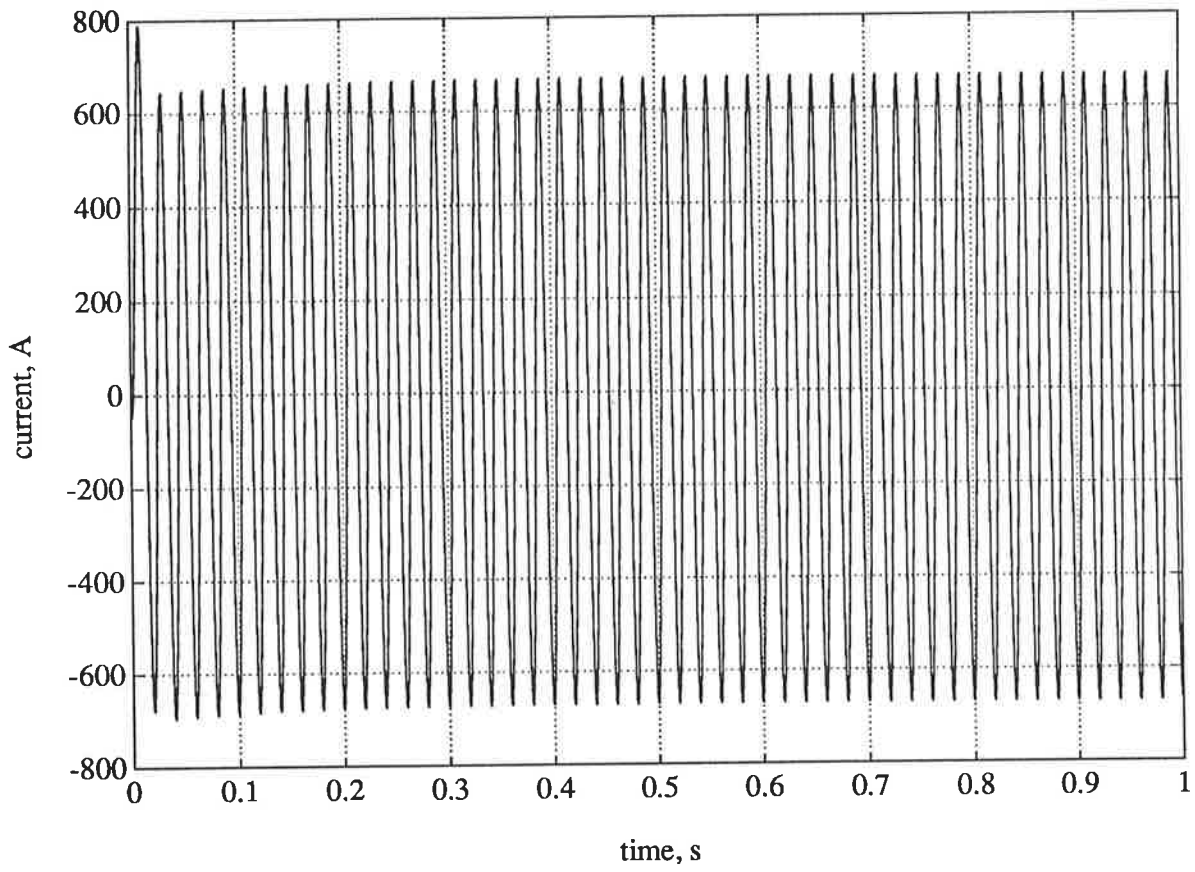


Figure 158

Simulated rotor current with blocked rotor for Machine II

(2-pole)



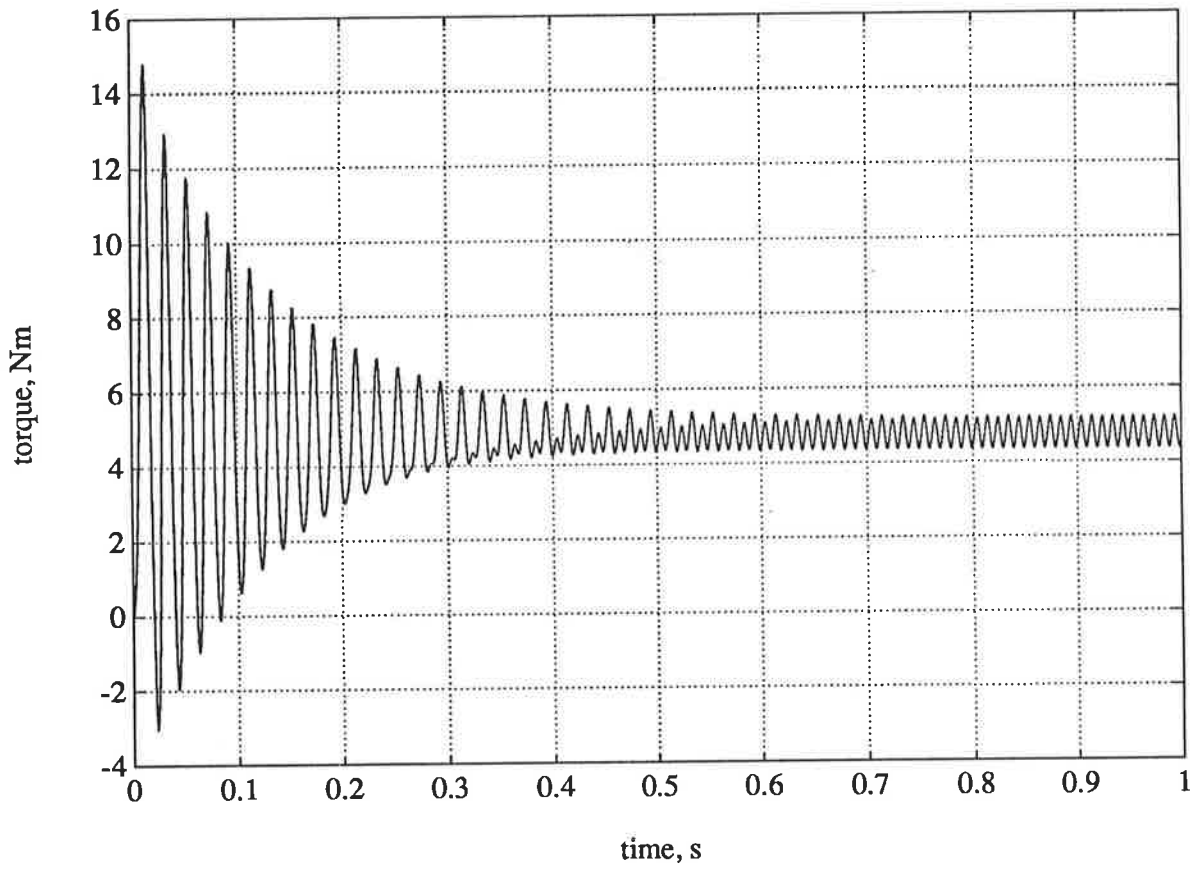


Figure 159

Simulated torque with blocked rotor for Machine II

(2-pole)

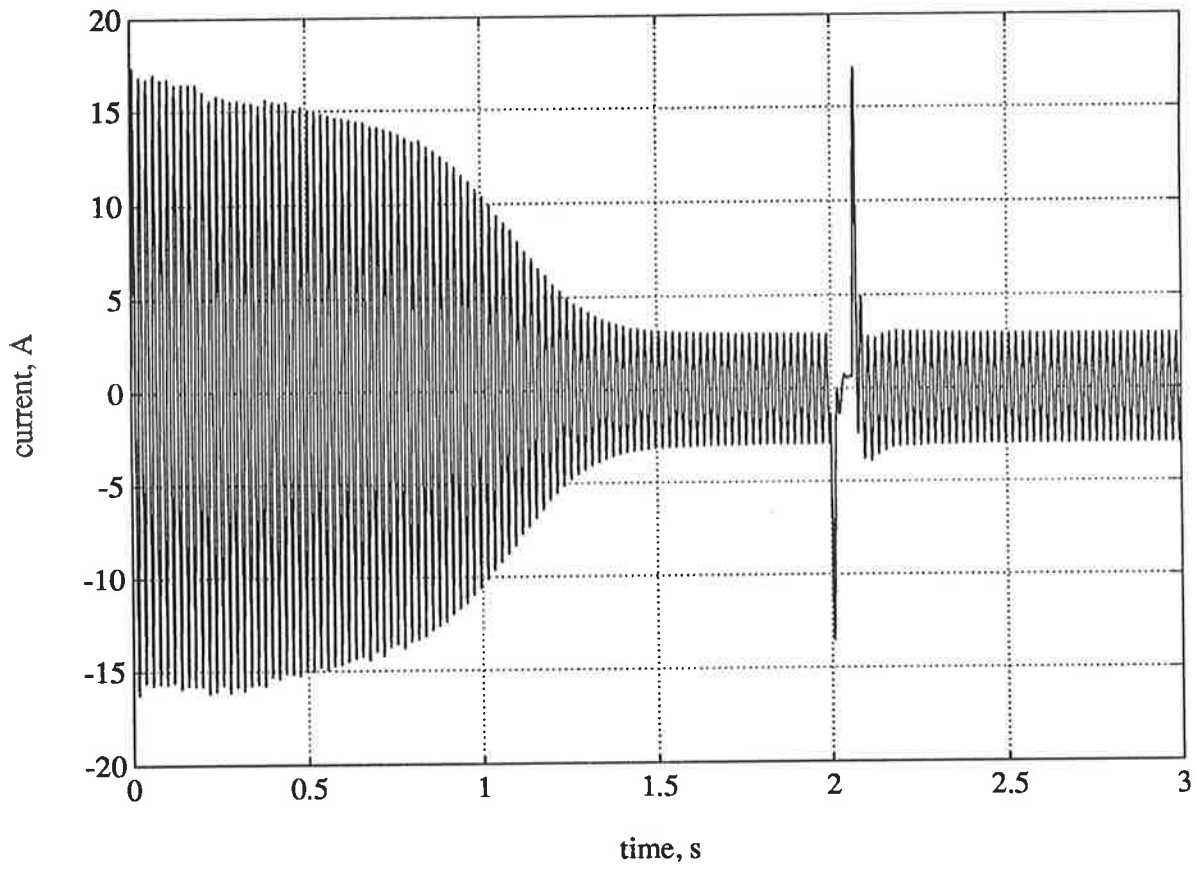


Figure 160

Simulated stator current at reswitching for Machine II

(2-pole)

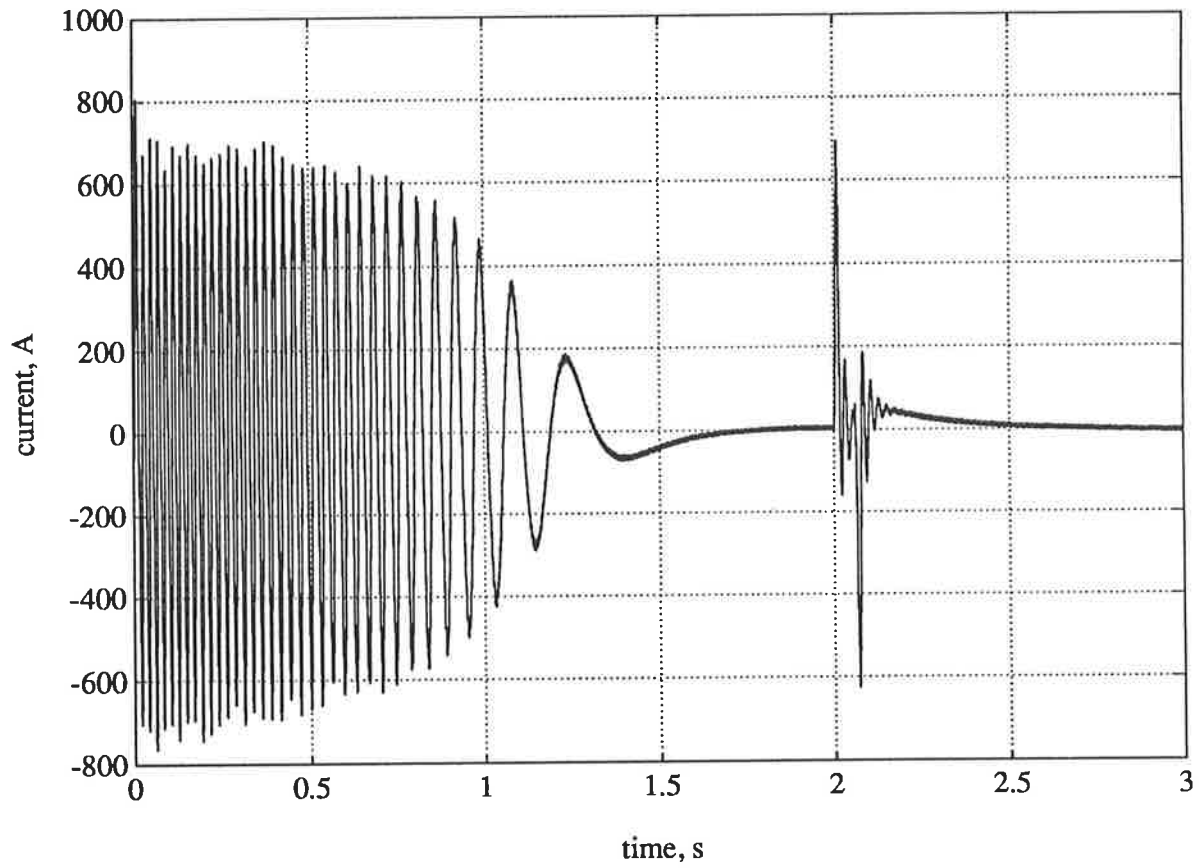


Figure 161

Simulated rotor current at reswitching for Machine II  
(2-pole)

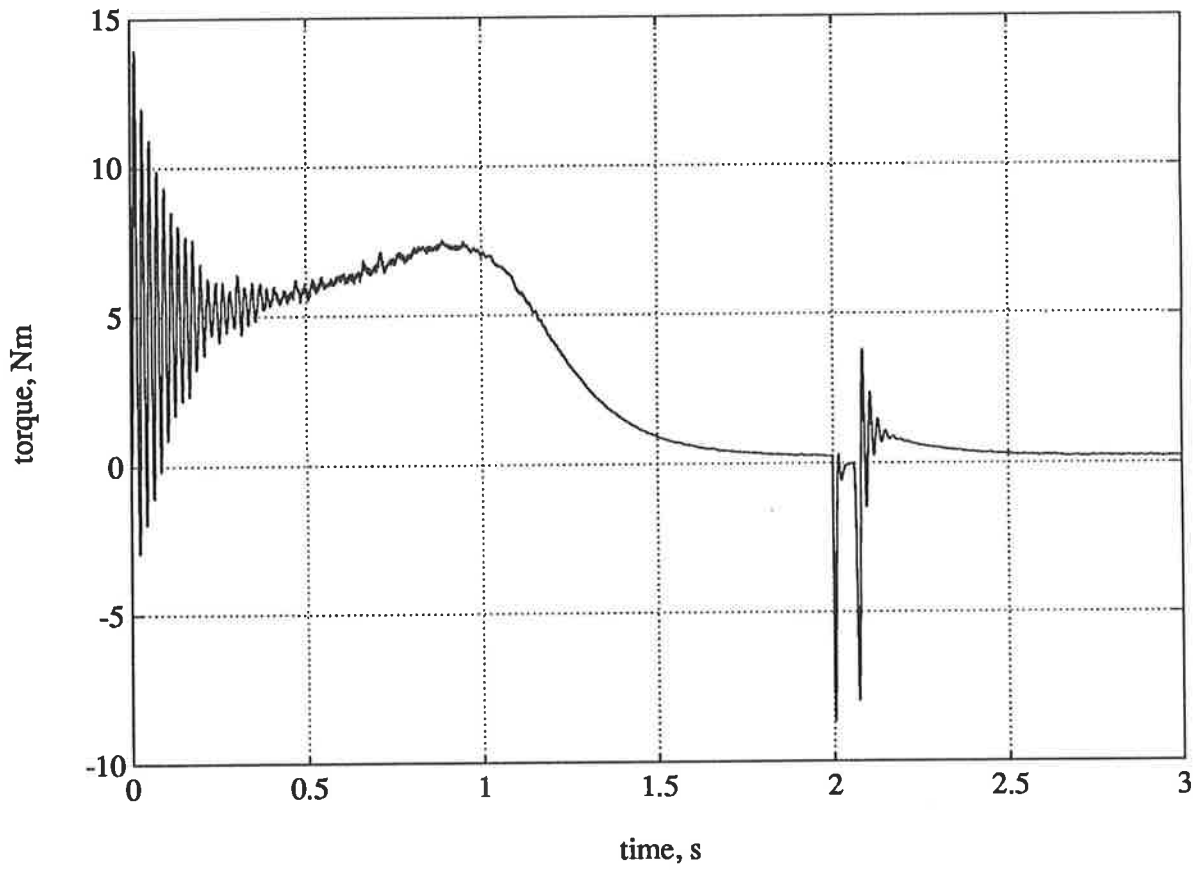


Figure 162

Simulated torque transients at reswitching for Machine II  
(2-pole)

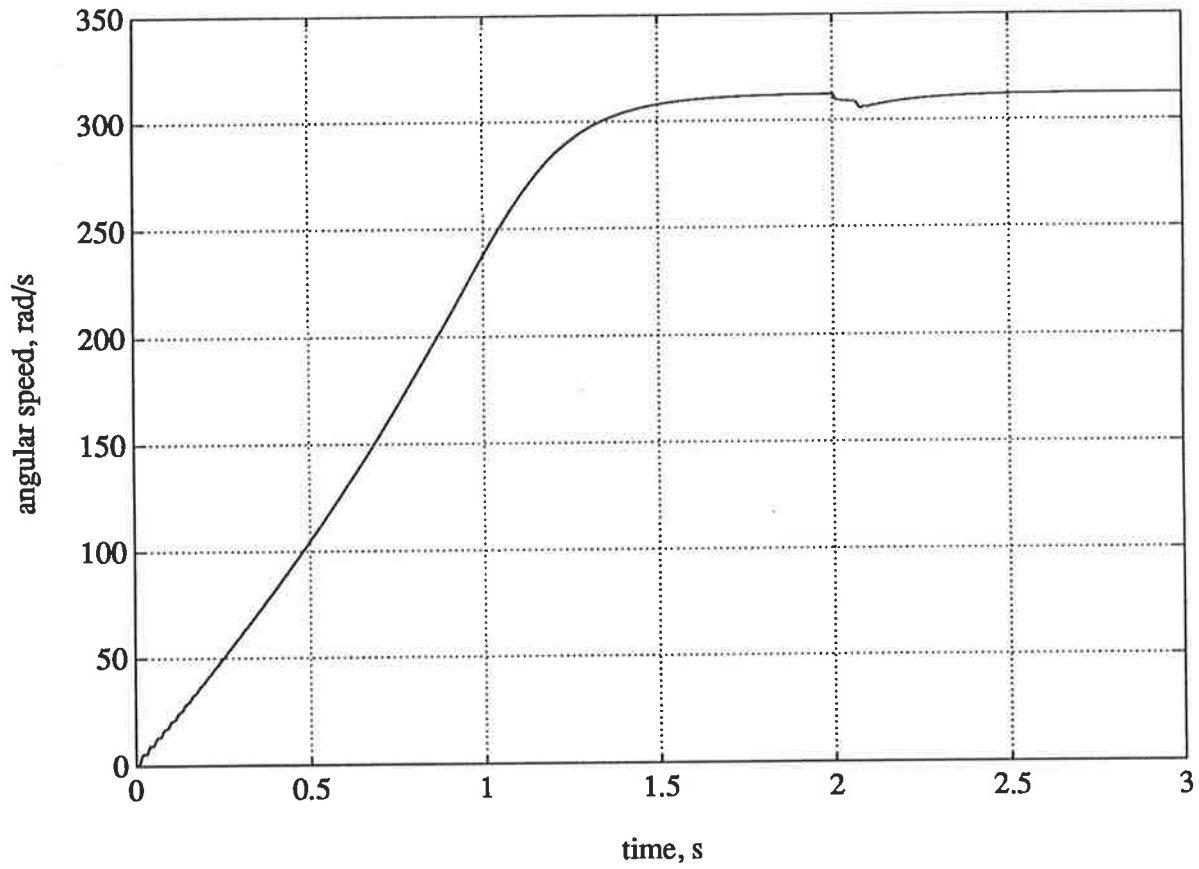


Figure 163

Simulated speed transients at reswitching for Machine II

(2-pole)

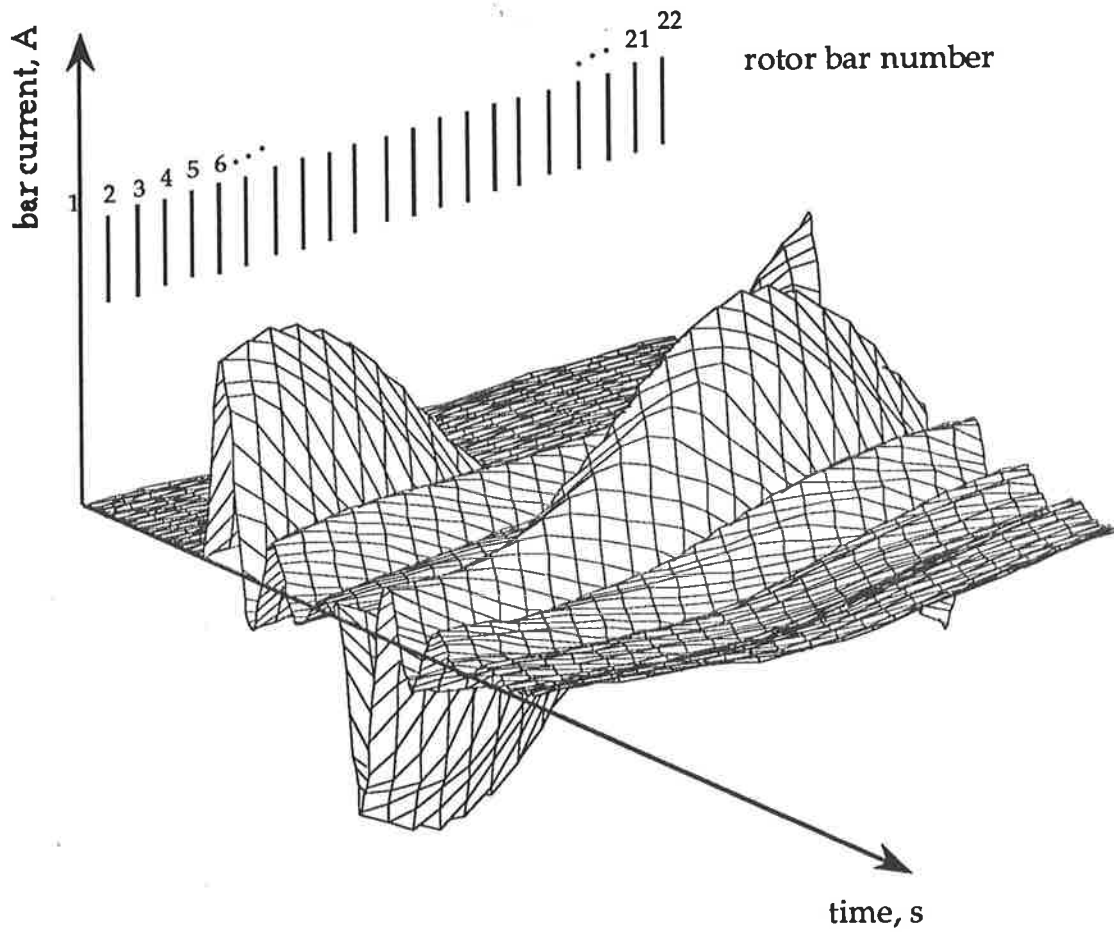


Figure 164

Simulated rotor bar currents at reswitching for Machine II  
(2-pole)

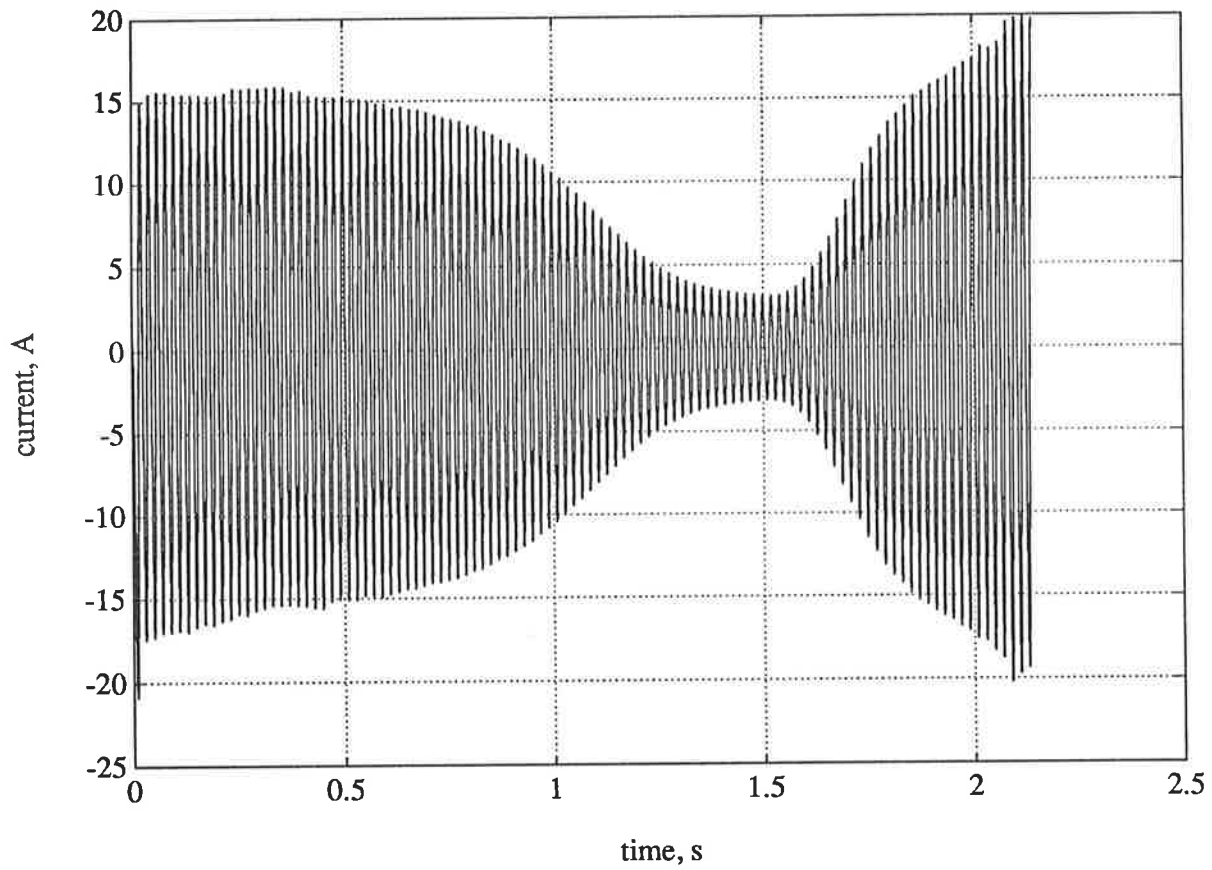


Figure 165

Simulated stator current during run-up and deceleration

(see text)

(2-pole)

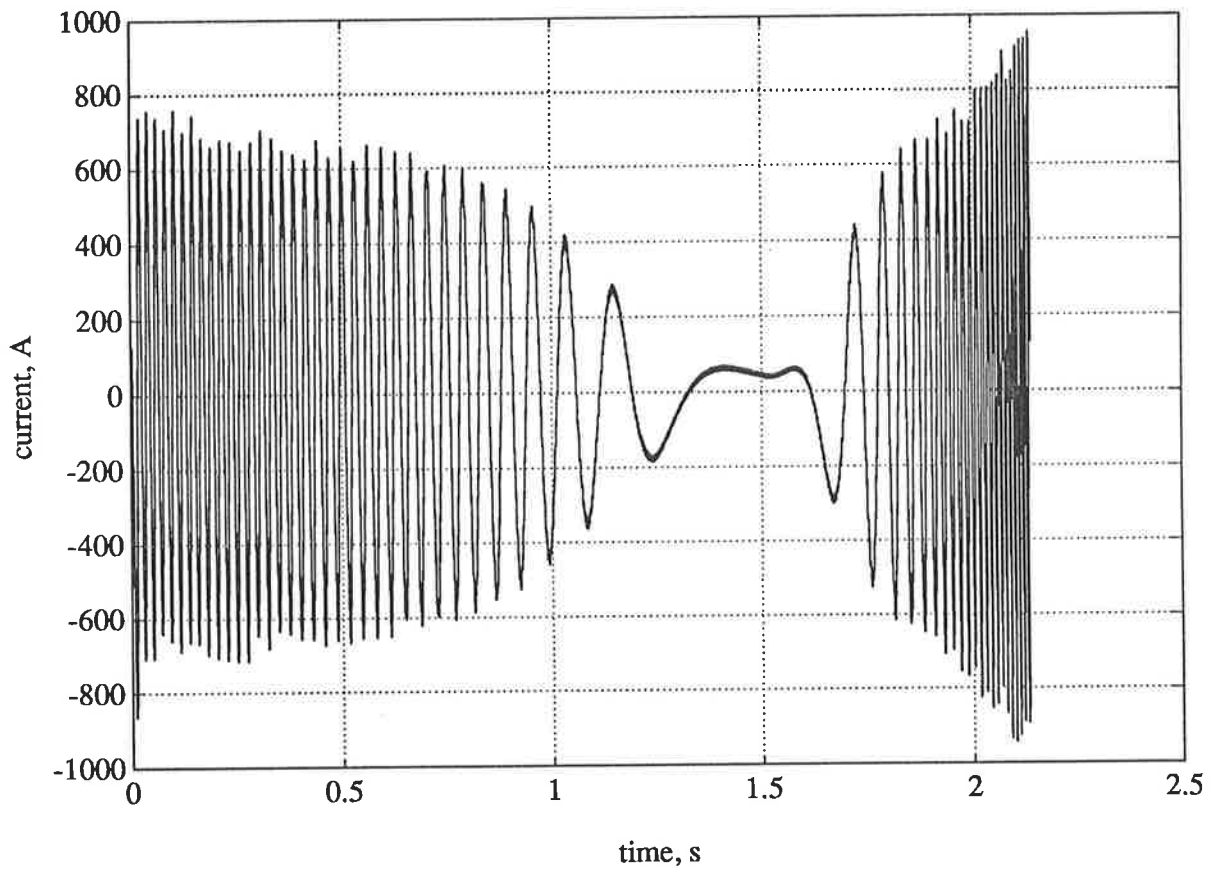


Figure 166

Simulated rotor bar current during run-up and deceleration

(see text)

(2-pole)



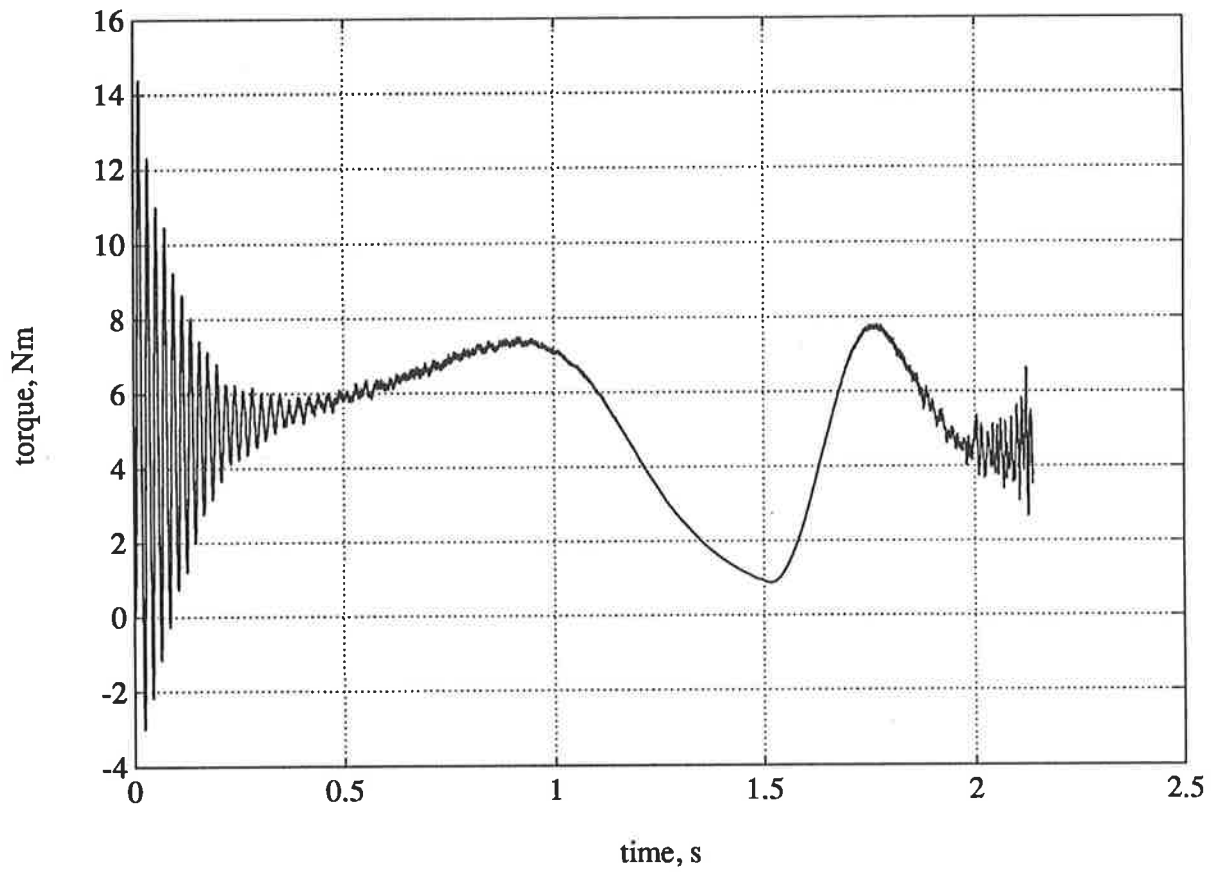


Figure 167

Simulated torque during run-up and deceleration (see text)

(2-pole)

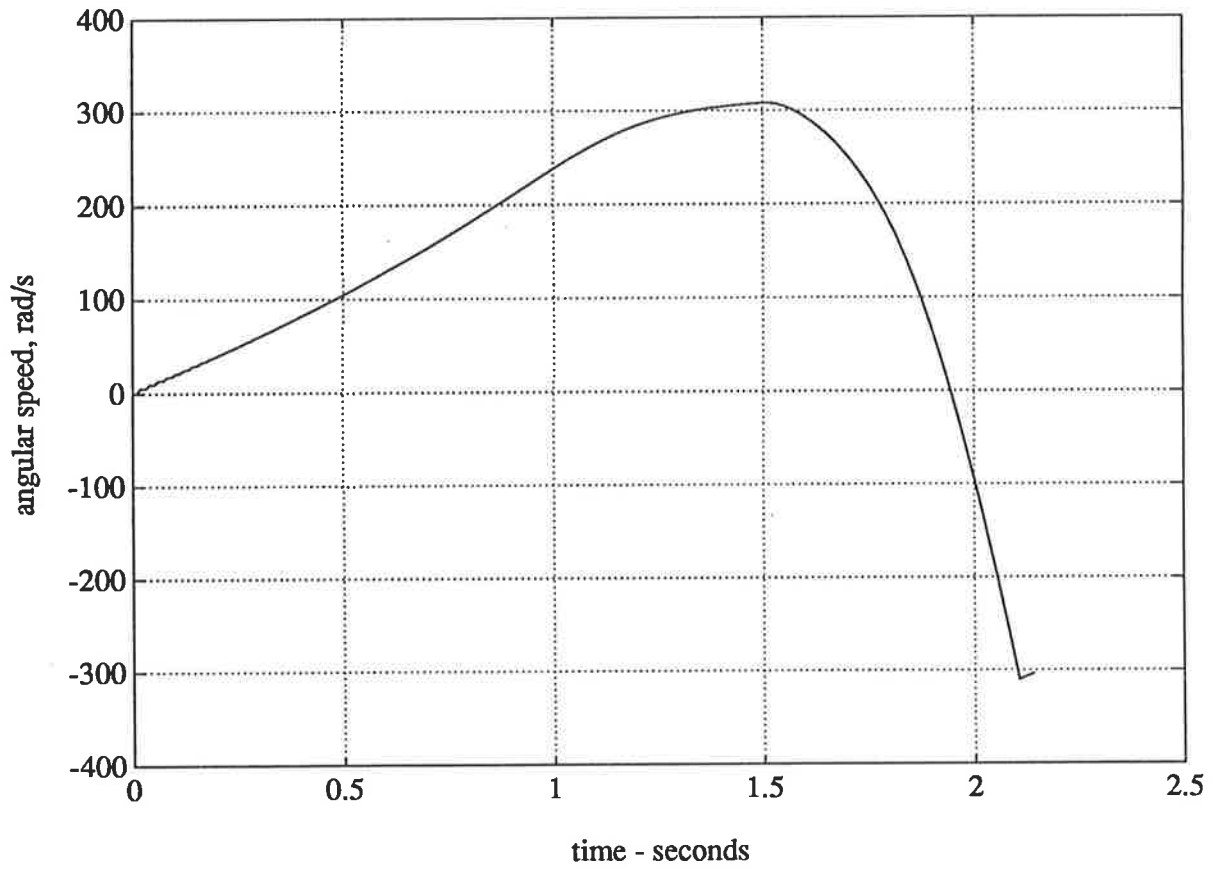


Figure 168

Simulated speed during run-up and deceleration (see text)

(2-pole)

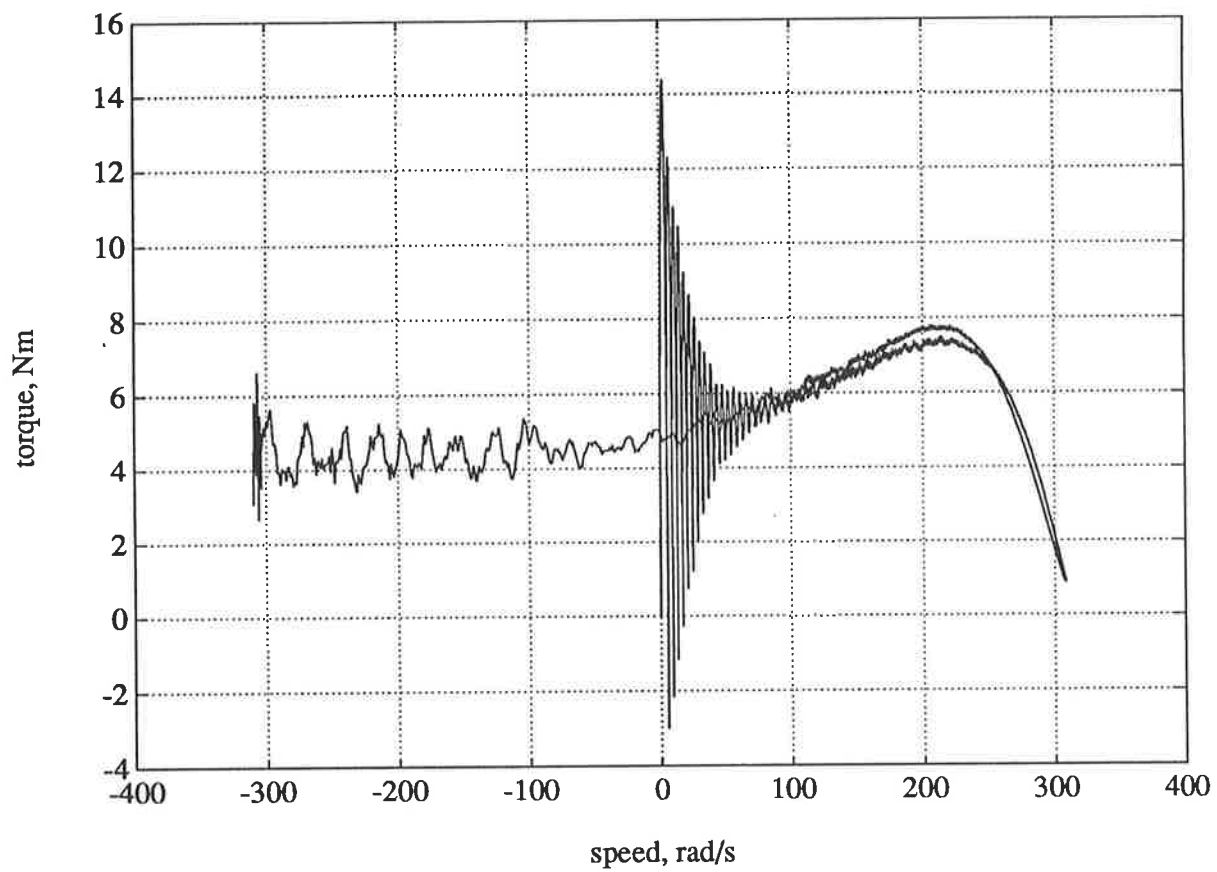


Figure 169

Simulated torque-speed characteristic during run-up and deceleration (see text)

(2-pole)

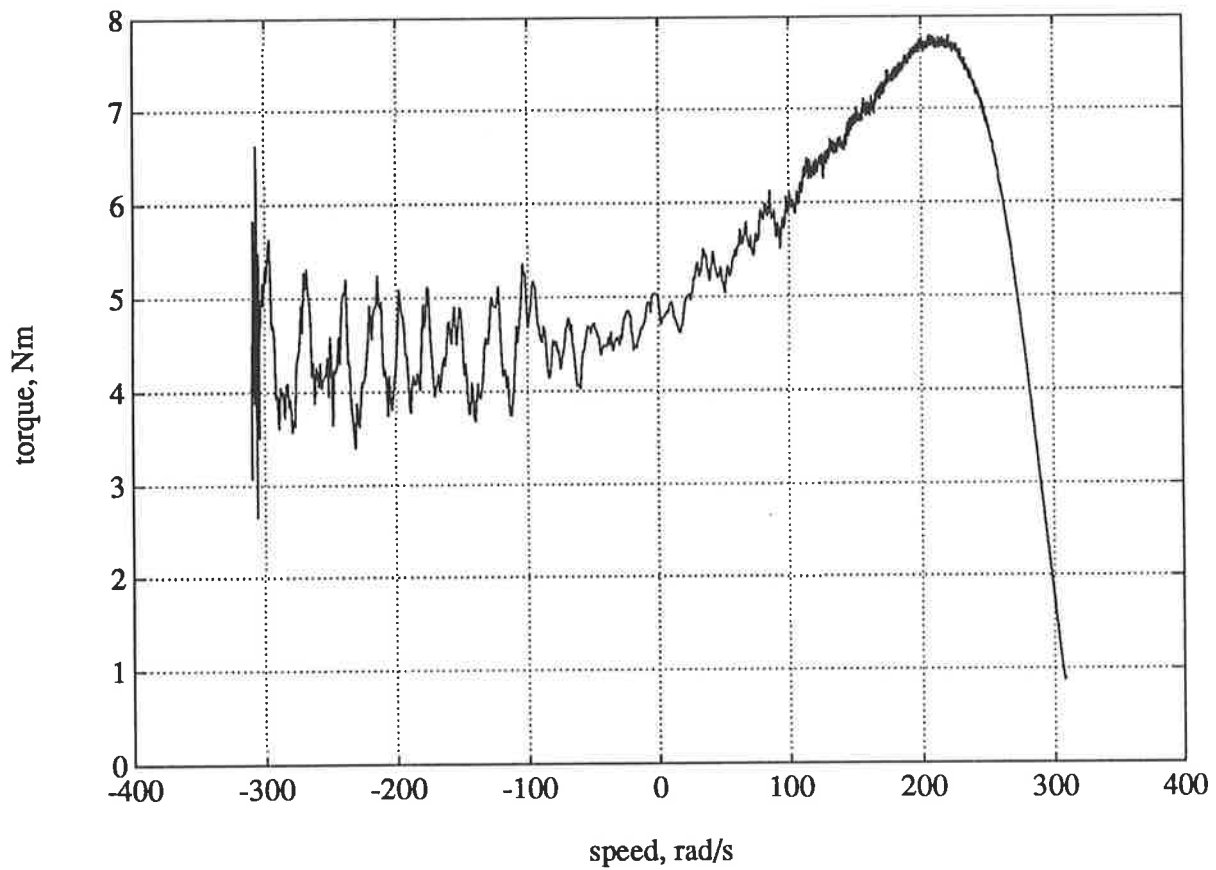


Figure 170

Simulated quasi steady-state torque-speed characteristic (see text)

(2-pole)

## 5.6 Observations

This chapter has demonstrated the use of various modelling techniques and has offered substantial experimental verification where feasible. Although early in the chapter deliberations have been on the steady state models, the main emphasis has been on the dynamic modelling of induction machines; the object of this thesis.

For the reasons explained previously, some attention has been paid to steady state modelling concepts. It has been shown that it is possible to considerably improve prediction accuracy by the incorporation in the models of phenomena which are commonly absent from such models. High fidelity harmonic circuit models arguably constitute the pinnacle of the deliberations presented in the earlier parts of this chapter. The increase in computational effort is modest, yet improvements in prediction accuracy under quasi steady-state operating conditions are substantial.

Dynamic modelling of induction machines has preoccupied electrical machine analysts for a long time, as evidenced by the existence of various types of model. This chapter has endeavoured to establish the applicability of such models to the analysis of a given induction machine with a view to predicting the transient characteristics accurately. It has been shown that such models lack in providing credible predictions even with balanced and symmetrical conditions. Evidently, these popular models are completely incapable of predicting machine performance when asymmetries are present such as fractured rotor bars, shorted coils and rotor eccentricity. This is where the discrete circuit model enters the picture.

Discrete circuit models are not subject to the same restrictive assumptions of the conventional models. They are formed on the basis of realistic considerations and are capable of predicting the machine performance under a variety of conditions ranging from normal operation to fault conditions. This has been demonstrated here by simulating the machine performance for different regimes. The simulation of the motor starting under direct-on-line in 2-pole mode gives clear evidence to the superiority of the discrete circuit model above conventional models; although not exact, prediction is much better than that possible with conventional models and the qualitative detail is striking. An additional bonus is the ability to directly gauge the effect on machine performance of design parameters such as the amount of skew, air-gap distance and slot topologies. However, what makes the discrete circuit model an invaluable tool is its capability of analysing the behaviour of machines with internal or external asymmetries and unusual designs. Various cases have been presented to underscore this capability.

# 6

## CONCLUSION

The intent of this thesis has been to develop dynamic models for induction machines. However, in the course of doing so, lumped parameter steady-state models have been revisited. The reason for this apparent detour is simple: the principles which apply to parameter determination in steady state circuit models are equally applicable to the parameter determination in dynamic models. As previously observed, steady-state modelling has been the main tool-of-trade in design offices of electrical machine manufacturers. That is why the opportunity has been seized to demonstrate that a more rigorous approach to the *a priori* steady-state modelling can result in dramatic improvements in prediction accuracy. The model development has been pursued on the basis of conventional lumped parameter modelling techniques and model fidelity has been improved by judiciously incorporating physically relevant phenomena. This has led to the formation of *high-fidelity* models suitable for frequency domain analysis under steady-state operating conditions.

Arguably, steady-state operation can be considered to be a special case, of the machine's dynamic behaviour. This explains why various aggregate circuit models have long been proposed and widely used for the dynamic analysis of induction machines. The main drawback of the commonly deployed dynamic models, the examples of which have been presented in considerable detail in the thesis, has been the idealisations on the basis of which such models have been obtained. Such idealisations have led to distortions in performance prediction, limiting the usefulness of conventional dynamic models.

The cardinal challenge in devising any dynamic model for *a priori* use is to achieve model fidelity: the accurate prediction of fine detail in the performance of an induction machine. This is of critical import, especially where the designer is faced with the task of predicting the performance of a machine of unusual design or is called upon to assess in advance the consequences of any deviation from normal operation. The latter evidently includes fault conditions. Unfortunately, the conventional models for dynamic analysis are unsuited to such universal use.

The above observations constitute the rationale for the development of **discrete circuit models** of this thesis. Discrete circuit models are not bound by the restrictions imposed upon the aggregate circuit models, hence they offer an infinitely greater flexibility in analysing machine behaviour under any operating conditions. Model sensitivity is high to parameter variations: for instance, the effect of varying the amount of slot skew can be readily evaluated. Furthermore the effects of asymmetries, either intrinsic to the design or arising during operation, can be analysed reliably. These are major strengths, which conventional dynamic models do not possess.



On the debit side are the greater computational demands for simulation, the confinement to *a priori* use and the deviation in prediction from the measured values within the *pull-out* region. The increased model complexity is responsible for the considerably extended computation time per simulation compared with conventional dynamic models. This is a consequence of the trade-off between model fidelity and computational effort. The suitability for *a priori* analysis stems from the desire to link topology to performance. Although providing a potent tool for analysis if topological detail is available, this excludes discrete circuit models, in the form presented here, from being used in *a posteriori* applications. Finally, more work needs to be done in improving the quantitative accuracy of prediction within the *pull-out* region; incorporation in the model of aspects neglected here are likely to make a positive impact in improving the quantitative accuracy.

The cases presented in Chapter 5 prove beyond doubt that the approach is successful; model fidelity is remarkably high. Measured aspects of behaviour can be reliably predicted which are impossible to predict with the aid of conventional models. Furthermore, the discrete circuit modelling approach represents an elegant and transparent method when compared with other more elaborate models based on magnetic equivalent circuit concepts [23]. Model utility is equally high in that the applicability of the model extends beyond the analysis of balanced, symmetrical and *healthy* machines. Unusual designs or fault conditions can be analysed with relative ease. It must therefore be concluded unequivocally that the task of devising dynamic models for induction machines, the object of this thesis, has been accomplished. Also noteworthy is the fact that the usefulness of the approach is not restricted to induction machines; other types of machine can be modelled using discrete circuit modelling techniques.

## BIBLIOGRAPHY

- 1 **Adams, C. A.** *The Design of Induction Motors - with Special Reference to Magnetic Leakage* AIEE Trans., Vol. 24, 1905, pp.649-684
- 2 **Richter, R.** *Elektrische Maschinen, Band IV : Die Induktionsmaschinen* Birkhäuser Verlag Basel und Stuttgart, 1954
- 3 **Stanley, H. C.** *An Analysis of the Induction Machine* AIEE Trans., Vol. 57, 1938, pp.751-575
- 4 **Wahl, A. M. and Kilgore, L. A.** *Transient Starting Torques in Induction Motors* AIEE Trans., Vol. 59, 1940, pp.603-607
- 5 **Richter, R.** *Elektrische Maschinen, Band I : Allgemeine Berechnungselemente - Die Gleichstrommaschine* Birkhäuser Verlag Basel und Stuttgart, 1967

- 6 Nürnberg, W. *Die Asynchronmaschine* Springer-Verlag, 1963
- 7 Liwshitz-Garik, M. and Whipple, C. C. *Alternating-Current Machines* Van Nostrand, 2nd Edition, 1961
- 8 Lloyd, T. C. and Stone, H. B. *Some Aspects of Polyphase Motor Design- The Design and Properties of the Magnetic Circuit* AIEE Transactions, Vol. 65, December 1946, pp.812-818
- 9 Hammond, P. and Rogers, G. J. *Use of equivalent fields in electrical-machine studies* PROC. IEE, Vol. 121, No. 6, June 1974, pp.500-507
- 10 Göl, Ö. *Induction Machine Models for Design* Proc. International Conference on Evolution and Modern Aspects of Induction Machines, 1986, Torino, Italy, pp. A 5-10
- 11 Drehmann, A. and Lenninger, L. *Drehmomenteinsattelungen, Störtöne und Rüttelkräfte bei Kurzschlußläufer-Motoren als Folge unzureichender Läufernutenzahlen* ETZ, Bd. 72 (1951) H.14, pp. 435-437
- 12 Kron, G. *Equivalent Circuits of Electric Machinery* Dover Publications, New York, 1967
- 13 Jones, C. V. *The Unified Theory of Electrical Machines* Butterworths, London, 1967

- 14 **Belmans, R., Findlay, R. D. and Geysen, W.** *A Circuit Approach to Finite Element Analysis of a Double Squirrel Cage Induction Motor* IEEE,PES 1990 SM,90 SM 287-3 EC, pp.1-6
- 15 **Williamson, S., Smith, A. C., Begg, M. C. and Smith, I. R.** *General Techniques for the Analysis of Induction Machines Using Finite Elements* Proc. International Conference on Evolution and Modern Aspects of Induction Machines, 1986, Torino, Italy, pp. 389-395
- 16 **Tindall, C. E. and Lees, M. J.** *Field-theory approach to induction motor analysis* PROC. IEE, Vol. 120, No. 4, April 1973, pp.469-476
- 17 **Wambacq, J., Lataire, Ph. and Maggetto, G.** *Suitability of an Induction Machine Model Including Saturation in the Description and Prediction of Transients* Proc. ICEM'80, International Conference on Electrical Machines, Athens, 1980, pp.1703-1715
- 18 **Hancock, N. N.** *Matrix Analysis of Electrical Machinery* Pergamon Press,1974
- 19 **Fudeh, H.R.** *Modeling and Analysis of Induction Machines Containing Space Harmonics* Ph.D. Thesis, Purdue University, 1982
- 20 **Göl, Ö.** *Induction Machine Models for Design and Analysis* M. E. Thesis, University of Melbourne, 1977
- 21 **Seiler, W.** *Synchrone Drehmomente durch Leitwertschwankungen bei Asynchronmaschinen* Bull.SEV/VSE 66(1975)6, pp.324-334

- 22 **Jufer, M.** *Transducteurs Électromécaniques* Traité d'Électricité, Volume IX, Éditions Georgi, 1979
- 23 **Ostovic, V.** *Dynamics of Saturated Electric Machines* Springer-Verlag, 1989
- 24 **Rogers, G.J.** *Induction-motor terminal-voltage equations* Proc. IEE, Vol.123, No 8, 1976, pp. 804-810
- 25 **Williamson, S. and Smith, A. C.** *Field analysis for rotating induction machines and its relationship to the equivalent circuit model* PROC. IEE, Vol. 127, Pt. B, No. 2, March 1980, pp.83-90
- 26 **Poloujadoff, M. and Perret, R.** *Étude d'une machine à induction par la méthode du vecteur de Poynting* Revue Générale d'Électricité, Tome 80, No.9, Septembre 1971, pp.667-674
- 27 **Massé, P.** *Analyse Méthodologique de la Modelisation Numerique des Equations de la Physique des milieux Continus a l'Aide de la Méthode des Éléments Finis. Flux-Expert: Un Systeme d'Aide a la Construction de Logiciels* Thèse d'Etat Grenoble, 1983
- 28 **Müller, W. and Euler, H.** *Numerical Calculation of Eddy Currents in Electrical Devices and Machines* Proc. ICEM'80, International Conference on Electrical Machines, Athens,1980, pp.1553-1559
- 29 **Chari, M. V. K., Tandon, S. C. and Armor, A. F.** *Finite-element solution of transient electromagnetic field problems in electrical machinery* Proc. ICEM'80, International Conference on Electrical Machines, Athens,1980, pp.1519-1526

- 30 **Crank, J. and Nicolson, P.** *A Practical Method for Numerical Evaluation of Solutions of Partial Differential Equations of the Heat Conduction Type* Proc. Camb. Phil. Soc., 43, 1947, pp.50-67
- 31 **Arkkio, A.** *Time-Stepping Finite Element Analysis of Induction Motors* Proc.ICEM'88, International Conference on Electrical Machines, Pisa, Italy, 1988, Vol. I, pp. 275- 280
- 32 **Shen, D. and Meunier, G.** *Modelling of Squirrel Cage Induction Machines by the Finite Elements Method Combined with Circuit Equations* Proc. International Conference on Evolution and Modern Aspects of Induction Machines, 1986, Torino, Italy, pp. 384-388
- 33 **Meunier, G.** *Application de la Méthode des Éléments Finis à la Modélisation des Micromoteurs* Thèse d'Etat Grenoble, 1981
- 34 **Göl, Ö. and Kearney, D.** *A Hybrid Modelling Approach to Induction Machine Design* Proc. eecon'87, An International Conference on Electrical Machines and Drives, Adelaide, Australia, 1987, pp. 73-77
- 35 **Obiozor, C.N.** *Finite Element Analysis of a Defective Induction Motor* Ph.D. Thesis, Ohio University, 1987
- 36 **Poloujadoff, M. and Ivanès, M.** *Comparaison de schémas équivalents au moteur asynchrone polyphasé* Revue Générale d'Électricité, Tome 76, No.1, Janvier 1967, pp.1-6
- 37 **Alger, P. L., Ivanès, M. and Poloujadoff, M.** *Equivalent Circuits for Double Cage Induction Motors* Electric Machines and Electromechanics, 2:137-145, 1978

- 38 **Hasse, K.** *Zum dynamischen Verhalten der Asynchronmaschine bei Betrieb mit variabler Ständerfrequenz und Ständerspannung* ETZ-A, Bd. 89 (1968) H.15, pp. 366-371
- 39 **Naunin, D.** *Berechnung des Drehmomentverlaufens einer Asynchronmaschine bei Speisung mit gepulsten Rechteckspannungen* Bull. SEV/VSE 62(1971)18, 4. September, pp.879-884
- 40 **Wiert, A.** *Association d'onduleurs et de machines asynchrones* Conférence SEE, Marseille, 1974, pp.3-16
- 41 **Park, R. H.** *Two Reaction Theory of Synchronous Machinery* AIEE Trans., Vol. 48, 1929, pp.716-727
- 42 **Booth, R. R.** *The Digital Calculation of Induction Motor Transients* Research Report No. 7 - 1966, University of Melbourne
- 43 **Jacovides, L. J.** *Analysis of Induction Motor Drives with a Nonsinusoidal Supply Voltage Using Fourier Analysis* IAS, Industry and General Applications Group IEEE, Annual Meeting Conference Record, 1970, pp.467-475
- 44 **Rehaoulia, H. and Poloujadoff, M.** *Transient Behaviour of the Resultant Airgap Field During Run-up of an Induction Motor* IEEE Trans. on Energy Conversion, Vol. EC-1, No. 4, December 1986, pp.92-97

- 45 **Koopman, R. J. W.** *Direct Simulation of AC Machinery Including Third-Harmonic Effects* IEEE Trans. on Power Apparatus and Systems, Vol. PAS 88, No. 4, April 1969, pp. 465-470
- 46 **Robertson, S. D. T. and Hebbar, K. M.** *A Digital Model for Three-Phase Induction Machines* IEEE Trans. on Power Apparatus and Systems, Vol. PAS 88, No. 11, November 1969, pp. 1624-1632
- 47 **Matsuse, K., Nishiyama, S. and Tagaki, K.** *Effect of Harmonic Voltage on the Starting Transient Characteristics of Three-Phase Induction Motor* Electrical Engineering in Japan, Vol.91, No.4,1971, pp.31-40
- 48 **Heller, B. and Hamata, V.** *Harmonic Field Effects in Induction Machines* Elsevier Scientific, 1977
- 49 **Oberretl, K.** *Saturation harmonics in induction machines* E und M, 78 (1961), pp.287-294
- 50 **Saito, Y.** *The Theory of the Harmonics of the m,n-Symmetrical-Machine* ETZ-A, Bd. 95 (1974) H.10, pp. 526-530
- 51 **Barton, T.H. and Dunfield, J.C.** *M.M.F.-harmonic effects in induction motors with phase wound rotors* PROC. IEE, Vol. 116, No. 6, JUNE 1969, pp.965-971
- 52 **Hommes, E. and Paap, G. C.** *The analysis of the 3-phase squirrel-cage induction motor with space harmonics- Part 1: Equations developed by a new time-dependent transformation* A.f.E.,67 (1984), pp.217-226



- 53 **Hommes, E. and Paap, G. C.** *The analysis of the 3-phase squirrel-cage induction motor with space harmonics- Part 2: The influence of the space harmonics on the transient behaviour* A.f.E.,67 (1984), pp.227-236
- 54 **Schetelig, H.** *Die Berechnung der magnetischen Flüsse in Drehstrom-Asynchronmaschinen mit Käfigläufer* Diss. Technische Universität Hannover, 1969
- 55 **Jordan, H. and Raube, W.** *Zum Problem der Zusatzverluste in Drehstrom-Asynchronmotoren* ETZ-A, Bd. 93 (1972) H.10, pp. 541-545
- 56 **Göl, Ö.** *Modelling of Parasitic Effects in Induction Machines* Proc. ICEM'86, International Conference on Electrical Machines, 1986, Munich, Germany, pp. 381-384
- 57 **Oberretl, K.** *Neue Erkenntnisse über parasitäre Drehmomente in Käfigläufermotoren* Bulletin Oerlikon, Nr. 348, 1962, pp. 130-155
- 58 **Rawicki, S.** *A method of calculation of characteristics of a three-phase induction machine with two-side asymmetry* Archiv für Elektrotechnik 67 (1984) 237-246
- 59 **Schuisky, W.** *Brüche im Kurzschlußkäfig eines Induktionsmotors und ihre Einflüsse auf das Verhalten des Motors* Archiv für Elektrotechnik, Vol.XXXV, No.5, 1941, pp 287-298

- 60 **Consoli, A. and Lipo, T.A.** *Orthogonal Axis Models for Asymmetrically Connected Induction Machines* IEEE Trans. on Power Apparatus and Systems, Vol.PAS-101, No.12, 1982, pp 4518-4526
- 61 **Jufer, M. and Abdelaziz** *Influence d'une rupture de barre ou d'un anneau sur les caractéristiques externes d'un moteur asynchrone à cage* Bull.SEV 69(1978)17,9, pp. 921-925
- 62 **Russell, A.P. and Pickup, I.E.D.** *An Analysis of the Induction Motor: Part 1- Steady-speed operation* PROC. IEE, Vol. 129, Pt. B, No. 5, September 1982, pp. 229-237
- 63 **Russell, A.P. and Pickup, I.E.D.** *An Analysis of the Induction Motor: Part 2-Damping and synchronising torque production* PROC. IEE, Vol. 129, Pt. B, No. 5, September 1982, pp. 238-242
- 64 **Russell, A.P. and Pickup, I.E.D.** *An Analysis of the Induction Motor: Part 3-Power/frequency relationships* PROC. IEE, Vol. 129, Pt. B, No. 5, September 1982, pp. 243-247
- 65 **Semlyen, A.** *Calculation of Transients in a System of Algebraically Connected Dynamic Components Using a New Numerical Algorithm* IEEE Transactions on Circuits and Systems, Vol. CAS-22, July 1975, pp. 622-628
- 66 **Ito, M., Fujimoto, N., Okuda, H. Takahashi, N. and Miyata, T.** *Analytical Model for Magnetic Field Analysis of Induction Motor Performance* IEEE Trans. on Power Apparatus and Systems, Vol.PAS-100, No.11, 1981, pp 4582-4590

- 67 **Salon, S. J.** *Finite Element Analysis of Electric Machinery* IEEE Computer Applications in Power, April 1990, pp. 29-32
- 68 **Hamels, D. and Deleroi, W.** *Some Problems Concerning Modelling of Induction Machines Operating at Hypersynchronous Speeds* Proc. ICEM'82, International Conference on Electrical Machines, Budapest, Hungary, 1982, pp.73-76
- 69 **Pfaff, G.** *Beitrag zur Berechnung transientser Vorgänge in Asynchronmaschinen bei unsymmetrischen Betriebsverhältnissen* ETZ-A, Bd. 89 (1968) H. 7, 155-160
- 70 **Al Turk, M.F., Mahmoud, M.I. and Perret, R.** *An Induction Motor Identification Method for Performance Study and Control Strategy Parameters Determination: Based on the Simplified Equivalent Circuit* Proc. ICEM'88, International Conference on Electrical Machines, 1988, Pisa, Italy, Vol.III, pp.239-244
- 76 **Potter, P. G. and Cambrell, G. K.** *A Combined Finite Element and Loop Analysis for Nonlinearly Interacting Magnetic Fields and Circuits* IEEE Trans. on Magnetics, Vol. MAG-19, No.6, Nov.1983, pp2352-2355
- 71 **Kumamoto, A., Tada, S. and Hirane, Y.** *Speed Regulation of an Induction Motor Using Model Reference Adaptive Control* IEEE Control Systems Magazine, October 1986, pp.25-29
- 72 **Nilsen, R. and Kazmierkowski, M.P.** *Reduced-order observer with parameter adaption for fast rotor flux estimation in induction machines* IEE Proc., Vol.136, Pt. D, No.1, January 1989, 35-43

- 73 **Smith, J.R., Stronach, A.F., Tsao, T. and Goodman, K.A.** *Prediction of dynamic response of marine systems incorporating induction-motor propulsion drives* PROC. IEE, Vol.127, Pt. B, No.5, September 1980, 308-315
- 74 **Abdel Hakim, M. M. and Berg, G. J.** *Dynamic single-unit representation of induction motor groups* IEEE Transactions on Power App. and Syst., Vol. PAS-95, No. 1, 1976, pp.155-161
- 75 **Ito, M., Okuda, H., Takahashi, N. and Miyata, T.** *Starting Current Analysis of Three-Phase Squirrel-Cage Induction Motor by Finite Element Method* Electrical Eng. in Japan, Vol. 99, No. 1, 1979, pp 36-42
- 77 **Kaizu, H.** *Determination of Equivalent Circuit Parameters for Calculating the Starting Transient Performance of Squirrel-Cage Induction Motors* Electrical Engineering in Japan, Vol. 93, No.3, 1973, pp.75-82
- 78 **Schuisky, W.** *Übergangsvorgänge bei Induktionsmaschinen* ASEA Research, No.2, 1959, pp.21-42
- 79 **Kovács, K. P. and Rácz, I.** *Transiente Vorgänge in Wechselstrommaschinen* Akadémiai Kiadó, 1959
- 80 **Kovács, K. P.** *Transient Phenomena in Electrical Machines* Elsevier, 1984

- 81 **Bausch, H., Jordan, H. and Weis, M.** *Digitale Berechnung des transienten Verhaltens von stromverdrängungsfreien Drehstrom-Käfigläufermotoren* ETZ-A, Bd. 89 (1968) H.15, pp. 361-366
- 82 **Novotny, D. W. and Wouterse, J. H.** *Induction Machine Transfer Functions and Dynamic Response by Means of Complex Time Variables* IEEE Trans. Power App. and Syst., Vol. PAS-97, No. 4, July/August 1978, pp.1430-1439
- 83 **Lees, M. J. and Tindall, C. E.** *Field-theory analysis of saturation harmonics in induction machines* PROC. IEE, Vol. 121, No. 4, April 1974, pp. 276-280
- 84 **Silvester, P. and Chari, M. V. K.** *Finite Element Solution of Saturable Magnetic Field Problems* IEEE Trans. on Power Apparatus and Systems, PAS-89, 1970, pp.5-32
- 85 **Poloujadoff, M.** *General rotating mmf theory of squirrel cage induction machines with non uniform air gap and several sinusoidally distributed windings* IEEE Transactions on Power Apparatus and Systems, Vol. PAS-101, No. 3, March 1982, pp.583-591
- 86 **Williamson, S. and Smith, A.C.** *Steady-state analysis of 3-phase cage motors with rotor-bar and end-ring faults* PROC. IEE, Vol. 129, Pt. B, No.3, 1982, pp93-100
- 87 **Carter, F. W.** *Air-Gap induction* Electrical World and Engineer, 1901, Vol. 38, No. 22, pp 884-888

- 88 **Carter, F. W.** *The magnetic field of the dynamo-electric machine*  
Journal of IEE, 1926, 64, pp. 1115-1138
- 89 **Hammond, P.** *The Calculation of the Magnetic Field of Rotating Machines. Part 3.- Eddy Currents Induced in a Solid Slab by a Circular Current Loop* IEE Monograph No. 514S, April 1962, pp. 508-515
- 90 **Lorenzen, H.-W.** *Der Einfluß der Stromverdrängung auf die erzwungenen Pendelungen von Asynchronmaschinen* ETZ-A, Bd. 88 (1967) H.18, pp. 445-451
- 91 **Bahr, K.** *Zur Theorie der Stromverdrängung in einer Maschinennut von rechteckigem Querschnitt* ETZ-A, Bd. 86 (1965) H.21, pp. 689-695
- 92 **Balchin, M.J. and Davidson, J.A.M.** *3-dimensional eddy-current calculation by the network method: Formulation using magnetic scalar potential for nonconducting regions* PROC. IEE , Vol. 130, Pt. A, No. 2, MARCH 1983, pp.88-92
- 93 **Swann, S.A. and Salmon, J.W.** *Effective Resistance and Reactance of a Solid Cylindrical Conductor Placed in a Semi-Closed Slot* IEE Monograph No. 527U, July 1962, pp. 611-615
- 94 **Alger, P. L.** *Induction Machines - Their Behavior and Uses* Gordon and Breach, 2nd Edition, 1970

- 95 **Weppler, R.** *Die Berechnung der Spaltstreuung bei Kurzschlußläufermotoren mit Berücksichtigung der Eisensättigung*  
Diss. Technische Hochschule Hannover, 1962
- 96 **Brown, J. E., Kovacs, K. P. and Vas, P.** *A Method of Including the Effects of Main Flux Path Saturation in the Generalised Equations of a.c. Machines* IEEE Trans on Power App. and Syst., Vol. PAS-102, No. 1, January 1983, pp. 96-103
- 97 **Oberretl, K.** *Magnetic Fields, Eddy Currents, and Losses, Taking the Variable Permeability into Account* IEEE Trans. on Power Apparatus and Systems, Vol. PAS 88, No. 11, November 1969, pp. 1646-1654
- 98 **Bausch, H., Buttkereit, H. and Jordan, H.** *Ständerstrom und Drehmoment ungeschrägter Asynchronmaschinen mit sättigungsabhängigen Kennwerten* ETZ-A, Bd. 89 (1968) H. 7, 160-164
- 99 **Engel, U. and Jordan, H.** *Über pendelmomentbildende Sättigungsfelder in Drehstrom-Asynchronmaschinen* ETZ-A Bd. 94 (1973) H.1, pp. 1-3
- 100 **Jimoh, A.A. and Findlay, R.D.** *Parasitic Torques in Saturated Induction Machines* IEEE Trans. on Energy Conversion, Vol.3, No.1, 1988, pp. 157-163
- 101 **Dabbous, A.A.** *Ermittlung des Kurzschlußstroms von ungeschrägten Asynchronmaschinen unter Berücksichtigung der Eisensättigung*  
ETZ-A Bd. 85 (1964) H3, pp. 76-79

- 102 **Dabbous, A.A.** *Sättigungseinfluß auf den Kurzschlußstromkennlinie von ungeschrägten Asynchronmaschinen* ETZ-A Bd. 85 (1964) H4, pp. 115-119
- 103 **Klingshirn, E. A. and Jordan, H. E.** *Polyphase Induction Motor Performance and Losses on Nonsinusoidal Voltage Sources* IEEE Trans. on Power Apparatus and Systems, Vol. PAS-87, No. 3, 1968, pp. 624-631
- 104 **Göl, Ö.** *Performance Analysis of Inverter/Induction Machine Drives* Proc. ICEM'82, International Conference on Electrical Machines, Budapest, Hungary, 1982, pp. 533-536
- 105 **Sliwinski, T.** *Harmonische Analyse des Magnetisierungsstromes von Drehstromasynchronmotoren* A.f.E.,59 (1977), pp.171-181
- 106 **Smith, G.** *Transients in A-C Motors and Generators* AIEE Transactions, Volume 65, May 1946, pp. 314-320
- 107 **Fallside, F. and Wortley, A.T.** *Steady-state oscillation and stabilisation of variable-frequency inverter-fed induction-motor drives* Proc. IEE, Vol.116, No.6,1969, pp.991-999
- 108 **Slemon, R.G.** *Modelling of Induction Machines for Electric Drives* IEEE Transactions on Industry Applications, Vol. 25, No.6, November/December 1989, pp. 1126-1131



- 109 **Ramsden, V. S., Zorbas, N. and Booth, R. R.** *Prediction of induction-motor dynamic performance in power systems* Proc. IEE, Vol. 115, No. 4, April 1968, pp. 511-518
- 110 **Hughes, F. M. and Aldred, A. S.** *Transient characteristics and simulation of induction motors* Proc. IEE, Vol. 111, No.12, December 1964, pp 2041-2050
- 111 **Smith, I. R. and Hamill, B.** *Effect of parameter variations on induction-motor transients* PROC. IEE, Vol. 120, No. 12, December 1973, pp.1489-1492
- 112 **Enslin, N. C., Kaplan, W. M. and Davies, J. L.** *Influence of transient switching currents and fluxes on the torque developed by a squirrel-cage induction motor* PROC. IEE, Vol. 113, No. 6, June 1966, pp.1035-1043
- 113 **Diana, G. and Harley, R. G.** *Transient Behaviour of Induction Motor Flux and Torque During Run-Up* IEEE Trans. on Energy Conversion, Vol.EC-2, No.3, September 1987, pp. 465-469
- 114 **Stern, R. and Novotny, D. W.** *A Simplified Approach to the Determination of Induction Machine Dynamic Response* IEEE Trans.Power App. and Syst., Vol. PAS-95, No. 4, July/August 1976, pp.1325-1335
- 115 **Richards, G. G. and Tan, O. T.** *Simplified Models for Induction Machine Transients under Balanced and Unbalanced Conditions* IEEE Trans. on Industry Applications, Vol. IA-17, No.1, January/February 1981, pp. 15-21

- 116 **Hanalla, A. Y.** *Analysis of Transient Field Problems in Electrical Machines Allowing for End Leakage and External Reactances* IEEE Trans. on Magnetics, Vol. MAG-17, No.2, March 1981, pp. 1240-1243
- 117 **Göl, Ö. and Kearney, D.** *Stress Analysis in the Cage of an Induction Motor* Journal of Electrical and Electronic Engineering Australia (in print)
- 118 **Maginniss, F. J. and Schultz, N. R.** *Transient Performance of Induction Motors* AIEE Trans., Vol. 63, 1944, pp.641-646
- 119 **Ku, Y. H.** *Transient Analysis of Rotating Machines and Stationary Networks by Means of Rotating Reference Frames* AIEE Trans., Vol. 70, 1951, pp.943-954
- 120 **Weygandt, C. N. and Charp, S.** *Electromechanical Transient Performance of Induction Motors* AIEE Transactions, Vol. 65, 1946, pp. 1000-1009
- 121 **Melkebeek, J. A. A.** *Magnetising-field saturation and dynamic behaviour of induction machines- Part 1: Improved calculation method for induction machine dynamics* PROC. IEE, Vol. 130, Pt. B, No. 1, January 1983, pp.1-9
- 122 **Melkebeek, J. A. A.** *Magnetising-field saturation and dynamic behaviour of induction machines- Part 2: Stability limits of a voltage-fed induction motor and of a self-excited induction generator* PROC. IEE, Vol. 130, Pt. B, No. 1, January 1983, pp.10-17

- 123 **Kovács, K. P.** *Untersuchung der transienten Vorgänge von Asynchronmotoren mit Hilfe von Analogrechnern* Acta Technica XXXIX/1-2 (1961), pp.215-241
- 124 **Matsuse, K. and Tagaki, K.** *Analog Simulation of Three-Phase Induction Motor by Use of Signal Flow Graph* Electrical Engineering in Japan, Vol. 90, No.2, 1970, pp.142-151
- 125 **Nasar, S. A. and Unnewehr, L. E.** *Electromechanics and Electric Machines* John Wiley & Sons, Second Edition, 1983
- 126 **Chalmers, B. J. and Dodgson, R.** *Waveshapes of flux density in polyphase induction motors under saturated conditions* IEEE Trans., 1971, PAS-90, pp.564-569
- 127 **Ghani, S.N.** *On simulating dynamic behaviour of three phase induction machines with squirrel cage rotor* Simulation 50:5, 182-193
- 128 **Weh, H. and Meyer, J.** *Die direkte Berechnung von Strom und Drehmoment bei Asynchronmaschinen* ETZ-A, Bd. 87 (1966) H.14, pp. 504-512
- 129 **Mittal, M. and Ahmed, N.U.** *Time Domain Modeling and Digital Simulation of Variable-Frequency AC Motor Speed Control Using PLL Technique* IEEE Trans. on Industry Applications, Vol. IA-19, No.2, March/April 1983, pp. 174-180
- 130 **Freeman, E.M.** *The Calculation of Harmonics, due to Slotting, in the Flux Density Waveform of a Dynamo-Electric Machine* IEE Monograph No. 523U, June 1962, pp. 581-588



## APPENDICES

### A.1 Calculation of Equivalent Coil Pitch

In the case of windings, in which the number of slots per phase belt is an integer, the m.m.f. distribution over a pole period is identical, regardless whether the winding comprises identical coils with the same coil pitch or axisymmetric coils with varying coil pitch. Therefore, any winding with identical coils can be evaluated by its substitute winding with axisymmetric coils.

The m.m.f. distribution, which is valid for both types of winding, is illustrated in Figure A.1. Table A.1 shows the correspondence between the coil pitch  $\tau_c$  for identical coils and its fictitious equivalent in terms of an axisymmetric coil. Thus, the fictitious equivalent coil pitch for the identical coils of a phase belt can generally be obtained as

$$\tau_{c_b} = \tau_c - (q-a) \kappa^s \quad (\text{A.1})$$

where

$$a = 2 \underline{b} - 1 \quad (\text{A.2})$$

with

$$\underline{b} = 1, 2, \dots, q \quad (\text{A.3})$$

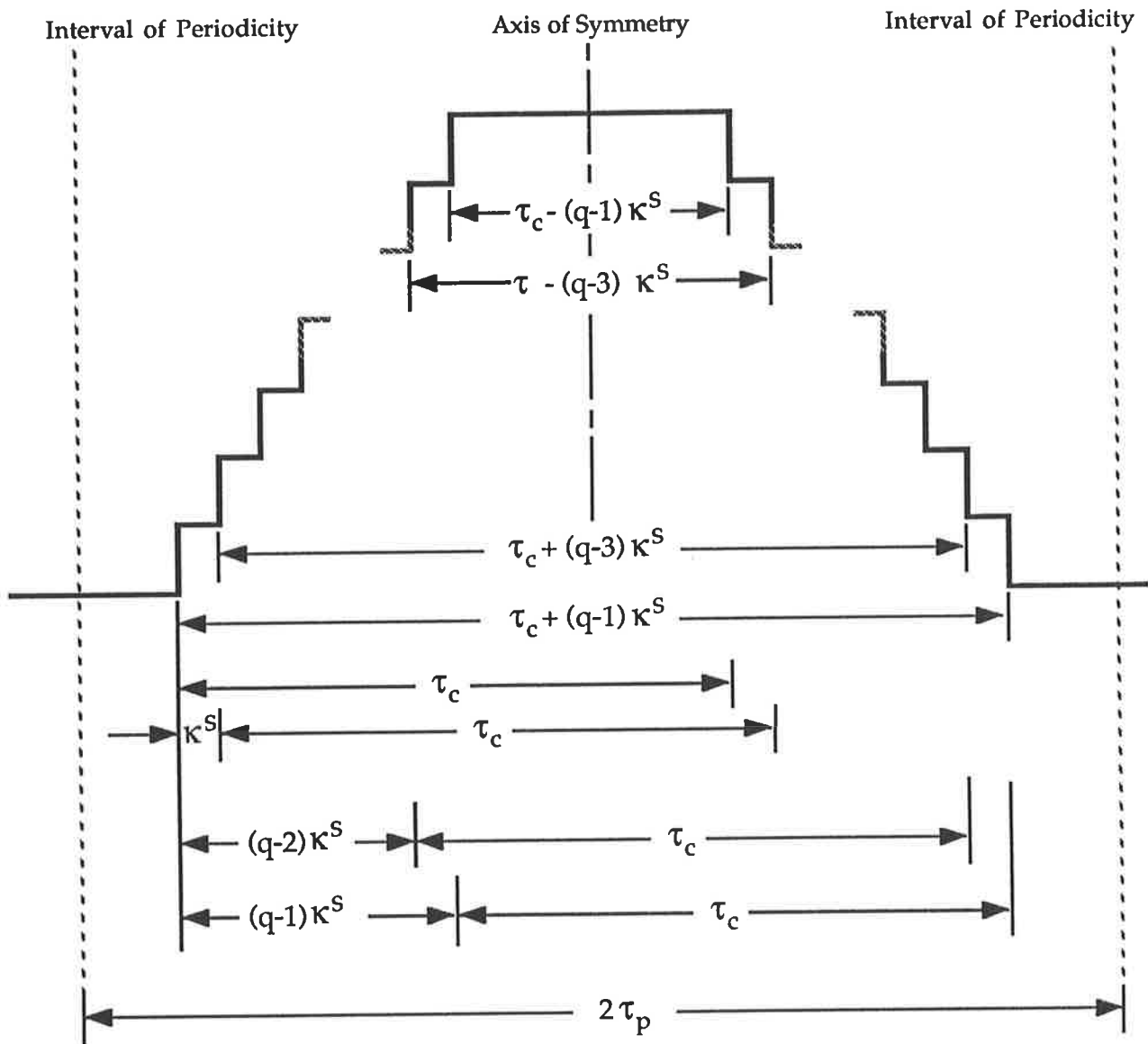


Figure A.1

m.m.f. distribution due to a single phase belt where  $q = \text{integer}$ , valid for both identical and axisymmetric coils

Table A.1

Number of coils per phase belt (q)	Coil Pitch	
	Axisymmetric Coils	Axisymmetric Equivalent for Identical Coils
1	$\tau_{c1}$	$\tau_c$
2	$\tau_{c1}$ $\tau_{c2}$	$\tau_c - \kappa^S$ $\tau_c + \kappa^S$
3	$\tau_{c1}$ $\tau_{c2}$ $\tau_{c3}$	$\tau_c - 2\kappa^S$ $\tau_c$ $\tau_c + 2\kappa^S$
4	$\tau_{c1}$ $\tau_{c2}$ $\tau_{c3}$ $\tau_{c4}$	$\tau_c - 3\kappa^S$ $\tau_c - \kappa^S$ $\tau_c + \kappa^S$ $\tau_c + 3\kappa^S$
.	.	.
.	.	.
q	$\tau_{c1}$ $\tau_{c2}$ $\tau_{c3}$ . . $\tau_{cq-1}$ $\tau_{cq}$	$\tau_c - (q-1)\kappa^S$ $\tau_c - (q-3)\kappa^S$ $\tau_c - (q-5)\kappa^S$ . . $\tau_c + (q-3)\kappa^S$ $\tau_c + (q-1)\kappa^S$

## A.2 Machine I - Details

### A.2.1 Name Plate Details (Machine I)

Voltage	380V
Frequency	50Hz
Winding Connection	$\Delta$
Shaft Output Power	140kW
Rating	Continuous
Current	250A
Speed	2970rpm

### A.2.2 Core Details (Machine I)

Core Length	0.250m
Stator Outer Diameter	0.453m
Stator Bore Diameter	0.264m
Rotor Outer Diameter	0.262m
Shaft Diameter	0.090m
Number of Stator Slots	48
Number of Rotor Slots	40
Material	Silicon Steel (3W/kg)



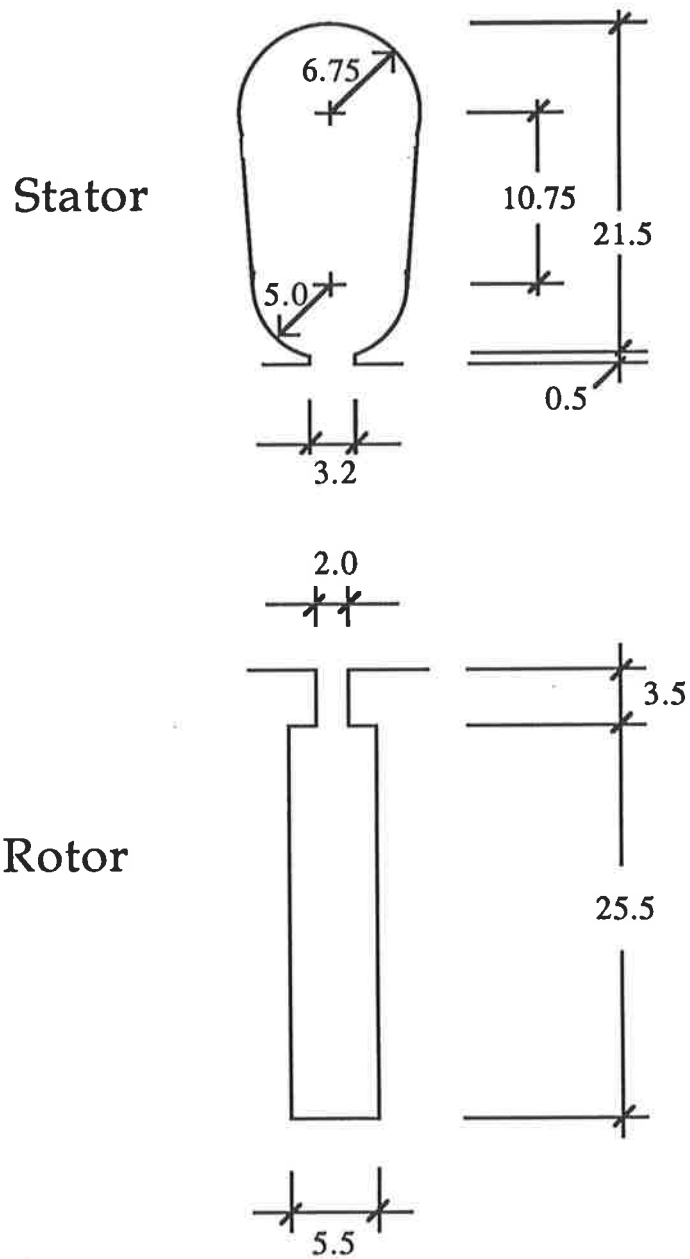


**Figure A.2**

Slot topology for Machine I

(Approximate Scale 2:1)

(All dimensions in mm)

### A.2.3 Stator Winding Details (Machine I)

Type of Winding	Single Layer
Type of Coil	Axisymmetric
Coil Pitch	1:18-20-22-24
Number of Turns	32
Number of Conductors per Turn	6
Number of Parallel groups	2
Conductor Diameter	$1.55 \times 10^{-3} \text{m}$

## A.2.4 Machine Data and Principal Model Parameters (Machine I)

### Machine Data

<b>Stator</b>		<b>Rotor</b>	
No. of stator slots	48	No. of rotor slots	40
Pole pitch (m)	0.414	Bar Length (m)	0.28
Coil pitch (m)	0.414	Bar X-section (m <sup>2</sup> )	0.000125
		Conductivity (Sm <sup>-1</sup> )	42000000
		End-ring Diameter (m)	0.230
No. of poles	2	Ring X-section (m <sup>2</sup> )	0.00063
No. of turns	32	Skewing (m)	0.035
Slot height(m)	0.01075	Slot height(m)	0.0255
Slot width(m)	0.01150	Slot width(m)	0.0055
Slot opening width(m)	0.00320	Slot opening width(m)	0.0020
Slot opening height(m)	0.00050	Slot opening height(m)	0.0035
Slot type	oval	Slot type	prismatic

### Winding Factors

Harmonic order	1	5	7	11	13
Skew factor	0.9970634	0.9281237	0.8620769	0.6804331	0.5722593
Distribution factor	0.9556118	0.1944379	-0.14131	-0.094791	0.0831294
Coil-pitch factor	1	1	-1	-1	1
Slot opening factor	0.9999998	0.9999962	0.9999926	0.9999817	0.9999744
Resultant winding factor	0.9528054	0.1804617	0.1218195	0.0644977	0.0475704
Winding factor ratio	1	0.1894004	0.1278535	0.0676924	0.0499266

## Model Parameters (Base Values)

### Rotor Resistances

Harmonic order	1	5	7
Eff. turns ratio	4.5734659	0.8662162	0.5847338
Bar resistance (referred)	0.014874	0.0005336	0.0002431
Ring resistance (referred)	0.0154647	2.332E-05	5.7E-06
Total cage resistance/phase	0.0303387	0.0005569	0.0002488

### Magnetising Reactances (unsaturated)

Harmonic order	1	5	7
Magnetising reactance	12.12	0.4347747	0.1981199

### Stator Differential Leakage Reactances (unsaturated)

Harmonic order	1	5	7
"Differential" reactance	0.0889204	-	-

### Rotor Differential Leakage Reactances (unsaturated)

Harmonic order	1	5	7
"Differential" reactance	0.6416431	0.0942277	0.1007085

### Stator Slot Leakage Reactances

Harmonic order	1	5	7
Slot leakage reactance	0.0266000	-	-

### Rotor Slot Leakage Reactances

Harmonic order	1	5	7
Slot leakage reactance	0.0906250	0.0032500	0.0014788

### Stator Coil-End Leakage Reactances

Harmonic order	1	5	7
Coil-end leakage reactance	0.1860000	-	-

**Skew Leakage Reactances (included in rotor)**

Harmonic order	1	5	7
Skew leakage reactance	0.0690000	0.0690000	0.0690000

**Rotor Resistances**

Harmonic order	1	5	7
Eff. turns ratio	4.5734659	0.8662162	0.5847338
Bar resistance (referred)	0.014874	0.0005336	0.0002431
Ring resistance (referred)	0.0154647	2.332E-05	5.7E-06
Total cage resistance/phase	0.0303387	0.0005569	0.0002488

**Core Loss Components**

Harmonic order	1	5	7
Stator core loss	205.913	0.257	0.052
Rotor hysteresis loss	594.824	4.100	0.999
Rotor eddy current loss	2796.920	3.860	0.671

### A.3 Machine II - Details

#### A.3.1 Name Plate Details (Machine II)

Voltage	240V
Frequency	50Hz
Winding Connection	Y/ $\Delta$ <sup>5</sup>
Shaft Output Power	1kW
Rating	Continuous
Current	8A
Speed	2880/1435rpm

#### A.3.2 Core Details (Machine II)

Core Length	0.100m
Stator Outer Diameter	0.165m
Stator Bore Diameter	0.086m
Rotor Outer Diameter	0.0853m
Shaft Diameter	0.0255m
Number of Stator Slots	18
Number of Rotor Slots	22
Material	Silicon Steel (3W/kg)

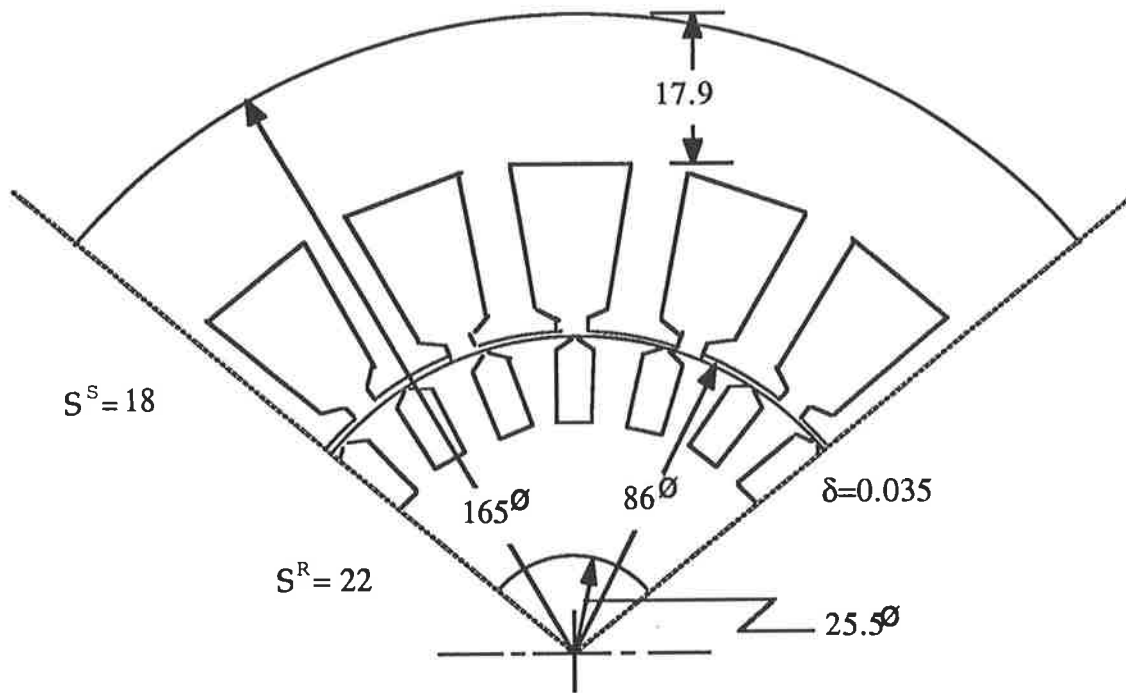


Figure A.3  
Core topology for Machine II  
(approximate scale 1:1)

### A.3.3 Stator Winding Details (Machine II)

Type of Winding	Double Layer, P.A.M. <sup>10</sup>
Coil Type	Identical
Coil Pitch	1: 6
Number of Turns	12
Number of Conductors per Turn	5
Parallel Groups	1
Conductor diameter	$0.35 \times 10^{-3} \text{m}$

---

<sup>10</sup>pole amplitude modulated



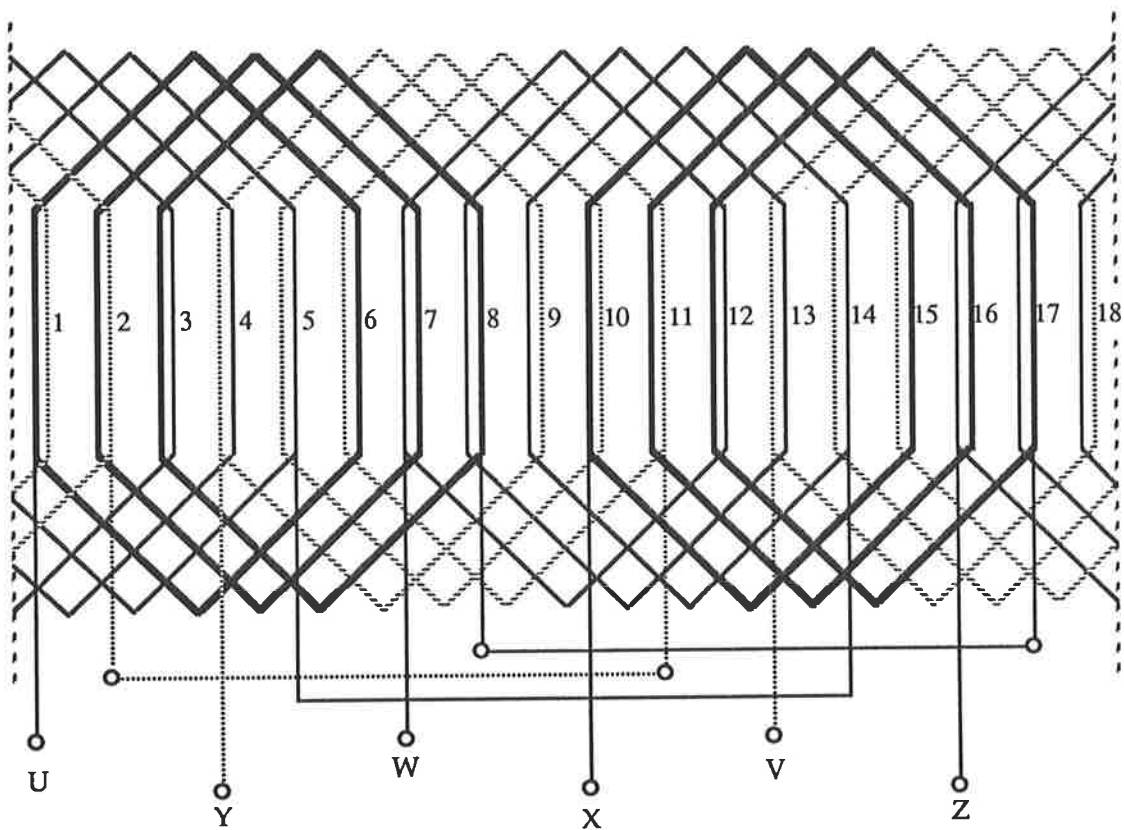


Figure A.4

Complete winding connection diagram for Machine II  
 showing the 2-pole connection of the double-layer P.A.M.  
 winding

### A.3.4 Model Parameters (Machine II)

#### Resistances

Stator Coil Resistance	$R_j^s$	0.231 $\Omega$
Rotor Bar Resistance	$R_b^r$	55.8 $\times 10^{-6}\Omega$
Rotor End-Ring-Segment Resistance <sup>11</sup>	$R_r$	3.04 $\times 10^{-6}\Omega$

#### Stator Inductances

Stator Airgap Inductance	$L_{\delta, j, j}^s$	2.399 $\times 10^{-3}\text{H}$
Stator Slot Leakage Inductance	$L_{s, j, j}^s$	59.4 $\times 10^{-6}\text{H}$
Stator Coil-End Leakage Inductance	$L_{ce, j, j}^s$	9.8 $\times 10^{-6}\text{H}$
Stator Self Inductance	$L_{j, j}^s$	2.468 $\times 10^{-3}\text{H}$

#### Rotor Inductances

Rotor Airgap Inductance	$L_{\delta, k, k}^r$	3.5 $\times 10^{-6}\text{H}$
Rotor Slot Leakage Inductance	$L_{s, k, k}^r$	3.6 $\times 10^{-6}\text{H}$
Rotor End-Ring Leakage Inductance <sup>12</sup>	$L_{ce, k, k}^r$	5.2 $\times 10^{-9}\text{H}$
Rotor Self Inductance	$L_{k, k}^r$	7.105 $\times 10^{-6}\text{H}$

#### Mechanical Parameters

System Inertia	J	0.025 kg m <sup>2</sup>
Damping Coefficient	D	0.0007 kg m <sup>2</sup> s <sup>-1</sup>

<sup>11</sup> for the end-ring segment between two neighbouring rotor bars

## INDEX

- airgap flux, 21,41,160  
airgap m.m.f., 23,29  
apparent slot opening, 82, 274  
Bashkow A matrix, 120  
Carter's factor, 41  
chording, 28  
coil-end length, 145, 147, 173  
coil group, 29  
coil group factor, 32  
coil pitch, 29  
coil pitch factor, 33  
connection matrix, 237,323  
constant matrix, 121  
coordinate transformation, 128,  
131  
Crank-Nicolson method, 13  
current displacement, 48  
current harmonics, 87,91  
current vector, 20,123  
damping coefficient, 115,257  
die-cast rotor, 51  
deep-bar, 49  
differential leakage reactance, 48,  
83, 96  
direct-on-line starting, 49, 113,  
258, 296  
discrete circuit modelling, 17, 21,  
135  
distribution factor, 33  
double-layer winding, 185  
double-cage, 170, 195  
dynamic modelling, 112, 119, 135  
eddy-current losses, 64  
efficiency, 102

- enhanced low-order model, 274
- equivalent coil pitch, 32, 414
- finite element analysis, 13, 20, 112
- flux displacement, 66
- frequency sensitivity, 72
- Helmholtz equation, 53
- full-pitch coil, 28
- harmonic truncation, 46
- hysteresis losses, 63
- high fidelity modelling, 23, 47, 82
- inductance
  - airgap, 148, 156, 162
  - coil-end leakage, 171
  - differential leakage, 48, 83, 274, 285
  - mutual (see mutual inductance)
  - self, 117, 142, 148, 186
  - skew leakage, 83
  - slot leakage, 148, 162, 167, 170
- input vector, 119, 120
- Lagrange's equation of motion, 110
- Lagrangian moment, 110
- Laplacian, 50
- lamination thickness, 64
- L'Hôpital's rule, 39
- low-order model, 15, 269
- magnetising reactance, 45
- magnetomotive force, 23, 30, 35, 143, 153, 160
- Maxwell's equations, 8
- model reduction, 98
- moment of inertia, 247
- mutual inductance
  - cage winding, 189
  - coils of a winding, 174, 180
  - double-layer winding, 181
  - phases, 117
- mutual inductance (between stator and rotor)
  - cage rotor, 215
  - cage rotor, skewed, 222
  - wound rotor, 196
- non-linearities, 11, 23, 87, 114, 119
- numerical methods 10, 18, 77
- output vector, 119
- P.A.M.-winding, 317, 325
- parasitic torques, 11, 250, 375
- partitioning ratio, 24, 151, 154, 160
- penetration depth, 42, 53, 68, 83
  - laminations, 68
  - rotor bar, 53
- permeance, 15, 79, 122, 141, 143
  - airgap, 150, 155
  - coil-end leakage, 172, 174

- end-ring leakage, 173
- slot leakage, 168
- permeance coefficient, 167, 180, 185, 195, 207
  - (see also: permeance)
- phase belt, 29, 34
- phase belt pitch, 34
- pole amplitude modulation,
  - (see: P.A.M.-winding)
- Poisson's equation, 76, 162
- Poynting vector, 11
- Raleigh dissipation function, 111
- reference frame, 16, 110, 112, 127, 132
- relative coil pitch, 27, 30, 43
- reluctivity, 13
- resistance
  - coil, 144
  - end-ring, 145
  - rotor bar, 12, 49, 145
  - rotor mesh, 146
- rotor asymmetry, 318
- Runge-Kutta method, 18, 327
- saturation, 76
- shaft deflection, 247
- shearing method, 79
- single-layer winding, 30
- secondary armature reaction, 46
- skewing, 83, 133, 222, 317, 328
- slot opening width, 24, 79, 150, 274
- slot height, 165
- slot pitch, 78, 155, 159, 161
- state-space models, 119
- slot region, 12
- space phasor, 112, 122, 311
- space harmonics, 23
- state variables, 120
- state vector, 119
- step-size, 327
- supply harmonics, 88
- supply model, 90
- time harmonics, 16, 23, 82, 91
- torque, 101, 105, 110, 131, 242
- truncation criterion, 47
- unit vector, 125
- vector magnetic potential, 9
- virtual work, 242
- winding factor, 47, 290